A Multi-scale Study of Ancient Ceramics Using a Series of Analytical Techniques

Wang Tian

Université de Toulouse

THÈSE

En vue de l'obtention du

DOCTORAT DE L'UNIVERSITÉ DE TOULOUSE

Délivré par :

Institut National des Sciences Appliquées de Toulouse (INSA de Toulouse)

Présentée et soutenue par :
WANG TIAN

Le 14/12/2016

Titre :

A Multi-scale Study of Ancient Ceramics Using a Series of Analytical Techniques

---

ED SDM : Physique de la matière - CO090

Unité de recherche :

CEMES-CNRS

Directeur(s) de Thèse :

Sciau Philippe, Directeur de Recherche CNRS Toulouse, CEMES

Rapporteurs :

BOUQUILLON Anne, Ingénieur de recherche, C2RMF
GOUDEAU Philippe, Directeur de recherche, Institut Pprime

Autre(s) membre(s) du jury :

JUBIER-GALINIER Cécile, Maître de conférences, Université de Perpignan - Examinateur
MALFANT Isabelle, Professeur, Universite Paul Sabatier - Examinateur
ROQUE-ROSELL Josep, Professeur adjoint, Universitat de Barcelona - Examinateur

Acknowledgments

Firstly, I would like to express my sincere gratitude to my supervisor Prof. Philippe Sciau and our collaborators, Prof. Corinne Sanchez, Prof. Cécile Galinier, Prof. Zhu Tiequan, Prof. Karen Trentelman and Prof. ZhangMaolin. Three years ago, I contacted with Prof. Philippe Sciau by email to express my will of conducting the thesis with him and got his welcomed reply soon. It is this reply that permitted me to have passed a meaningful period in France. During this period, I have opportunity to work with Prof. Philippe Sciau and with his professionalism he provided a lot of professional advises to me to perform the work, including how to learn the background of the subject effectively, how to understand the issues, how to look for the solutions to solve the issues and how to perform the work and express the results to others (how to explain the profound theories in a simple way, how to prepare a clear oral presentation and write a well-founded article). Under his guidance and support, I have been able to get insight into the subject: study of ancient ceramics and, more important, I find my own interest career which I would like to work for whole life. Besides, I am also so grateful to Prof. Corinne Sanchez, Prof. Cécile Galinier, Prof. Zhu Tiequan and Prof. Zhang Maolin for that they friendly have shared their rich archaeological experiences and precious ceramic fragments with us. Thanks to this agreeable and highly effective cooperation, I was able to successfully complete my doctoral thesis.

Secondly, I would like to express my great gratitude to my colleagues in CEMES: Magali Brunet, Audrey Cochard, Ariane Pinto, Xiao Tingting, Fu Xiaoxiao, Nie Chunyang, Wang Rongrong for their support and encouragement to me for the period in the laboratory. Especially, Magali Brunet, Audrey Cochard and Xiao Tingting, they have not only supported and encouraged me to work but also shown great kindness and friendship to my daily life. More than colleagues, they are my French family that I can share my happiness and sorrow of work and life with them. The same importantly, I would like to express my sincere thanks to my friends of the Chinese program UT-INSA: Wu Zhenjun, Xue Rui, Zhao Yu, Wang Yiwei, Gao Yanfeng, Li Tao, Yang Zhuo There were many things we came over together or I came over under their help. Especially, Wu Zhenjun and Xue Rui, as the senior Ph.D. students, they helped me to adapt to French life as soon as possible with their great patience and support.

Thirdly, I am so grateful to the service persons of CEMES, ESRF (Grenoble, France), SSRL (California, USA) and Sun Yat-sen University (Canton, China). In the laboratory CEMES, Cathy Crestou, Dominique Lamirault and Robin Cours, who work in the preparation room, have always been helpful and provide a lot of help

and support to me; Christophe Deshayes, who is responsible for SEM-EDS, taught me how to use the technique and treat the SEM-EDS data; Sébastien Moyano and Frédéric Neumayer, who are responsible for Raman spectroscope, have always debugged the technique to the best condition when I perform the experiments; Nicolas Ratel-Ramond, who is responsible for XRD, taught me how to use the technique and also help me prepare the Tomo-sample; Florent Houdellier, Sébastien Joulie and Cécile Marcelot, who are responsible for TEM, taught me the theory of TEM and organized the practical TEM training with their professionalism and patience; Elodie Jean-Alphonse, the receptionist of CEMES, her smile face always makes me feel happy every work day. Also, other service colleagues in CEMES, who I am familiar with but do not know their name, I am so grateful to them for their support in the passed three years. The same importantly, I would like to thank Marine Cotte, Emeline Pouyet and Barbara Fayard, who work in ESRF, Grenoble, France. Every time we arrived in Grenoble, we felt so welcomed worked with them and more important, they always supported us obtain interesting data with they professional knowledge. Besides, I also would like to thank Apurva Pouyet, who works in SSRL, California, USA, for teaching me how to treat the full-field XANES data using TXM-Wizard software.

Fourthly, I would like to express my sincere gratitude to my master instructors Prof. Wang Hao (Hubei University, Wuhan, China), Prof. Zhang Jun (Hubei University, Wuhan, China) and my friend, Tang Linhui, Tan Wei. In 2012, it was Prof. Wang Hao who informed me this French Ph.D. position that may interest me. Under his support, I successfully passed the examinations of Ph.D. and obtained the Chinese scholarship to France. Besides, Prof. Zhang Jun, obtaining her Ph.D. in England, provided a lot of useful advises to me with her rich experiences.

Finally, I would like to thank greatly every member of my family for their understanding and supporting all along, especially, my mother, An Maiping and my husband, Jia Fangchao. Mrs. An Maiping, as the mother of whole world, have always expressed her selfless affection to me and encourage me to come over every difficulty. Although she had not been France with me, she had never moved her eyes on me. During the period when I were in California, the period when I were in Wroclaw, the day when I defended my thesis , she held the same feelings with me and besides encouragement, she always gives me a great comfort. Therefore, I would like to thank Mrs. An Maiping and tell her, “You are the greatest mother in the world!” The same importantly, I would like to express my great gratitude to Mr. Jia Fangchao. All along, he has helped me take care of my parents attentively, which let me not have to worry about them. Meanwhile, he has always shown his great understanding, extraordinary patience, remarkable toleration and spiritual and

material support to me. Although he has not accompanied with me in France, his heart has always been with me. Also, I sincerely thank Mr. Jia Fangchao for his three-year waiting.

This work was financially supported by the China Scholarship Council, the XU GUANGQI 2015 (No.: 34389UD), the PHC CAI YUANPEI 2016 (No. 36708RD) program, the National Science Foundation of China (No. 41103013), and the ARCHIMEDE Labex program: IA-ANR-11-LABX-0032-01.

Abstract:

Ceramic artifacts have a long history and have been discovered worldwide. Their conservations are rarely impacted by the burial sites. Thus, they are ideal materials for understanding the human history and culture. The main archaeological studies concerning ancient ceramics contains provenance (dating, workshop, trade), raw materials (identification, origin), manufacturing process and utilization (analysis of content residues). For my work, I focused on the investigation of the manufacturing process.

The main steps of fabrication process of ancient ceramics is composed of selection of raw materials, preparation (leaching, purification, body, glaze or slip, pigments), shaping (the plastic paste is shaped to the lathe or using the molds). Then, there are two possibilities: either the vase is fired before the decoration stage, or the decoration is applied to the raw vase. To finish, the whole is fired. My objective is to obtain information on the manufacturing process by analyzing the structure of ancient ceramics, and in particular the structure of decorative layers. The structure of ancient ceramics is complex with heterogeneities at different scales (mm to nm). A decorated ceramic generally is composed of a body and a coating, which including of the decoration. The coating could contain different natures. The thickness can be variable from mm to nm. The decorative layer can be a part of the coating or the whole coating. The decorative layer can be constituent of an amorphous vitrified phase and diverse crystals, such as colorant crystals, feldspar, quartz, etc., of which the size varies from several microns to nanometer. The description of such structure requires the analysis at high resolution (nm) with large representative zone (often, several mm^3). It is difficult to realize.

In my work, I proposed an alternative approach. The approach is based on three stages. Firstly, the rapid investigations (principally, optical microscopy) at low resolutions are effected to analyze and select the zone requiring analysis at high resolution. Secondly, the selected zone is analyzed at high resolution by appropriate techniques according to the information sought. Thirdly, I try to construct the structure of the object based on the partially data, and therefore deduce the manufacturing process. I will illustrate this approach through three examples. The first one concerns the yellow pigment of the Roman marbled terra sigillata (Chapter III). The second one is about the firing process of Attic potteries (Chapter III). The third one concerns the color variations of blue decoration of Qinghua porcelains (Chapter IV).

Key words: Ancient ceramics; Terra sigillata; Attics; Qinghua porcelains; Synchrotron radiation; FF-XANES; Raman spectroscopy; SEM-EDS

Résumé:

Les artefacts en céramique ont une longue histoire et ont Récupérées dans presque toutes les régions du monde. La conservation n'est que rarement impactée par le milieu d'enfouissement. Donc, ils sont des matériaux idéaux pour comprendre l'histoire et la culture de homme. Les principales études archéologiques sur les céramiques anciennes concernent la provenance (datation, atelier, commerce), les matières premières (identification, origine), le processus de fabrication et l'utilisation (analyse des résidus de contenu). Mon travail porte plus précisément sur le processus de fabrication.

Les principales étapes du processus de fabrication sont: la sélection des matières premières, la préparation, le façonnage, salle de bains, sur deux possibilités. Soit le vase est cuit avant l'étape de décoration, soit la décoration est appliquée sur le vase cru. Pour finir, l'ensemble est cuit. Mon objectif est d'obtenir des informations sur le procédé de fabrication en analysant la structure des céramiques anciennes, et en particulier, la structure des couches décoratives. La structure des céramiques anciennes est c Une structure complexe en couches avec des hétérogénéités à différentes échelles (mm à nm). Une céramique décorée est généralement composée d'une pâte et d'un revêtement, y compris de la décoration. Le revêtement peut contenir des natures différentes. L'épaisseur peut être variable de mm à nm. La couche décorative peut être une partie ou du tout la revêtement. La couche décorative peut être constitutive d'une phase vitrifiée amorphe et divers cristaux, tels que cristaux colorants, feldspath, quartz, etc., dont la taille varie de plusieurs microns à nanomètre. La description de cette structure nécessite l'analyse à haute résolution (nm) avec grande zone représentative (souvent plusieurs mm^3). C'est difficile à réaliser.

Dans mon travail, j'ai proposé une autre approche. L'approche est basée sur trois étapes. Premièrement, les analyses rapides (principalement microscopie optique) à faibles résolutions sont effectuées pour analyser et sélectionner la zone nécessitant une analyse à haute résolution. Ensuite, la zone sélectionnée est analysée à haute résolution par des techniques appropriées en tenant compte des informations recherchées. Troisièmement, on essaie de construire la structure de l'objet sur la base des données partielles, et d'en déduire le processus de fabrication. Je vais illustrer cette approche par trois exemples. La première concerne le pigment jaune de la terre sigillée marbrée romaine (chapitre III). Le second concerne le processus de cuisson des poteries attiques (chapitre III). Le troisième concerne les variations de couleur de la décoration bleue des porcelaines Qinghua (chapitre IV).

Mots clés: Céramiques anciennes ; Terra sigillata; Attics ; Porcelaine Qinghua ; Rayonnement synchrotron ; FF-XANES; Spectroscopie Raman ; MEB

Table of Content

Chapter I General Introduction

1 Ceramic artifacts in archaeology

Ceramic artifacts, made out of clay and then hardened by heat, were the first synthetic material created by humans with unique ingenuity (Lawrence and West 1982; Li 1998; Rice 2015). The history of ceramics encompasses roughly twenty thousand years. The oldest ceramics can be dated back to at least 25,000 BC, discovered at Dolni Vestonice and Pavlov in Moravia sites (Czech Republic) (Vandiver et al. 1989; Bougard 2011). They were the famous Gravettian ceramics with the form of human and animal figurines (Figure 1.1).

Figure 1.1 Replica of the Venus of Lespugue, a Venus figurine, a statuette of a nude female figure of the Gravettian, dated to between 26,000 and 24,000 years ago; France, Musée de L'Homme, Paris. (Credit: Public Domain)

But the first appearance of pottery vessels was at the end of the Paleolithic period or soon thereafter, which was interpreted as marking the movement of human societies from “Upper Savagery” into “Lower Barbarism” (Morgan 1877). Until the settlement of human beings during Neolithic period, potteries were started to be frequently used, such as the potteries painted with red-and-black geometric decorations discovered in Yangshao villages of China, dated from around 5000 BC to 3000 BC (Li 1998). After 4,000 BC, the general technique for ceramic production was gradually well known to potters and many manufacture techniques were developed, which intensively increased the pottery productions, such as the innovations of potter’s wheel and mold (Hofmann 1971; Roux and Miroschedji 2009). Two famous cases are Greek figured pottery (manufactured during the sixth through fourth centuries BC in Athens) (Noble 1960; Folsom 1975) and Roman red gloss pottery (dated from the first century BC to the fourth century AD) (Oswald and Pryce 1920), which represent the outstanding technique achievement (Figure 1.2).

Figure 1.2 Left photo: Greek black figured pottery, 440-430 BC, produced in Athens, now conserved in Staatliche Antikensammlungen, Munich; right photo: Roman red gloss terra sigillata bowl with relief decoration (Credit: World Imaging, CC BY-SA 3.0)

During 14th century BC, the stonewares productions were created because of the development of the kiln. For instance, Chinese stonewares made during the Middle Shang period (15th -14th century BC) was produced in the kiln capable of reaching 1200 °C (Li 1998). At around the same time, glazes appeared and were used to cover vessels by a “natural kiln glost” and protected them from wood ash during the firing (Rice 2015). With the development of manufacture techniques, the most enduring legacy of potters, i.e. porcelains, appeared during the Tang dynasty (7th to 10th century AD) in China (Li 1998), such as Tang Sancai (Figure 1.3). But it is during the Song and Yuan dynasty (10th to 14th century AD) that the porcelain productions reached their finest development. During the Ming and Qing dynasty (14th -17th century AD), the productions were massively produced and spread to the whole world (Li 1998). One of famous Chinese porcelains is blue and white porcelain (Figure 1.3), identified by its transparent glaze with undergalzed blue decors (Li 1998). The export of Chinese porcelains to European heavily influenced the manufacture industry of local productions. For instance, in Delft, Netherlands, blue and white ceramics taking their designs from Chinese export porcelains made for the Dutch market were produced in large numbers throughout the 17th century (Jorg 1984; Moore 2009).

Figure 1.3 Sancai glazed ceramic horse, Tang Dynasty of China, 7th-8th Century, photographed at the Musée Guimet, Paris, France.

Besides the long history and the recovery of ancient ceramics in almost all parts of world, their presence is rarely restricted by geological or environmental situations or conditions of preservations. Although a vessel may break, its fragments may survive for millennia due to their non-perishability as a function of the physical properties. Therefore, ancient ceramics are an ideal material for scientists to understand the history and culture of human beings.

Ceramic artifacts have been studied from various points of view, including artistic, aesthetic, classificatory, mineralogical, and chemical (Li 1998; Tite 2008; Rice 2015). In particular, many archaeological researches have been devoted to study the chemical and mineral composition of ancient ceramics to identify their date, origin, the raw materials and manufacture process and to finally get an insight into the history and culture of human beings (Li 1998; Tite 2008; Rice 2015; Sciau and Goudeau 2015). For example, the earliest large-scale pottery provenance study, using optical emission spectroscopy, was the chemical analysis of Minoan and Mycenaean painted pottery (Catling et al. 1963; Catling and Millett 1965) and the results indicated that during the period from 1400 BC to 1200 BC, the Mycenaeans were the dominant mercantile power in the eastern Mediterranean, exporting pottery to Melos, Chios, Cyprus, Rhodes, Syria (Tell Atchana) and Egypt (Amarna). My work is precisely focused on the manufacturing process of ancient ceramics.

The principle procedure of manufacturing process is illustrated as Figure 1.4. It contains the selection of raw materials, the preparation of raw materials (including of washing the raw materials to obtain fine clay, preparing the body mixture, the glaze or slip liquid and pigment compounds, etc.) and shaping the body on the wheels by hands or using a mould. Then, there are two possibilities: either the vase is applied directly by decoration or the vase is pre-fired to be biscuit before the application of decoration. Finally, the decorated vase is fired in

the kiln to obtain a beautiful object.

Figure 1.4 The flow diagram of the manufacturing process of ceramics.

My aim is to obtain the information concerning manufacturing process by analyzing the structure of ancient ceramics, in particular, the structure of decorative layers. From a Material Science viewpoint, the structure of pottery is a rather complex layered structure with heterogeneities at different scales (nm to mm) (Figure 1.5). A typical ceramic generally contains a body and a coating (slip or glaze). The coating could be composed of different natures. The thickness of coating is variable, which can vary from tens of microns to hundreds of microns. The coating contains bubbles and/or cracks and the decorative layers. The decoration can be a part of the coating or the whole coating. The decoration is composed of an amorphous phase and diverse crystals, such as colorant crystals, feldspars etc., of which the size can vary from several microns to nanometer. The description of this type of structure requires the scan of a large (representative) volume (several mm^3) at high resolution (nm). This approach is actually difficult to perform. Therefore, I try to propose an alternative approach in my work. The approach is based on a selection of sampling and analytical techniques. Firstly, rapid investigations at low resolution (often optical observation) are used to select and define the zones requiring higher resolution investigations. Secondly, the selected zones are analyzed with high resolution by appropriate techniques taking into account the information sought. Finally, based on the data obtained, I try to reconstruct the structure of the objects and thus deduce the information concerning manufacturing process. It is also obvious that the number of sampling and the involved techniques must be small and for this, it is necessary to include in the selection the type of required information.

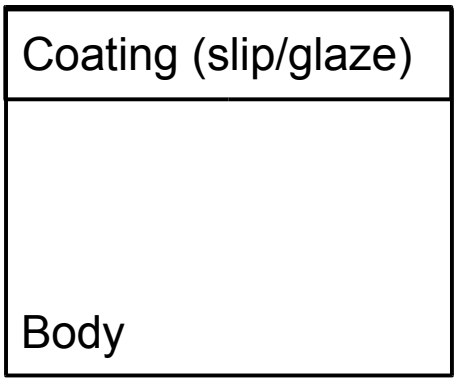

Figure 1.5 Schematic diagram of the structure of ancient ceramics.

2 Content of this work

In the following chapters, Chapter II describes the implementation of the approach in detail. A variety of sample preparations were designed and diverse analytical techniques with different probe sizes were selected to achieve the approach. Then, different methodological strategies were developed specific to two different classes of ancient ceramics, shown in Chapter III and Chapter IV, respectively. The first class was related to the investigation of potteries with iron rich slip: Roman marbled terra sigillata and Attic black gloss potteries (Chapter III). The second class was related to the study of porcelains made by cobalt materials: Chinese Qinghua porcelains made during the Yuan and Ming dynasty (Chapter IV). Finally, Chapter V gives the concluding remarks and perspectives.

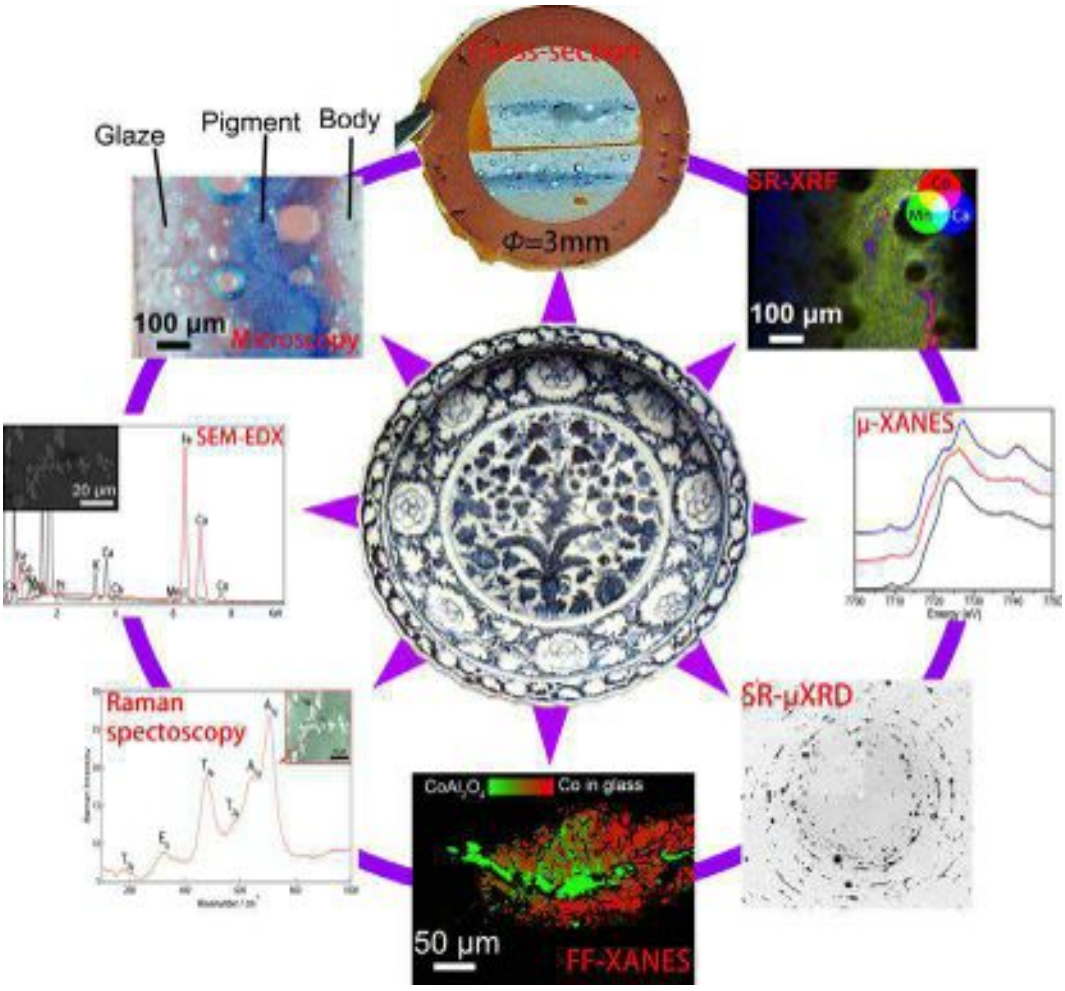

Figure 2.1 An example of the study of Chinese porcelain by using different techniques. The plate is the blue and white plate (1271-1368), unearthed in Jingdezhen, Jiangxi Province (Credit: World Imaging, CC BY-SA 3.0).

3 Reference

Bougard, E., 2011, Les céramiques gravettiennes de Moravie : derniers apports des recherches actuelles, *L'Anthropologie*, Art prehistorique, **115**(3–4), 465–504.

Catling, H. W., Richards, E. E., and Blin-Stoyle, A. E., 1963, Correlations between composition and provenance of Mycenaean and Minoan pottery, *Annual of the British School at Athens*, **58**, 94–115.

Catling, H. W., and Millett, A., 1965, A Study in the Composition Patterns of Mycenaean Pictorial Pottery from Cyprus, *Annual of the British School at Athens*, **60**, 212–24.

Folsom, R. S., 1975, *Attic Black-Figured Pottery*, Noyes Pubns, Park Ridge, N.J.

Hofmann, B., 1971, Les relations entre potiers, fabricants de moules et artistes producteurs de poinçons., *Rei Cretariae Romanae Fautorum acta, 13.1971*.

Jorg, C. J. A., 1984, *Interaction in ceramics: Oriental porcelain & Delftware*, The Council, Hong Kong.

Lawrence, W. G., and West, R. R., 1982, *Ceramic Science for the Potter* 2 edition ed., Chilton Book Co., Radnor, Pa.

Li, J. Z., 1998, *History of Science and Technology in China, Ceramics Volume*, Science Press, Beijing.

Morgan, L. H., 1877, *Ancient Society*, University of Arizona Press.

Moore, N. H., 2009, *Delftware Dutch and English*, BiblioLife.

Noble, J. V., 1960, The technique of Attic vase-painting, *American Journal of Archaeology*, **64**(4), 307–18.

Oswald, F., and Pryce, T. D., 1920, *An introduction to the study of terra sigillata treated from a chronological standpoint*, London, New York: Longmans, Green and Co.

Rice, P. M., 2015, *Pottery Analysis, Second Edition: A Sourcebook*, University of Chicago Press.

Roux, V., and Miroschedji, P. de, 2009, Revisiting the History of the Potter's Wheel in the Southern Levant, *Levant*, **41**(2), 155–73.

Sciau, P., and Goudeau, P., 2015, Ceramics in art and archaeology: a review of

the materials science aspects, *The European Physical Journal B*, **88**(5), 132.

Tite, M. S., 2008, Ceramic production, provenance and use—a review, *Archaeometry*, **50**, 216–31.

Vandiver, P. B., Soffer, O., Klima, B., and Svoboda, J., 1989, The origins of ceramic technology at dolni vecaronstonice, czechoslovakia, *Science (New York, N.Y.)*, **246**(4933), 1002–8.

Chapter II A multi-scale analytical approach

1 Introduction

The structure of ancient ceramic is very complex and heterogeneous. It contains different components, which includes well-defined ones, such as body and coating (glaze/slip), and partially independent ones, such as the diffused pigment zone in the glaze (e.g., the Ming Qinghua porcelain, Figure 1.1). Each component can decompose into several partially independent sub-systems observed at various scales (nm to mm), such as crystal phases (nm to μm), amorphous phases and cracks/bubbles (μm to mm). The valuable information on how these ceramics were created is embraced into the chemical and structural nature of these heterogeneous materials. To reveal the hidden information from the ancient ceramics, we have to not only study the surface components but also, more importantly, study the in-depth components and their sub-systems.

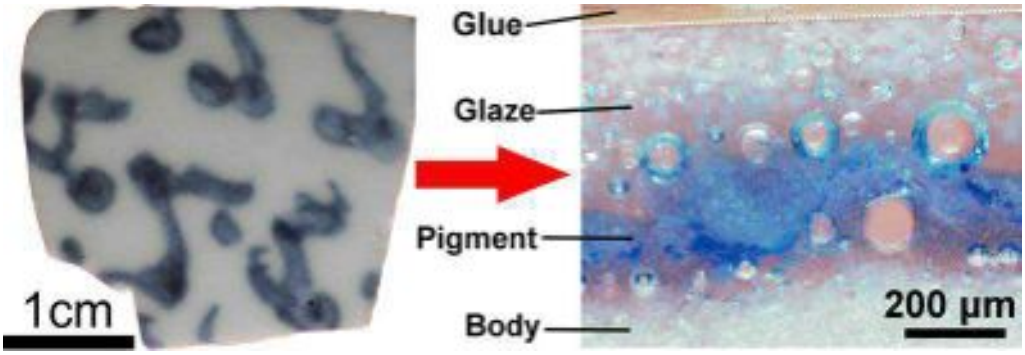

Figure 1.1 A fragment from the Ming Qinghua porcelain (left side) and a prepared cross-section (right side) containing all pertinent systems (body, pigment and glaze) and their interaction zones.

Most traditional investigations of ancient ceramics have been performed using non-destructive techniques on the surface of precious objects (Colomban et al. 2004; Wen et al. 2007). These investigations, however, could not guarantee to access the in-depth information, which is vital in some cases. Even though some scholars tried to get in-depth information by increasing the power of incident energy (Kock and De Waal 2007), the results could be not accurate due to the difficulty to position it at the center of crystallites. To get the in-depth accuracy, one has no choice but to sacrifice a part of the objects. Fortunately, it is not necessary to perform in-depth investigation directly on the masterpieces but on equivalent fragments (made from the same raw materials and with the similar manufacturing processes), which are rather easily found, especially for potteries. Besides, the specimens prepared can be very small for nanometer scale analytical methods.

After selecting the adapted fragments, various samples can be prepared

according to the objectives of the analysis. The samples can be prepared to extract the information from all components, to study the component repartition for instance, or in-depth information from one relatively independent component. Regarding to the fragment, diverse sample orientations can be required to collect all information. In the case of ancient ceramics or potteries, cross-sections and plane view samples are commonly prepared. Cross-section allows us to access the component repartition from the surface to the body (Figure 1.1) while the plane view can be used to study the uniformity inside each component. For instance, the pigment distribution can be observed after removing the upper glaze by polishing.

To obtain data on each component and their organization, a multi-scale approach is required to analyze the materials. The analyzed zones have to be chosen according to the objectives. Depending on the zone (size and scale) where the relevant information can be found, the techniques should be selected with an adapted sampling. Among the techniques, different probe sizes (from nm to μm) should be selected to study the elemental and structural composition at different scales. Large probes allow us to analyze wide zones (from hundreds of square micron to several square millimeter, including several systems such as body, interphase and slip) while small probes allow us to scan small zones with high resolution. The techniques associated with their characteristics (requirements of samples, size of spatial resolution and analytical zone and the relevant information obtained) are listed in the Table 1.1. An appropriate selection of techniques allows us to study composition and structure of specific component or the interfaces among different components. The different method strategies are designed specifically for different types of ancient ceramics.

Basis	Techniques	Sample preparation	Spatial resolution	Size of analytical zone	Information obtained
Lab-based techniques	Microscope	No preparation/Cross-section (bulk and thin)/ plane view	Micron	Millimeter	Morphology stratigraphy and color
	Lab-XRF	No preparation (analyzed on the surface of the fragments)	Several hundreds of microns		Elemental composition
	Raman spectroscope	Cross-sections (bulk and thin)/ plane view samples	Several microns	Few tens of microns	Identification and distribution of crystals
	Electron microprobe (EPMA)	Cross-sections (bulk ones, covered with conductive layer)	Few microns		Elemental composition
	SEM-EDS	Cross-sections (bulk ones, covered with conductive layer)/plane view samples	Several submicrons	Several millimeters	Composition and distribution of major (>1 wt%) elements
Synchrotron radiation (SR)-based techniques	SR-μ-XRF	Thin cross-sections	Several submicrons	Several millimeters	Composition and distribution of both major (>1 wt%) and minor (<1 wt%) elements
	SR-μ-XANES	Thin cross-sections	Several submicrons		The speciation* of selected element both in the concentrated and dilute zone
	FF-XANES	Thin cross-sections	Several submicrons	Several millimeters	The speciation distribution of selected element in the concentrated zone
	SR-μ-XRD	Thin cross-sections	Several submicrons	Several tens of microns	Confirm the present of well-crystallized phases

Table 1.1 Techniques involved in the multi-scale approach. *Speciation: formal valence and coordination (e.g. tetrahedral, octahedral) of element.

In fact, such multi-scale approach is well suited to analyze the various decors of ancient ceramics. For instance, it is particularly efficient to study the heterogeneous decor of marbled terra sigillata of Roman period as will be shown in Chapter III. The slip of this type of terra sigillata is characterized by a yellow color with red veins (Figure 1.3). The two color compounds are intimately mixed, as shown in the right image of Figure 1.3. A red layer (thickness of ~4μm) is well observed within the yellow compound. The study of each compound requires small probe sizes while the global study requires investigation of large zones. Therefore, the application of multi-scale approach allows us to analyze all components of these sigillata and, in particular, to determine the nature of the yet very poorly understood yellow compound.

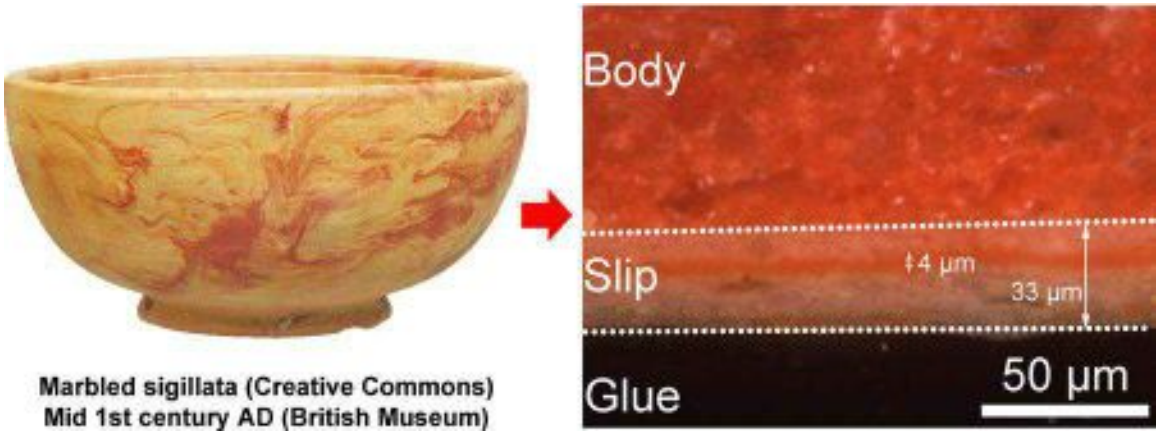

Figure 1.3 A typical Roman marbled terra sigillata bowl (left side) and a prepared cross-section sample containing all pertinent components (body and slip).

In this chapter, before presenting the techniques involved in the multi-scale approach, I am going to try to describe the diverse sample preparations. The multi-scale approach contains a series of tools including traditional laboratory-based tools and synchrotron radiation-based tools. This diversity of the techniques requires different sample types, which should be prepared with various orientations (cross-section or plane view) including either all components (body, pigment zone and glaze/slip) or only a specific component.

2 Sample preparations

The sample preparation is a crucial point to obtain quality data and should take into account two aspects. Firstly, the zone of interest must be accessible to analyze. Secondly, although some techniques, such as optical microscope, laboratory XRF or Raman spectroscopy, do not call for special sample preparation, many techniques request specific shape of sample. For instance, synchrotron radiation X-ray microscopy (TXM) should be carried out on thin section with appropriate thickness to get the best condition for recording the absorption signal in transmission mode (Calvin 2013). In addition, some techniques such as SEM can require a conducting layer (carbon or platinum) to avoid charging problem. Moreover as the sampling is limited, all sample types cannot be made so that a preparation strategy should be developed.

The prepared samples can be divided into two sets: the “thin” samples for the transmission observation and the “bulk” samples for reflection observations. I will begin by this last class, which includes the majority of samples involved in lab-based techniques such as electron microprobe, Raman spectroscopy or SEM-EDS. The second class is more constraining and includes the specific preparations for transmission electron and X-ray microscopies.

2.A Bulk sample preparation

Because of the structure in layers of ancient ceramics, cross-section samples are suited to study their different components (body, decoration and glaze) and this sample orientation was systematically used. Nevertheless, samples in plane view orientation were made to determine the distribution of elements in some components.

2.A.1 Cross-sections

The preparation of a cross-section sample from a ceramic fragment does not exhibit particular difficulty. It is illustrated in Figure 2.A.1.1. A small piece of fragment containing yellow slip with red veins is cut using a wire saw. The piece is then mounted in a mold (diameter of 25 mm) and is embraced with epoxy. After being polished with silicon carbide papers (from14 µm to 5 µm) and diamond pastes (from 5 µm to 1 µm), the sample containing all significant components (body and slip) is ready to be observed and analyzed. For instance, the optical observation allows us to measure the slip thickness (~30 µm) and to observe the body and slip structures. More importantly, in our case, the optical

observation allows us to verify the absence of red veins before performing quantitative elemental analysis.

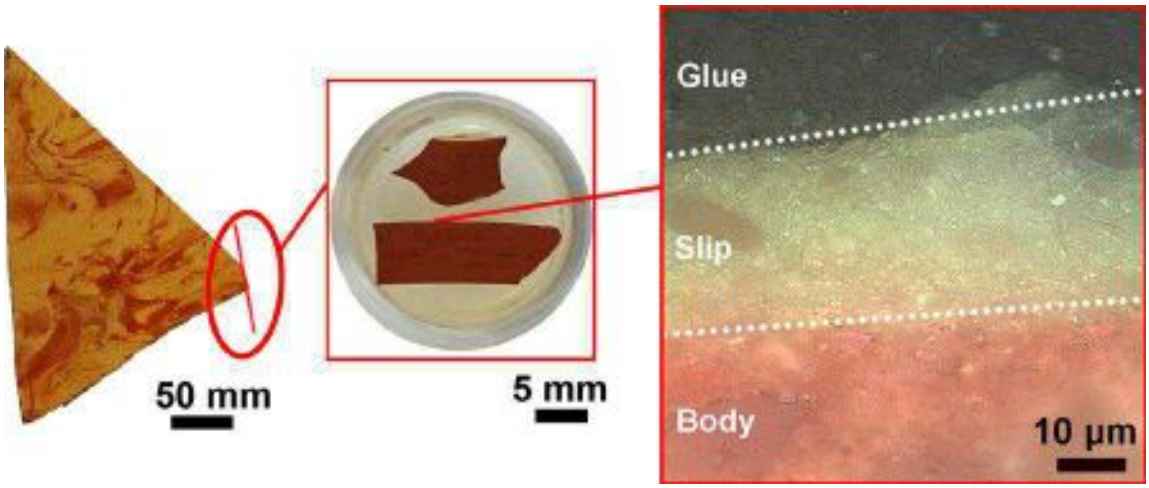

Figure 2.A.1.1 Example of a cross-sectional preparation from the marbled terra sigillata (sample CS27).

2.A.2 Surface sample

For some cases, the study focused only on a specific compound of ancient ceramic, such as the investigation of blue decorations of the Yuan Qinghua porcelains. The sample preparation is shown in Figure 2.A.2.1. A fragment of the porcelain is collected and a small area with blue decors is cut to obtain a small piece. The piece is mounted on a mold and polished as described above until the white glaze is removed and the fresh bare blue decor is appeared. It can be notable that the dark zone/spots contrasts well with the blue zone under optical observation, which allows us to study the crystals of dark zones by Raman spectroscopy and SEM-EDS. Because SEM investigation requires carbon or metal deposition, the Raman study was performed firstly (Wang et al. 2016b).

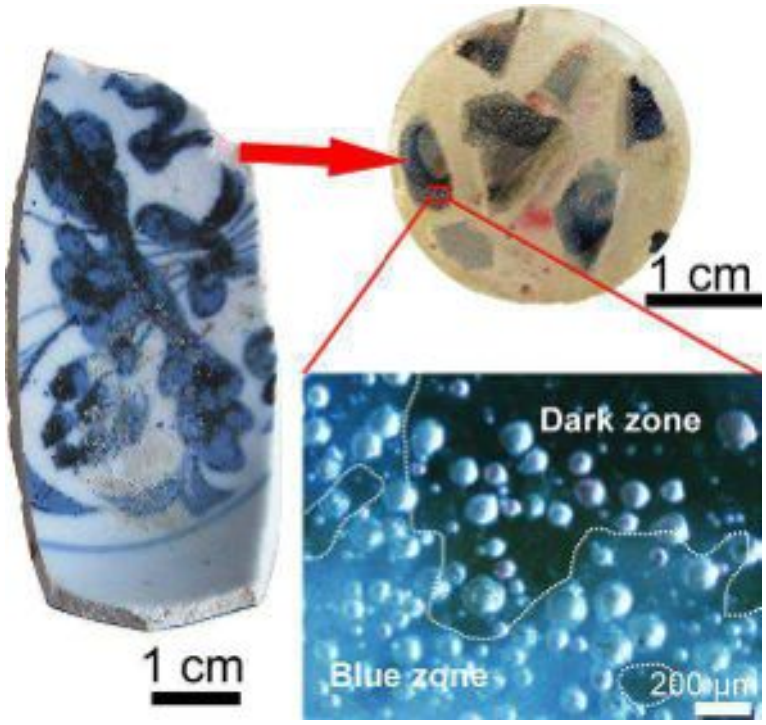

Figure 2.A.2.1 Example of a surface preparation from the Yuan Qinghua porcelain (sample YH-1).

2.B Thin-section preparation

The preparation of a thin cross-section sample was firstly performed for full-field XANES experiments, which require X-ray transparent samples. The thickness was determined using the Bourguer' Law (p51, Scott Calvin 2013) taking into account the elemental composition and the energy edge studied. In order to conserve all the information of the top layers and to benefit from the experience of our laboratory, we chose a preparation method inspired from the TEM sample preparation. Two examples are given to illustrate the main steps of sample preparation.

The first given example is related to the preparation of Ming Qinghua porcelain shown as Figure 2.B.1. After several cutting steps (1-3) in order to obtain two strips with blue decors (4), the two strips are glued together glaze against glaze using Gatan G-1 epoxy to form a sandwich (5). Subsequently, the sandwich is cut into several ~500 mm slices and then each one is embraced with glue and placed on a glass slide (6). Slices are temporarily mounted on a movable support in brass with a dental wax (7). After polishing the first face, the movable support is heated in order to melt the wax. The sample is flipped and glued with wax. The second face of the slice is polished down to have the

required thickness (about 60-70 µm). Finally, a copper washer (8) was glued to the final thin-section for safeguarding the samples and facilitating their transport (9) and installation on ID21 sample-holder, which can support several samples (10). One can evidently observe all compounds of the porcelain, including white body, blue pigment zone and white glaze (9).

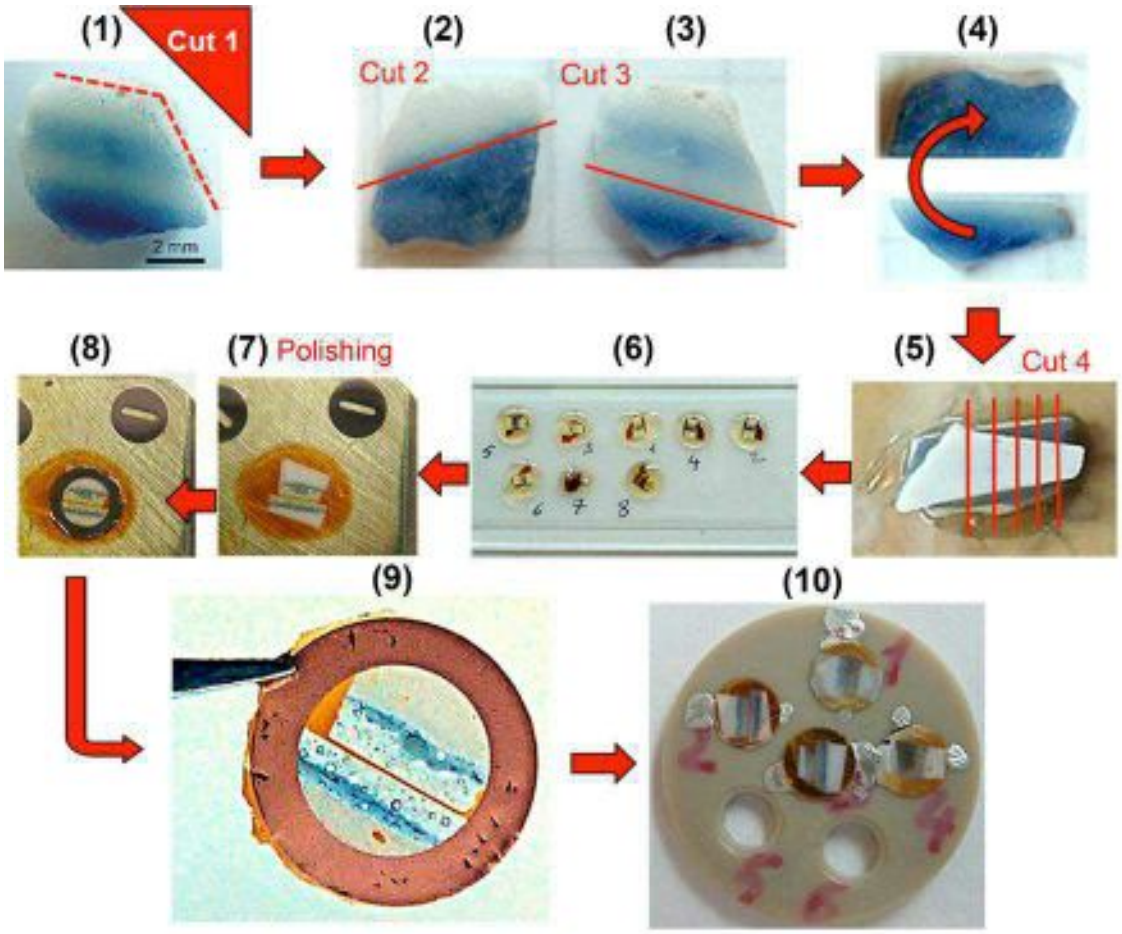

Figure 2.B.1 Main steps of the cross-section preparation: from the fragment sampling (1) to the thin cross-section lamella (9) placed on the specific ID21 sample holder (10).

The second example is related to the preparation of Greek ceramic shown as Figure 2.B.2. After the same preparation, the slice was polished down to have the required thickness, which is here around of 40-50 µm. Observed by optical microscope, a red slip with thickness of 7-10 µm is found beneath the black slip with thickness of 8-11 µm.

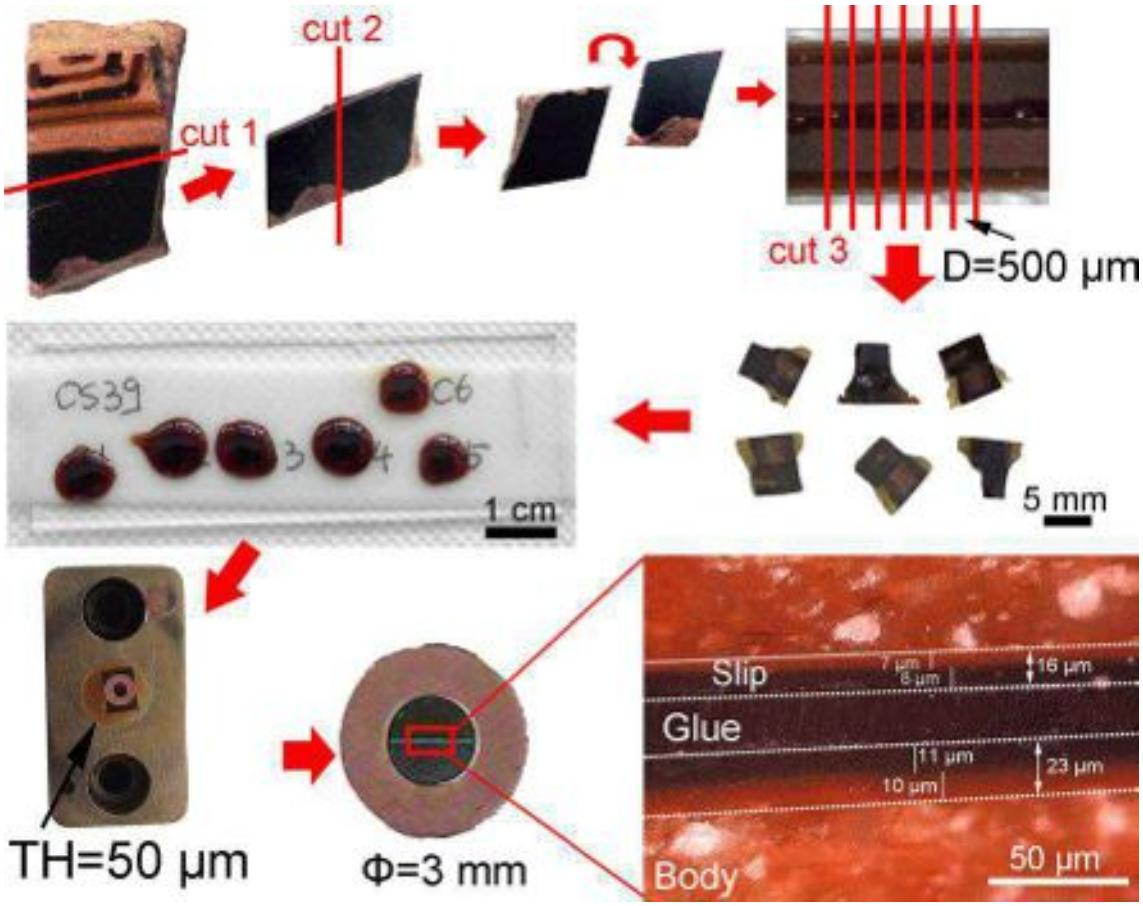

Figure 2.B.2 Thin cross-section sample preparation of Greek ceramics (sample CS39).

The main advantages of this sample preparation are to protect the slip/glaze surface from damage and to conserve the in-depth information and thus to be able to study the internal red slip of potteries (Figure 2.B.2) or the diffusion of chromophores elements in the glaze as well at the interphase body-glaze of porcelains (Figure 2.B.1). These thin cross-sections are not only well suitable to be analyzed by FF-XANES but also by other synchrotron radiation-based techniques including µ-XRF, µ-XANES and µ-XRD. They can be also used for lab-based analyses such as Raman spectroscopy and SEM-EDS. Moreover, TEM samples can be extracted in the interesting zones by FIB.

2.C Focused ion beam cutting (FIB)

A few 3D small samples were prepared by the focused ion beam (FIB) systems for XRF tomography experiments on ID16B ESRF beamline.

The sample preparation is described in-detail shown in Figure 2.C.1. Prior installing the fragment into FIB systems, the fragment needs to be polished (body

side) to obtain the thin-section with the thickness of less than 50 μm (here about 15 μm) and then adhered onto a needle-like holder. The holder with the thin-section is put into FIB systems. After positioning the part of interest by SEM microscope, FIB starts to cut the thin-section along left (a) and then right side (b) to finally obtain a thin cylinder (c). Its height (here is 151.9 μm) and width (here is 40.7 μm) can be controlled during cutting.

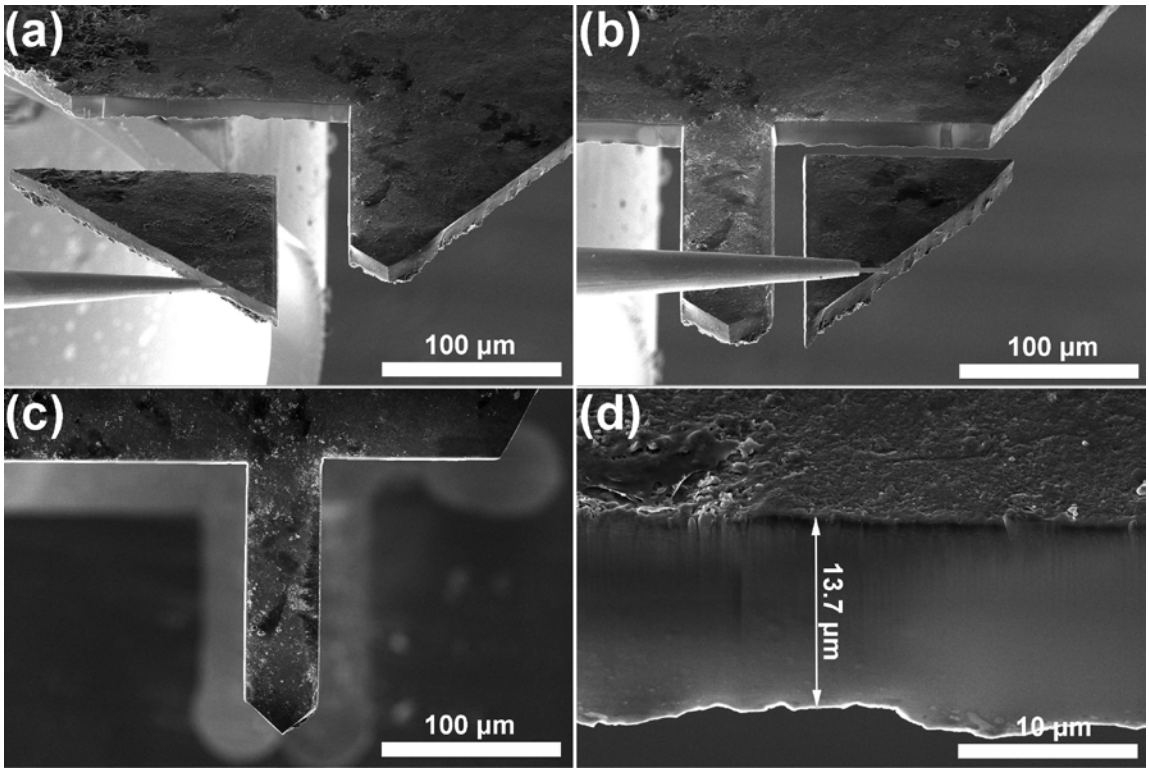

Figure 2.C.1 Main steps of thin cylinder preparation by FIB technique: cut of the left (a) and right (b) side of the thin section to obtain a cylinder with 151.9 (H)×40.7(W)×13.7(T) μm.

3 Analytical techniques

Ancient ceramics, as artifact materials prepared by potters, do no differ from other materials. The analytical techniques developed for material science could be also effective to investigate ancient ceramics. But the ceramic materials are more complex and heterogeneous, the multi-scale approach, involving a series of lab-based techniques and synchrotron radiation-based techniques, could well locate and analyze all systems and sub-systems of ancient ceramics.

3.A Laboratory-based techniques

Lab-based techniques, including optical observation, Raman spectroscopy, X-ray based techniques (XRD, XRF) and electron microscopy (SEM-EDS, EPMA) are effective to analyze elemental and mineral compositions. They are also well suitable to study ancient ceramics from the millimeter to micrometer scales. In all possible measurements, electron microscopy analysis should be performed in the last place in case the carbon/metal deposition may influence other analyses. In this part, I will present the techniques accordingly.

3.A.1 X-ray fluorescence analysis (Lab-XRF)

Lab-XRF is a useful tool to identify precisely elemental compositions. In this part, I will describe a brief principle and application of XRF in archaeology. The corresponding experimental details used in this work are presented.

3.A.1.a Principles and application

Based on wavelength-dispersive spectroscopic principles, XRF technique is adapted to analyze elemental and chemical compositions of materials (Artioli 2010). In X-ray fluorescence analysis, primary X-rays bombard samples, leading to displace electrons from the inner orbits of the constituent atoms, which are then filled by electrons from the outer levels. The energy released in this process is shown as the emission of characteristic fluorescent X-rays, the wavelengths of which are unique to every element and can be used to perform identification. XRF analysis can be used to determine more than 80 elements and trace their quantities and especially suitable for those above atomic number 12 (magnesium) on the periodic table.

The wide availability and low cost make XRF practical for ceramic provenience analysis (Mantler and Schreiner 2000; Pillay et al. 2000; Padilla et al.

2006; Papachristodoulou et al. 2006; Wen et al. 2007; Majumdar et al. 2012; Zhu et al. 2015). For instance, Wen et al. studied the chemical compositions of the glazes and pigments of the Ming and Yuan Qinghua porcelains through XRF and found that there are two significant changes of provenance of blue pigment during the Ming Dynasty and that some kinds of pigment were most probably imported from the Middle East (Wen et al. 2007).

3.A.1.b Experimental details

The macro X-ray fluorescence (XRF) measurements were carried out by the team of Professor T.-Q. Zhu at the archaeometry lab of the School of Sociology and Anthropology of Sun Yat-sen University. Macro X-ray fluorescence spectrometer (Eagle-III.XXL, EDAX, Mahwah, New Jersey, USA) was operated at 40 kV-230 mA voltage-current of the Rh X-ray tube, with the vacuum optical route and a beam size of 300 μm diameter. The resolution was 137.5 eV at Mn Kα line and the dead time was 25–30%. The background substraction software and analysis was Vision32 equipped with the instrument.

3.A.2 Raman spectroscopy

As an effective tool to study mineral composition of materials, Raman spectroscopy has been used in the study of ancient ceramics for long time. In this part, I will describe a brief principle and application of this technique in archaeology before to present the experimental details used in this work.

3.A.2.a Principles and application

Raman effect is based on the interactions between photons and molecules (Larkin 2011). The detailed theory of the Raman effect is explained elsewhere (Clark and Dines 1986) and the schematic of Raman spectroscope is shown in Figure 3.A.2.a.1 (Smith and Clark 2004; Bayle 2014). The lasers are positioned parallel and behind the spectrometer, which can generate various wavelengths to excite samples. The excitation beam is directed to the microscope by beam steering optics. The microscope allows samples to be measured visually at high magnification and permits specific areas as small as 1-μm-diameter to be analyzed selectively. A camera and white lamp are used to facilitate the observations. The photons (including Rayleigh and Raman ones) are back-collected through the same microscope objectives and then directed to a pre-monochromator and spectrometer. The pre-monochromator allows removing the Rayleigh scattered photons to avoid saturation of the detector or overwhelm the

comparatively weak Raman signal and selecting a frequency range. A spectrometer is equipped to disperse the Raman spectrum. Finally a CCD camera will record the signal.

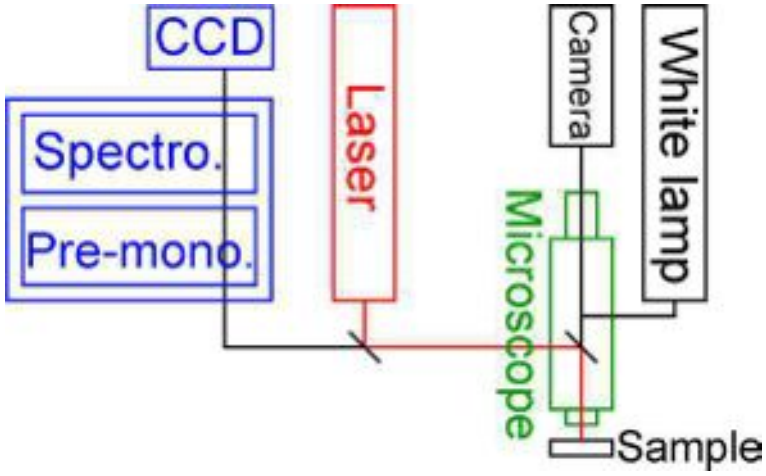

Figure 3.A.2.a.1 Necessary experimental device for measuring a Raman spectrum [Bayle 2014].

Raman spectroscope, as an important tool to analyze and classify ancient ceramics, is becoming commonplace. In one aspect, it allows a non-destructive remote analysis and the 180º geometry of the collection optics allows samples of any size or shape to be examined in situ (Smith and Clark 2004). In another aspect, based on the high sensitivity and resolution, Raman spectroscope allows identifying crystalline in both body and glaze, including the nano-sized pigments coloring the glaze (Colomban 2004). Exampled as the Ming porcelains, the blue decors of the porcelains were identified by Raman spectroscopy as a spinel-structural cobalt blue ($CoAl_2O_4$) (Kock and De Waal 2007) while the dark spots in the blue decors were identified by Raman spectroscopy as manganese oxides (Coutinho et al. 2014).

3.A.2.b Experimental details

In this work, I used two types of Raman spectroscope, including an XploRA spectrometer (CEMES) and a Renishaw inVia spectrometer (Getty Conservation Institute (GCI), Los Angeles). The investigations in GCI were performed during my one-month trip there, which was only carried out on the samples of Greek ceramics. The other investigation for marbled terra sigillata, the Ming and Yuan Qinghua porcelain was performed in CEMES.

The analyses in CEMES were performed at room temperature using an XploRA spectrometer (Horiba, Ltd., Kyoto, Japan) equipped with a Peltier cooled

CCD detector under the 532 nm excitation line providing by a solid-state laser. A 2 to 3-µm-diameter laser spot was provided with a 100× microscope objective used to focus laser beam and collect scattered light. A laser power of 0.8 mW was employed to optimize the signal/background ratio without avoiding any thermal effect. The Igor Pro software was used to fit and plot the Raman spectra.

The analyses in GCI were performed at room temperature using Renishaw inVia micro-Raman spectrometer (Renishaw plc, Gloucestershire, UK), equipped with a cw 785-nm excitation laser and L-50×/0.50 objective (Leica). The spectrometer was calibrated to the 520.5 cm^{-1} band of silicon. The power of the laser at the sample was kept below 1 mW to prevent beam damage and laser induced re-oxidation and spectral acquisition time was 60s. Individual Raman spectra were background corrected and fit with Lorentzian curves using Origin 8.5. Raman maps were performed in line scan mode and the data processed with WiRE 3.4 software.

3.A.3 Electron microprobe

Besides XRF, electron microprobe (EPMA [1]) can be used to determine the quantitative elemental composition of decors of ancient ceramics. As previously, I will begin by presenting a brief principle and application of the technique before describing the experimental details used.

3.A.3.a Principles and application

EPMA is an electron micron-beam (typical energy = 5-30 keV) used primarily for on-site non-destructive chemical analysis of small volumes of solid materials (Goldstein et al. 2003; Goodge 2007; Reed 2010). The basic theory is the following: a beam of electrons, fired on the sample, causes that the various elemental species of sample emit X-rays at their characteristic frequency. These signals can be detected by the detector, which can provide precisely quantitative elemental analyses at small sizes of one to two microns.

EPMA equipped with X-ray wavelength dispersive spectrometer can be used to conduct quantitative analysis at very high sensitivity and trace precisely both major and minor elements. This capability is well suited to analyze the chemical composition of ancient ceramics, which is related to the corresponding archaeological information (Roqué et al. 2006; Ionescu et al. 2011; Leon et al. 2015). For instance, Corina Ionescu et al. used electron microprobe to determine the elemental composition of Late Bronze Age ceramic pottery from Ilişua, Transylvania (Romania) and showed that the most probable raw materials were

[1] EPMA: The abbreviation of the "Electron Probe Micro-Analyzer"

the Badenian illitic silty clays mixed with soils that came from the surroundings of the Ilişua site (Ionescu et al. 2011).

3.A.3.b Experimental details

I performed the elemental analyses at Centre de Microcaractérisation Raimond Castaing, using a CAMECA SXFive micro-probe. Prior analysis, the samples were covered by a thin layer of carbon. The accelerating voltage was 15 kV with beam current of 20 nA. The size of analyzed surface was around 2×2 μm^2. Natural and synthetic minerals were used as standards (McQuire et al. 1992). The procedures for the minimization of beam-induced losses and gains in alkali metals have been taken into account (Spray and Rae 1995).

3.A.4 Scanning electron microscope with X-ray microanalysis (SEM-EDS)

SEM-EDS was also used to analyze the elemental composition and to observe the texture of ceramics. It could provide not only punctual analysis but also mapping information to reflect the distribution of elements. As previously, a brief principle and application of the technique will be described before presenting the experimental details used.

3.A.4.a Principles and application

Scanning electron microscopy is fundamentally the same as electron microprobe, with an electron beam scanning across the surface of samples (Goldstein et al. 2003). When the electron beam strike the materials, various signals are generated and the detection of specific signal will produce either chemical or topological information. One imaging signal is the emission of secondary electron (SEs). SEs are emitted only from the surface of specimen within nanometers, which can produce an interpretable image of the surface. The contrast of the image is related to the specimen morphology. Due to the small size of primary electron beam, the image can be depicted with high resolution (few tens of nanometers). Backscattered electrons (BSEs) originate from primary electrons, which are reflected or back-scattered out of the specimen interaction volume by elastic scattering interactions with specimen atoms. They have higher energies than SEs and are affected less by surface morphology but strongly by the atomic number of the elements. This signal can produce an image, where contrast is related to the atomic number of elements in the sample. The image can therefore reflect the distribution of chemical phases, but due to these electrons from a depth of the sample, the resolution of the image is not as good as SEs (~0.5 μm).

The primary electrons interacted with the sample can also cause the emission of X-rays. Characteristic X-rays have wavelengths and energies unique to the parent elements. Detection and measurement of the X-ray energy (energy dispersive X-ray spectroscopy, abbreviated as EDS) permit element analysis including identification and quantitative analysis.

The main components of SEM mainly contain electron source (gun, a tungsten filament cathode at CEMES), electron lenses, sample stage, detectors for different signals and vacuum system, shown as Figure 3.A.4.a.1.

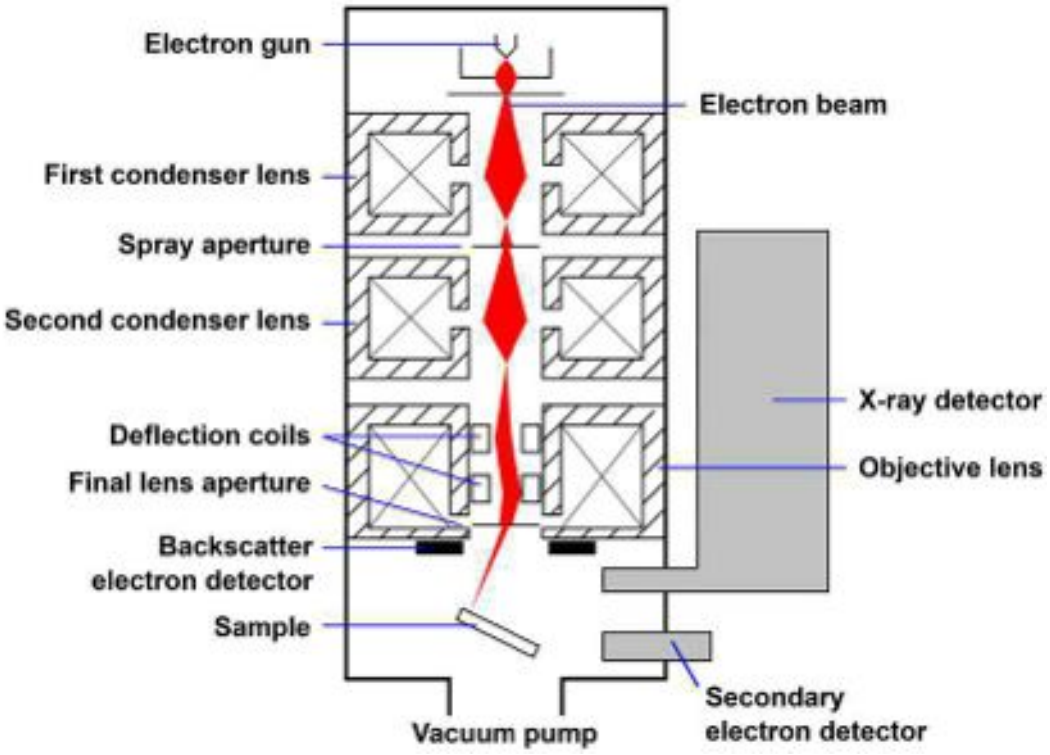

Figure 3.A.4.a.1 Schematic diagram of a typical SEM (Credit: World Imaging, CC BY-SA 3.0).

Ceramic artefacts are well suited to be characterized using SEM-EDS (Frahm 2014). On the basis of the capability in imaging and providing composition information, SEM-EDS can be used to identify compositions of pottery coatings, such as opacifiers and colorants (Llusar et al. 2001; Mazzocchin et al. 2003; Padilla et al. 2005; Haswell et al. 2008; Charalambous et al. 2010; Coutinho et al. 2014). For instance, Coutinho et al. used variable pressure scanning electron microscope to study the dark spots of the Ming blue and white porcelains and observed the presence of manganese oxide compounds with acicular radial and dendritic shapes (Coutinho et al. 2014).

3.A.4.b Experimental details

In this work, I used two types of SEM, including a JEOL JSM 6460 LV SEM (CEMES) and a FEI/Philips XL30 ESEM FEG SEM (Getty Conservation Institute, GCI, Los Angeles). The investigations in GCI were performed during my one-month trip there, which was only carried out on the samples of Greek ceramics. The other investigation for the Yuan Qinghua porcelain was performed in CEMES.

Prior to SEM-EDS analyses in CEMES, the samples were covered by a thin layer of platinum. The elemental analysis were conducted using a JEOL JSM 6460 LV (JEOL Ltd., Akishima, Tokyo, Japan) SEM operating at 20 kV and equipped with an Oxford INCA PentaFETx3 EDS. Elemental mappings were performed on 256x192 pixels images with a pixel size of about 0.2 mm and quantified afterwards thanks to internal standards.

The SEM-EDS analyses in GCI were performed on the same samples used for EMPA analysis. Elemental analysis was performed in a field-emission environmental SEM (FEI/Philips XL30 ESEM FEG, FEI Company Inc., Hillsboro, Oregon), with an energy-dispersive X-ray detector (30 mm^2 SiLi detector with INCA Software, Oxford Instruments, UK).

3.B Synchrotron radiation X-ray based techniques

Synchrotron radiation (SR)-based techniques such as μ-XRF, μ-XANES, FF-XANES, μ-XRD) are increasingly used for the study of ancient ceramics due to their enhanced spatial resolution and chemical sensitivity (Cotte et al. 2010; Pouyet 2014). SR-μ-XRF allows determining the elemental distribution of large areas including all components of ancient ceramics (glaze/slip, pigment zone and body). While FF-XANES approach allows defining the speciation distribution of concentrated zones over large areas with relative high speed, μ-XANES performed in fluorescence mode is able to check the speciation of low concentrated zones by only recording a few spectra. The speciation concerns formal valence and coordination environment (e.g., octahedral, tetrahedral coordination). Then the presence of well-crystallized phases can be confirmed by μ-XRD. Through constructing the set of data, we can make assumptions concerning the origin of color variations and the manufacturing process. In the next parts, I will present the techniques accordingly.

3.B.1 SR-μ-XRF

SR-μ-XRF has been effectively used to determine the elemental distribution of the decor and body of ancient ceramics. Before presenting the application of the

technique in the study of ancient ceramics, a brief principle is described firstly and the experimental details are presented in the last part.

3.B.1.a Principles and application

The main theory of SR-based μ-XRF is the same as the one of lab-based XRF (Janssens et al. 1993). When performed with micro-focused beams at synchrotron sources, it enables to obtain the elemental composition at sub-micrometre scale with 2D and even 3D imaging capabilities and with enhanced detection limits (ppm). The details of XRF theory and set-up in ID21 beamline of ESRF were described elsewhere (Pouyet 2014).

When performing μ-XANES or μ-XRD analyses, their combination with μ-XRF is usually straightforward and provides an elemental mapping preliminary or complementary to molecular and structural analyses respectively. In addition to the major elements identification, it also allows probing the localization of less concentrated elements such as trace elements that could bring important information on understanding the origin of color variation and understanding the pigment's history (provenance, production, etc.) (Janssens et al. 2000; Cotte et al. 2010; Leon et al. 2010; Sciau et al. 2011; Janssens et al. 2013).

3.B.1.b Experimental details

SR-μ-XRF mappings were carried out using scanning x-ray microscope (SXM) at ID21 beamline (Salomé et al. 2013). At the exit of the monochromator, the incident beam is focused with Kirkpatrick-Baez mirrors down to a size of 0.7×0.3 μm² (h×v). The initial flux of 5.109 ph/s is attenuated down to 1.109ph/ s using a 100μm Al foil to avoid saturation of the XRF detector (dead time kept below 15%). A photodiode (i0) is placed upstream the sample to continuously measure the incident beam flux, and to correct its variations over time. Samples are mounted raster scanned under vacuum, in a vertical plane, with an angle of 62° with respect to the incident beam. This explains some "shadow effects" observed on μXRF maps. XRF signal is collected in the horizontal plane and at 69° with respect to the incident beam using a silicon drift detector (Xflash 5100, Bruker with Moxtek thin polymer window). 2D μ-XRF maps are obtained by raster scanning the samples in continuous mode, with 100 ms dwell time. The PyMca software is used to batch-fit the XRF spectra, generate the elemental maps (from Na to Co) and normalize them with incident intensity (Pouyet 2014).

3.B.2 SR-μ-XANES

SR-μ-XANES (X-ray Absorption Near Edge Structure) is effective to analyze the speciation of elements of interest including both amorphous and crystallized ones, which is well suitable to analyze the pigment zone of ancient ceramics. A brief principle and application of the technique are described before presenting experimental details.

3.B.2.a Principles and application

X-ray absorption spectroscopy (XAS) consists in measuring the variation of the X-ray absorption coefficient of an element of interest while scanning the energy of the probing X-ray photons around one of its absorption edges. With the absorption of an X-ray photon, a core electron is excited into unoccupied electronic states. Accordingly, X-ray absorption fine structure (XAFS) is the details of how X-rays are absorbed by an atom at energies near and above the core-level binding energies of that atom. XANES (X-ray Absorption Near Edge Spectroscopy) focuses on a ~100 eV region above the absorption edge, which is strongly sensitive to formal oxidation state (ion valence) and coordination chemistry (e.g., octahedral, tetrahedral coordination) of the absorbing atom. Synchrotron sources offer not only the necessary continuous spectral range, but also the necessary intensity to allow high spectral and lateral resolution with good detection limits (in particular when XANES experiments are performed in the XRF detection mode). The details of XANES theory and set-up in ID21 beamline of ESRF were described elsewhere(Pouyet 2014).

XANES technique is efficient to study the pigments based on the first series of metal transition elements (Barilaro et al. 2007; Monico et al. 2011; Zhu et al. 2013). It allows not only for identifying the valence state of metal transition ion but also its atomic environment, which is directly linking to the color. For example, the investigation in blue decorations of the Qinghua porcelain (Wang and Wang 2011; Figueiredo et al. 2012; Wang et al. 2016c), the XANES spectra could identify the Co speciation and microstructure and thereby decipher the origin of blue decorations.

3.B.2.b Experimental details

In this work, the SR-μ-XANES was performed at ID21 beamline. The Spectra were acquired at the K-edge of the element of interest over a few points by scanning the energy of the incoming beam and measuring the XRF signal of K-lines.

3.B.3 Full-field XANES (FF-XANES)

FF-XANES, as a powerful 2D analytical technique, can acquire sets of hyper-spectral data containing 2D images. It allows accessing redox information on the element of interest and mapping the speciation distribution to understand the origin of color variation or firing technology of ancient ceramics. In the part, a brief introduction of the technique is described and the related application in tackling archaeological issues is exampled in the previous study of Roman ceramics (Meirer et al. 2013).

3.B.3.a Principles and application

XANES-based 2D technique has been a useful approach to access redox information on the element of interest (Pouyet 2014). Speciation can be obtained by three approaches: 1) in scanning mode; 2) 2D raster-scanned XANES acquisition; 3) transmission X-ray microscopy. Considering the limitations of first two approaches (the field of view is limited by dwell time in scanning mode and the accessible field of view and the ultimate resolution is limited in raster-scanned acquisition), transmission X-ray microscopy with the unique capability of combing spectroscopy and imaging has been used for investigation of ancient ceramics. This development is followed by the implementation of XANES analysis on hard X-ray lens-less imaging (full-field imaging) microscope. The details of FF-XANES theory and set-up in ID21 beamline of ESRF were described elsewhere (Fayard et al. 2013; Pouyet 2014). The main requirement of this technique is that the element of interest is sufficiently concentrated and that the sample is prepared at an optimal thickness. Two methods of sample preparation have been already described in-detail in the 2.B and 2.C part, respectively. The calculation of optimal thickness for different ceramics will be described in the Chapter III and IV.

The FF-XANES study have been successfully used to investigate Roman (Meirer et al. 2013) and Greek ceramics (Cianchetta et al. 2015). Exampled as Roman pottery from *La Graufescenque* (Aveyron) (Figure 3.B.3.a.1) (Meirer et al. 2013), a fragment of pre-sigillata with black slip was investigated by full-field XANES. The results present that the surface of slip is mainly oxidized hematite while the core of the slip is mainly reduced hercynite (Figure 3.B.3.a.1d), indicating the potters of this vessel were able to successfully re-oxidize the body to Fe^{3+} while preventing the slip from re-oxidizing.

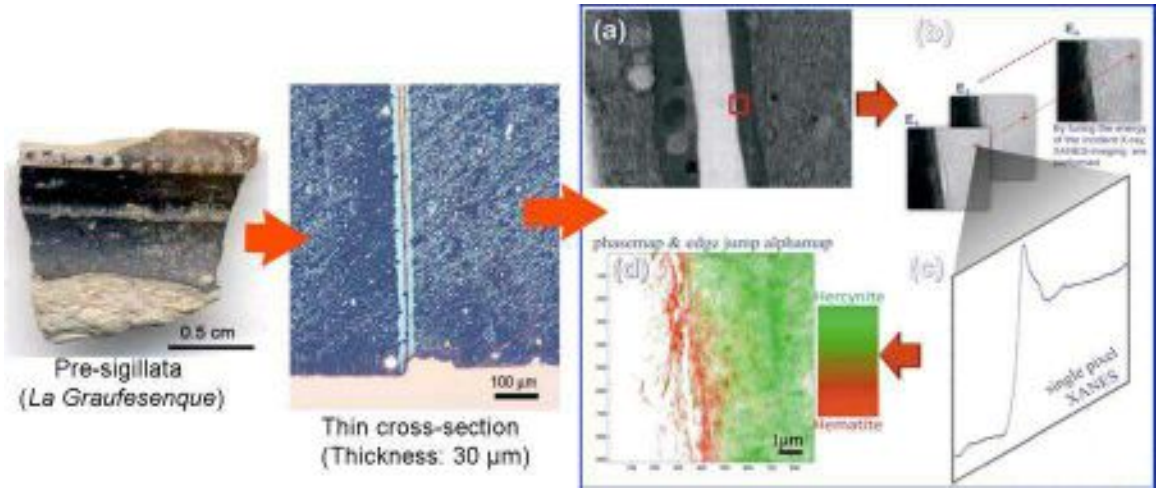

Figure 3.B.3.a.1 A fragment of pre-sigillata with black slip was selected and prepared to be thin cross-section (the thickness of slip: 30 µm). The principles of data processing for full-field XANES microscopy: (a) a zone of interest is focused; (b) one image is acquired in absorption contrast at each energy in the XANES scan; (c) XANES are constructed from each pixel plotting normalized absorption versus energy; (d) XANES from each pixel is fit to create a chemical phase map.

3.B.3.b Experimental details

The FF-XANES analyses were carried out using the dedicated apparatus in ID21 beamline. The energy of incident X-ray beam is tuned: 1) over the Co K-edge (208 different energies, from 7670.2 to 7910.1 eV, with energy steps from 0.3 to 2.2 eV depending on the energy domain) for the Ming Qinghua samples; 2) over the Fe K-edge (213 different energies, from 7060.0 to 7302.1 eV, with energy steps from 0.3 to 2.2 eV depending on the energy domain) for both the Ming Qinghua samples and Greek samples; 3) over the Ti K-edge (531 different energies, from 4920.1 to 5200.0 eV, with energy steps from 0.7 to 1.1 eV depending on the energy domain) for marbled terra sigillata samples.

In this set-up, the beam is unfocused. X-ray images are converted into visible images thanks to a Lu_2SiO_5: Tb scintillator located less than 2 mm downstream the sample. A 20x optical objective is used to magnify the image onto a CMOS PCO edge camera, giving a pixel size of 0.35×0.35 µm² and the spatial resolution can be estimated to be around 0.7 µm. The maximum field of view is around 0.7x0.7 mm^2 but can be reduced in moderate size in function of the interest zones on the samples. After data pre-processing (flat field correction and image alignment), the FF-XANES stack consists of a series of normalized images that characterize the sample absorption across the absorption edge of interest. This technique is therefore capable of identifying the chemical speciation and the oxidation state but also precisely mapping the chemical compounds distributions

even with subtle changes in mineralogical aspect.

All data were processed in the approach of principle component analysis (PCA) and subsequent k-means clustering (Jackson 2004) using the freely available software package TXM-Wizard (Liu et al. 2012) During data processing, the pixels with a too weak edge and/or noisy XANES spectrum were filtered out.

3.B.4 SR-μ-XRD

SR-μXRD complements the other SR-spectroscopy instruments by offering specific information about the identification of crystallized phases. It could help to provide a more accurate identification of the composition of pigments (Wang et al. 2016c). Before presenting its application in studying ancient ceramics, I will begin by presenting a brief principle of the technique and the experimental details are descirbed in the last part.

3.B.4.a Principles and application

The principle of XRD originates from the constructive interferences of X-rays elastically scattered by a regular array of atoms, which can be used to identify the chemical species in a crystalline material. Compared with conventional sources, XRD based on a synchrotron source have high lateral resolution and the access to high energies, which makes it possible to analyze thick and absorbing materials (De Nolf et al. 2014). The more details about diffraction acquisition modes and related opportunities were described in elsewhere (Pouyet 2014).

In the context of the analysis of ancient ceramics, μ-XRD is extensively used to identify various crystallized colorant ingredients (Pradell et al. 2006; Constantinescu 2007; Roqué et al. 2008; Leon et al. 2010; Wang et al. 2016c). For example, Leon et al. used SR-XRD to investigate the yellow pigment of the marbled terra sigillata and found that the color is due to the formation of a pseudobrookite (Fe_2TiO_5) phase (Leon et al. 2010).

3.B.4.b Experimental details

SR-μ-XRD mappings were carried out at the recently opened μ-XRD end-station, at ID21 beamline. The X-ray beam is deviated on the side-branch, with a Si wafer covered with a W/B4C multi-layer, also acting as an energy filter (ΔE/E=0.9% at 8.53keV). A channel-cut monochromator is available to further select the energy (ΔE/E~10-4). The incident monochromatic beam was focused with Kirkpatrick-Baez mirrors down to a size of 1.8×1.0 μm² (h×v). A photodiode is placed upstream the sample to continuously measure the incident beam flux, and to

correct its variations over time. Samples are mounted and raster scanned in air, in a vertical plane, perpendicularly to the incident beam. XRD patterns are acquired at each pixel of the 2D maps, and collected thanks to 2D taper FReLoN CCD. Simultaneously, XRF signal is collected using a Ketek 80 mm^2 Silicon Drift Diode, in the horizontal plane and at 69° with respect to the incident beam. 2D µ-XRD/µ-XRF maps are obtained by raster scanning the samples in continuous mode, with 10 s dwell time. Data are analyzed thanks to the PyFAI (Ashiotis et al. 2015) and the XRDUA software (De Nolf et al. 2014). The sample to detector distance was calibrated thanks to an alumina powder. It was further assessed on the sample, by acquiring a 50×50 $µm^2$ map in the body part of MM1-C2 thin section.

Being in the body or in the enamel, 2D patterns are azimuthally integrated, indexed with powder diffraction database search tool (Match) and fitted with a constrained Rietveld refinement model, fixing atomic parameters.

4 Conclusion

In this chapter I tried to describe the main outlines of multi-scale approach developed to study ancient ceramics. In principle this approach should be capable of locating and analyzing all systems and sub-systems of ancient ceramics at different scales (from nm to mm). However, it requires a diversity of sample preparations and both lab-based techniques and synchrotron radiation-based techniques, which are not always easy to achieve and require time, facility access and available samples. These restrictions, in particular the sampling restrictions and/or sample preparations, limit the investigation possibilities and require making choices and defining an adapted strategy. In the next chapters, I try to present this through studies of two types of ceramics decorations: the slips rich in iron of antique ceramics (Chapter III) and the blue and white decors of Chinese Qinghua porcelains (Chapter IV). The first ceramic type was provided by the *Laboratoire Archéologie des Sociétés Méditerranéennes* (Lattes/Montpellier, France). The fragments were numerous and enough to be analyzed by almost all techniques involved. The methodology adaptation concerned only the experiment time and the limit days of synchrotron. The second type was provided by the *Archaeometry Lab* of Sun Yat-Sen University (Guangzhou, China). The number of fragments was very small. Moreover, many of them were smaller with very small interesting areas. In addition to the restrictions mentioned above, it was not possible to prepare different types of samples from the same fragment, and the strategy had to be adapted in consequence as presented in Chapter IV.

5 Reference

Artioli, G., 2010, *Scientific methods and cultural heritage*, Oxford University Press.

Ashiotis, G., Deschildre, A., Nawaz, Z., Wright, J. P., Karkoulis, D., Picca, F. E., and Kieffer, J., 2015, The fast azimuthal integration Python library: pyFAI, *Journal of Applied Crystallography*, **48**(Pt 2), 510–9.

Barilaro, D., Crupi, V., Majolino, D., Venuti, V., Barone, G., D'Acapito, F., Bardelli, F., and Giannici, F., 2007, Decorated pottery study: Analysis of pigments by x-ray absorbance spectroscopy measurements, *Journal of Applied Physics*, **101**(6), 064909–16.

Bayle, M., 2014, Architectures plasmoniques enterrées : élaboration, propriétés optiques et applications, Phd, Université de Toulouse, Université Toulouse III - Paul Sabatier.

Calvin, S., 2013, *XAFS for Everyo*ne, CRC Press.

Charalambous, A. C., Sakalis, A. J., Kantiranis, N. A., Papadopoulou, L. C., Tsirliganis, N. C., and Stratis, J. A., 2010, Cypriot byzantine glazed pottery: a study of the Paphos Workshops, *Archaeometry*, **52**(4), 628–43.

Cianchetta, I., Trentelman, K., Maish, J., Saunders, D., Foran, B., Walton, M., Sciau, P., Wang, T., Pouyet, E., Cotte, M., Meirer, F., Liu, Y., Pianetta, P., and Mehta, A., 2015, Evidence for an unorthodox firing sequence employed by the Berlin Painter: deciphering ancient ceramic firing conditions through high-resolution material characterization and replication, *Journal of Analytical Atomic Spectrometry*, **30**(3), 666–76.

Clark, R. J. H., and Dines, T. J., 1986, Resonance Raman spectroscopy, and its application to inorganic chemistry. New Analytical Methods (27), *Angewandte Chemie International Edition in English*, **25**(2), 131–58.

Colomban, P., Milande, V., and Lucas, H., 2004, On-site Raman analysis of Medici porcelain, *Journal of Raman Spectroscopy*, **35**(1), 68–72.

Colomban, P., 2004, Raman spectrometry, a unique tool to analyze and classify ancient ceramics and glasses, *Applied Physics A*, **79**(2), 167–70.

Constantinescu, B., 2007, Phase and chemical composition analysis of pigments used in Cucuteni Neolithic painted ceramics, *Documenta praehistorica*, **34**.

Cotte, M., Susini, J., Dik, J., and Janssens, K., 2010, Synchrotron-based X-ray absorption spectroscopy for art conservation: looking back and looking forward, *Accounts of Chemical Research*, **43**(6), 705–14.

Coutinho, M. L., Muralha, V. S. F., Mirao, J., and Veiga, J. P., 2014, Non-destructive characterization of oriental porcelain glazes and blue underglaze pigments using mu-EDXRF, mu-Raman and VP-SEM, *Applied Physics a-Materials Science & Processing*, **114**(3), 695–703.

De Nolf, W., Vanmeert, F., and Janssens, K., 2014, XRDUA: crystalline phase distribution maps by two-dimensional scanning and tomographic (micro) X-ray powder diffraction, *Journal of Applied Crystallography*, **47**(3), 1107–17.

Fayard, B., Pouyet, E., Berruyer, G., Bugnazet, D., Cornu, C., Cotte, M., Andrade, V. D., Chiaro, F. D., Hignette, O., Kieffer, J., Martin, T., Papillon, E., Salomé, M., and Sole, V. A., 2013, The new ID21 XANES full-field end-station at ESRF, *Journal of Physics: Conference Series*, **425**(19), 192001.

Figueiredo, M. O., Silva, T. P., and Veiga, J. P., 2012, A XANES study of cobalt speciation state in blue-and-white glazes from 16th to 17th century Chinese porcelains, *Journal of Electron Spectroscopy and Related Phenomena*, **185**(3–4), 97–102.

Frahm, E., 2014, Scanning electron microscopy (SEM): applications in archaeology, In *Encyclopedia of Global Archaeology* (ed. C. Smith), 6487–95, Springer New York.

Goldstein, J. I., Newbury, D. E., Echlin, P., Joy, D. C., Lyman, C. E., Lifshin, E., Sawyer, L., and Michael, J. R., 2003, *Scanning electron microscopy and X-ray microanalysis*, Springer US, Boston, MA.

Goodge, J., 2007, Electron probe micro-analyzer (EPMA), *Techniques*, URL: http://serc.carleton.edu/research_education/geochemsheets/techniques/EPMA.html.

Haswell, R., Zeile, U., and Mensch, K., 2008, Van Gogh's painting grounds: an examination of barium sulphate extender using analytical electron microscopy – SEM/FIB/TEM/EDX, *Microchimica Acta*, **161**(3-4), 363–9.

Ionescu, C., Hoeck, V., and Ghergari, L., 2011, Electron microprobe analysis of ancient ceramics: A case study from Romania, *Applied Clay Science*, Environment and Archaeology at the 14th International Clay Conference,

53(3), 466–75.

Jackson, J. E., 2004, A User's Guide to Principal Components, URL: http://eu.wiley.com/WileyCDA/WileyTitle/productCd-0471471348.html.

Janssens, K., Vincze, L., Adams, F., and Jones, K. W., 1993, Synchrotron radiation-induced x-ray microanalysis, *Analytica Chimica Acta*, **283**(1), 98–114.

Janssens, K., Vittiglio, G., Deraedt, I., Aerts, A., Vekemans, B., Vincze, L., Wei, F., De Ryck, I., Schalm, O., Adams, F., Rindby, A., Knöchel, A., Simionovici, A., and Snigirev, A., 2000, Use of microscopic XRF for non-destructive analysis in art and archaeometry, *X-Ray Spectrometry*, **29**(1), 73–91.

Janssens, K., Alfeld, M., Snickt, G. V. der, Nolf, W. D., Vanmeert, F., Radepont, M., Monico, L., Dik, J., Cotte, M., Falkenberg, G., Miliani, C., and Brunetti, B. G., 2013, The use of synchrotron radiation for the characterization of artists' pigments and paintings, *Annual Review of Analytical Chemistry*, **6**(1), 399–425.

Kock, L. D., and De Waal, D., 2007, Raman studies of the underglaze blue pigment on ceramic artefacts of the Ming dynasty and of unknown origins, *Journal of Raman Spectroscopy*, **38**(11), 1480–7.

Larkin, P., 2011, *Infrared and Raman Spectroscopy; Principles and Spectral Interpretation*, Elsevier.

Leon, Y., Sciau, P., Goudeau, P., Tamura, N., Webb, S., and Mehta, A., 2010, The nature of marbled Terra Sigillata slips: a combined μXRF and μXRD investigation, *Applied Physics A*, **99**(2), 419–25.

Leon, Y., Sciau, P., Passelac, M., Sanchez, C., Sablayrolles, R., Goudeau, P., and Tamura, N., 2015, Evolution of terra sigillata technology from Italy to Gaul through a multi-technique approach, *Journal of Analytical Atomic Spectrometry*, **30**(3), 658–65.

Liu, Y., Meirer, F., Williams, P. A., Wang, J., Andrews, J. C., and Pianetta, P., 2012, a program for advanced data collection and evaluation in full-field transmission X-ray microscopy, *Journal of Synchrotron Radiation*, **19**(2), 281–7.

Llusar, M., Forés, A., Badenes, J. A., Calbo, J., Tena, M. A., and Monrós, G.,

2001, Colour analysis of some cobalt-based blue pigments, *Journal of the European Ceramic Society*, **21**(8), 1121–30.

Majumdar, S., Peralta-Videa, J. R., Castillo-Michel, H., Hong, J., Rico, C. M., and Gardea-Torresdey, J. L., 2012, Applications of synchrotron μ-XRF to study the distribution of biologically important elements in different environmental matrices: A review, *Analytica Chimica Acta*, **755**, 1–16.

Mantler, M., and Schreiner, M., 2000, X-ray fluorescence spectrometry in art and archaeology, *X-Ray Spectrometry*, **29**(1), 3–17.

Mazzocchin, G. A., Agnoli, F., and Colpo, I., 2003, Investigation of roman age pigments found on pottery fragments, *Analytica Chimica Acta*, **478**(1), 147–61.

McQuire, A. V., Francis, C. A., Dyar, M. D., 1992, Mineral standards for electron microprobe analysis of oxygen, American Mineralogist, **77**(9-10), 1087-1091.

Meirer, F., Liu, Y., Pouyet, E., Fayard, B., Cotte, M., Sanchez, C., Andrews, J. C., Mehta, A., and Sciau, P., 2013, Full-field XANES analysis of Roman ceramics to estimate firing conditions—A novel probe to study hierarchical heterogeneous materials, *Journal of Analytical Atomic Spectrometry*, **28**(12), 1870–83.

Monico, L., Van der Snickt, G., Janssens, K., De Nolf, W., Miliani, C., Dik, J., Radepont, M., Hendriks, E., Geldof, M., and Cotte, M., 2011, Degradation process of lead chromate in paintings by Vincent van Gogh studied by means of synchrotron X-ray spectromicroscopy and related Methods. 2. original paint layer samples, *Analytical Chemistry*, **83**(4), 1224–31.

Padilla, R., Schalm, O., Janssens, K., Arrazcaeta, R., and Van Espen, P., 2005, Microanalytical characterization of surface decoration in Majolica pottery, *Analytica Chimica Acta*, **535**(1–2), 201–11.

Padilla, R., Espen, P. V., and Torres, P. P. G., 2006, The suitability of XRF analysis for compositional classification of archaeological ceramic fabric: A comparison with a previous NAA study, *Analytica Chimica Acta*, **558**(1–2), 283–9.

Papachristodoulou, C., Oikonomou, A., Ioannides, K., and Gravani, K., 2006, A study of ancient pottery by means of X-ray fluorescence spectroscopy, multivariate statistics and mineralogical analysis, *Analytica Chimica Acta*,

Instrumental Methods of Analysis -IMA 2005, **573–574**, 347–53.

Pillay, A. E., Punyadeera, C., Jacobson, L., and Eriksen, J., 2000, Analysis of ancient pottery and ceramic objects using x-ray fluorescence spectrometry, *X-Ray Spectrometry*, **29**(1), 53–62.

Pouyet, E., 2014, New methods for the preparation and analyses of paint samples from cultural heritage artifacts with combined hyperspectral techniques, , Ecole Doctorale de Physique de Grenoble, Grenoble, France.

Pradell, T., Molera, J., Bayés, C., and Roura, P., 2006, Luster decoration of ceramics: mechanisms of metallic luster formation, *Applied Physics A*, **83**(2), 203–8.

Reed, S. J. B., 2010, *Electron microprobe analysis and scanning electron microscopy in geology* 2 edition ed., Cambridge University Press, Cambridge.

Roqué, J., Molera, J., Sciau, P., Pantos, E., and Vendrell-Saz, M., 2006, Copper and silver nanocrystals in lustre lead glazes: Development and optical properties, *Journal of the European Ceramic Society*, **26**(16), 3813–24.

Roqué, J., Molera, J., Cepriá, G., Vendrell-Saz, M., and Pérez-Arantegui, J., 2008, Analytical study of the behaviour of some ingredients used in lustre ceramic decorations following different recipes, *Phase Transitions*, **81**(2-3), 267–82.

Salomé, M., Cotte, M., Baker, R., Barrett, R., Benseny-Cases, N., Berruyer, G., Bugnazet, D., Castillo-Michel, H., Cornu, C., Fayard, B., Gagliardini, E., Hino, R., Morse, J., Papillon, E., Pouyet, E., Rivard, C., Solé, V. A., Susini, J., and Veronesi, G., 2013, The ID21 Scanning X-ray Microscope at ESRF, *Journal of Physics: Conference Series*, **425**(18), 182004.

Sciau, P., Leon, Y., Goudeau, P., Fakra, S. C., Webb, S., and Mehta, A., 2011, Reverse engineering the ancient ceramic technology based on X-ray fluorescence spectromicroscopy, *Journal of Analytical Atomic Spectrometry*, **26**(5), 969–76.

Smith, G. D., and Clark, R. J. H., 2004, Raman microscopy in archaeological science, *Journal of Archaeological Science*, **31**(8), 1137–60.

Spray, J. G., and Rae, D. A., 1995, Quantitative electron-microprobe analysis of alkali silicate glasses; a review and user guide, *The Canadian Mineralogist*,

33(2), 323–32.

Wang, L., and Wang, C., 2011, Co speciation in blue decorations of blue-and-white porcelains from Jingdezhen kiln by using XAFS spectroscopy, *Journal of Analytical Atomic Spectrometry*, **26**(9), 1796–801.

Wang, T., Sanchez, C., Groenen, J., and Sciau, P., 2016a, Raman spectroscopy analysis of terra sigillata: the yellow pigment of marbled sigillata, *Journal of Raman Spectroscopy*. DOI: 10.1002/jrs.4906.

Wang, T., Zhu, T., Brunet, M., Deshayes, C., and Sciau, P., 2016b, Raman study of Yuan Qinghua porcelain: the highlighting of dendritic $CoFe_2O_4$ crystals in blue decorations, *Journal of Raman Spectroscopy*. DOI: 10.1002/jrs.5029.

Wang, T., Zhu, T. Q., Feng, Z. Y., Fayard, B., Pouyet, E., Cotte, M., De Nolf, W., Salomé, M., and Sciau, P., 2016c, Synchrotron radiation-based multi-analytical approach for studying underglaze color: The microstructure of Chinese Qinghua blue decors (Ming dynasty), *Analytica Chimica Acta*, **928**, 20–31.

Wen, R., Wang, C. S., Mao, Z. W., Huang, Y. Y., and Pollard, A. M., 2007, The chemical composition of blue pigment on Chinese blue-and-white Porcelain of the Yuan and Ming dynaties (ad 1271–1644)*, *Archaeometry*, **49**(1), 101–15.

Zhu, J., Luo, W., Chen, D., Xu, W., Ming, C., Wang, C., and Wang, L., 2013, New insights into the role of Mn and Fe in coloring origin of blue decorations of blue-and-white porcelains by XANES spectroscopy, *Journal of Physics Conference Series*, **430**, 012066.

Zhu, T.-Q., Zhang, Y.-C., Xiong, H., Feng, Z.-Y., Li, Q., and Cao, B.-L., 2015, Comparison of the different types of Qinghua porcelain from Jingdezhen in the Yuan dynasty of China (ad 1271–1368) by micro X-ray fluorescence spectroscopy (μ-XRF) and microscopy, *Archaeometry*. DOI: 10.1111/arcm.12215.

Chapter III Iron-rich slips of antique ceramics

General abstract

Pottery decors based on Fe-rich clay are quite common and were widespread in several societies from the Neolithic time. In particular during the Greek and Roman periods, high gloss coatings were developed both to decorate and to render vessels waterproof. By exploiting the different iron valences, the potters were able to obtain red (trivalent iron oxides) or black (bivalent iron oxides) colors but also yellow color (marbled terra sigillata) using Ti and Fe rich clays. In collaboration with the archaeologists from Lattes (Montpellier III university), I applied and adapted the multi-scale approach to study two types of decors of antique period. The first one concerns the slip of the marbled terra sigillata made during the Roman time in the La Graufesenque workshop (Millau, France). Previous study showed that the yellow color was certainly due to the presence of pseudobrookite (Fe_2TiO_5) (Leon et al. 2010b) and my work was to verify this point on a significant corpus and to determine the manufacturing process. The second one concerns the black and red coatings of Attic pottery made in Athens and found in the excavations of antic city of Lattara (Lattes, France). The aim was to study the firing process and in particular to establish if different protocols were used for obtaining these ceramics in relation with the new assumptions proposed by the Paul Getty team (Walton et al. 2013).

1 Roman marbled terra sigillata

1.A State of the art

1.A.1 Archaeological and historical knowledge

Terra sigillata, as the most famous fine ware of the Roman period, represents a milestone of the manufacture of potteries with high gloss coating and relief decoration (Oswald et al. 1966). In addition to the terra sigillata production with a red high gloss coating, the largest Gallic workshop (La Graufesenque) made a special type of terra sigillata, called “marbled” by the archeologists and characterized by a singular yellow gloss coating with red veins (Figure 1.A.1.1) (Hermet 1934; Genin 2007). From the archaeologists, this production should be a specialty of La Graufesenque workshop and no other Roman workshop had manufactured marbled terra sigillata.

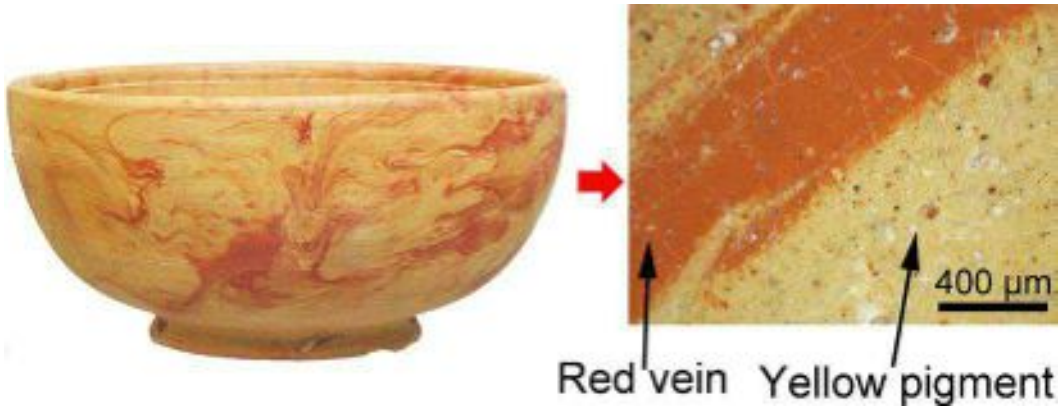

Figure 1.A.1.1 Bowl of marbled terra sigillata (Mid 1st century AD. British Museum, London, Credit: World Imaging, CC BY-SA 3.0). The zooming image came from a similar fragment of marbled terra sigillata found in La Graufesenque (labeled as TSGM-C sample).

The manufacturing of marbled terra sigillata began around 30 AD and continued until the end of the first century AD (Leon et al. 2010b). Although marbled sigillata represents only a few percent of La Graufesenque productions of the first century AD, many *officines*[2] had been involved in its manufacturing and the index of shapes was also large (Genin 2007). Marbled terra sigillata was

[2] The workshop of La Graufesenque, as other terra sigillata workshops, is constituted of several officines identified by their stamps or potter marks.

traded as widely as that of standard terra sigillata, with a slightly stronger representation in the Mediterranean Basin. Its absence in some areas, in particular northern provinces, is to be highlighted: marbled terra sigillata seems absent in the Netherlands and very rare in England or Germany (Genin 2007).

1.A.2 Manufacture process

The manufacture process of marbled terra sigillata was subject to similar criteria and regulation of the standard terra sigillata (i.e., sizes, shapes and patterns and firing conditions) (Genin 2007, Sciau et al. 2008). The decorative forms were obtained as standard terra sigillata using molds and certainly same molds were used to make standard and marbled terra sigillata. The discovered pottery molds have thick walls and the decoration was printed on the interior surface using stamps (Hofmann 1971). The molds were probably fired at around 800~900 °C, to remain porous and thus they were easy removal of the vessels. Potters firstly applied a clay slab that was plastered on the inside wall. After the body dried, the shrinkage was enough for it to be withdrawn from the mold. The finishing work was performed on the dried body then, including the addition of foot-rings and treatment of the rims (shaping, cleaning, smoothing) in order to then the application of slips.

Once dried, the pieces may be then dipped into mixture of two different liquid slips, before being fired. However, the contemporary craftsmen do not use this process for similar production and prefer to dip the vessel in the first liquid slip and splash the second slip with a brush. The red part of the slip was prepared from the similar varnish as the standard red sigillata slip used in La Graufesenque workshops (Leon et al. 2010b), which was obtained from a Fe rich clay. From the first analysis, the varnish made for yellow slip contains less iron and more magnesium and titanium. M. Picon proved that the clay used come from the alteration of volcanic materials (Picon 1994).

The high quality of the sigillata was due to the vitrification of its slip and in order to preserve its red color, the vitrification had to be performed under oxidizing condition (oxygen-rich). For this, special kilns were developed by Roman potters to isolate the pieces from flames (Vernhet 1981). Inside the kilns, the vases were stacked and separated from each other by separators. The firing process had to last several days and a batch could contain thousands of potteries, according to the inventory engraved on the plates by the potters. The accidents of firing process happened occasionally, such as over fired vases deforming and sticking to each other (Vernhet 1981).

Firing process generally went through four stages: 1) firstly, the temperature raised slowly to about 500 °C depending on the clay; 2) then, the temperature would follow a more rapid rise until the final firing temperature; 3) thirdly, an

appropriate time at that temperature was applied; 4) finally, the pieces were cooled.

1.A.3 Issues and research objectives

In summary, marbled sigillata coating resulted from the use of two different liquid slips. The red part of the fired slip was similar to the slip of the standard terra sigillata, which got its color from the hematite (Sciau et al. 2008), while the yellow component was obtained from a titanium-rich clay preparation. Micron-X-ray powder diffraction analysis demonstrated that the yellow color comes from the formation of pseudobrookite (Fe_2TiO_5) during firing process (Leon et al. 2010b).

Indeed, pseudobrookite was proposed as yellow pigment for modern ceramics and studies were devoted to its syntheses (Dondi et al. 2007; Dondi et al. 2008). However, due to stability problems and its high abilities to react with the ceramic matrix, it was not used until now. In fact, its color highly depends on the matrix composition, because of its ability to undergo substitution changes with the matrix, and syntheses conditions. Therefore, it seems that both the composition of the clay and the firing conditions used by the Roman potters were suited to obtain a stable yellow color. The study of the manufacture process could provide suggestions concerning the syntheses of the yellow pigment. Conversely, the high sensitivity of pseudobrookite to its surrounding could be used to study the homogeneity and quality of the production.

The previous study concerned only a few fragments coming from the La Graufesenque site and moreover selected for their nice yellow color. The aim of my work is to have a more representative description of marbled terra sigillata produced in La Graufesenque workshop. For this, we have selected with the archaeologists (A. Vernhet and C. Sanchez) 20 fragments (labeled as TSGM-) coming from the excavation of La Graufesenque workshop and 23 fragments excavated from the old city of Narbonne (labeled as CS) (Appendix 1 and 2). Narbonne was an important center in the trade of La Graufesenque sigillata for the Mediterranean Basin (Sanchez 2003).

1.B Method strategy

Due to the quite large number of fragments and the information already obtained in the previous study, I chose to focus my investigation on yellow component of the slip. In a first step, I completed the determination of elemental composition by EPMA. Previous studies showed that the EPMA was a powerful tool to determine the global elemental composition of slip and to define the chemical characteristic of a production (Leon et al. 2015). In the second step, synchrotron radiation based

techniques (μ-XRF and FF-XANES) were used to study large zones in detail on a selection of a few fragments. μ-XRF was applied to study the elemental distribution of the main elements. To investigate the distribution of Ti-based phases (pseudobrookite, anatase and rutile), FF-XANES analyses were performed along the Ti K-edge. The results allow positioning the pseudobrookite for the next local analysis (Raman spectroscopy). In the third step, I focused on the structural characteristic of pseudobrookite crystals by Raman spectroscopy. In the case of sigillata, Raman spectroscopy does not allow us to identify all crystallographic phases present in slip. It is difficult to detect spinel and corundum, but it is very efficient for titanium and iron oxides (Leon et al. 2010a). It is one of the ideal tools to study the structural feature of pseudobrookite in presence of other phases such as spinel ($MgAl_2O_4$) or corundum (Al_2O_3).

The EPMA and Raman measurement were performed on cross-section sample (cf. chapter II, § 2.A.1) while synchrotron investigations were carried out on dedicated samples (cf. chapter II, § 2.B)

As no good reference Raman spectrum of pseudobrookite is available in the literature, we asked to M. Dondi to send us synthesized pseudobrookite powder, labeled as P47 (Dondi et al. 2007; Dondi et al. 2008). This powder was analyzed by X-ray diffraction, and it is constituted of 97% pseudobrookite and 3% hematite (Dondi et al. 2007). Hematite crystals are easily identified by Raman spectroscopy, and the other crystals (majority) present all similar Raman spectra, which were attributed to pseudobrookite.

1.C Archaeological samples

Forty-three sherds of marbled terra sigillata were selected by the archaeologists (Appendix 1 and 2). The sherds are dated between 30 AD and the end of the first century AD and were produced in La Graufesenque workshop. Figure 1.C.1 displays the TSGM-Q sample, which exhibits a well-marked yellow color with well-contrasted red veins.

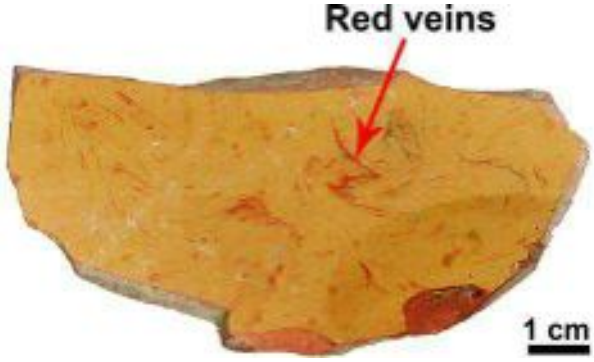

Figure 2.C.1 Photography of TSGM-Q sherd (La Graufesenque excavation) shows the yellow slip covered of red veins.

1.D Results

1.D.1 EPMA analyses

The analyses were performed on the CAMECA microprobe of GET before the transfer of activity at *Centre de Microcaractérisation R. Castaing*. During 6 months the service was interrupted and we were not able to analyze all samples. Like 13 yellow zones coming from 11 sherds of La Graufesenque (TSGM type) were already analyzed by Y. Leon (Leon 2010), I focused my investigation on the Narbonne samples (CS type). The whole results are given in Appendix 3 while Table 1.D.1.1 gives the average composition. Compared to the standard red slip, the yellow component of slip is characterized by a higher Ti and Mg rates. The concentration of Fe is lower and Ca is a little higher. Si, Al and K concentrations are very similar for the red and yellow slips. The samples from the two excavation sites show similar elemental compositions. Some samples from Narbonne contain less Ti and Fe but these samples are also characterized by a light yellow color. The color of yellow part of CS15 sample, which contains only 1% of Ti, is almost white. The difference between the two groups seems only to indicate that vessels with light colors were also marketed. The yellow component is more heterogeneous than the standard red slip, leading to the higher values of the standard deviations (Appendix 3). It is particularly true for the Ti and Fe distributions and consistent with the hypothesis of volcanic origin (Picon 1994). The clays present great variations of composition, which is not the case of Triassic[3] clays used for the preparation of red standard slip.

Shard	Na_2O	MgO	Al_2O_3	SiO_2	P_2O_5	K_2O	CaO	TiO_2	MnO	Fe_2O_3	BaO
Yellow-Narb (17)	0.09	2.6	25.82	54.88	0.07	8.13	1.74	2.66	0.03	3.85	0.25
	(0.06)	(0.64)	(3.90)	(2.25)	(0.03)	(0.91)	(0.53)	(0.78)	(0.01)	(0.90)	(0.33)
Yellow-Grauf (13)	0.05	2.73	22.74	56.72	0.18	7.81	1.60	3.81	0.03	4.16	0.20
	(0.02)	(0.18)	(1.11)	(1.18)	(0.18)	(0.46)	(0.27)	(0.62)	(0.01)	(0.64)	(0.05)
Red Standard (38)	0.07	0.89	23.27	55.7	0.15	8.19	1.24	0.72	0.05	9.62	0.08
	(0.02)	(0.15)	(2.44)	(2.3)	(0.03)	(0.76)	(0.27)	(0.1)	(0.01)	(0.82)	(0.02)

Table 1.D.1.1 Mean elemental compositions of the yellow component compared to the one of red standard slips (Sciau et al. 2007). The standard deviations are given in brackets.

[3] The Triassicis a geologic period and system which spans 50.9 million years from the end of the Permian Period 252.17 million years ago (Mya), to the beginning of the Jurassic Period 201.3 Mya.

1.D.2 Synchrotron radiation based technique investigations

1.D.2.a SR-μ-XRF study

Three samples (2 from Narbonne and 1 from La Graufesenque) were investigated by SR-μ-XRF. The trichromatic diagrams (K, Ca, Si) (Figure 1.D.2.a.1a) identify clearly the different zones (body and slip). The thickness of slips is similar and around 30-40 μm for the three samples. It is similar with the thickness of the standard red slip of the La Graufesenque productions (Sciau et al. 2006). The surface layer of TSGM-D rich in calcium is due to the accumulation of material deposited on the ceramic surface during the burial stage. The high K rate of slips is evident as well as the high Ca rate of bodies. The high Si rate (green grains) corresponds to quartz grains. One can notice that the difference of grain sizes between the body and the slip. Only a few small crystals are observed in the slips while in the body grains up to 40 μm are observed. K seems homogenously distributed in the slips. The Fe/Ti maps show that the Ti distribution is quite heterogeneous. Even if the samplings were performed in yellow zones trying to avoid the red veins, some small inclusions appear in the maps as Fe-richer zones indicated with white arrows on Figure 1.D.2.a.1b.

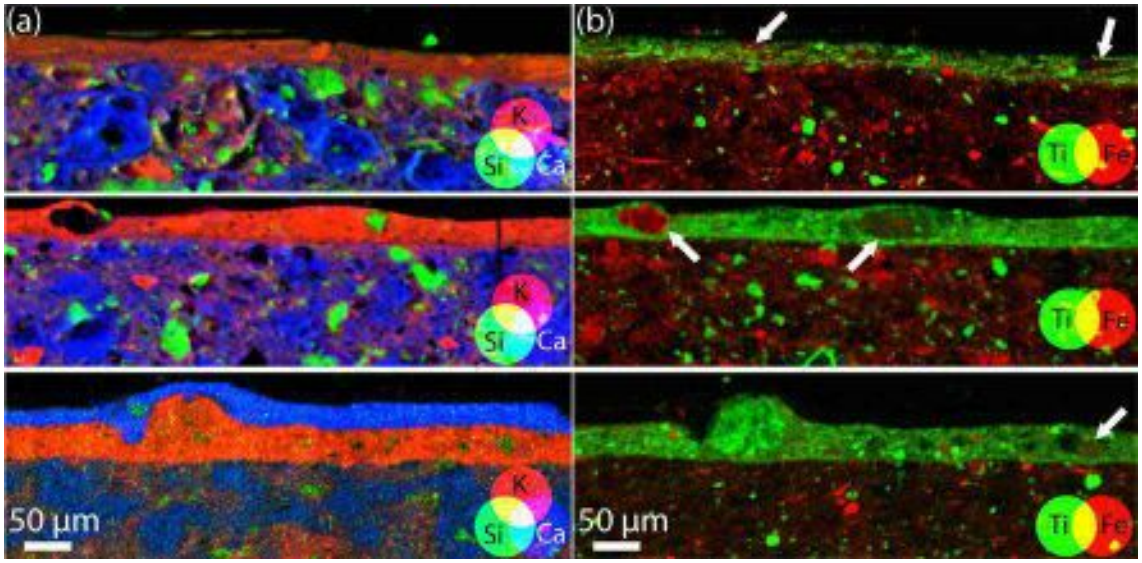

Figure 1.D.2.a.1 Trichromatic diagrams (K, Ca, and Si) (a) and Fe/Ti map (b) obtained by synchrotron radiation micro X-ray fluorescence on thin sections at ID21 (ESRF): the sample from top to bottom is CS16, CS24, and TSGM-D, respectively.

1.D.2.b FF-XANES investigations along Ti K-edge

One sample (CS27) was examined using the FF-XANES approach, shown in Figure 1.D.2.b.1. The transmission image recorded at 4920.1 eV, below the Ti K-edge, shows that the slip of the thickness of ~30 µm, is denser and much more homogeneous than the body. The edge jump map, corresponding to the variation of titanium concentration, is consistent with the XRF measurements and also indicates that titanium is mainly concentrated in the slip, while only some Ti rich grains are observed in the body.

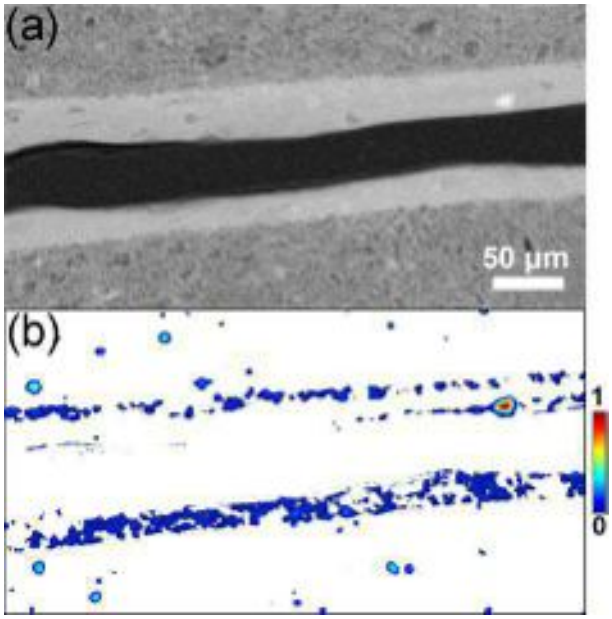

Figure 1.D.2.b.1 Results of FF-XANES analyses performed at the Ti K-edge for CS27 with: (a) the transmission image of sample thin-section recorded at 4920.1 eV and (b) the edge jump map (correlated to Ti concentration). The scale bar for the edge jump map reports the values of the (absorption) edge jump.

After a *k*-means clustering which revealed three different types of XANES spectra close to anatase, rutile and pseudobrookite spectra, a least squares linear combination was performed. The resulting phase map is shown in Figure 1.D.2.b.2. The main phase in the slip is pseudobrookite with some anatase and rutile crystals. Pseudobrookite is not present in the body and only titanium oxides (anatase and rutile) were detected. This is in accordance with the previous SR-µXRD study (Leon et al. 2010b), which revealed that the pseudobrookite was only present in the yellow part. However, the low spatial resolution of the mineralogical map prevented showing the heterogeneity of repartition. In contrast, the higher resolution and the large field of view of FF-XANES approach allow us to observe both the heterogeneity of repartition and the imbrications

pseudobrookite/anatase on a representative zone.

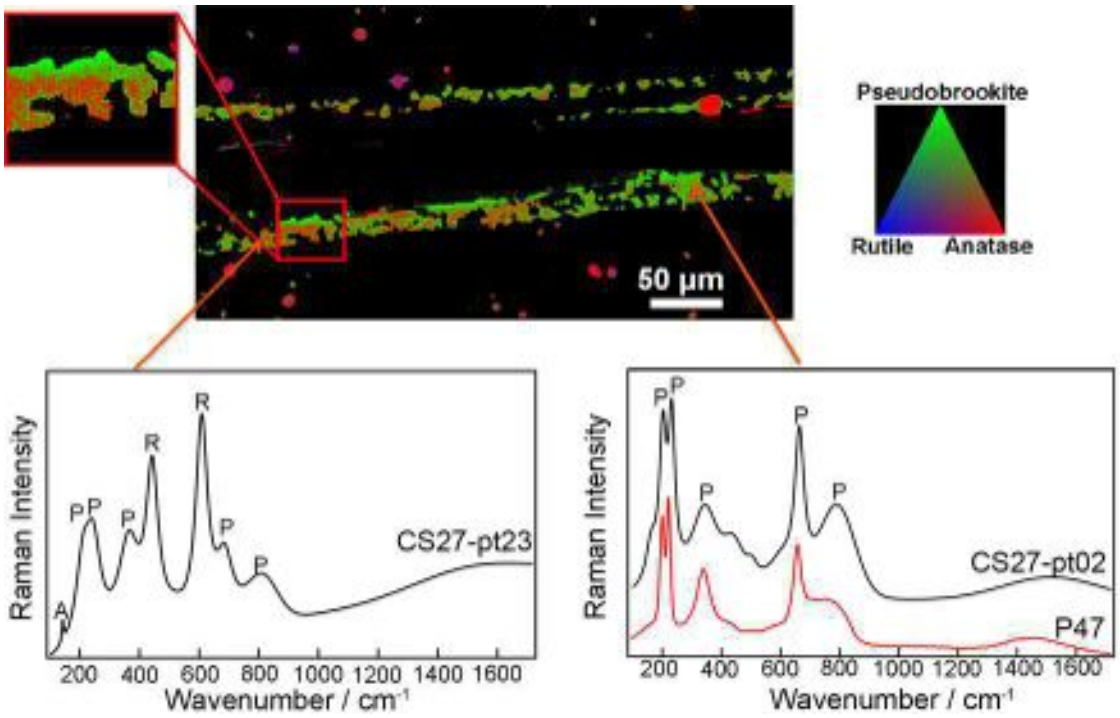

Figure 1.D.2.b.2 Phase map obtained from the least squares linear combination fitting of each XANES pixel using the references XANES for pseudobrookite (P), rutile (R) and anatase (A) of ALS database. Raman spectrum of mixed zone (CS27-pt23) and Raman spectrum of pure pseudobrookite zone (CS27-pt02) with the Raman spectrum of synthesized pseudobrookite (P47).

1.D.3 Raman spectroscopy study

The CS27 thin cross-section sample was investigated by Raman spectroscopy to identify the Raman spectrum of pseudobrookite. All the records performed in identified pseudobrookite zones by FF-XANES approach show similar characteristic with the CS27-pt02 spectrum of Figure 1.D.2.b.2 (bottom right). They are also similar to the ones recorded from the reference powder (P47). They present the 6 peaks assigned to the pseudobrookite by Bersani et al (Bersani et al. 2000). In contrast, they do not show the characteristic lines of titanium oxides (anatase, rutile, brookite) (Tompsett et al. 1995) or ferric oxides (hematite, maghemite) (Jubb and Allen 2010). Besides, the Raman spectra recorded in zones containing titanium oxides from the phase map obtained by FF-XANES, shows the characteristic bands of rutile (442 cm^{-1}, 609 cm^{-1}), anatase (143 cm^{-1}) as shown in Figure 1.D.2.b.2 (bottom left). After identifying the spectrum of pseudobrookite, we sought to study more specifically pseudobrookite crystals by

Raman spectroscopy on a significant corpus.

For this, we recorded around fifteen spectra of pseudobrookite rich zones per sample. To get a more precise determination of Raman spectrum variations, the pseudobrookite (P47) powder synthesized by M. Dondi was used as the reference (Dondi et al. 2007). Figure 1.D.3.1 shows some spectra obtained from the CS27 cross-section sample. The spectra acquired from the red inclusions exhibit all the characteristic of hematite with, in particular, a high intense peak at 1350 cm^{-1}. These spectra are identical in all respects to the spectra recorded in red standard slip of La Graufesenque workshop (Leon et al. 2010a). In contrast, the spectra recorded in the yellow component do not present the characteristic peaks of hematite and a majority of them are similar to the ones of powder synthesized with however some systematic differences i.e. a shift to higher wavenumbers and a broadening of all peaks. The others recorded in the yellow component present the characteristic peaks of rutile and/or anatase.

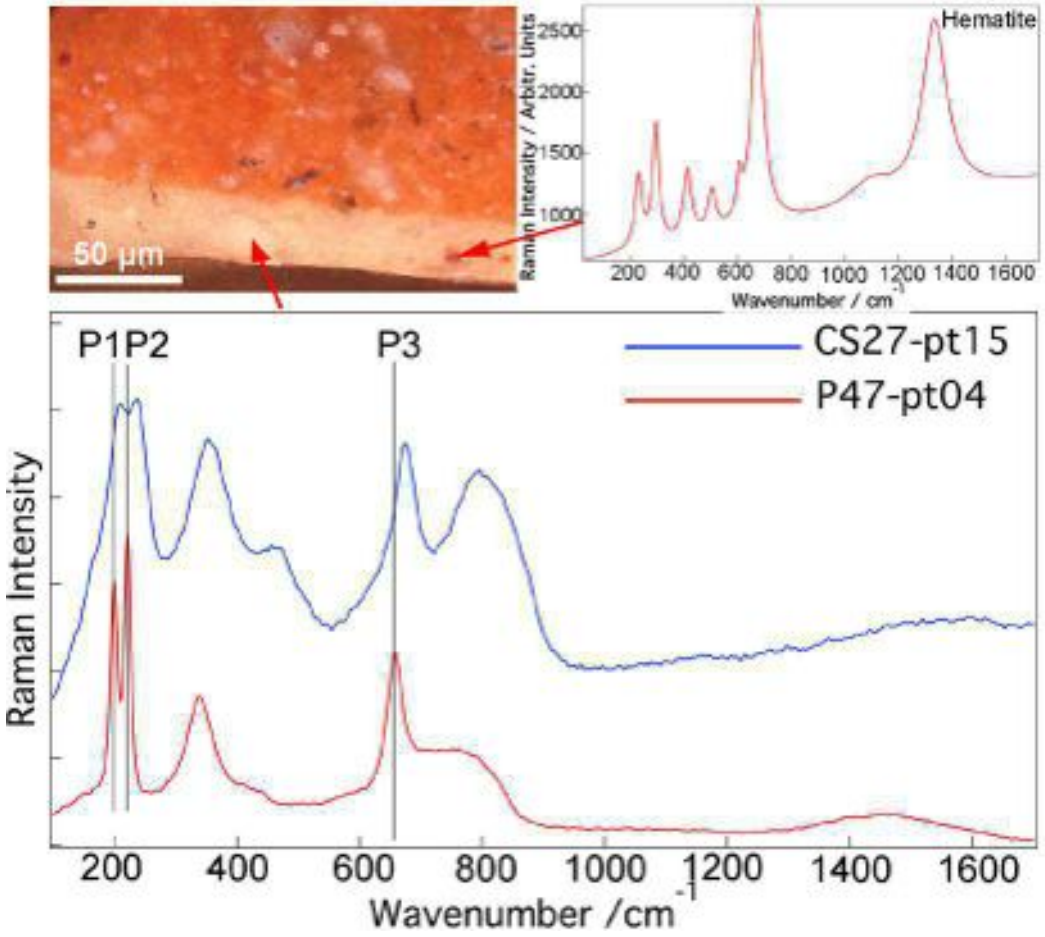

Figure 1.D.3.1 Optical image (top left) of the CS27 cross-section sample showing the yellow slip with red inclusions. Raman spectra recorded in a red inclusion (top right) and in yellow zone (bottom). The comparison with the synthesized powder (P47) shows the shift peaks.

The pseudobrookite spectra present small differences among them. Also, we tried to characterize these differences by focusing on the three well-defined peaks (P1, P2, P3). For this, we compared their positions and full width at half maximum (FWHM) with ones of synthesized pseudrobrookite (P47) using boxplot graphs (Figure 1.D.3.2). It can be noticed that P2 and P3 are twice more shifted (20 cm^{-1}) than P1, but the dispersion of values is greater (Figure 1.D.3.2a). Regarding the reference, the evolution of FWHM is both notable and comparable for the three peaks with an increase of about 23 cm^{-1} (Figure 1.D.3.2b).

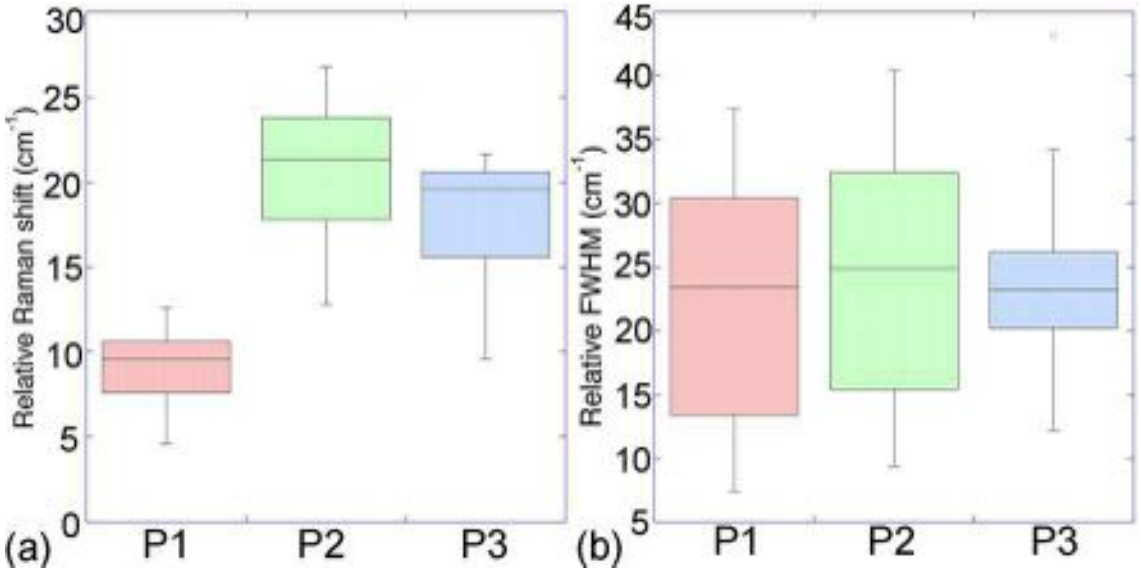

Figure 1.D.3.2 Boxplots representation of the distributions of relative Raman shifts (a) and relative FWHM (b) of the three well-defined peaks with respect to the peak position of P47 reference (P_i(CS27) –P_i(P47)).

The other 42 samples revealed similar features i.e. peak shifts to higher wavenumbers and a significant line broadening of the first two peaks. Some dispersion is also observed inside the spectra coming from the same sample as shown in Figure 1.D.3.3. It can be noticed that the samples with the smallest shifts (as CS16) have a narrower distribution. The line broadenings of TSGM-N are significantly higher than the ones of CS16 (Figure 1.D.3.4). To detect a possible trend of the evolution among different samples of marbled terra sigillata, we calculated the standard deviations and the average values corresponding to each sample. The results show that the line broadening of all peaks increases with the shift (Figure 1.D.3.5a, b, and c). The increase of P1 and P2 peak shifts seem to be associated to a wider of dispersion (Figure 1.D.3.5d and e). The effect is less marked for P3 (Figure 1.D.3.5f) for which the standard deviation is almost independent on the shift. The two series (Narbonne and La Graufesenque) of samples do not present any specific difference except for the first peak for which

two samples from Narbonne show a higher standard deviation. However, this singularity, which was not found in other parts of Raman spectrum, cannot be attributed to a significant difference between the two series but instead a too limited corpus. From the viewpoint of Raman spectroscopy, the pseudobrookite crystals of the two series exhibit the same characteristics. It is in good agreement with archaeological study, which attributed the samples found in Narbonne to the production of La Graufesenque workshop (Genin 2007).

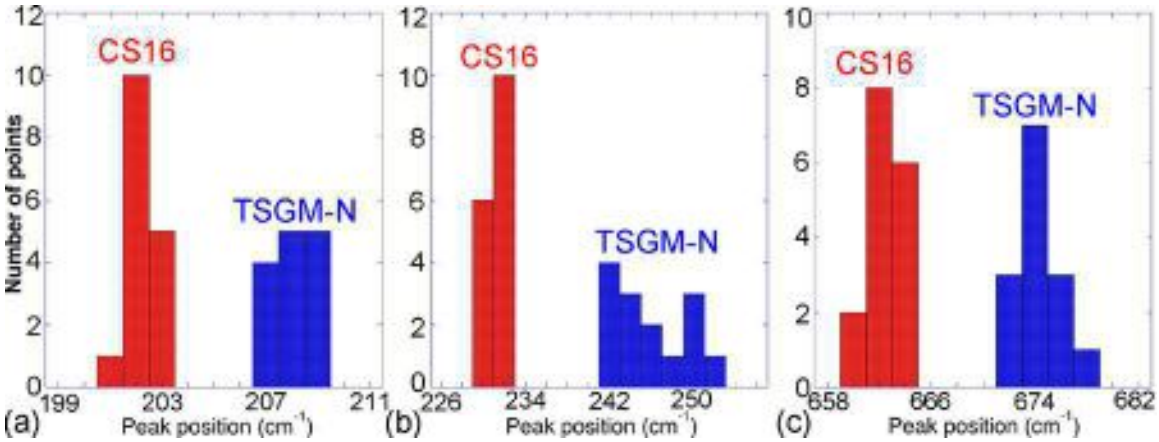

Figure 1.D.3.3 Distributions of the Raman shifts of the three well-defined peaks for two different samples CS16 and TSGM-N.

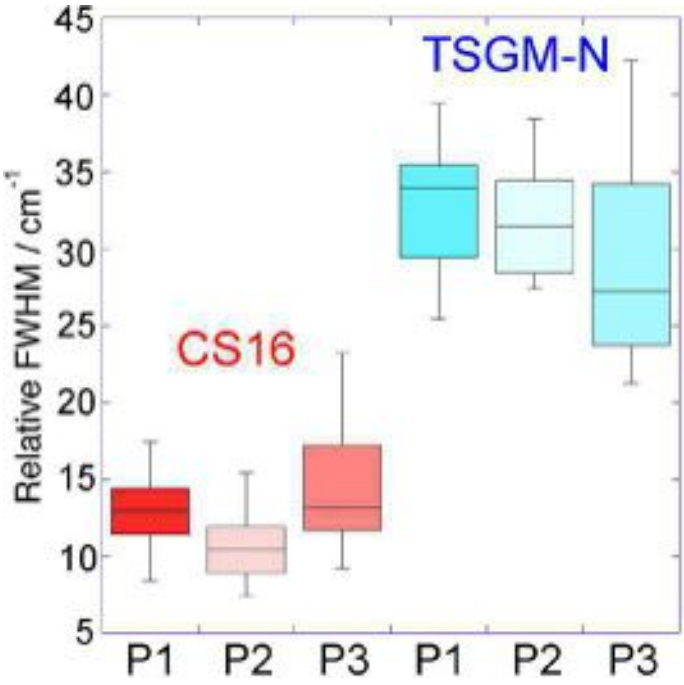

Figure 1.D.3.4 Boxplot of relative FWHM for CS16 and TSGM-N samples.

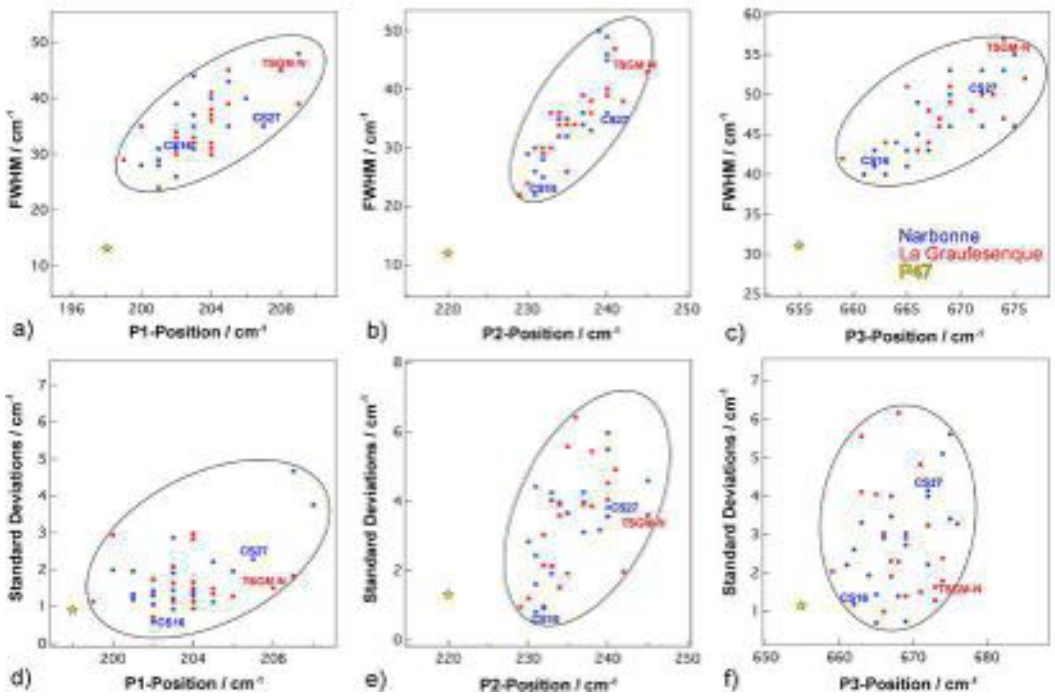

Figure 1.D.3.5 Graphical representations of P1, P2, and P3 peak positions versus full width at half maximum (FWHM) (a, b and c) and versus standard deviations (d, e and f) and for all samples (Narbonne and La Graufesenque).

1.E Discussion

The association of FF-XANES and Raman results performed on the same sample zone allowed us to identify the Raman spectrum of pseudobrookite crystals contained in marbled terra sigillata slips. The Raman spectra of pseudobrookite crystals in terra sigillata reveal several differences with respect to pure pseudobrookite, which is characteristic to this ceramic production. Unfortunately, without a detailed study of vibrational modes and force constant calculations, it is difficult to identify the origin of these differences. On the base of force constant calculations, the Raman bands of anatase below 400 cm^{-1} were attributed to O–Ti–O bending-type vibrations while those earlier were ascribed to Ti–O stretching-type vibrations (Ohsaka et al. 1978). In their Raman study of brookite, Tompsett et al. have considered that it is also true for this more complex structure (Tompsett et al. 1995). Even if the structure of brookite and pseudobrookite is not isostructural and the chains of edge-sharing octahedra are not the same, one can assume that the two first strong peak (P1 and P2) correspond to bending-type vibrations while the P3 peak could be attributed to stretching-type vibrations.

However, the shifts and the increasing of line broadening are consistent with substitutions of Fe and/or Ti by other ions. In the paper concerning the color of pseudobrookite, M.Dondi specified that the structure accepts various substitutions

and in particular he points out that Al and Mg substitutions allow for obtaining yellow-ochre colors (Dondi et al. 2007). The color of pure pseudobrookite is too dark and goes to brown (Maloney 2002). The yellow zones of slips contain a substantial amount of Al and Mg. Mg participates to the formation of spinel crystals ($MgAl_2O_4$) detected by X-ray diffraction (Leon et al. 2010b). However, it cannot be excluded that a part of Mg was integrated in pseudobrookite structure through the substitution 2 $Fe^{3+} \rightarrow Mg^{2+} + Ti^{4+}$ to give a compound of $(Fe_{2(1-x)}Mg_xTi_x)TiO_5$ type. These slips, obtained from clay preparation, contain a high amount of Al, and it is quite likely that during the formation of pseudobrookite, this ion was integrated in its structure as it was integrated in the structure of hematite of red terra sigillata (Zoppi et al. 2008). In addition, it was demonstrated that the Al → Fe substitution in hematite lead to an increase of line broadening and peak shifts to higher wavenumbers (Zoppi et al. 2008). Even if the marbled terra sigillata was fired under oxidation condition by potters mastering perfectly this type of firing, one cannot exclude the presence of a small amount of Fe^{2+} in the pseudobrookite structure because there is a solid state solution $Fe^{3+}{}_2Ti^{4+}O_5$ (pseudobrookite) and $Fe^{2+}Ti^{4+}{}_2O_5$ (ferropseudobrookite) [Guo 1999]. However, the presence of Fe^{2+} and Fe^{3+} in the same structure increases highly the optical absorption and leads to dark colors.

The peak shifts to higher wavenumbers are consistent both with Al and Mg substitutions. Indeed, Al–O and Mg–O bonds being shorter than Fe–O and Ti–O bonds, the incorporation of these ions in the structure leads to compressive strains on the $[FeO_6]$ and $[TiO_6]$ octahedrons (Guo et al. 1999; Liermann et al. 2006). The substitution induces also structural disorders, which accounts for the line broadening we have observed (Figure 1.D.3.1 and 1.D.3.5). Disorder is known to relax wavevector conservation and thus to allow additional modes to be Raman active. We emphasize that the intensity of broad bands (around 430 and 790 cm^{-1}) is significantly increased and that the broadening of the well-defined peaks is asymmetric on the low wavenumber side (Figure 1.D.3.5). The latter effect results from the negative phonon dispersion.

The variations among the spectra recorded from the same sample could be due to fluctuation of Al and/or Mg rate inside the pseudobrookite structure. Transmission electron microscopy revealed that the pseudobrookite crystals are mainly grouped within the matrix and form clusters of a few micrometers (Sciau et al. 2009). Inside the clusters, the porosity is high, and the center of the largest clusters is only constituted of pseudobrookite crystals. The matrix comes from the vitrification of clay minerals containing Al and Mg. A small amount of Al and maybe Mg could be also integrated in the pseudobrookite structure during its formation and specially, for the crystals on the edge of the clusters, which could explain a variation of substitution rate inside the pseudobrookite structure and thus the dispersion in the Raman data within a given sample (Figure 1.D.3.5).

Further transmission electron microscopy investigations, including elemental analysis, are in progress to verify this point and to define precisely the nature of the substitution.

1.F Conclusion

The multi-scale approach, associating lab-based techniques (EPMA and Raman spectroscope) and SR-based techniques (μ-XRF and FF-XANES), allowed us to obtain major information concerning the yellow component of marbled terra sigillata slips. It also permitted to obtain significant data concerning the pseudobrookite, a potential yellow pigment for modern ceramic industry. The extension of EPMA measurements, on a more significant corpus, has confirmed the results obtained on a few samples, i.e., the yellow component contains more titanium, less iron, and more magnesium than red standard one. It has also revealed that the distribution of elemental composition was larger with the commercialization of vessels with light yellow color containing few Ti concentrations (about 1%). SR-μ-XRF displayed distribution of elements and, in particular, allowed revealing the difference in composition and structure between the body and the slip. It also confirmed that the FF-XANES investigations were well performed in yellow component containing a few red veins (Fe-rich inclusions). The association of FF-XANES and Raman measurements allowed us to identify the Raman spectrum of pseudobrookite crystals contained in marbled terra sigillata slips.

Pseudobrookite is thermodynamically unstable with a positive enthalpy of formation, its structure being stabilized by the configurational entropy of formation (Navrotsky 1975) due to a partial cationic disorder (Teller et al. 1990). The presence of other cations such as Mg in octahedral sites increases the structural disorder and thus improves the structure stability. The yellow color of marbled terra sigillata is consistent with Al and/or Mg substitutions indicated by the peak shifts and line broadening observed on the Raman spectra.

Although pseudobrookite is a potential ceramic pigment, it is not used nowadays because, in addition to the difficulties to synthesize it with a well-defined color, its coloring performance also depends on the physico-chemical properties of the ceramic matrix (Dondi et al. 2007). According to the thermodynamic instability, various elements of the ceramic matrix can be incorporated in the pseudobrookite structure during the manufacturing process leading to color modifications. In the case of marbled terra sigillata, the pseudobrookite is formed during the firing, and it is natural that elements of surrounding compounds are incorporated in its structure in order to stabilize it.

The characteristic yellow color of marbled terra sigillata results from the formation of substituted pseudobrookite crystals containing certainly a small

amount of Al and/or Mg in addition to Ti and Fe. Although the marbled terra sigillata slips contain several phases such as quartz, corundum, anorthite, spinel, hematite, rutile (present study), anatase (present study) and pseudobrookite (Leon 2010), the multi-scale approach allowed us to focus on a specific component (here the yellow part of slip) with an adapted resolution (here the micrometer) and a selective technique (here the Raman spectrometry) and to be able to study the in-depth structural characteristic of a specific phase (here the pseudobrookite).

2 Attic potteries

2.A State of the art

2.A.1 Archaeological and historical knowledge

The potteries, produced in Athens between the sixth and fourth centuries BC, are one of the most successful artistic and technological achievements of ancient Greek craftsmen. In the late seventh century BC, Athenians adopted a new decorative technique which came from Corinth (Folsom 1975; Boardman 2006), called "black-figure", which appeared at the beginning of seventh century BC in Corinth (Figure 2.A.1.1, left image). Based on this technique, Athenians invented a new “red-figure” decorative technique around the beginning of the last quarter of the sixth century BC (Figure 2.A.1.1, right image) (Boardman 1985). During the late sixth and the fifth century, it was the golden period of Attic pottery. The production was manufactured by more precise technology and produced massively. It was widely exported to Western Mediterranean (Greek colonies of the West, like Marseille) and also in some areas by Punic traders or Iberian (Py 2000). In the fourth century, the quality of traditional red figure Attic potteries had declined. But the production continued to find new markets and was experiencing a resurgence of activity between 370 and 320 BC (Py 2000). At the end of the Classic period, the production of ceramics with red figures disappeared.

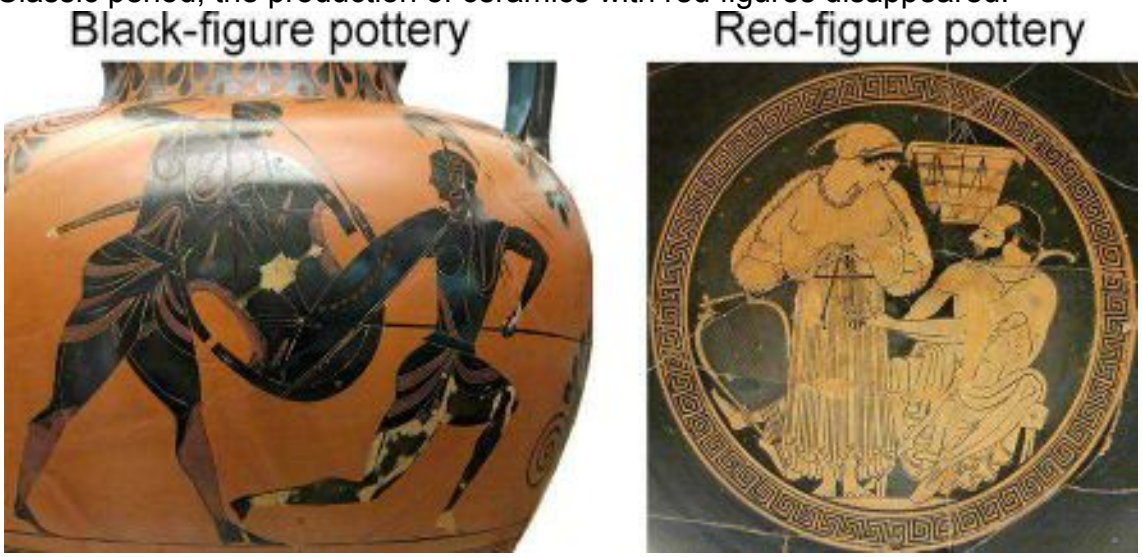

Figure 2.A.1.1 Patterns of black-figure pottery (left side) and red-figure pottery (right side). (Credit of the two images: World Imaging, CC BY-SA 3.0).

2.A.2 Manufacturing process

The manufacturing process of Attic pottery is composed of the preparation of un-fired vessels and the firing process (Noble 1960).

The clay was firstly washed and settled to get rid of impurities. Then it was dried to a workable consistency. The vessel was formed either by potter's wheel or by molds. After smoothing the surface of well-shaped vessels with burnisher, potters pointed the sketch using charcoal stick and could directly paint the picture to obtain black-figure pottery, or outlined figures with broad band of heavy glaze using brush ("quarter-inch" stripe) and filled the background up to the outline of broad band to obtain red-figure pottery.

The well-painted wares were then fired in a high-temperature kiln alternating between oxidative and reductive environments (Noble 1960; Lapatin 2008). They went through three-stage firing applying alternating oxidizing–reducing–oxidizing conditions in the kiln (Figure 2.A.2.1). Firstly, potters heated the kiln up to 800 ºC with all the vents on the sides open to let air in to get oxidative atmosphere. In this stage, both body and slip of pottery turned to red color. Once the temperature reached to 800 ºC, potter added organic matter (green plants, leaves etc.) and closed all the vents to deplete the kiln of available oxygen through the formation of carbon dioxide to get reductive atmosphere. The temperature could rise to 950 °C and then drop back to 875 °C. During this stage, both body and slip turned black. The final stage was the cooling stage that potters reopened the vents let all air in to allow the kiln to be cooling. In this stage, the body was turned to be red again whereas the slip remained black due to its vitrification in second stage. Finally, the painted area remained black and the bare area stayed red.

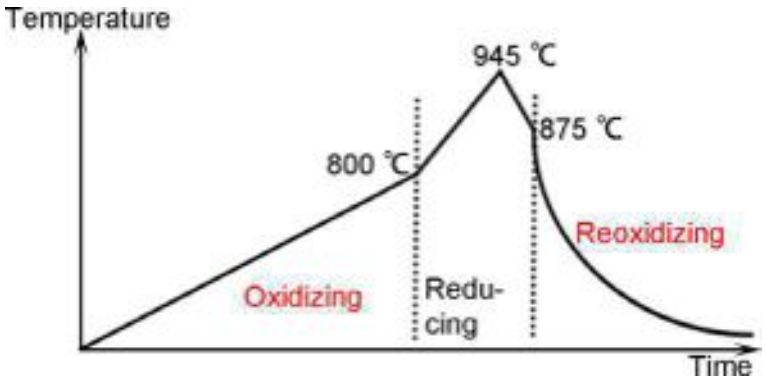

Figure 2.A.2.1 Schematic diagram of the firing process to make an Attic vase (Noble 1960; Lapatin 2008).

2.A.3 Issues and research objectives

The firing process of Attic ceramics have aroused great interests from scholars for many years (Noble 1960; Hofmann 1966; Gliozzo et al. 2004; Ospitali et al. 2005; Walton et al. 2009; Walton et al. 2013; Cianchetta et al. 2015a; Cianchetta et al. 2015b; Cianchetta et al. 2016). Early, Noble proposed an assumption of a three-stages firing protocol to obtain the ceramics with high gloss coating (Noble 1960), which was confirmed by the later chemical and mineral investigation (Hofmann 1966; Gliozzo et al. 2004; Ospitali et al. 2005). The results of these analyses indicated that the black coating was made from a thin illite clay suspension and after it was painted on the body of the vase, the unfired vase was fired with an oxidizing-reducing-reoxidizing cycle at a maximum temperature of 800-950 ºC (Hofmann 1966; Gliozzo et al. 2004; Ospitali et al. 2005). On the other hand, Getty's team proposed a different assumption (Walton et al. 2013; Cianchetta et al. 2015a; Cianchetta et al. 2015b; Cianchetta et al. 2016). They find that the relief line structure could only be produced through a separate firing at the higher temperature than one used for the contour line and black gloss background. However, as we have seen, this assumption was concluded only from very recent investigations and based on rare objects (only one fragment analyzed in the work of Walton et al. 2013 and one fragment analyzed in the work of Cianchetta et al.).

The objective of my work is to understand extensively the firing protocols of Attic ceramics based on a significant corpus and to verify the two previous assumptions. We have selected two series of fragments with the archaeologist (Eric Gailledrat): the first series containing 16 fragments (labeled from CS30 to CS45) was received during 2015 and the second series containing 12 fragments (labeled from CS46 to CS57) was received during 2016. They were excavated from the Lattes site, France.

2.B Method strategy

Due to the fact that iron state is sensitive to firing process, I focused my work on investigating the distribution of iron valence in the different component of ceramics i.e. in the slip and body. For this, I chose FF-XANES technique which allowed to analyze large zones (about mm^2) with a submicrometer resolution (about 0.7 µm). FF-XANES has been successfully applied to study the firing conditions of Roman pottery in association with Raman spectroscopy (Meirer et al. 2013). XANES is a powerful tool to determine the speciation of iron however it is not always easily to identify all the components of complex mixture. For instance, the XANES spectrum of an equal proportion of hercynite ($FeAl_2O_4$) and hematite

(α-Fe_2O_3) is very similar to the one of pure magnetite (Fe_3O_4). Likewise, a mixture of hercynite/ maghemite (γ-Fe_2O_3) gives a spectrum very close to the one of pure magnetite (Fe_3O_4). In fact, in presence of hercynite and trivalent iron oxide (α or γ) it is very difficult to detect magnetite. On the other hand, this phase is very easily detected by Raman spectroscopy. Hence, I also used Raman spectroscopy to eliminate the ambiguity.

Before performing FF-XANES and Raman analyses, I performed a more "standard" investigation of fragments including EPMA and SEM-EDS to compare them to the data of literature.

The EPMA, SEM-EDS and Raman measurement were performed on cross-section sample (cf. chapter II, § 2.A.1) while FF-XANES investigations were carried out on dedicated samples (cf. chapter II, § 2.B)

2.C Archaeological samples

The detail of sample description is shown in Appendix 4 and 5. These samples are dated to between the sixth and fourth centuries BC. Most of samples present black gloss without figure and only some of samples present red-figure (CS45, CS46, CS49, CS50, CS52, CS53, CS54 and CS57, for example, Figure 2.C.1). In addition, CS48 has the exterior black slip and interior red slip and CS34 presents red slip on both sides. CS38 shows white gloss, which was not considered in this work.

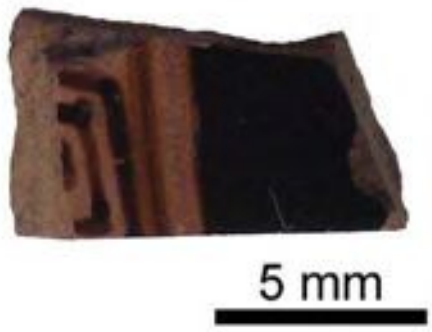

Figure 2.C.1 Photography of CS45 fragment

From optical observation, two types of samples were observed (Figure 2.C.2): one type shows a single layer of the slip, while another type presents two notable layers (CS33, CS39, CS45, CS47, CS53 and CS55).

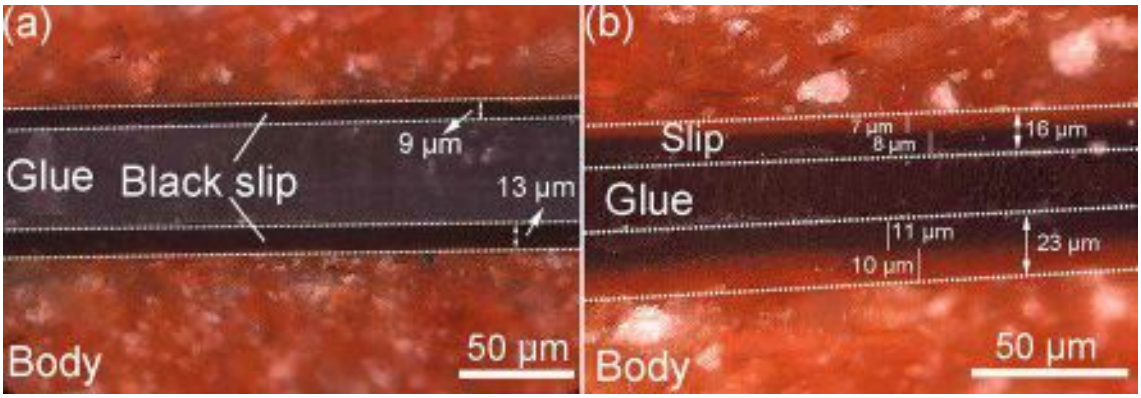

Figure 2.C.2 Two types of sample: CS32 (a) and CS39 (b).

2.D Results

2.D.1 EPMA study

The EMPA measurements were performed in Center de Microcaractérisation R. Castaing, Toulouse. First, I collected perpendicular profile lines (body to surface) to verify if it is possible to observe some difference between the two slip layers (CS33, CS39 and CS45). But as no significant difference was found, I just tried to determine the average composition. The results are given in Appendix 6. The coatings present low rate of Ca while a high K and Fe rate. These values are very consistent with the values already published for Attic ceramics Table 2.D.1.1

Slip	Na_2O	MgO	Al_2O_3	SiO_2	K_2O	CaO	MnO	FeO	Cr_2O_3	BaO	TiO_2	P_2O_5
General average (23)	0.50 (0.25)	1.91 (0.23)	28.89 (1.82)	45.50 (1.10)	5.32 (1.16)	0.51 (0.29)	0.07 (0.02)	14.66 (2.46)	0.06 (0.02)	0.01 (0.01)	0.65 (0.16)	0.25 (0.13)
Maniatis et al. 1993 (3)	0.63 (0.28)	1.89 (0.17)	30.44 (1.29)	45.38 (1.39)	5.27 (1.24)	0.63 (0.39)	0.09 (0.06)	14.95 (1.30)	--	--	0.61 (0.28)	--
Mirti et al. 2006 (1)	0.67 (0.07)	2.10 (0.40)	30.48 (0.50)	45.87 (0.60)	5.40 (0.40)	0.70 (0.10)	--	13.99 (1.00)	--	--	0.80 (0.10)	--

Table 2.D.1.1 Chemical composition of the slip of Attic pottery determined by EPMA. Comparison with other examples from Maniatis et al. 1993 and Mirti et al. 2006 obtained by SEM-EDS.

2.D.2 SEM-EDS analyses

SEM images (Figure 2.D.2.1) show that the slip appears as a dense layer of a few tens of micrometers, which is denser and more homogeneous than the body. The grain size difference between the materials used for the coating and the body is evident. Large crystals of tempers (such as quartz, spinel, feldspars ...) are

observed in the body. The two layers, which could be observed under optical microscope (CS33 and CS39), show no difference under SEM observations (CS33 and CS39 in Figure 2.D.2.1).

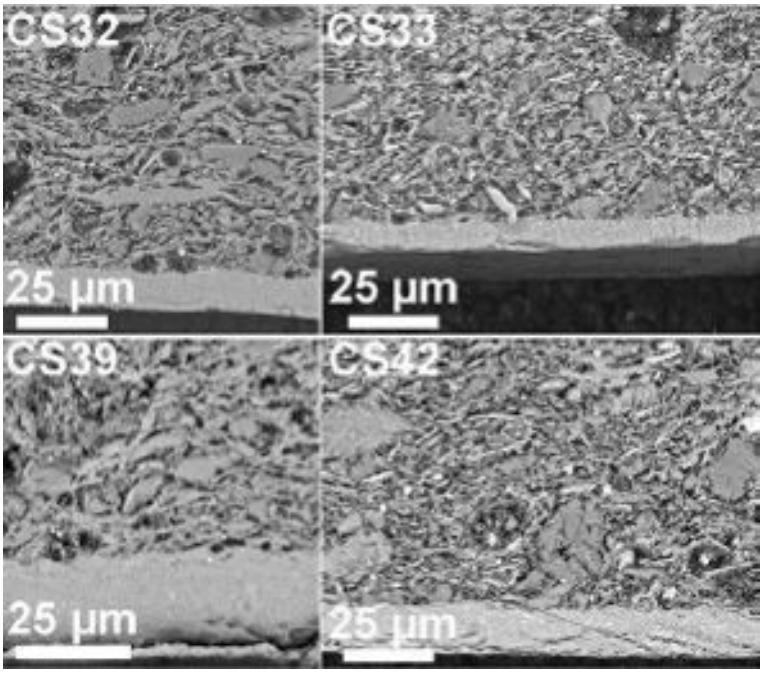

Figure 2.D.2.1 SEM image of cross-sections of sample CS32 (single black slip layer), CS33 (double slip layers), CS39 (double slip layers) and CS42 (single black slip layer).

The corresponding elemental distribution is showen in Figure 2.D.2.1 Consistent with EPMA results, no significant difference was found in the double slip layers (CS33 and CS39). But the differences between the bodies and slips can be clearly observed. The high K rate of slips is evident as well as the high Ca rate of bodies. Fe and Al are mostly located in the slips. They seem homogenously distributed in the slips. The high Si rate in the bodies corresponds to quartz grains. One can hardly observe crystals in the slips whereas in the body the grains up to several tens of microns are observed.

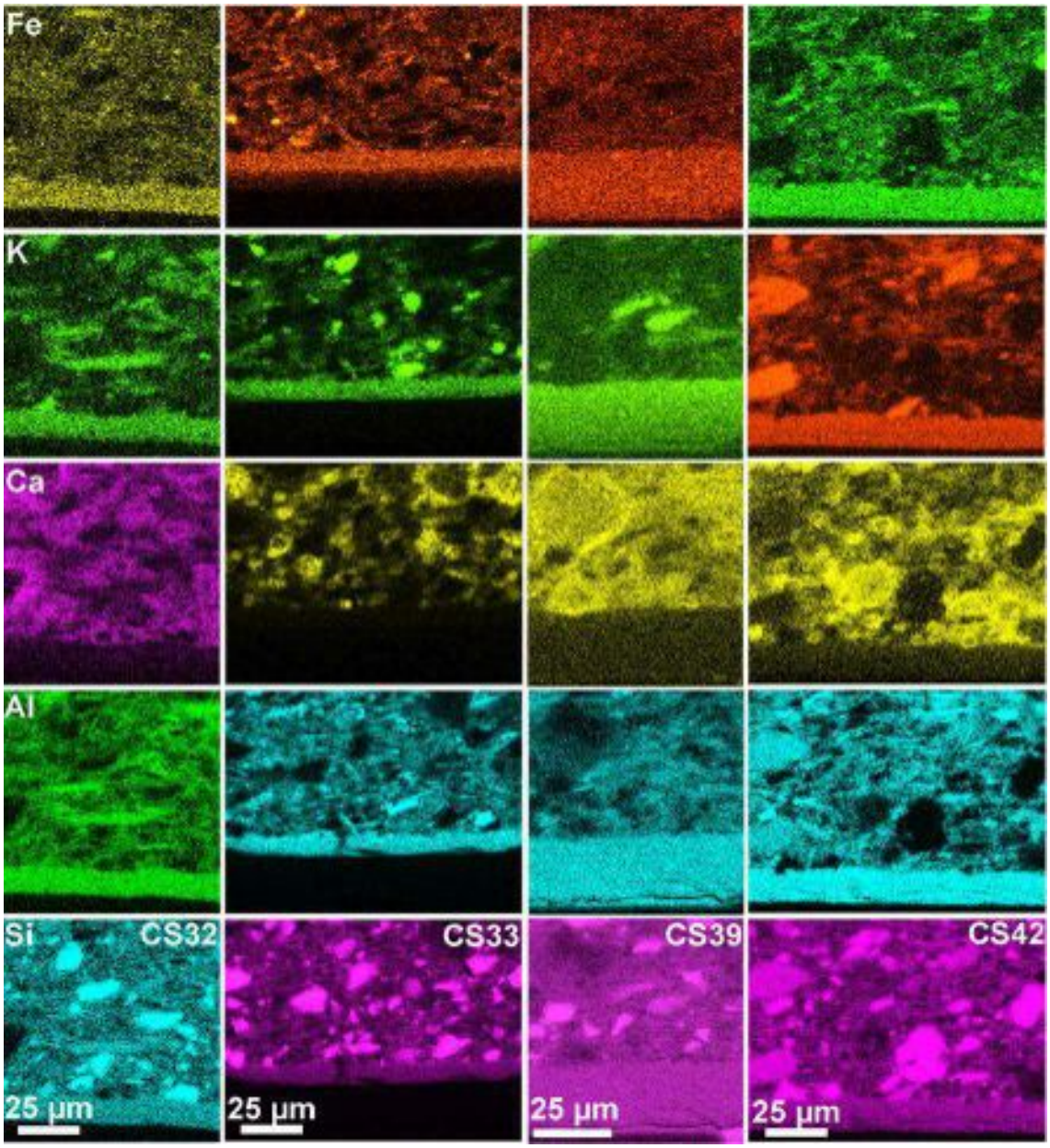

Figure 2.D.2.2 Elemental maps (Si, Al, Ca, K, Fe: from bottom to top) of CS32 (first column), CS33 (second column) CS39 (third column) and CS42 (right column) samples.

2.D.3 FF-XANES analyses along the Fe K-edge

FF-XANES analyses were primarily performed on the first type of sample (with single black slip layer). The transmission image (Figure 2.D.3.1a) shows that the slip is more homogeneous and denser than the body, consistent with the results of SEM (Figure 2.E.1). Then, the edge jump map (Figure 2.D.3.1b) was calculated to analyze the Fe distribution. It illustrates that Fe mostly concentrates in the slip, consistent with the iron map obtained by SEM-EDS (Figure 2.D.2.2).

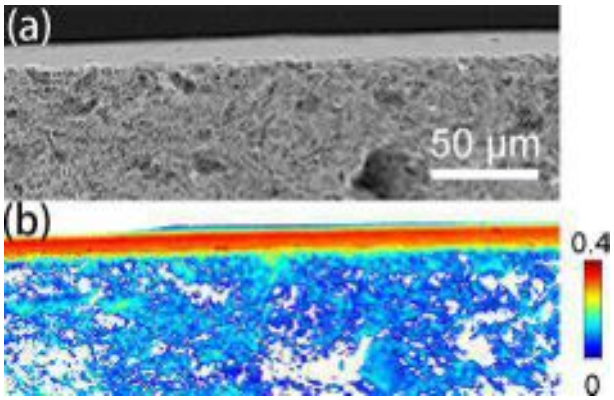

Figure 2.D.3.1 FF-XANES results for CS32: (a) transmission image recorded at 7060 eV below the Fe absorption edge. Based on the XANES evaluation, the edge jump map (b) (corresponding to the Fe concentration) has been calculated. The scale bar reports the value of the absorption edge jump.

The correspondent edge energy map (Figure 2.D.3.2, top image) was obtained from the pixels with high signal to noise (SNR) ratio. It shows that the state of iron is mainly bivalent in the slip, while it is mainly trivalent in the body. The value of edge energy was also calculated (Figure 2.D.3.2 bottom image). It shows a notable fluctuation between ~7121.0 and ~7124.3 eV in the body. The value presents 0 eV at ~68 µm and ~112 µm due to the porosity of the body. The average edge energy of the body is around 7122.5 eV (Table 2.D.3.1), prone to the trivalent iron (Giuli et al. 2003; Berry et al. 2003). The value of edge energy decreases significantly along the interphase of body and slip. It keeps relatively stable around ~7119.1 eV in the slip and increases slightly to ~7119.4 eV in the surface of the slip. The average value of edge energy of the slip is around ~7119.1 eV (Table 2.D.3.1), prone to the bivalent iron (Giuli et al. 2003; Berry et al. 2003).

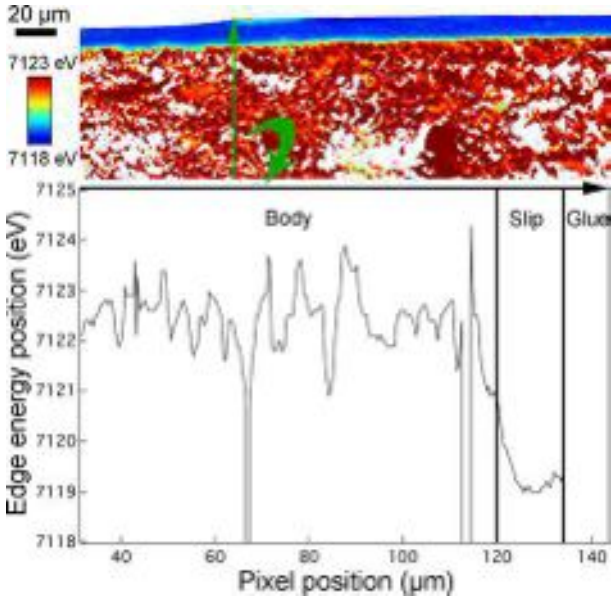

Figure 2.D.3.2 The correspondent edge energy map of CS32 (top image) and the curve of variation of edge energy position along the body to the surface of slip (bottom plot). The color scale bar reports the energy of the position of absorption edge in eV.

	Body	Black slip	Red slip	The surface
CS30	7122.5 (0.10)	7119.7 (0.33)		7119
CS31	7122.8 (0.07)	7119.4 (0.14)		7119.2
CS32	7122.5 (0.52)	7119.1 (0.13)		7119.4
CS36	7122.5 (0.39)	7119.2 (0.09)		7119.3
CS39	7123.1 (0.2)	7119.3 (0.29)	7122.7 (0.21)	7118.8
CS42	7122.5 (0.27)	7119.2 (0.10)		7119.4
CS43	7122.5 (0.27)	7119.6 (0.33)		7120.1

Table 2.D.3.1 The average value of edge energy of the slip and body of the samples. The corresponding standard deviations are given in the brackets and the value of the surface of slip is also given.

Principal component analysis (PCA) approach and subsequent k-means clustering were applied for a closer inspection. The first three principal components were considered to cover the cardinal significant information and clustered into two groups: the slip (blue line) and the body (red line) (Figure 2.D.3.3a). Then, the corresponding XANES spectra were fitted by a least squares

linear combination fitting of reference XANES of hercynite, hematite and maghemite (Figure 2.D.3.3a, the green line and cyan line correspond to the slip and body, respectively). The R-factor is lower than 0.004, indicating the high quality of the fitting (Boesenberg et al. 2013). The main iron-based mineral composition for the slip and body was shown in the bar chart (Figure 2.D.3.3b). The slip contains mainly hercynite (close to 80%) and a few of maghemite (less than 20%). The body is mainly composed of maghemite (reach to 50%), hematite (reach to 40%) and a few of hercynite (around 10%). The results are consistent with the edge energy map (Figure 2.D.3.2).

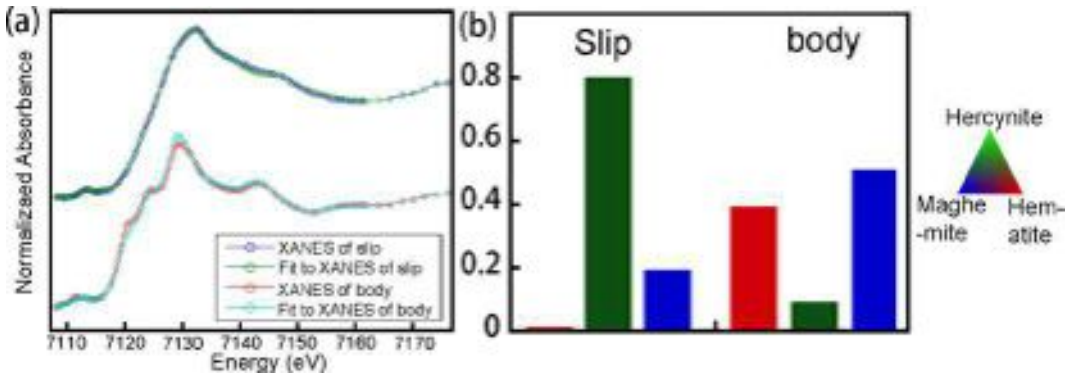

Figure 2.D.3.3 (a) The average XANES of the slip (blue line) and the body (red line) and a least squares linear combination fitting of reference XANES for hercynite, hematite, and maghemite to the each cluster (green and cyan line is the fit to XANES of slip and body, respectively). (b) Bar chart of iron-based mineral composition for the slip and body.

FF-XANES analyses were then performed on the second type of sample (double slip layers) (Figure 2.D.3.4). The transmission image (Figure 2.D.3.4a) shows no distinct difference between the two slip layers, consistent with the above results. To analyze the iron state, the edge energy map was calculated (Figure 2.D.3.4b). It presents a significant difference between the two slip layers. The iron valence is mainly trivalent in red slip layer while it is mainly bivalent in the black slip layer. To investigate closely the variation of iron valence, the value of edge energy was plotted along body to the surface of the slip (Figure 2.D.3.4c). It fluctuates between ~7122.5 and ~7123.5 eV in the body and the average value is around ~7123.1 eV (Table 2.D.3.1), prone to the trivalent iron (Giuli et al. 2003; Berry et al. 2003). It shows 0 eV in the several points due to the porosity of the body. Then the value keeps relatively stable even up to in the red slip layer and then significantly decreases from ~7123 to ~7118.8 eV through the red slip layer the black slip layer. The average value of the black slip layer is around 7119.3 eV, prone to the bivalent iron(Giuli et al. 2003; Berry et al. 2003). Due to difficulty in

defining precisely the black gloss and red gloss, instead of calculating the average XANES of each component (body, red and black slip), an RGB map (Figure 2.D.3.4d) is calculated by the at least squares linear combination fitting of reference XANES for hercynite, hematite, and maghemite to the each XANES. It shows that the black slip layer mainly contains hercynite while the red slip layer mainly contains hematite. The body mainly contains a mixture of maghemite (majority) and hematite (minor).

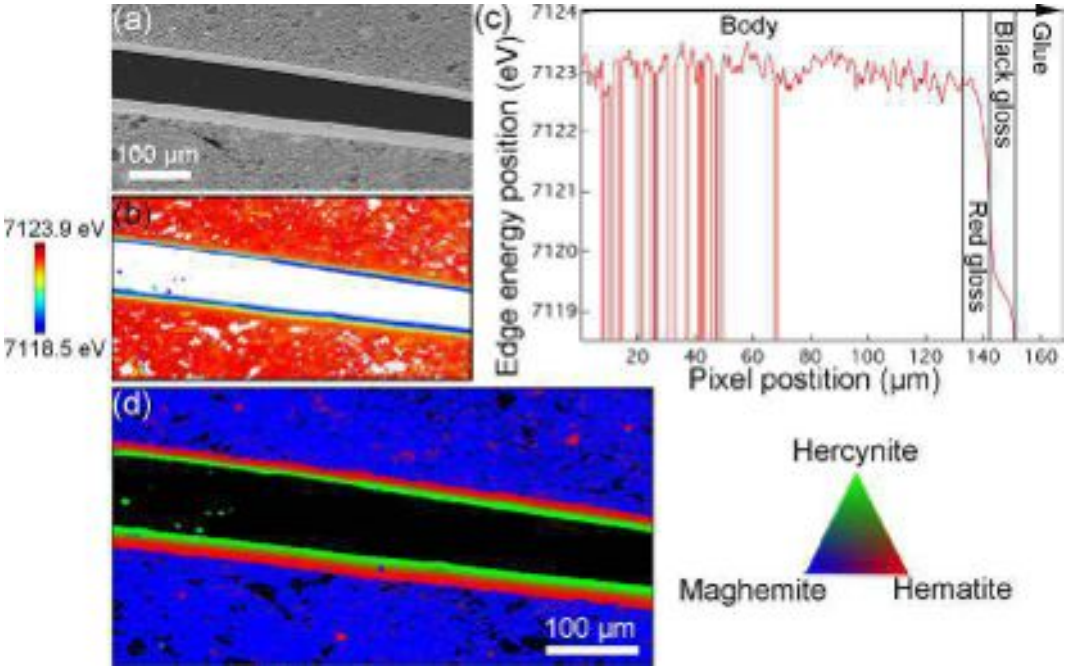

Figure 2.D.3.4 Results of FF-XANES analysis performed on sample CS39 (double slips): (a) the transmission image recorded at 7060 eV, below the Fe absorption edge; (b) the edge energy map (correlated to Fe valence, the scale bar reports the value the energy of the position of absorption edge in eV); (c) the curve of the variation of edge energy along body to the surface of slip; (d) RGB phase map generated by the fit of single pixel XANES spectra with iron oxide standards.

The FF-XANES results of the other samples of the first type were also illustrated (Figure 2.D.3.5). The results are in accordance with ones of CS32.

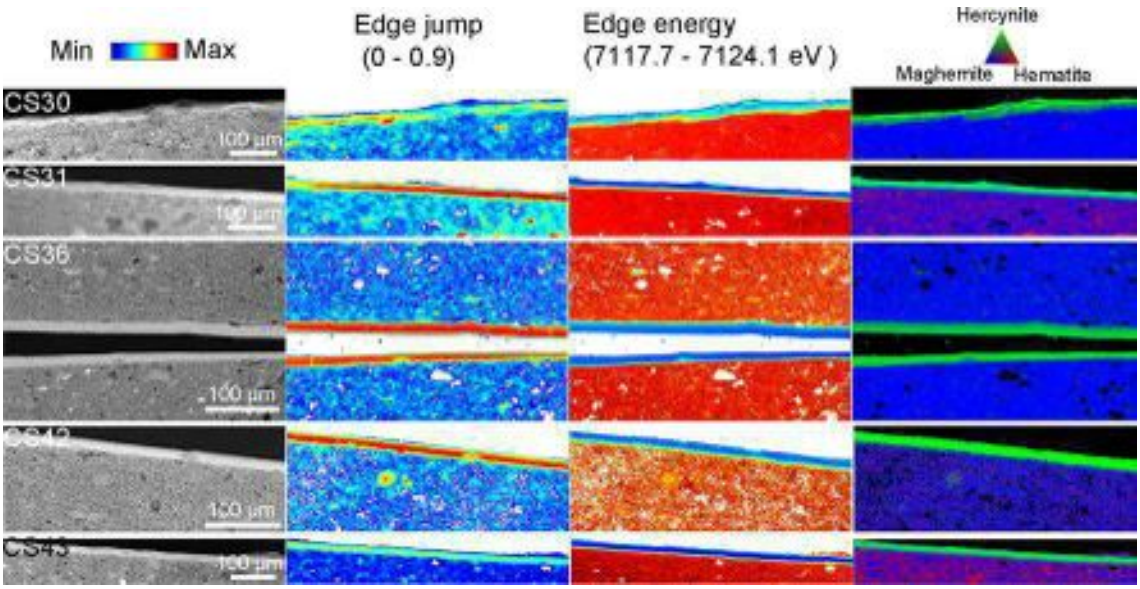

Figure 2.D.3.5 FF-XANES results of sample CS30, CS31, CS36, CS42 and CS43, from top to bottom. From left to right: the first column is the corresponding transmission images recorded at 7060 eV below the Fe absorption edge; the second column is the edge jump map, correlated to Fe concentration; the third column is the edge energy map, related to Fe valence. The scale bars report the values of the absorption edge jump (the second column) and the energy of the position of absorption edge in eV (the third column), respectively. The forth row shows the RGB phase maps generated by the fit of single pixel XANES spectra with iron oxide standards.

The corresponding curves of edge energy were calculated to closely inspect the iron valence (Figure 2.D.3.6). The curves of CS30, CS31, CS42 and CS43 have similar trend with the one of CS32 (Figure Figure 2.D.3.2), showing a distinct difference between slip and body. In the body, the average value of CS39 is the highest value and the one of CS31 is higher than others (Table 2.D.3.1). The average values of others are the same, but the one of CS36 present a large fluctuation due to a large standard deviation (Table 2.D.3.1). In the slip, the average value of the slip of CS30 is the highest and one of CS32 is the lowest (Table 2.D.3.1). The values of the surfaces of CS30, CS31, CS39 are slightly lower than ones in the core of the slip. Conversely, the values of the surfaces of CS32, CS36, CS42 and CS43 are slightly higher. These results are consistent with their edge energy maps (the third column images, Figure 2.D.3.5).

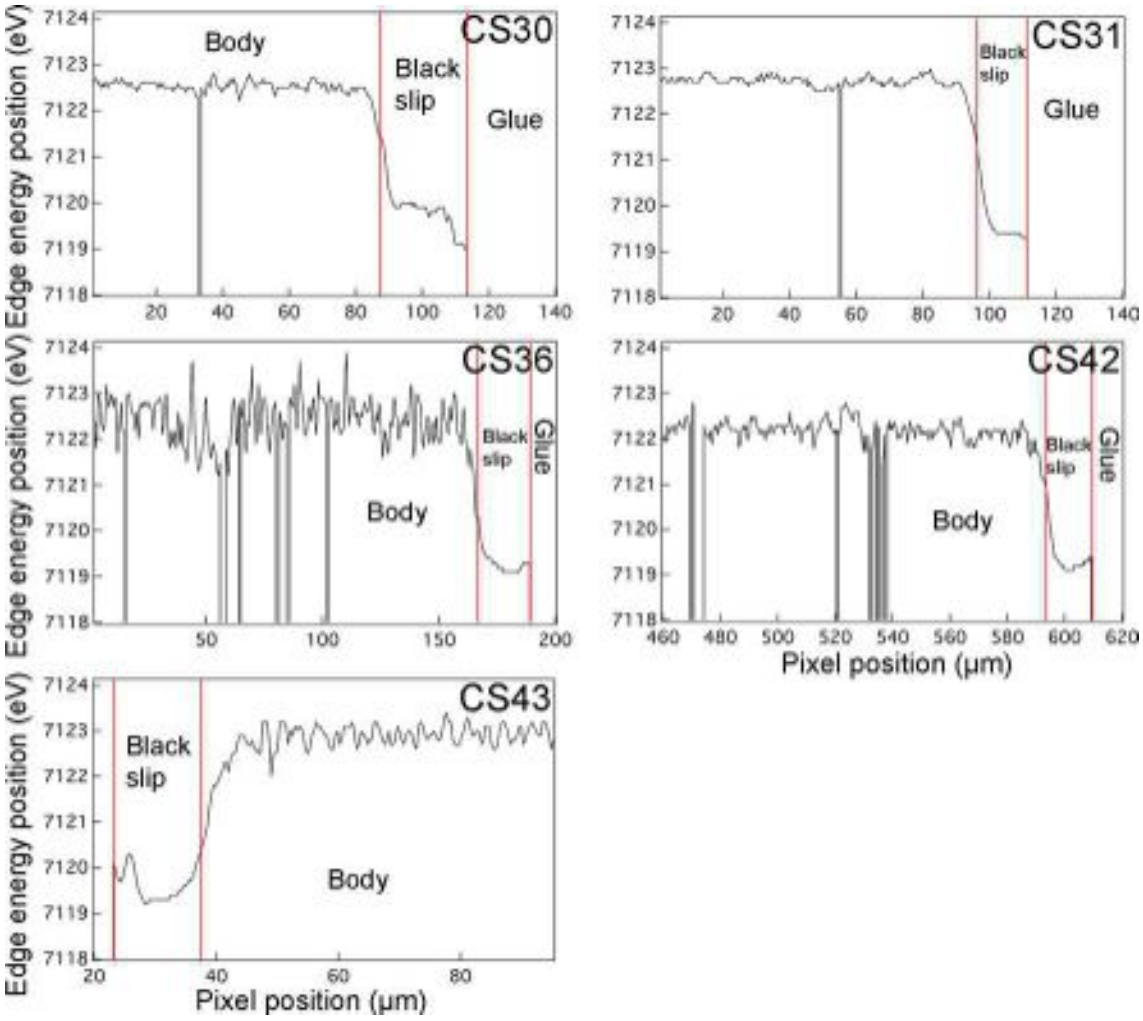

Figure 2.D.3.6 Plots of the variation of edge energy along the body to the surface of the slip for sample CS30, CS31, CS36, CS42 and CS43, respectively.

2.D.4 Raman spectroscopy analyses

The Raman mapping was performed at GCI, Los Ageles. The distribution of the magnetite and hematite of the first type sample is outlined in red and green zone, respectively, in blue rectangle (Figure 2.D.4.1a) and the representative spectra were also given (Figure 2.D.4.1b and Figure 2.D.4.1c). The map shows that magnetite mainly locates in the slip and more concentrated in the slip, while hematite is mainly distributed in the body.

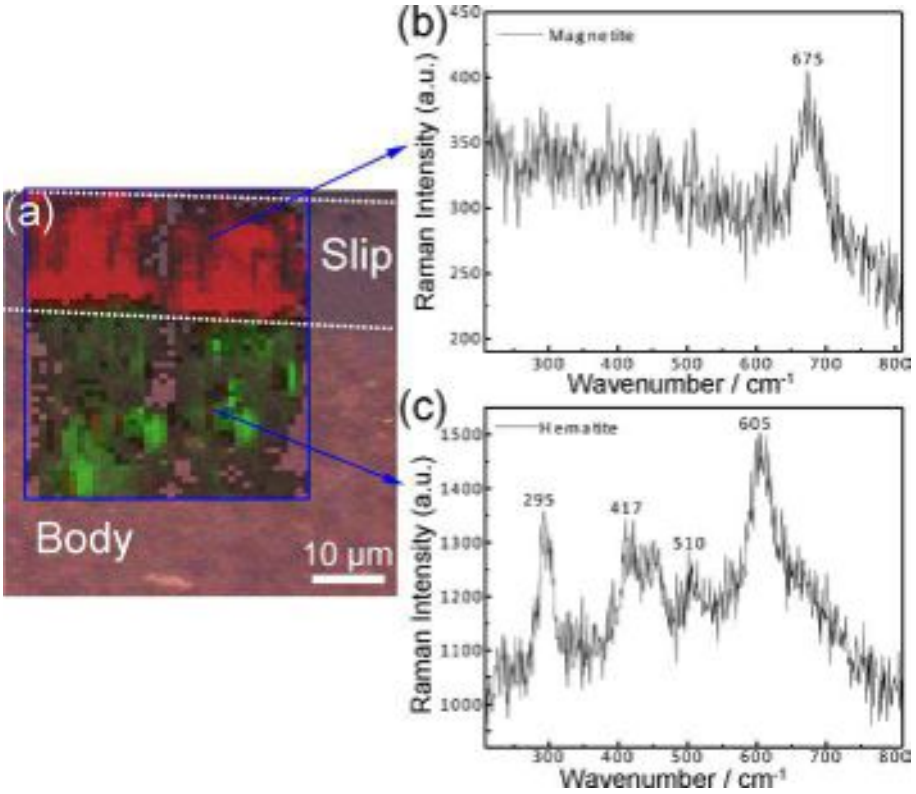

Figure 2.D.4.1 (a) Photomicrograph of the cross section of sample CS36 (left side); the area mapped by Raman spectroscopy is indicated by the blue rectangle. The map of the center position of the magnetite band at 675 cm^{-1} (red part) and of the hematite band at 295 cm^{-1} (green part). The representative spectra of magnetite (b) and hematite (c) are given. The measurements were collected with help of Ilaria Cianchetta and Karen Trentelman at GCI, Los Angeles, USA.

Besides, Raman mapping was also performed on the second type of sample (double slip layers) (Figure 2.D.4.2). The selected area (Figure 2.D.4.2a) is indicated by the red rectangle and then reduced to a reasonable zone with size of 30 x 40 µm indicated by the blue rectangle, which was mapped by Raman spectroscopy (Figure 2.D.4.2b). Like above, the distribution of the magnetite and hematite is outlined in red and green zone, respectively (Figure 2.D.4.2b). It shows that magnetite mainly locates at the interphase of the black and red slip layer and is so rare in the surface of the slip. Hematite is mainly distributed at the red slip layer and a small amount was detected in the body.

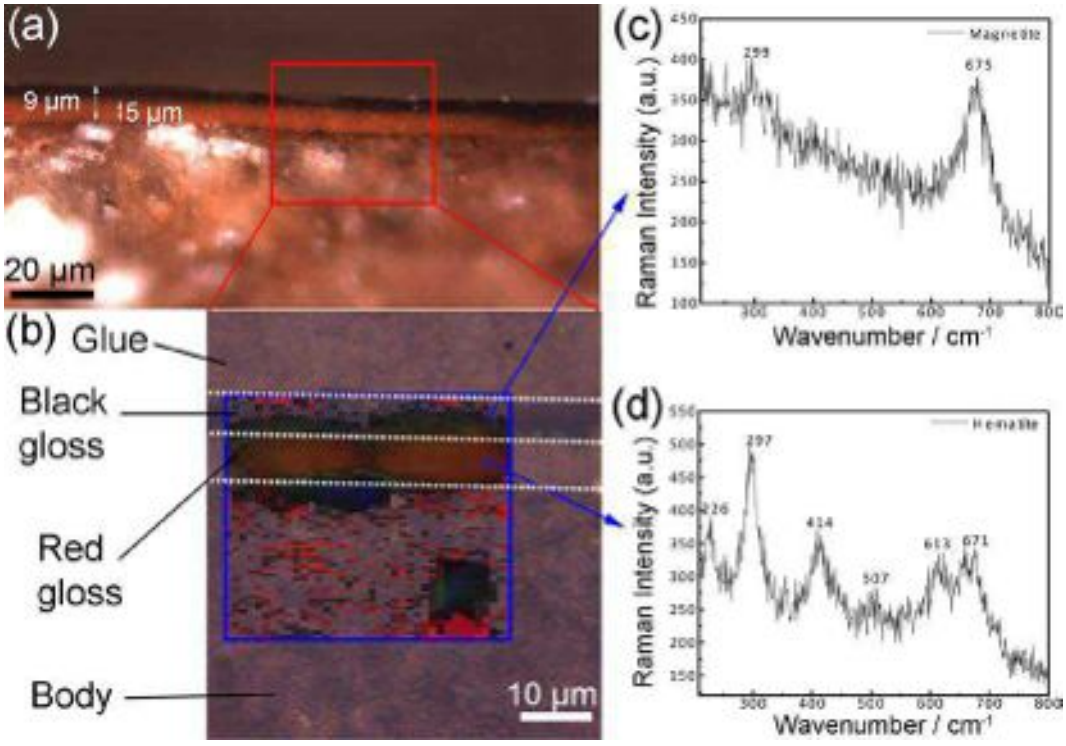

Figure 2.D.4.2 (a) Optical image of cross section of sample from CS33 and the selected area is indicated by the red rectangle; (b) the selected area was then reduced to be a zone with size of 30 x 40 µm (indicated by the blue rectangle), which was mapped by Raman spectroscopy. The map of the center position of the magnetite band at 675 cm^{-1} (green part) and of the hematite band at 297 cm^{-1} (red part) (b); the representative spectra of magnetite (c) and hematite (d) are given.

2.E Discussion

The slips of the first group (only one black slip layer) have elemental composition (EPMA) and texture (SEM) in agreement with literature data. FF-XANES revealed that in these slips, iron was essentially bivalent and in $FeAl_2O_4$ crystals. In the bodies, the iron was essentially trivalent with both presence of maghemite and hematite. These results are consistent with the firing protocol proposed by Noble (1960) in three oxidizing-reducing-reoxidizing stages. FF-XANES also revealed that the iron in the slip surface could be more (CS30 and CS31) or less (CS32, CS36, CS42 and CS43) reduced than in the slip core. These two situations are compatible with the Noble's protocol. This only indicates that the end of reducing stage was a higher temperature of CS30 and CS31 samples and inversely that the reoxidizing phase began at higher temperature for CS32, CS36, CS42 and CS43 samples. The presence of a thin layer strongly reduced (CS30 and CS31) in which the crystals of hercynite seem more crystalized (XANES spectra well define

and closer to the one of well-crystalized hercynite crystal) could indicate a fast increase of temperature (kindling smoke) at the end of the reduce step.

EPMA and SEM-EDS investigations did not reveal significant differences between the two slip layers of CS33, CS39 and CS45. On the other hand, FF-XANES showed that the iron valence was well different in agreement with the colors observed by optical microscopy. The high presence of hematite in the red slip layer (intermediate layer), higher than in body, indicates that this phase was formed during the first firing stage and was not obtained during the third reoxidizing stage. In fact, the temperature during the first stage was high enough to partially vitrify the slip and during the second reducing stage only the top layers of slip had to be reduced and totally vitrified. During the final stage, the iron of body was reoxidized and transformed in maghemite. Of course this layer structuration is also in accordance with the firing protocol into two separated firings proposed by the Getty's team (Walton et al. 2013). Without a zone with a red slip layer in surface it not possible to choose between the two assumptions.

2.F Conclusion

The FF-XANES, associating lab-based techniques (EPMA, SEM-EDS Raman spectroscope), allowed us to obtain new information concerning the firing process of Attic potteries. All studied samples are in agreement with the protocol proposed by Noble. The study of iron valence repartition from the surface to the body allowed for determining variations among samples and thus to show that for some of them, the first oxidizing stage was at higher temperature or for others, the second stage (reduction) was more or less reduced. The existence of a double firing cannot be either confirmed or rejected from the studied samples.

The FF-XANES study of CS53 or CS57, which present both a red and black slip in surface, could help to confirm the existence of a double firing (Figure 2.F.1). The two slips have the same elemental composition and it is difficult to envisage that they were obtained together during a unique firing. Unfortunately, these samples arrived too late and we are waiting for the next possibility to perform ID21 experiments.

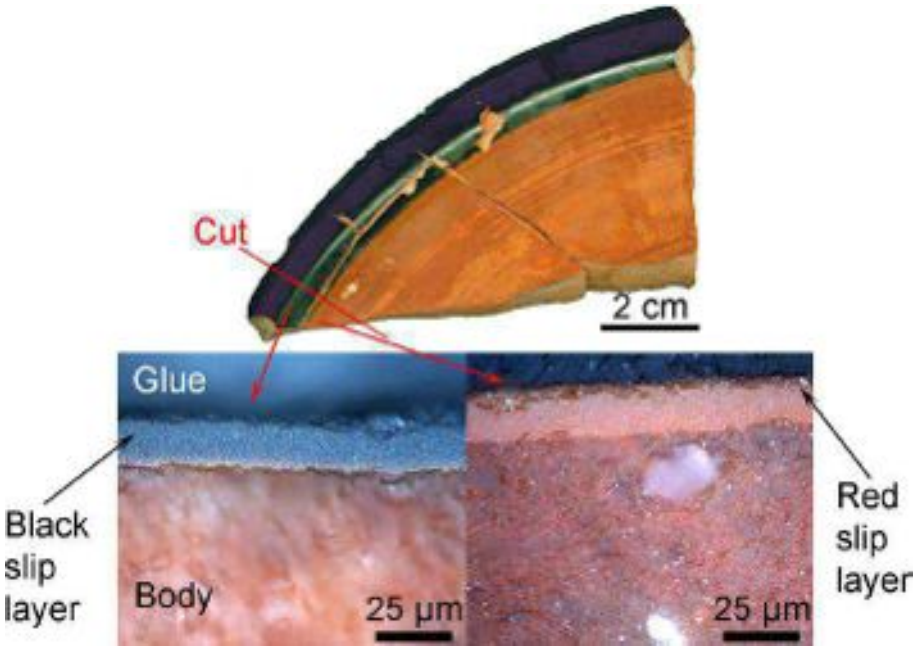

Figure 2.F.1 Photography of the fragment of CS53 (top image) and the optical images of cross-section from two different zones (bottom left one from black zone and bottom right one from red zone).

3 Reference

Berry, A. J., O'Neill, H. S. C., Jayasuriya, K. D., Campbell, S. J., and Foran, G. J., 2003, XANES calibrations for the oxidation state of iron in a silicate glass, *American Mineralogist*, **88**(7), 967–77.

Bersani, D., Lottici, P. P., and Montenero, A., 2000, A micro-Raman study of iron-titanium oxides obtained by sol-gel synthesis, *Journal of Materials Science*, **35**(17), 4301–5.

Binns, C. F., and Fraser, A. D., 1929, The genesis of the Greek black glaze, *American Journal of Archaeology*, **33**(1), 1–9.

Boardman, J., 1985, *Athenian red figure vases: the Archaic period: a handbook* reprint edition ed., Thames & Hudson, London.

Boardman, J., 2006, *The History of Greek Vases*, Thames & Hudson, London.

Boesenberg, U., Meirer, F., Liu, Y., Shukla, A. K., Dell'Anna, R., Tyliszczak, T., Chen, G., Andrews, J. C., Richardson, T. J., Kostecki, R., and Cabana, J., 2013, Mesoscale phase distribution in single particles of $LiFePO_4$ following lithium deintercalation, *Chemistry of Materials*, **25**(9), 1664–72.

Cianchetta, I., Trentelman, K., Maish, J., Saunders, D., Foran, B., Walton, M., Sciau, P., Wang, T., Pouyet, E., Cotte, M., Meirer, F., Liu, Y., Pianetta, P., and Mehta, A., 2015a, Evidence for an unorthodox firing sequence employed by the Berlin Painter: Deciphering ancient ceramic firing conditions through high-resolution material characterization and replication, *Journal of Analytical Atomic Spectrometry*, **30**(3), 666–76.

Cianchetta, I., Maish, J., Saunders, D., Walton, M., Mehta, A., Foran, B., and Trentelman, K., 2015b, Investigating the firing protocol of Athenian pottery production: A Raman study of replicate and ancient sherds, *Journal of Raman Spectroscopy*, **46**(10), 996–1002.

Cianchetta, I., Trentelman, K., Walton, M. S., Maish, J., Mehta, A., and Foran, B., 2016, Reverse engineering ancient Greek ceramics: Morphological and spectral characterization of replicates, *Journal of the American Ceramic Society*, **99**(5), 1792–801.

Dondi, M., Matteucci, F., Cruciani, G., Gasparotto, G., and Tobaldi, D. M., 2007, Pseudobrookite ceramic pigments: Crystal structural, optical and technological properties, *Solid State Sciences*, **9**(5), 362–9.

Dondi, M., Cruciani, G., Balboni, E., Guarini, G., and Zanelli, C., 2008, Titania slag as a ceramic pigment, *Dyes and Pigments*, **77**(3), 608–13.

Folsom, R. S., 1975, *Attic Black-Figured Pottery*, Noyes Pubns, Park Ridge, N.J.

Genin, M., 2007, *La Graufesenque, Millau, Aveyron. Volume II, Volume II,* Éditions de la Fédération Aquitania, Pessac.

Giuli, G., Paris, E., Pratesi, G., Koeberl, C., and Cipriani, C., 2003, Iron oxidation state in the Fe-rich layer and silica matrix of Libyan Desert Glass: A high-resolution XANES study, *Meteoritics & Planetary Science*, **38**(8), 1181–6.

Gliozzo, E., Kirkman, I. W., Pantos, E., and Turbanti, I. M., 2004, Black gloss pottery: production sites and technology in Northern Etruria, part II: gloss technology, *Archaeometry*, **46**(2), 227–46.

Guo, W. Q., Malus, S., Ryan, D. H., and Altounian, Z., 1999, Crystal structure and cation distributions in the $FeTi_2O_5$ -Fe_2TiO_5 solid solution series, *Journal of Physics: Condensed Matter*, **11**(33), 6337–46.

Hermet, F., 1934, *La Graufesenque, Condatomago : I, Vases sigillés ; II, Graffites*, Vol. 2 volumi, librairie Ernest Leroux, Paris.

Hofmann, B., 1971, Les relations entre potiers, fabricants de moules et artistes producteurs de poinçons., *Rei Cretariae Romanae Fautorum acta, 13.1971*.

Hofmann, U., 1966, Die Chemie der antiken Keramik, *Naturwissenschaften*, **53**, 218–23.

Jubb, A. M., and Allen, H. C., 2010, Vibrational spectroscopic characterization of hematite, maghemite, and magnetite thin films produced by vapor deposition, *ACS Applied Materials & Interfaces*, **2**(10), 2804–12.

Leon, Y., Lofrumento, C., Zoppi, A., Carles, R., Castellucci, E. M., and Sciau, P., 2010a, Micro-Raman investigation of terra sigillata slips: a comparative study of central Italian and southern Gaul productions, *Journal of Raman Spectroscopy*, **41**(11), 1550–5.

Leon, Y., Sciau, P., Goudeau, P., Tamura, N., Webb, S., and Mehta, A., 2010b, The nature of marbled terra sigillata slips: a combined μXRF and μXRD investigation, *Applied Physics A*, **99**(2), 419–25.

Leon, Y., 2010, Etude de la diffusion en Gaule d'une technique romaine

d'élaboration de Sigillées à travers l'analyse microstructurale des surfaces décoratives (ou engobes), Phdthesis, Université Toulouse 3 Paul Sabatier (UT3 Paul Sabatier).

Leon, Y., Sciau, P., Passelac, M., Sanchez, C., Sablayrolles, R., Goudeau, P., and Tamura, N., 2015, Evolution of terra sigillata technology from Italy to Gaul through a multi-technique approach, *Journal of Analytical Atomic Spectrometry*, **30**(3), 658–65.

Liermann, H. P., Downs, R. T., and Yang, H. X., 2006, Site disorder revealed through Raman spectra from oriented single crystals: A case study on karooite (MgTi2O5), *American Mineralogist*, **91**(5-6), 790–3.

Maloney, J., 2002, High Performance Pigments, 53.

Meirer, F., Liu, Y., Pouyet, E., Fayard, B., Cotte, M., Sanchez, C., Andrews, J. C., Mehta, A., and Sciau, P., 2013, Full-field XANES analysis of Roman ceramics to estimate firing conditions—A novel probe to study hierarchical heterogeneous materials, *Journal of Analytical Atomic Spectrometry*, **28**(12), 1870–83.

Navrotsky, A., 1975, Thermodynamics of formation of some compounds with the pseudobrookite structure and of the $FeTi_2O5$-Ti_3O_5 solid solution series, *American Mineralogist*, **60**, 249–56.

Noble, J. V., 1960, The technique of Attic vase-painting, *American Journal of Archaeology*, **64**(4), 307–18.

Ohsaka, T., Izumi, F., and Fujiki, Y., 1978, Raman spectrum of anatase, TiO2, *Journal of Raman Spectroscopy*, **7**(6), 321–4.

Ospitali, F., Sabetta, T., Tullini, F., Nannetti, M. C., and Di Lonardo, G., 2005, The role of Raman microspectroscopy in the study of black gloss coatings on Roman pottery, *Journal of Raman Spectroscopy*, **36**(1), 18–23.

Oswald, F., Pryce, T. D., and Simpson, G., 1966, *An introduction to the study of terra sigillata,* Gregg Press, Farnborough, Hants.

Picon, M. 1931-2014, 1994, Quelques observations sur l'origine des vernis jaunes des sigillées marbrées de La Graufesenque.

Py, M., Sabatini, B., 2000, *La céramique attique de Lattes (Hérault, France) au IVe s. av. n.è. dans La céramique attique du IVe s. en Méditerranée Occidentale*, Actes du colloque d'Arles, Collection du Centre Jean Bérard,

Naples, 2000, p.167-200.

Sanchez, C., 2003, *Le mobilier céramique de Narbonne et sa région: pour une approche du processus de romanisation*, Lyon 2.

Sciau, P., Relaix, S., Roucau, C., Kihn, Y., and Chabanne, D., 2006, Microstructural and microchemical characterization of Roman period terra sigillate slips from archeological sites in Southern France, *Journal of the American Ceramic Society*, **89**(3), 1053–8.

Sciau, P., Relaix, S., Mirguet, C., Goudeau, P., Bell, A. M. T., Jones, R. L., and Pantos, E., 2008, Synchrotron X-ray diffraction study of phase transformations in illitic clays to extract information on sigillata manufacturing processes, *Applied Physics A*, **90**(1), 61–6.

Sciau, P., Salles, P., Roucau, C., Mehta, A., and Benassayag, G., 2009, Applications of focused ion beam for preparation of specimens of ancient ceramic for electron microscopy and synchrotron X-ray studies, *Micron*, **40**(5-6), 597–604.

Teller, R. G., Antonio, M. R., Grau, A. E., Gueguin, M., and Kostiner, E., 1990, Structural analysis of metastable pseudobrookite ferrous titanium oxides with neutron diffraction and Mossbauer spectroscopy, *Journal of Solid State Chemistry*, **88**(2), 334–50.

Tompsett, G. A., Bowmaker, G. A., Cooney, R. P., Metson, J. B., Rodgers, K. A., and Seakins, J. M., 1995, The Raman spectrum of brookite, TiO_2 (Pbca, Z = 8), *Journal of Raman Spectroscopy*, **26**(1), 57–62.

Vernhet, A., 1981, Un four de la Graufesenque (Aveyron) : la cuisson des vases sigillés, *Gallia*, **39**(1), 25–43.

Walton, M., Trentelman, K., Cummings, M., Poretti, G., Maish, J., Saunders, D., Foran, B., Brodie, M., and Mehta, A., 2013, Material evidence for multiple firings of ancient Athenian red-figure pottery, *Journal of the American Ceramic Society*, **96**(7), 2031–5.

Walton, M. S., Doehne, E., Trentelman, K., Chiari, G., Maish, J., and Buxbaum, A., 2009, Characterization of coral red slips on Greek Attic Pottery*, *Archaeometry*, **51**(3), 383–96.

Zoppi, A., Lofrumento, C., Castellucci, E. M., and Sciau, P., 2008, Al-for-Fe substitution in hematite: the effect of low Al concentrations in the Raman

spectrum of Fe_2O_3, *Journal of Raman Spectroscopy*, **39**(1), 40–6.

Chapter IV Chinese Qinghua porcelain: blue decors made from cobalt materials

General abstact

Cobalt materials are a common source of blue pigment and which has been long used in Chinese porcelains (Li 1998). One of famous case is the Qinghua porcelain, which is characterized of white porcelain decorated under the glaze with the blue pigment. In collaboration with the archaeological team of Sun Yat-sen University, I made use of the multi-scale approach to analyze the blue decors of the Qinghua porcelains from two different periods. The first one was the Ming production, which is dated from the Ming Chenghua to Zhengde era of the Ming dynasty (late 15th to early 16th Century). My goal was to extract the integrate information concerning elements and minerals and to final establish an assumption of the origin of color variations of the blue decors. The second one was the Yuan production, which is dated from the mid 13th to the mid 14th century. Since up to now, this production has been few studied, my aim was to extract fundamental information concerning the blue decors based on a significant corpus.

1 State of the art

1.A Archaeological and historical knowledge

1.A.1 Origin and development

Blue and white Porcelain, also called as Qinghua porcelain in China, was actually developed under the Yuan dynasty (1279-1368AD). During the next dynasties (the Ming and Qing) the production increased significantly and was exported into the whole world (Qiu and Chen 2009).

Indeed, Tang (618-907AD) pieces were not real porcelain but rather earthenware with greenish white slip made from cobalt pigments. They were very rare and unknown before 1985 (Wood 1999). Real blue and white porcelain seems to be made during the Song dynasty (960-1279 AD) but failed to prevail, because it was not consistent with the local aesthetic preferences instead of technical limitation (Li 1998).

The porcelain achieved its mature under the Yuan dynasty. On one hand, potters of Jingdezhen invented a new manufacturing recipe of adding kaolin into porcelain stones. This secondary formulation elevated the firing temperature and deduced the deformation, bringing out possibility of large-sized production. Besides, the potters mastered expertly both painting and firing techniques to obtain rich ornamentations as well as various colors. The painting mixture was prepared by the imported cobalt materials, which contained low manganese and high iron (Du and Su 2008). Due to the low manganese, decors could present a kind of gaudy blue color, and due to the high iron, there were dark spots formed naturally in decors, which could contrast finely with the blue part (e.g., Figure 1.A.1.1). With the handy control of firing processes (temperature and atmosphere), under-glazed painting mixture could incorporate properly with white glaze to achieve the wash tints similar to ink paintings. Additionally, because the Yuan emperors were interested in profitable international commerce with the Middle East, the Indies and the West, they encouraged the expansion of the porcelain industry for trade with these countries, which also facilitating its mass production (Li 2015).

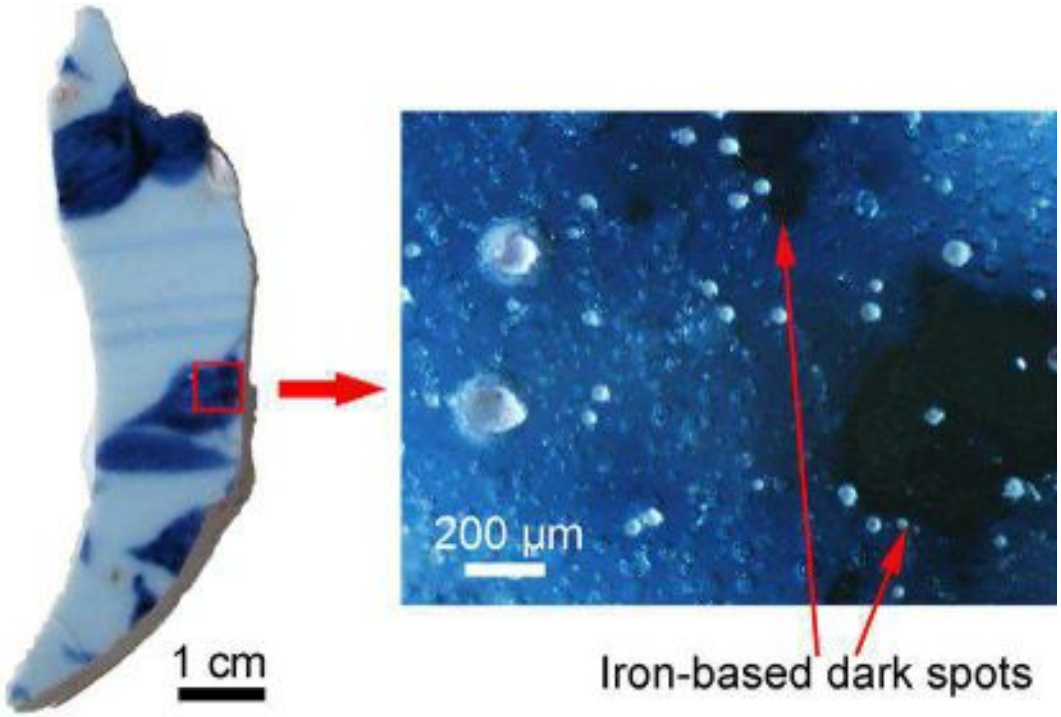

Figure 1.A.1.1 Photo of a fragment of the Yuan blue and white porcelain presenting the iron-based dark spots finely contrasted with the gaudy blue part.

This object enjoyed its golden age during the Ming dynasty (1368-1644 AD) based on the establishment of imperial kiln plants in pursuit of perfection in porcelain industry. In terms of time, the Ming blue and white productions can be divided into three periods: the early Ming (1368-1435 AD), the mid Ming (1436-1521 AD) and the late Ming (1522-1644 AD) productions. The first period is a transitional period from the Yuan porcelain to the Ming porcelain. At that time, potters utilized imported cobalt material to achieve decoration presenting sapphire blue color with dark spots similar to the Yuan production (e.g., Figure 1.A.1.2 (a)). It was until to the Xuande period (1426-1435 AD) that the Ming porcelain achieved its own prominence. During the mid Ming period, local cobalt minerals were increasingly used and mixed with imported cobalt material or solely (Li 1998). The use of local cobalt ores, containing high manganese and less iron (Wen et al. 2007), enriched the blue patterns (e.g., Figure 1.A.1.2 (b)). Also these rich pigment sources allowed for a significant increase of production. In the late Ming dynasty, folk workshops were thriving and prosperous enough to compete with contemporary official workshops, even superior to the latter at the end of the Ming dynasty (Li 1998, p.19). They produced a significant amount of fine blue and white porcelains with high quality and unique artistic style (e.g., Figure 1.A.1.2 (c)).

Figure 1.A.1.2 Blue and white porcelains produced in Jingdezhen during the Ming (a) Yongle era (1403-1424 AD), photographed at Musee Guimet; (d) Zhengde (1506-1521 AD), photographed at Musee Guimet; (c) Wanli (1573-1620), photographed at Nanjing Museum, respectively (Credit of the three images: World Imaging, CC BY-SA 3.0).

During the Qing dynasty, the manufacture process was subject to similar criteria and regulation of the Ming dynasty and the classic patterns were reproduced and enhanced (e.g., Figure 1.A.1.3). Because the Qing emperors had been very fond of the porcelain, both the process technology and the volume of production reached a peak at that time.

Figure 1.A.1.3 Blue and white export porcelain produced during the Qing Kangxi era (1690-1700 AD), photographed at Musee Guimet (Credit of the four images: World Imaging, CC BY-SA 3.0).

1.A.2 Manufacturing process

Blue and white porcelain is a kind of once-fired underglaze colored ceramic (Lu 2014). From the Yuan dynasty, its manufacture process was subject to strict criteria and regulation (Wen et al. 2007). The body, made from raw clay, was firstly formed by throwing, stamping, carving or plastic extrusion (Huang and Huang 2007a). The blue pattern was ornamentally drawn on the formed body with cobalt pigment. Then the well-painted ware was covered with clear glaze by splashing, dipping, or sufflation (Huang and Huang 2007b). Finally, the unfired ware was once fired under 1280°C ± 20°C at reducing atmosphere (Huang and Huang 2006).

1.A.2.a Raw materials for body and glaze

The raw material of porcelain body was made from a secondary formulation that porcelain stone mixed with kaolin. The porcelain stone (quartz-feldspar-mica rocks) contains Al_2O_3 of ~17% (Tite et al. 1984), while kaolin contains Al_2O_3 more than 33%. Adding kaolin into porcelain stone, the concentration of Al_2O_3 in body can reach more than 19%, which could elevate the firing temperature and reduce the deformation, giving possibility of large size production (Huang and Huang 2006; Qiu and Chen 2009). After being fired, porcelain can obtain a kind of vitrified and low-porosity body, presenting white, or even sometimes translucent.

The glaze of the Yuan blue and white porcelain was developed from Song shadowy blue porcelain. The raw material was obtained from the mixture of glaze stone, similar to porcelain stone used for the body, added with glaze ash, generally limestone, wood ash or feldspar (Tite et al. 1984). The glaze of the Yuan production contained the glaze stone of 86~90% and glaze ash of 14~10%. After being fired, the glaze could present white and glossy surface.

1.A.2.b Cobalt materials

Besides the high know-how for fabricating white body and translucent glaze, the blue decorations also require extreme dexterity. One of the key steps is the manufacture of the blue pigment obtained from cobalt ores. The natural cobalt-containing minerals were mainly existing as the compounds of cobaltite (CoAsS), skutterudite ($CoAs_3$), smaltitechloanthite ($(Co,Ni,Fe)As_{3-2}$), and safflorite ($(Co,Fe)As_2$) (Colomban 2013). In order to obtain the blue pigment, the minerals were refined through four major steps: selection, elutriation, calcination (~800°C) and a final selection.

From the Yuan dynasty to the Ming Xuande period, the sources of cobalt

materials are not clearly established and could depend on importation of pigments known as “Smalte”, “huiqing”, etc (Watt 1979). After the mid Ming dynasty, it is proved that local cobalt minerals were increasingly used mixed with imported cobalt material or solely (Wen et al. 2007). These variations in pigment source enriched the blue patterns of the mid Ming Qinghua ceramics. Besides, the new rich pigment sources allowed for a significant increase of production.

1.B Issues and research objectives

Beside the designs, the success of Qinghua porcelain is attributed to the association of brilliant white translucent glaze and a blue pattern painted under glaze. The blue color is mainly due to cobalt (Cowell and Zhang 2001), but other transition metal elements including iron and manganese are also present in the decors as attested by elemental analysis with X-ray Fluorescence (Yu and Miao 1996; Colomban et al. 2004; Wood et al. 2007; Zhu et al. 2015b). In fact, color variations are significant both in brightness (light blue to dark blue) and in tint (greenish to black hue). Archaeometric researches have been focused on the chromogenic mechanisms and have tried to explain the chromatic variations. Many works were focused on the Ming production and less on the Yuan production.

1.B.1 The blue decors of the Ming Qinghua procelains

Many work about the Ming productions were performed including of investigating the chemical (Cheng et al. 2002; Cheng et al. 2004; Cheng et al. 2005; Wen et al. 2007; Du and Su 2008) and crystallographic composition (Wu et al. 2007; Kock and De Waal 2007; Zuo et al. 2007; Wang and Wang 2011; Figueiredo et al. 2012; Qu et al. 2014). Based on elemental composition, scholars have tried to correlate the color variations with Co/Fe and Co/Mn ratios (Wen et al. 2007). Iron and manganese oxides (Fe_2O_3, Fe_3O_4, Mn_3O_4 and $MnFe_2O_4$) were observed in dark spots of blue decors showing their influence in the darkness of the color (Wu et al. 2007; Zuo et al. 2007). Different Co based crystals were also found in different variety of the Ming productions (Kock and De Waal 2007; Zuo et al. 2007; Wang and Wang 2011; Figueiredo et al. 2012; Qu et al. 2014) but without satisfactory correlation between color and nature of these phases.

The problem is that most previous studies were carried out in several points rather than in an integrate aspect leading to lose the key information concerning the crystalline size, concentration and phase distributions. Without such information it is really difficult to clarify the color variations. Such microstructural data is essential to understand the color variations. Only the recent Qu's work

addresses the microstructure of blue decorations but without any conclusion concerning the color variations (Qu et al. 2014). The aim of my work was to postulate actual assumptions concerning the origin of color variations of the Ming productions. For this, I selected four typical fragments of the Ming production with the archaeological team of Sun Yat-sen Unversity.

1.B.2 The blue decors of the Yuan Qinghua procelains

The investigation in the Yuan productions is significantly less than the Ming productions because the discovered number is also very small. And many investigations of chemical composition were simply carried out on the surface to identify the provenance or the color variations (Yaocheng et al. 1994; Cheng et al. 2004; Cheng et al. 2005; Wen et al. 2007; Du and Su 2008; Zhu et al. 2015a), whereas the study of the crystallographic composition still remains in the basic stage (Wu et al. 2007; Wang and Wang 2011). Only Wang et al. reported that divalent cobalt ions located at tetrahedral sites could be responsible for the color but had not given the conclusive identification of the phase. Iron oxides were simply observed in the dark spots of blue decors until now (Wu et al. 2007).

The goal of my work was to provide more fundamental information concerning the blue decors and to final enrich the knowledge of the Yuan porcelain. For this, I selected 22 fragments of the Yuan Qinghua porcelains with the archaeological team of Sun Yat-sen University. They can be divided into three groups on the base of exterior appearance. The fragments (noted as YJ) of first group came from Luomaqiao site while the fragments of the others two groups (noted YH and YG respectively) come from Shibaqiao site (Appendix 7 and 8).

2 Synchrotron radiation-based multi-analytical approach for studying underglaze color: the microstructure of the Ming Qinghua blue decors

2.A Method strategy

In order to establish an integrate aspect concerning the crystalline size, concentration and phase distributions of the blue decors, I envisaged to use FF-XANES technique to analyze the blue decors. The full-field XANES (FF-XANES) approach is capable of determining the speciation and repartition of Co-based phases with high spatial resolution (0.7 μm) and on a large representative zone (mm^2). This technique has been successfully used to analyze Ti speciation distribution of the Roman terra sigillata and Fe speciation distribution of the Attic ceramics (Chapter III). However, different from Ti (~3 wt%) and Fe (~14 wt%) rich in the slips, in this case, the average concentration of Co in the blue decors is lower than 1 wt% (measured at Sun Yat-sen University). The FF-XANES performed in transmission mode is not well suitable to study element in too low concentration. For this it is better to use SR-μ-XANES technique but the scanning of a large zone with a submicrometric resolution is too time-consuming for analyzing even only one sample. Hence, I chose to combine the advantage of the two techniques. Firstly, I used SR-μ-XRF to investigate the elemental distribution of the blue decors, in particular, the colorant elements (Mn, Fe and Co), which allowed me to determine the Co concentrated and dilute zones. Then, SR-μ-XANES was used to accurately analyze the speciation of Co in a few points. To have a general view, I performed FF-XANES on large zones to analyze the Co speciation distribution. Finally, the nature of crystals was confirmed by SR-μ-XRD.

The synchrotron investigations were carried out on dedicated samples (cf. chapter II, § 2.B) while the Lab-XRF (Sun Yat-sen University) was performed directly at the surface of ceramic fragments both on white and blue glaze zones. 6 analyses were carried out for each sample (3 in blue zone and 3 in white zone).

2.B Archaeological descriptions

Four typical Ming Qinghua fragments produced by folk workshops in Jingdezhen (reference MM1, MM2, MM3 and MM4) were selected. They were excavated from the Maojiawan archaeological site of Beijing and provided by Beijing Archaeological Institute (Beijing Archaeological Insititute 2007). All samples are dated from the Ming Chenghua to Zhengde era of the Ming dynasty (late 15th to early 16th Century), according to the archaeological layer where they were found and on the basis of archaeological classification. The four samples present blues of different intensity (light blue to dark blue) and tint (greenish to black hue) (Figure 2.B.1). MM1 shows also a typical blue decoration but the white glaze is lightly bluish. MM2 is representative of darker blue decors. MM3 is typical of blue decorations. Finally, MM4 is characterized by very dark, almost black, decorations. The sampling zones are indicated with red arrows on Figure 2.B.1.

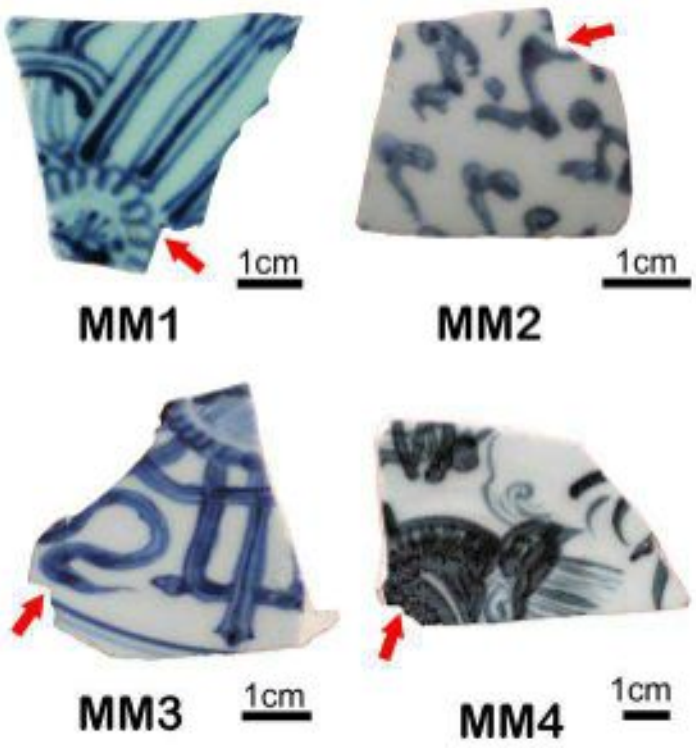

Figure 2.B.1 Photographs of the four studied shreds. The sampling zones are indicated with red arrows.

2.C Results

2.C.1 Macro-XRF

The results of quantitative macro-XRF analyses performed by the archaeometry team of Sun Yat-sen University are given in Table 2.C.1.1. The measurements were carried out directly on the surface of fragments both in pigmented (MMx-P) and white glaze areas (MMx-G). In each zone, three analyzed points were performed. The variations are slightly higher in the decor zones as attested by the standard deviations given in brackets in Table 2.C.1.1. Large variations are observed for Na in MM1 (MM1-P2, MM1-P3) and MM4 (MM4-P2, MM4-P3) samples. The composition of decorated zones is more heterogeneous that the one of white glaze because it was obtained using a more complex mixture (cobalt pigment + clear glaze). Moreover, there were interactions and diffusions during the firing between the painting mixture and the upper glaze. Besides, these decors are underglazed and the thickness of the upper glaze layer varies from one point to another, which directly impacts the XRF signal measured on the ceramic surfaces. The compositions (glaze and decor) of the four samples are well in agreement with the production of folk workshops with SiO_2, Al_2O_3 and K_2O close to 65-70%, 12-14% and 4-5% (Li 1998). Si, Al, Mg and K relative amounts show no significant differences between white glazes and decors, whereas those of Na and Ca vary noticeably. The samples MM1, MM2 and MM3 contain ~20% (in oxide wt%) higher Ca in glazes than in the decors. Conversely, Ca amount is ~ 20% (in oxide wt%) higher in the decor than in the glaze for MM4. For Na, MM1 MM3 and MM4 show values twice higher in the uncolored glaze than the pigment zones. Conversely, in MM2, Na is slightly (~ 15 in oxide wt%) more concentrated in the blue regions. In addition to the variation in Na and Ca amounts, the main differences between the glaze and decor zones are the amount of Co and Mn elements. Mn is present in glaze but in very little amount (< 0.1 in oxide wt%) compared to its amount in the decor zone (0.3-2 in oxide wt%). For all samples, Co and Mn amounts show significant enrichment in colored zones. In contrast, relative amounts of Fe are rather similar in decors and glazes, and are even lower in the blue decor than in the white regions for MM3.

In order to try to correlate the hue with transition element concentrations, the pertinent ratios among the concentration of these elements were calculated and the results are given in Table 2.C.1.1 (noted Mn/Co and Fe/Co). The two samples (MM1 and MM3), which exhibit the pure blue hue in decors, have also the highest content in Co and Mn. Although the sample MM1 contains about twice more Co and Mn than does MM3, both show rather equivalent values of Mn/Co and Fe/Co ratios. Conversely, the decors of the other samples (MM2 and MM4) present a

very low Co rate and quite high Mn and Fe rates. They are defined by higher values of Mn/Co and Fe/Co ratios. The sample MM4, which is characterized by a very dark, almost black decor, contains the significantly highest values of Mn/Co and Fe/Co ratios. There is no evident variance of Mn and Fe rates in the glazes for four samples except for MM3, which shows a slightly higher concentration in Fe.

	Oxide:	Na_2O	MgO	Al_2O_3	SiO_2	P_2O_5	K_2O	CaO	TiO_2	MnO	Fe_2O_3	CoO	Mn/Co	Fe/Co
MM1-G	point-1	8.56	3.00	12.38	65.32	0.27	3.98	5.76	0.04	0.06	0.61	/		
	point-2	9.16	2.73	12.32	65.00	0.05	4.01	5.85	0.03	0.06	0.70	/		
	point-3	9.23	3.22	12.24	64.84	0.49	3.88	5.58	0.05	0.06	0.52	/		
	average	**8.98 (0.37)**	**2.98 (0.25)**	**12.32 (0.07)**	**65.05 (0.24)**	**0.27 (0.22)**	**3.96 (0.07)**	**5.73 (0.14)**	**0.04 (0.01)**	**0.06 (0.00)**	**0.61 (0.09)**	/		
MM1-P	point-1	3.94	1.06	13.12	68.57	0.31	4.85	4.76	0.04	1.87	1.19	0.29	5.86	3.45
	point-2	5.97	2.11	12.94	66.46	0.00	4.39	5.16	0.07	1.52	1.14	0.23	6.00	4.17
	point-3	1.87	0.00	13.17	69.97	0.62	5.26	4.31	0.01	2.20	1.23	0.35	5.71	2.96
	average	**3.93 (2.05)**	**1.06 (1.06)**	**13.08 (0.12)**	**68.33 (1.77)**	**0.31 (0.31)**	**4.83 (0.44)**	**4.74 (0.43)**	**0.04 (0.03)**	**1.87 (0.34)**	**1.19 (0.05)**	**0.29 (0.06)**	**5.86 (0.14)**	**3.45 (0.61)**
MM2-G	point-1	6.23	2.26	13.88	68.51	0.06	4.26	4.12	0.04	0.06	0.57	/		
	point-2	7.26	2.12	13.72	67.78	0.10	4.16	4.11	0.03	0.05	0.66	/		
	point-3	7.21	2.11	13.62	67.31	0.10	4.13	4.08	0.03	0.05	0.66	/		
	average	**6.90 (0.58)**	**2.16 (0.08)**	**13.74 (0.13)**	**67.87 (0.61)**	**0.09 (0.02)**	**4.19 (0.07)**	**4.10 (0.03)**	**0.03 (0.01)**	**0.05 (0.01)**	**0.63 (0.05)**	/		
MM2-P	point-1	8.45	3.16	12.44	66.63	0.51	4.26	3.26	0.05	0.45	0.73	0.05	8.18	12.28
	point-2	8.88	3.32	13.07	69.96	0.54	4.47	3.42	0.05	0.47	0.77	0.05	8.54	12.95
	point-3	8.45	3.16	12.45	66.63	0.51	4.26	3.26	0.05	0.45	0.73	0.05	8.18	12.28
	average	**8.59 (0.25)**	**3.21 (0.09)**	**12.65 (0.36)**	**67.74 (1.92)**	**0.52 (0.02)**	**4.33 (0.12)**	**3.31 (0.09)**	**0.05 (0.00)**	**0.46 (0.01)**	**0.74 (0.02)**	**0.05 (0.00)**	**8.36 (0.21)**	**12.45 (0.39)**
MM3-G	point-1	8.58	2.82	12.82	66.8	0.26	4.43	3.32	0.06	0.06	0.83	/		
	point-2	7.84	2.64	12.00	67.63	0.55	4.41	3.85	0.05	0.07	0.95	/		
	point-3	7.85	2.65	12.02	67.73	0.55	4.41	3.86	0.05	0.07	0.95	/		
	average	**8.09 (0.42)**	**2.70 (0.10)**	**12.28 (0.47)**	**67.39 (0.51)**	**0.45 (0.17)**	**4.42 (0.01)**	**3.68 (0.31)**	**0.05 (0.01)**	**0.07 (0.01)**	**0.91 (0.07)**	/		
MM3-P	point-1	5.38	1.47	13.02	70.45	0.09	5.25	2.8	0.04	0.83	0.54	0.13	5.80	3.49
	point-2	5.69	2.14	13.82	68.56	0.28	5.04	2.77	0.06	0.98	0.52	0.14	6.36	3.12
	point-3	6.00	2.82	14.62	66.66	0.47	4.83	2.74	0.08	1.13	0.50	0.15	6.84	2.80
	average	**5.69 (0.31)**	**2.14 (0.68)**	**13.82 (0.80)**	**68.55 (1.90)**	**0.28 (0.19)**	**5.04 (0.21)**	**2.70 (0.03)**	**0.06 (0.02)**	**0.98 (0.15)**	**0.52 (0.02)**	**0.14 (0.01)**	**6.3 (0.52)**	**3.12 (0.35)**
MM4-G	point-1	7.92	2.64	12.61	67.32	0.28	4.50	4.00	0.05	0.05	0.49	/		
	point-2	7.45	2.51	12.63	67.31	0.21	4.41	3.90	0.04	0.04	0.41	/		
	point-3	7.53	2.54	12.77	68.05	0.21	4.46	3.94	0.04	0.04	0.41	/		
	average	**7.63 (0.25)**	**2.56 (0.07)**	**12.67 (0.09)**	**67.56 (0.42)**	**0.23 (0.04)**	**4.46 (0.05)**	**3.95 (0.05)**	**0.04 (0.01)**	**0.04 (0.01)**	**0.44 (0.05)**	/		
MM4-P	point-1	3.60	0.87	12.65	68.48	3.07	5.01	5.22	0.05	0.16	0.67	0.03	4.85	18.78
	point-2	4.12	0.50	12.69	68.73	3.03	4.83	5.33	0.04	0.02	0.68	0.03	0.61	19.06
	point-3	1.57	2.35	12.62	68.12	3.25	5.78	4.83	0.09	0.73	0.63	0.03	22.11	17.66
	average	**3.10 (1.35)**	**1.24 (0.98)**	**12.65 (0.04)**	**68.44 (0.31)**	**3.12 (0.12)**	**5.21 (0.51)**	**5.13 (0.26)**	**0.06 (0.03)**	**0.30 (0.38)**	**0.66 (0.03)**	**0.03 (0.00)**	**9.09 (11.39)**	**18.50 (0.74)**

Table 2.C.1.1 Analytical results (wt%) obtained by the archaeometry team. The

glaze without color and pigment was abbreviated as G and P, respectively. Three analyzed points were performed in each zone to estimate the homogeneity. The mean and standard deviation (in brackets) are given in bold. Additionally, the mass ratios of Mn/Co and Fe/Co were also calculated.

2.C.2 SR-μ-XRF analyses

Figure 2.C.2.1 shows the visible picture of the MM1-C2 thin section (with two fragments, face to face, and for each, the presence of body, pigment and glaze zones), as well as the trichromatic element maps (K, Ca and Si). The different zones are clearly identified, both in the visible and X-ray images. The “shadow effect” observed in particular on bubbles is due to the fact that the sample is not orthogonal to the beam as mentioned in experimental details. The difference between the right and left cross-sections is in agreement with the difference in blue intensity of the two decor lines (A and B) used in the sample preparation (Figure 2.C.2.1). It can be noticed that the body contains Si (green) and K (red), but no Ca. Si is present as crystals up to ~20 μm (certainly quartz and/or cristobalite grains). K is more concentrated in the glaze than in the colored region (when present) while higher level of Ca (blue) characterizes the pigment zones. Many very thin (~5 μm) and long (~50 μm) needle crystals are observed in the pigment zones (concentrated as a 20-30μm thick heterogeneous layer). In addition to Ca, they contain Al (Cf. insert map in Figure 2.C.2.1), and are possibly anorthite crystals ($CaAl_2Si_2O_8$) as already mentioned in various papers (Qu et al. 2014). The density of these crystals is higher in the darker decor (B), but these needle crystals are also present in the light blue stripe (A).

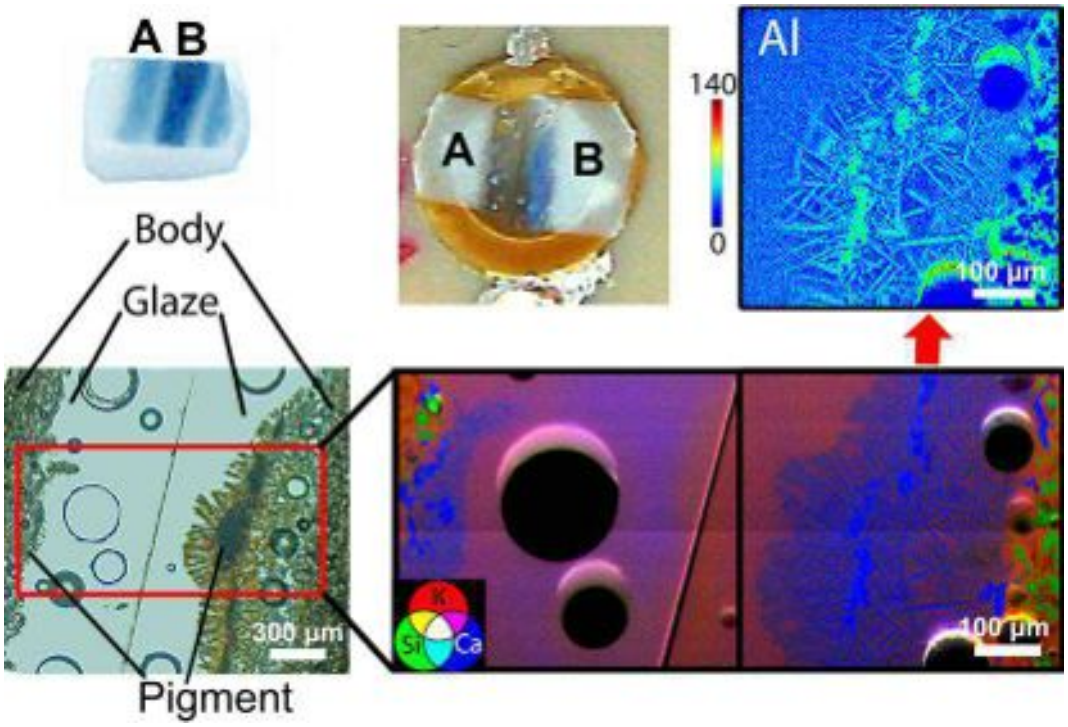

Figure 2.C.2.1 MM1 fragment, the cross-section sample (MM1-C2) obtained from the A and B bleu lines, the optical transmission image (objective x50) showing the bubbles and the different zones (body, pigment and glaze) as well as the trichromatic diagram of red box zone obtained by SR-µXRF (ID21 beamline). The inserted map corresponds to Al distribution.

Results obtained for the other samples are given in Figure 2.C.2.2. MM2-C3 and MM3-C1 present some similarities with the previous sample. Their pigment zones are also characterized by higher level of Ca and the presence of needle crystals, especially for the sample MM2-C3. However the upper glaze is slightly thicker and contains more Si-based particles (certainly quartz and/or cristobalite grains). MM4-C2 sample is essentially different (Figure 2.C.2.2). The glaze is much more homogeneous without any observable crystal.

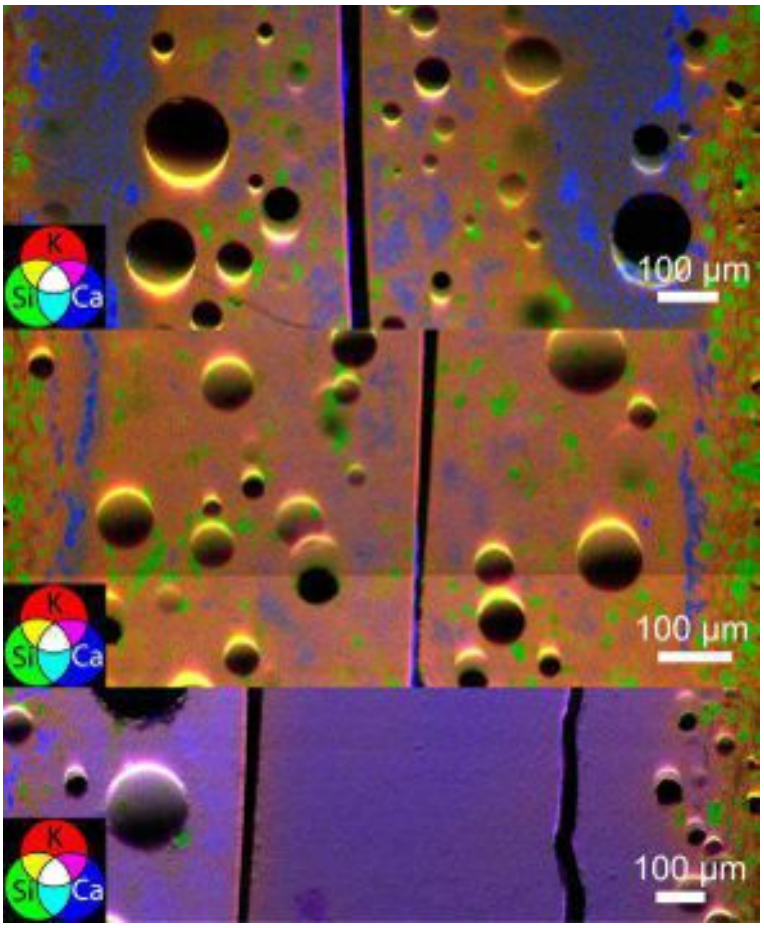

Figure 2.C.2.2 Trichromatic diagrams (K, Ca, Si) obtained by SR-µXRF (ID21 beamline) on the other samples (from top to bottom: MM2-C3, MM3-C1, MM4-C2).

Figure 2.C.2.3 shows the Mn, Fe and Co µXRF maps for the 4 samples corresponding to their visual images. Color scales are fixed for each element, to allow a direct comparison from one sample to another. Here again, MM4-C2 exhibits a completely different behavior, compared to the 3 other samples, with transition metals homogeneously distributed in the glaze (however, one can note that the maxima of intensity for each element do not coincide exactly). For the 3 other samples, the results are significantly different. Mn, Fe and Co are more concentrated in the pigment zones, but with specific distributions. The distribution of Co and Mn in the upper glaze is quite limited, only Fe has a more remarkable diffusion with a higher concentration in the surface. The high concentration zones in Co are associated with lower amounts of Fe and Mn.

Figure 2.C.2.3 Fluorescence intensity maps of transition elements obtained by SR-μXRF at ID21 beamline (From top to bottom: optical images, Mn, Fe and Co maps) for the four samples (from left to right: MM1-C2, MM2-C3, MM3-C1 and MM4-C2).

2.C.3 Comparison between macro-XRF and micro-XRF

From the colorant element maps (Figure 2.C.2.3), one can understand that Co amount measured by macro-XRF at the surface on the sample is not representative of internal Co amount. The values given in Table 2.C.1.1 are more consistent with the composition of upper glaze than with the composition of pigment zone. Co maps of MM2 and MM3 show that the upper glaze hardly contains Co and this is in agreement with the macro-XRF measurements (Table 2.C.1.1). Conversely, all samples show a higher Fe concentration in surface, which can explain the rather high value of Fe obtained by macro-XRF.

In order to closely inspect variations of colorant elements (Mn, Fe and Co), the pertinent ratios are also calculated from μ-XRF investigations as shown in Figure 2.C.3.1. The comparison between the three points acquired in macro-XRF (MM1-P) and the results obtained by μ-XRF for MM1-C2 shows interesting correlations. The three points (MM1-P) exhibit a quite constant Fe rate (Fe mass rate: 0.83±0.03, variation ~ 4%), but rather variable rates of Mn and Co (Mn mass rate: 1.44±0.3, variation ~20%; Co mass rate: 0.23±0.05, variation ~20%). However the ratio Mn/Co is quite stable (Mn/Co mass ratio: 5.9±0.2, variation ~3%). In μXRF mode, the two fragments from MM1-C2 show strong dissimilarities (Figure 2.C.2.3 and Figure 2.C.3.1). The right (darker blue) fragment exhibits more Co particles, more needles, more Mn and Co in the glaze matrix and a decrease of both elements, (also observed in left fragment) near the surface of the glaze. Conversely, the Si, K (Figure 2.C.2.3) and Fe (Figure 2.C.2.3 and Figure 2.C.3.1) XRF intensities are quite similar on both left and right samples. Si

and K concentrations are rather constant over the full glaze, while Fe shows the enrichment at the upper surface. Very interestingly, the depth profile of Mn/Co (Figure 2.C.3.1) shows that this ratio is quite constant over the full glaze thickness and from one fragment to another, being only lower in some Co-rich particles zones. Consequently the Mn/Co ratio obtained from macro-XRF measurements is quite representative of the bulk value. In contrast, the ratio Fe/Co varies a lot (Figure 2.C.3.1) and macro-XRF measurements on the surface cannot be used reliably to estimate deeper bulk values.

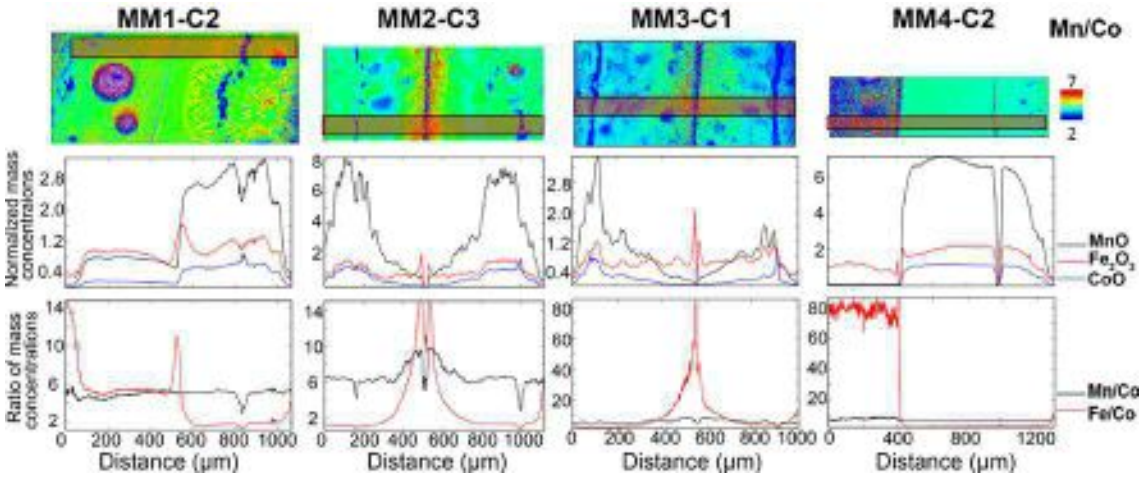

Figure 2.C.3.1 Focus on the evolution of Mn, Co and Fe concentration over the four thin sections. Top: Mn/Co XRF map (same conditions as Figure 2.C.2.3). The red rectangle represents the line chosen to calculate the following profiles (sum over an height of 100µm: 50 pixels). Middle: 1D profiles of Co, Fe and Mn. Bottom: 1D profiles of Mn/Co and Fe/Co.

The two (left/right) fragments in MM2-C3 and MM3-C1 have similar compositions. However, it is interesting to note that the stability of the Mn/Co ratio is also observed within both samples: while these two samples show a strong decrease of Co and Mn rates, from the pigment to the surface of the object (variation ~x1/5), the ratio Mn/Co is much more stable, over the stratigraphy, only lower in some Co-rich particles zones (variations of less then 50%) (Figure 2.C.3.1).

MM4-C2 shows the same trend as MM1-C2. While the two (left/right) fragments show huge differences in concentration of Mn and Co (with a factor x80 for Co and x100 and Mn) and a quite constant rate in Fe (variation of only 40% between left and right), the ratio Mn/Co is quite similar between and within the two fragments (variation of ~±12% over the left fragment, and of less than 1% when comparing the average values on the two fragments).

Finally, the average values of Mn/Co mass ratios over glaze thickness

calculated from the μXRF measurements (MM1-C2: 5.1±0.8; MM2-C3: 7±1; MM3-C1: 5±1 and MM4-C2: 6±1) are comparable to the values obtained by Macro-XRF (MM1-P: 5.9±0.2, MM2-P: 8.4±0.2, MM3-P: 6.4±0.3 and MM4-P: 9±10). The very large standard deviation of MM4-P is due to the great difference among the 3 measurements, which comes from the manganese rate (Table 2.C.1.1).

Besides, these graphs (Figure 2.C.3.1) show the huge variation of Fe/Co mass ratios at the surface of the glaze, due to both the strong increase of Fe rate and decrease of Co rate, which is agreement with the rather high values and huge variations of concentrations obtained by macro-XRF (MM1-P: 3.5±0.6, variation ~17%; MM2-P: 12.5± 0.4, variation ~3%; MM3-P: 3.1±0.4, variation ~13%; MM4-P: 18.5±0.8, variation ~4%).

2.C.4 SR-μ-XANES along the Co K-edge

In order to get a better insight into Co speciation, μ-XANES spectra were acquired on a few points over Co-rich particles and diluted Co in glassy matrix, for samples MM1-C2, MM2-C3 and MM4-C2. Representative spectra are displayed in Figure 2.C.4.1. Over Co-rich particles (Figure 2.C.4.1a), the spectra exhibit the pre-edge at ~7709 eV and the edge energy at ~7717 eV consistent with bivalent Co (Co^{2+}) (Maurizio et al. 2010; Figueiredo et al. 2012). In addition, with a white line at ~7726 eV and the energy crests (~7741, ~7758, ~7781 eV), these XANES spectra are congruent with the ones of cobalt aluminate ($CoAl_2O_4$) particles in which Co^{2+} ions are in tetrahedral coordination (Maurizio et al. 2010; Figueiredo et al. 2012). Compared to these spectra, the XANES spectra recovered in glassy matrix (Figure 2.C.4.1b) exhibit the same pre-edge and same rising edge, also indicating a dominant bivalent state for the cobalt ions. However, the energy crests and the white line are clearly different. The white line is broader and moves to lower energy (~7724 eV).

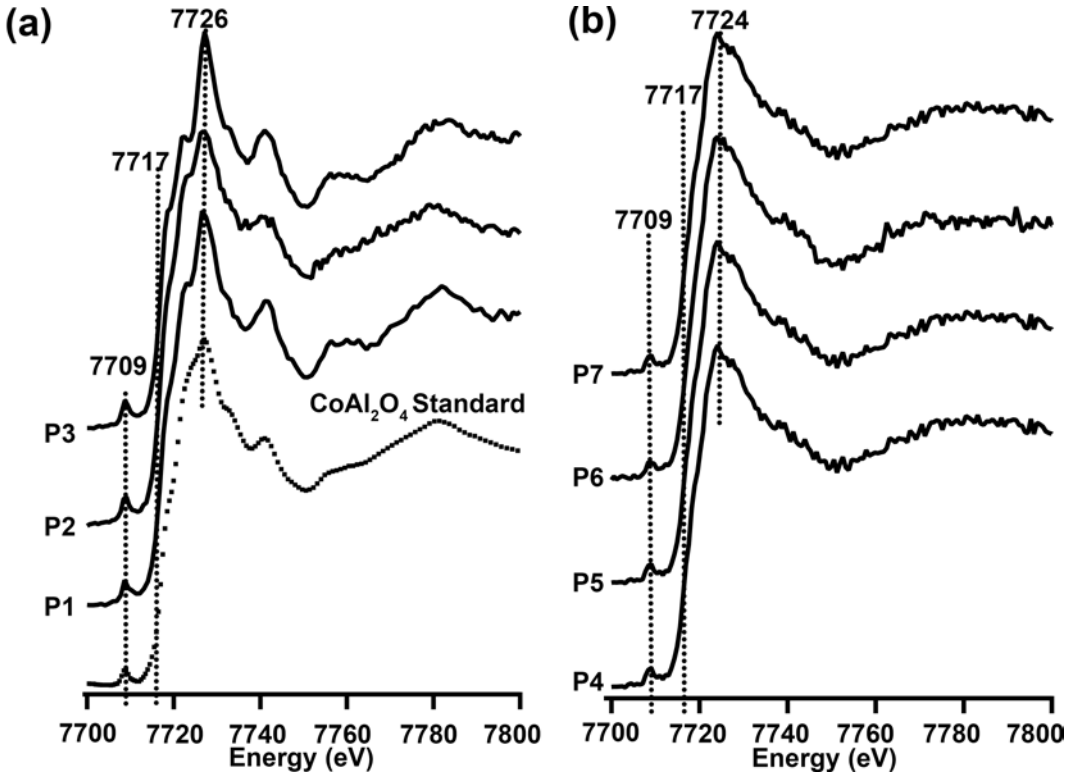

Figure 2.C.4.1 Normalized Co K-edge XANES spectra collected on representative points over Co-rich particles (a) compared with the standard $CoAl_2O_4$ spectrum (from Figueiredo et al. 2012) and diluted Co in glassy matrix (b). P1 and P2 respectively come from Co-rich particle of MM1-C2 line A and B respectively while P3 come from Co-rich particle zone of MM2-C3. P4 and P5 respectively come form diluted Co zone and more concentrated Co zone of MM1-C2; P6 and P7 come from diluted Co zone of MM2-C3 and MM4-C2 respectively.

To further investigate the comparative variation of edge feature, the first derivatives of normalized Co K-edge XANES spectra were calculated (Figure 2.C.4.2). The edge energy is more clearly observed as the maximum in the first derivative (~7717 eV). Moreover, for both Co-rich particles (Figure 2.C.4.2a) and diluted Co (Figure 2.C.4.2b), the first derivatives exhibit a small trough at ~7719 eV, corresponding to the typical shoulder of tetrahedral coordination (Kim and Yo 1999; Maurizio et al. 2010). It is well in agreement with the existence of $CoAl_2O_4$ particles mentioned above, but in addition this calculation reveals that Co speciation in glassy matrix could be also in tetrahedral coordination. It is consistent with the absence of high intense white line at ~7724 eV and the presence of a rather high pre-edge at ~7709 eV (Figure 2.C.4.1b) (Robinet et al. 2011).

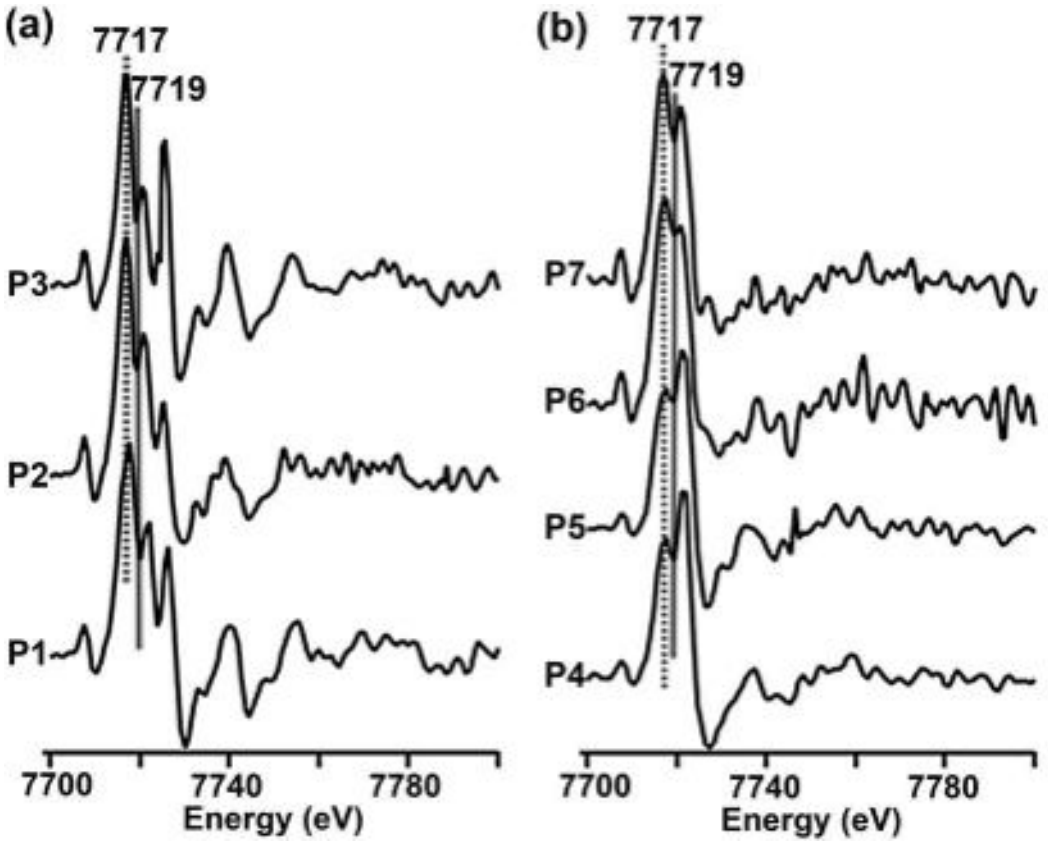

Figure 2.C.4.2 First derivatives of normalized Co K-edge micro-XANES spectra collected on representative points over Co-rich particles (a) and diluted Co in glassy matrix (b). (a) P1 and P2 respectively come from Co-rich particle zone and less Co-rich particle zone of MM1-C2; P3 come from Co-rich particle zone of MM2-C3. (b) P4 and P5 respectively come form diluted Co zone and more concentrated Co zone of MM1-C2; P6 and P7 respectively come from diluted Co zone of MM2-C3 and MM4-C2.

These spectra were acquired on a few points per sample. In order to have a full 2D picture of Co speciation over the full stratigraphy, FF-XANES maps were acquired as well, on the four samples.

2.C.5 FF-XANES analyses

The investigated areas were focused on the pigment region. The results obtained for the MM2-C3 sample are shown in Figure 2.C.5.1. The transmission image recorded at 7670 eV, below the Co K-edge, revealed the presence of several large bubbles-pores (diameter of ~100 µm or smaller) and a multitude of long narrow strips in the pigment zone attributed to anorthite crystals (Figure 2.C.5.1a). The edge jump map (Figure 2.C.5.1b) shows a distribution similar to the Co map,

obtained in μXRF mode. The edge energy map (Figure 2.C.5.1c) obtained from pixels with a signal to noise (SNR) level superior to 0.014 shows no significant spectral features variation, with a edge energy at ~7717 keV, consistent with bivalent cobalt (Kim and Yo 1999; Robinet et al. 2011; Figueiredo et al. 2012). PCA approach and subsequent k-means clustering were processed for a closer inspection. The first three principal components were considered to cover the cardinal significant information, clustered into k = 6 groups. The corresponding XANES spectra can be divided into two groups according their similarities: cluster 1, 2 and 4 and cluster 3 and 6 were grouped as G1 and G2 respectively (Figure 2.C.5.1e). Cluster 5 was not taken into account due to a low SNR value. Compared with the μXANES spectra, the average spectra from clusters 1, 2 and 4 have similar traits with spectra P1, P2 and P3 (Figure 2.C.5.1a), indicating the presence of aluminate ($CoAl_2O_4$) particles. On the other hand, the clusters 3 and 6 are also consistent with μXANES spectra of bivalent Co in the glassy matrix (Figure 2.C.5.1b). Therefore, from the distributions of the two groups illustrated in the zooming image segmentation (Figure 2.C.5.1d), the diffusions of cobalt aluminate particles and bivalent Co in a glassy matrix are presented clearly.

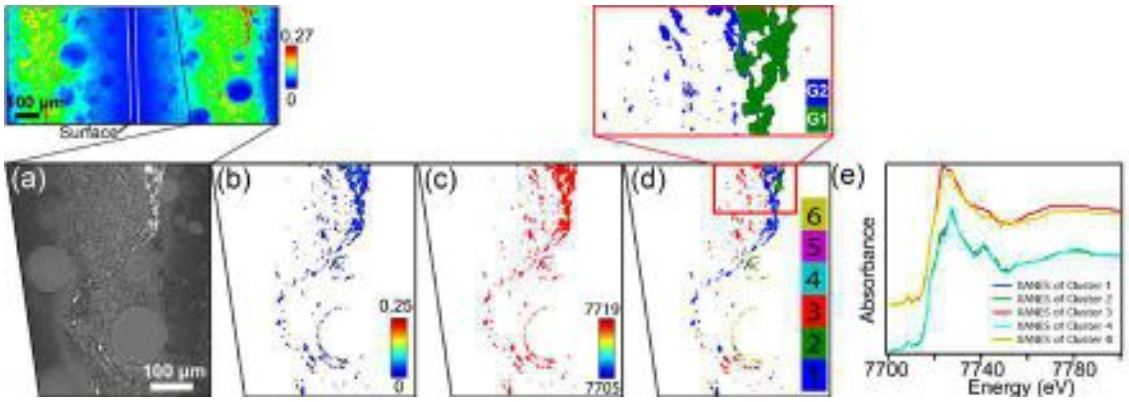

Figure 2.C.5.1 Results of FF-XANES (ID21 beamline) analyses performed at the Co K-edge for MM2-C3. (a) the transmission image recorded at 7670 eV, (b) the edge jump map (correlated to Co concentration) and (c) the edge energy map (correlated to Co valence). The scale bars report the values of the absorption edge jump (b) and the energy of the position of absorption edge in eV (c), respectively. (d) the image segmentation obtained by PCA and k-means clustering and (e) the corresponding average XANES spectra of each six cluster. Cluster 1, 2 and 4 spectra are very close and were grouped as G1 while cluster 3 and 6 were grouped as G2 as shown in the zooming image segmentation.

A second sample of the same specimen (MM2-C1) was analyzed the same way (Figure 2.C.5.2). The results are similar but the higher Co content outside the particles results in a higher SNR, which allows including increasing pixels

numbers in the PCA processing. The differences between the spectral features in the particles and in the glassy matrix are clearer: the cluster 1 and 2 showed the similar traits with group 1 and 2 (Figure 2.C.5.1), corresponding to the cobalt aluminate particles and bivalent Co in glassy matrix, respectively. Thus, the distributions of both clusters accurately portray the distributions of particles and Co ions in the glassy matrix.

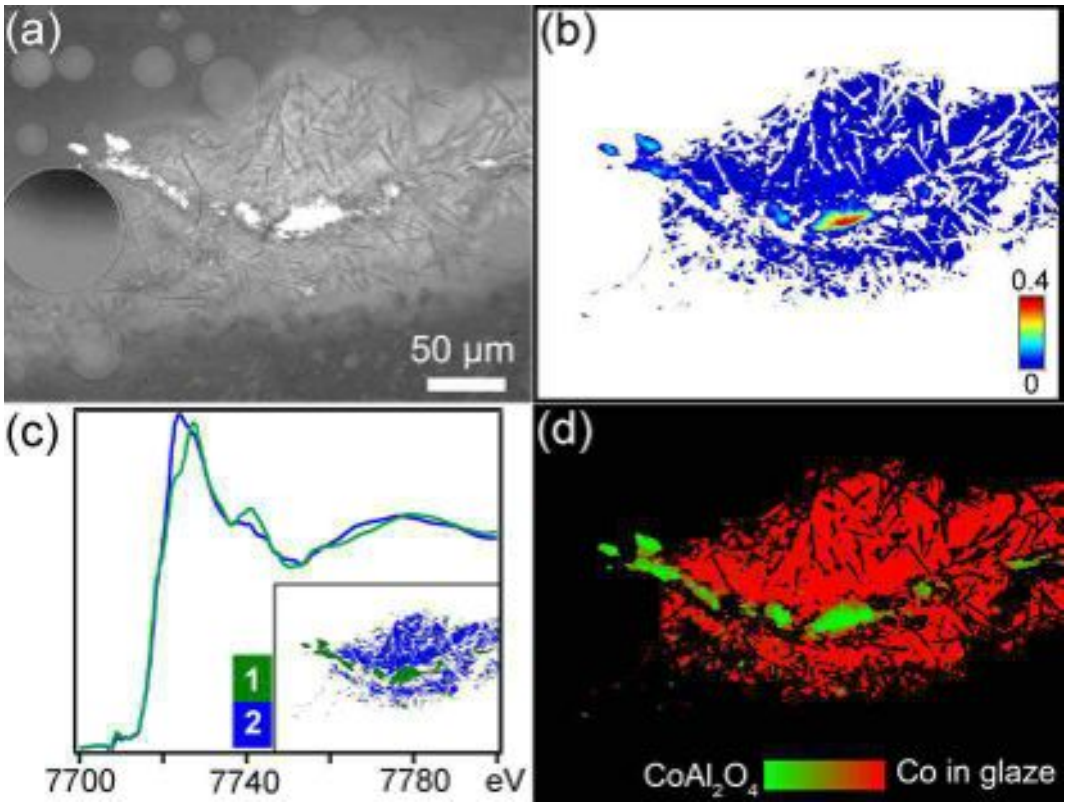

Figure 2.C.5.2 Results of FF-XANES (ID21 beamline) analysis across the Co K-edge for MM2-C1: (a) the transmission image recorded at 7670 eV, (b) the edge jump map, (c) the image segmentation based on PCA and k-means clustering (insert map) and the corresponding average XANES for cluster 1 and 2. For comparison, the phase map obtained from the least squares linear combination fitting (standards CoAl2O4 (P3) and Co in glaze (P6)) of each single pixel is shown in (d).

MM1-C1, MM1-C2 and MM3-C1 exhibit similar results with high Co concentrated zone corresponding to cobalt aluminate particles (Figure 2.C.5.3). In contrast, no based Co particles were detected in MM4-C2 in agreement with SR-XRF investigation, which revealed a quite homogeneous distribution of Co.

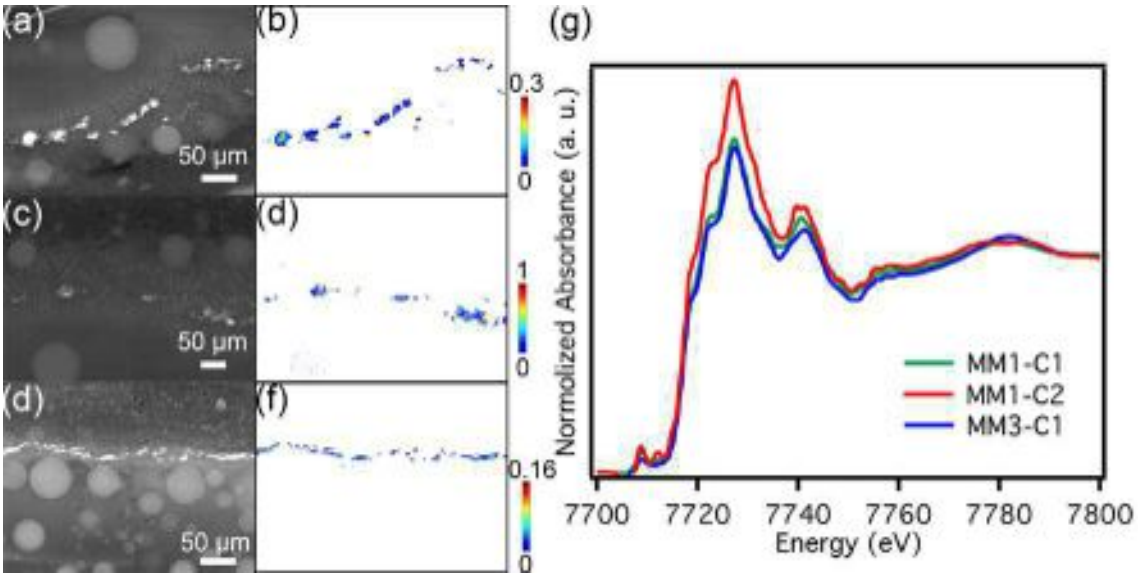

Figure 2.C.5.3 Results of FF-XANES (ID21 beamline) analysis performed at the Co k-Edge. The transmission image was recorded at 7670 eV from top to bottom for MM1-C1, MM1-C2, MM3-C1, as shown in (a), (c) and (d), respectively. Image (b), (d) and (f) presents respectively the edge jump map of each sample. The average XANES of each cluster was also displayed in (g).

Two samples were also analyzed by FF-XANES across the Fe K-edge (Figure 2.C.5.4). The results confirmed the absence of Fe-based particles. For MM1-C2, the edge jump map reveals a rather homogeneous distribution around the long narrow strips (anorthite crystals) and the cobalt aluminate particles. There is no variance of the edge energy (~7120 eV) and the PCA approach confirms that there is only one type of XANES spectrum. The spectrum is very close to the one of bivalent iron dispersed in a glassy matrix (Giuli et al. 2003; Berry et al. 2003). The Fe-rich thin layer present on the surface of the glaze was not included in the field of view, which was focusing on Co particles. By contrast to MM1-C2, the edge jump map of MM4-C2 indicates a more homogeneous distribution of Fe, consistent with XRF scanning measurements. The PCA approach also revealed only one type of XANES spectra but the edge energy is slightly higher which can be and indicator of the presence of a small amount of trivalent iron.

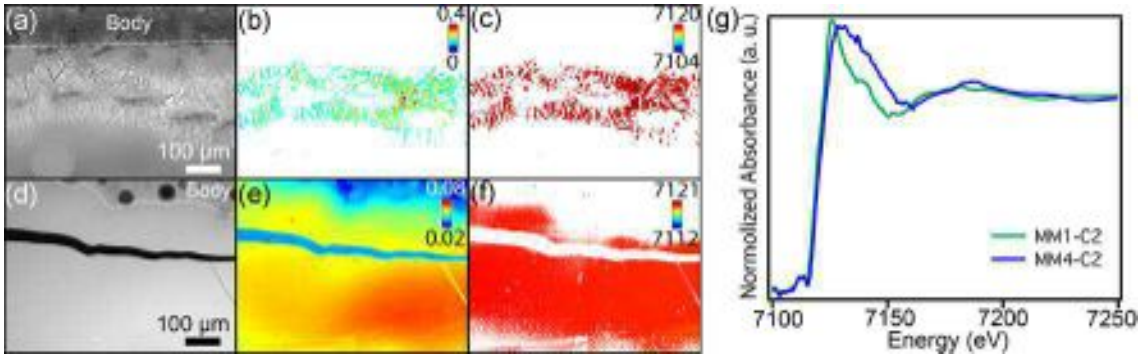

Figure 2.C.5.4 Results of FF-XANES (ID21 beamline) analysis of MM1-C2 (a, b, c and g) and MM4-C2 (d, e, f and g) across the Fe K-edge. (a, c) transmission images recorded at 7050 eV, (b, e) the edge jumps (correlated to Fe concentration) and (c, f) the positions of the edge energy map (correlated to Fe valence). PCA and k-means clustering lead to only one cluster in each case. The corresponding average XANES spectra are shown in (g).

2.C.6 SR-µ-XRD study

In order to further assess the identification of Co pigments, a µ-XRD/µ-XRF analysis was carried out on the MM1-C2 sample at ID21 beamline end-station. First, a large µ-XRF map was acquired over the glaze layer to locate Co particles. Then, a detailed µ-XRD/µ-XRF map was performed, with pixel size of 2×2 µm².

To verify the calibrated sample-detector distance, a µXRD map was first acquired in the body. XRD patterns show mainly mullite Debye rings (cf. Figure 2.C.6.1). Based on these rings and comparing to the reference pattern (Mullite_96-901-0160), a shift of -34 µm is observed. This can be explained by the fact that the MM1-C2 thin section is ~40-60 µm thick and that the sample was aligned by focusing its visible image on the side facing the incoming X-ray beam.

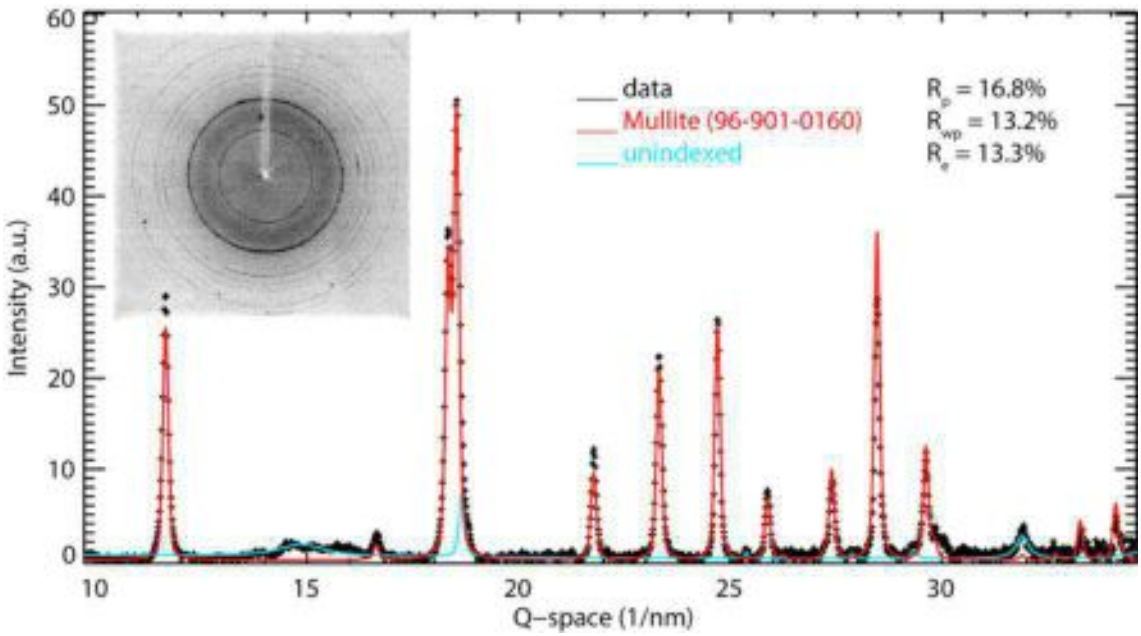

Figure 2.C.6.1 For μ-XRD experiments (ID21 beamline), the sample-detector distance was re-calibrated (after a first calibration with alumina powder in a glass capillary giving a distance of 59.662mm) acquiring a map in the paste. The figure shows a typical 2D XRD pattern and the corresponding azimuthally integrated 1D pattern. Most of the Bragg peaks can be assigned to mullite (96-901-0160), with only a few exceptions simulated as the “unindexed” contribution (turquoise pattern). Rietveld refinement fixing all structural atomic parameters gave a sample detector shift of -0.034±0.017mm with agreement factors Rp(%): 17.3 ± 0.9, Rwp(%): 13 ± 2 and Re(%): 15 ± 6.

In Figure 2.C.6.2, results from μ-XRF and μ-XRD are presented. The Co-based pigments are localized in the upper half part of the map. In this region, three Bragg peaks give similar distribution to Co (obtained by μ-XRF). As an example, the black XRD pattern (point A) corresponds to the pixel where the second Bragg peak is most intense. The reference peaks for $CoAl_2O_4$, as provided in database (96-901-6166, lattice parameter a=8.1047 Å) are plotted in dark blue. The three Bragg peaks observed on the pigment grains correspond to the three main peaks of the spinel structure apart from a shift. However this shift is larger than the one introduced by the sample thickness and determined from mullite pattern. A fit of Bragg peaks provided a lattice parameter of 8.1498 Å using the distance determined from the mullite signal (red curve). Attributing the shift to a change of the sample-detector distance would give a variation of -466 μm, which is not realistic for a sample thickness of ~40-60 μm. Instead, this variation from the reference spinel structure is more certainly due to a partial substitution leading to a change in the lattice parameter. Elemental maps show some

correlations among Co, Mn and Ni rates, which maybe in relationships with the substitution. Mn^{2+} and Ni^{2+} have an ionic radius larger than Co^{2+} radius and a substitution Mn/Co or Ni/Co may lead to an increase of the cell parameters.

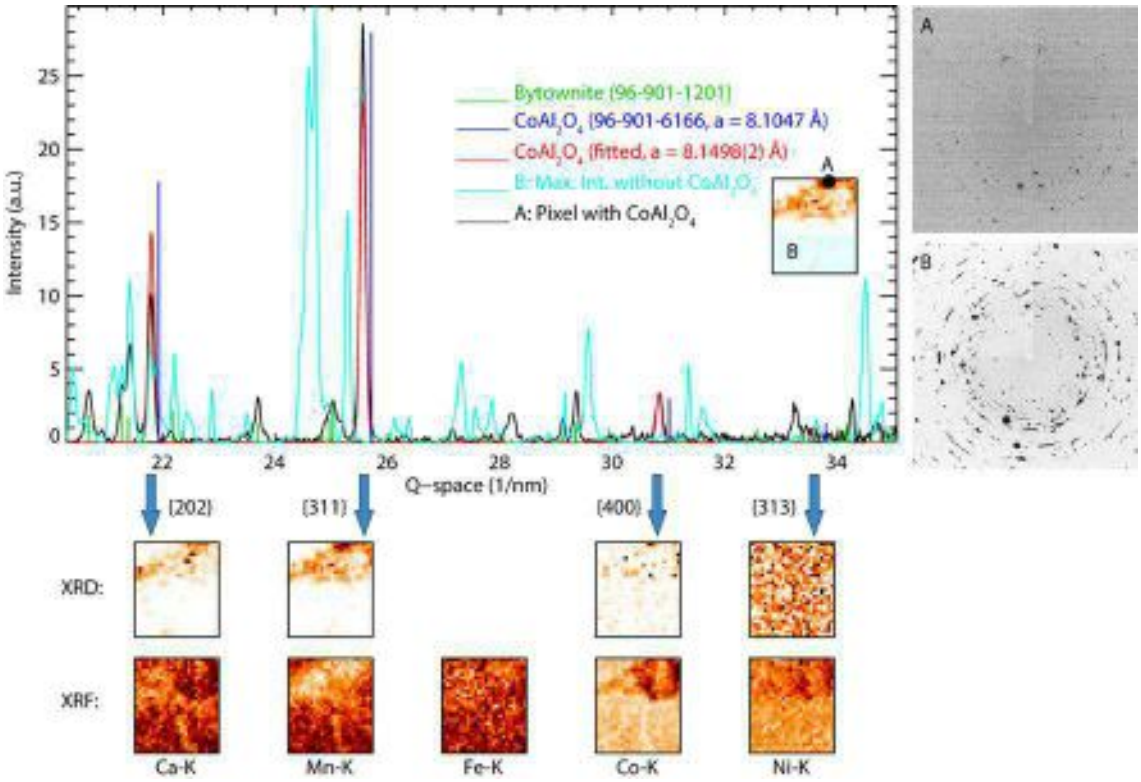

Figure 2.C.6.2 Results of μXRD and μXRF mappings from blue-pigmented area of sample MM1-C2. The two diffraction patterns correspond to a single pixel for A and to the superimposed pattern over non-pigment region (displayed as the blue rectangle) for B. Rietveld refinement with the model containing $CoAl_2O_4$ (dark blue) and bytownite (dark green) reveal a shift of the lattice parameter of the spinel (shifted pattern is displayed in red). Lattice parameters are indicated in the figure. Bragg peak intensity maps were calculated over the four most intense Bragg peaks of $CoAl_2O_4$, the fourth one (313) being below the detection limit (pixel size: 2 μm in both directions; map size: 48 × 52 μm²). Below, the elemental maps obtained by μ-XRF show distribution of Ca, Mn, Fe, Co and Ni.

The full map was fitted using two phases (spinel and feldspar (bytownite, 96-901-1201)) by fixing the sample-detector distance to the calibrated value obtained from the body. Lattice parameter obtained for the spinel structure varies around 8.149 ± 0.004 Å over the pigment grains. These measurements confirm those obtained by μ-XANES and open the way to a further investigation of Co-pigment composition. A more detailed analysis (e.g. with TEM) of the crystal structure could provide additional information concerning the substitution in the

spinel structure.

2.D Discussion

For the first three samples, the constant Mn/Co ratio of each object is in favor of the fact that both elements were introduced together, during the painting step. The different amounts of pigment deposited on different parts of the same object (e.g. MM1-C2, left and right) would explain the different rates of Mn and Co released in the glaze, together with the constant Mn/Co ratio. Conversely, the different Mn/Co ratios from one object to another would be attributed to the use of different pigments. Regarding the Fe concentration, the fact that its rate is almost constant over each object, whatever the pigment amount, could be due to the fact that it mainly comes from the glaze, and that, if any Fe is additionally present in the pigment, it does not significantly contribute to the total Fe concentration (this is consistent with the low Fe content coming from native cobalt materials as mentioned in archaeological background) (Wen et al. 2007). Finally, MM4 shows a perfect diffusion of transition metal elements in the glaze. Calcium is also homogeneously distributed in the glaze up to the surface. Contrasted with the other samples, MM4 is characterized by the absence of a specific zone containing Co-particles and anorthite crystals between the glaze and the body.

Cobalt aluminate ($CoAl_2O_4$) particles have a major influence on the color density of the first three samples. The dark blue decors (MM2, MM3 and right side of MM1) contain many more particles than the light blue decor (left side of MM1). Even if the macro-XRF analysis revealed small amounts of cobalt, these decors have a dark blue color thanks to their very dense layer of cobalt aluminate particles. The cross-sections show indeed that the thicknesses of glaze layers are more than 300 µm and that the Co grains are concentrated in the deeper part of the glaze. Consequently, macro-XRF does not probe directly Co pigment particles. Besides, as seen in MM1, in more particular, in MM2 and MM3, Co concentration strongly decreases from the pigment zone to the surface. Therefore, it is normal that Co rate measured from the surface with macro-XRF is very low. Fe content increases at the uppermost surface. These variations make hard to establish correlations between color and metal element ratios on the only basis of macro-XRF measurements.

MM4 shows a more homogeneous distribution of the transition elements. Although its Mn/Co ratio is equivalent to the one in other samples, the high value of Mn amount confirm the influence of Mn on the darkness color (almost black) of the decor.

In all samples, the oxidation state of cobalt was only detected as bivalent, which is its stable valence at high temperatures. Above 800°C, all cobalt compounds (oxides, carbonate, chlorate, sulfate) present in the painting

mixtures are transformed into the bivalent cobalt. With the increase of temperature and depending on the composition of glaze, Co^{2+} can interact with Si^{4+} or Al^{3+} to form either Co_2SiO_4 with octahedral coordination [CoO_6] or $CoAl_2O_4$ with tetrahedral coordination [CoO_4]. The former gives rise to a violet color while the latter lead to a blue color (Monari and Manfredini 1996; Llusar et al. 2001). In our case, cobalt aluminate is well at the origin of the blue color of the first three samples and, because of its high tinting action, the particles density is directly correlated to the density of blue color. Besides, out of the cobalt aluminate particles, Co^{2+} reacts with the glaze network in tetrahedral coordination, which also gives rise to the blue color (Hunault et al. 2014). However, due to its lower tinting contribution the density of color is lower. Co diffusion is much larger in the MM1 sample with an almost homogeneous rate in the glaze up to the surface. This larger diffusion could explain the bluish tint of the white glaze.

μ-XRD seems to indicate that the $CoAl_2O_4$ spinel crystals are partially substituted. This substitution can be linked to the composition of cobalt source, to the one of surrounding glass matrix and/or to the firing conditions. It could vary among different production types and the measurement of the cell parameter of the spinel structure could be a discriminant parameter.

2.E Conclusion

After SR-μ-XRF defining the Co distribution, FF-XANES associated with SR-μ-XANES was successfully used to detect the Co speciation in the concentrated and dilute zones of the blue decors. SR-μ-XANES at the Co K-edge, collected from both the concentrated and dilute zones, reveals that Co is present under two chemical forms: $CoAl_2O_4$ in the pigment particles, and Co ions in the glassy matrix. However, the speciation is in bivalent ion forms and tetrahedral coordination, giving the blue tint in the pigments. At the Co concentrated zone, FF-XANES was performed to have a more complete visualization of the distribution of the different Co-species on a significantly large zone. Results showed that all Co concentrated regions are associated to $CoAl_2O_4$ particles and present significant differences in the distribution of these particles among samples. SR-μ-XRD results confirmed the presence of these particles. They play a key role in the blue color and the variations of distribution are the main cause of the hue and color intensity variations. Fe ions, also present in similar rate in the white parts, have not a significant role in the color. Inversely, Mn has an influence on the darkness of blue decors and can lead to black color, if $CoAl_2O_4$ particles are not present. However, even though the manufacturing process of Qinghua porcelains was subject to strict criteria after the Yuan dynasty, Qinghua porcelains were produced in very great quantity in different workshops. To have a significant overview, the corpus must be extended and further investigations are necessary.

In conclusion, the proposed methodological approach is an efficient way to determine the complex structure of underglaze decors. It allows us not only to identify the color pigments and the speciation of colorant ions but also to observe how they are distributed in the glaze matrix.

3 The study of the Yuan Qinghua porcelain: the highlighting of dendritic $CoFe_2O_4$ crystals in blue decorations

3.A Methodological strategy

Since the Yuan production has been few studied, I chose lab-based techniques SEM-EDS and Raman spectroscopy to extract information concerning the blue decors based on a significant corpus (22 fragments). Firstly, SEM-DES was used to analyze the elemental distribution of blue decors. The image from the signal of backscattered electrons allowed me to position colorant elements (Mn, Fe and Co) and look for the related crystals, due to the larger atomic number of colorant elements than ones of others (Si, Al, K, Ca, Na and Mg). Then, Raman spectroscopy was used to analyze the nature of these crystals. Both SEM-EDS and Raman spectroscopy was carried out on the plane view sample (cf. chapter II, § 2.A.2).

3.B Archaeological descriptions

The archaeological details are shown in Appendix 7 and 8. The fragments were recovered at the Luomaqiao and Shibaqiao archeological sites in Jingdezhen (Jiangxi Province, China) and dated to the Yuan dynasty (13th -14th century AD). They were divided into three types due to different exterior (Appendix 8). The first type (labeled as YJ-) is characterized a greenish white glaze and pure blue decors. The second group (labeled as YH-) is characterized of a white glaze and grey-blue decors. The third group (labeled as YG-) is characterized of a greyish white glaze and greyish blue decors.

3.C Results and discussion

The blue decors of the majority of fragments coming from Luomaqiao site (YJ-1, YJ-3, YJ-4, YJ-5, YJ-7, YJ-8) and a part of YH fragments from Shibaqiao site (YH-1, YH-4, YH-7 and YH-8) show dark zones in which dendritic crystals were observed as shown in Figure 3.C.1. EDS revealed that these crystals contain mainly Co and Fe in addition to oxygen. On the largest crystals (a few micrometers), quantitative analyses could be performed and have confirmed that Ca, Si and Al are not present in theses crystals. Besides, these analyses allowed us to determine the Fe/Co ratio with a high enough accuracy to show that this ratio varies from a sample to another (the obtained values are reported in Figure

3.C.3).

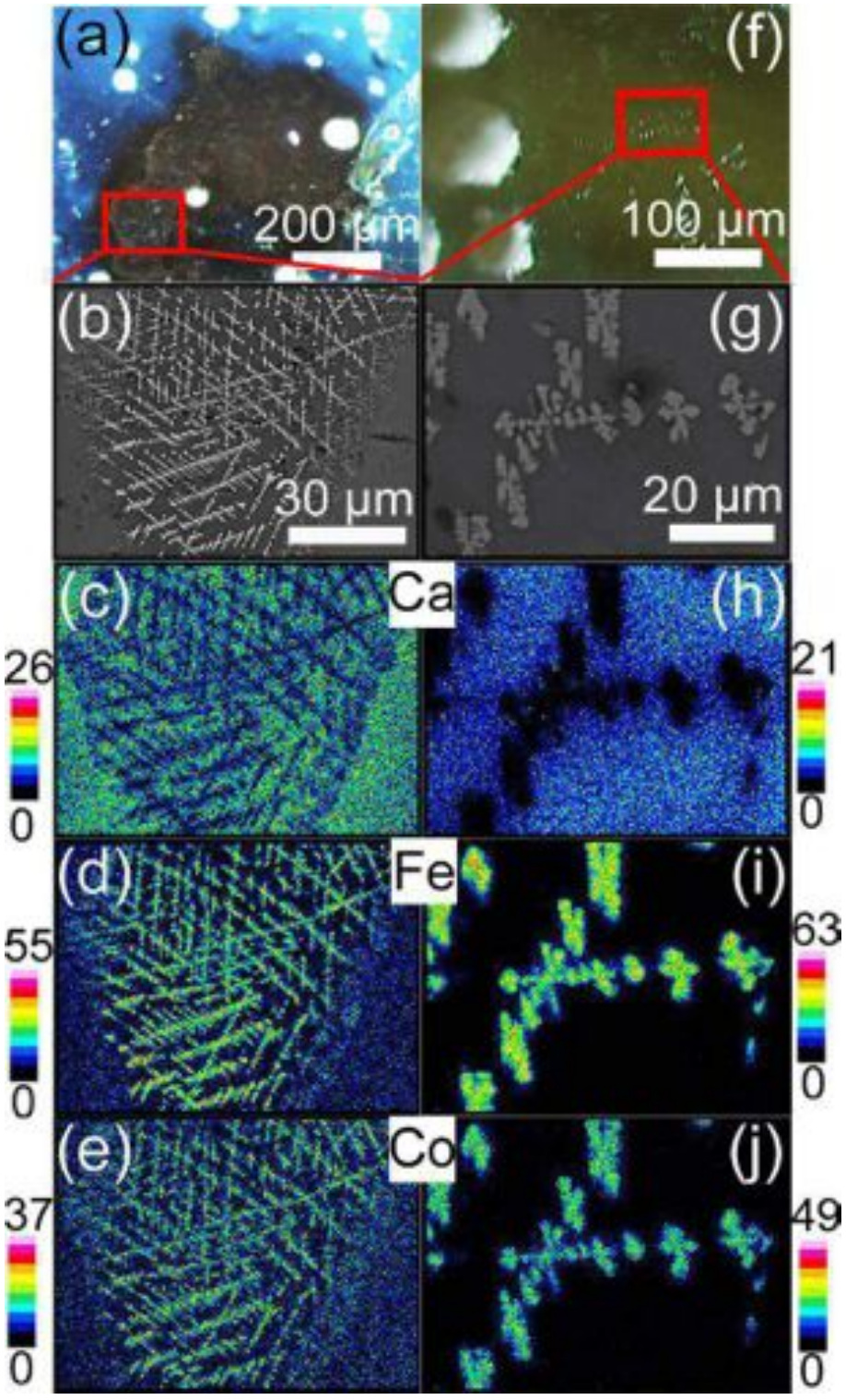

Figure 3.C.1 Optical images (a, f), SEM images (b, g) and the corresponding elemental maps (Ca (c, h), Fe (d, i), Co (e, j)) of YJ7 (left column) and YH1 (right column) samples respectively.

Raman spectroscopy was carried out to try to identify these crystals. Figure 3.C.2 shows one of the spectra recorded from YH-1 sample for which the Fe/Co ratio is close to 2. This spectrum is similar to the one of $CoFe_2O_4$ spinel crystal with 6 peaks at: 177 (T_{2g}), 327 (E_g), 479 (T_{2g}), 573 (T_{2g}), 641 (A_{1g}) and 705 (A_{1g}) cm^{-1} (Wang and Ren 2006; Chandramohan et al. 2011). The symmetry of $CoFe_2O_4$ structure is described as the space group $Fd\bar{3}m$ (No. 227) and the group theory predicts only five first order Raman active modes ($A_{1g} + E_g + 3T_{2g}$) (Gasparov et al. 2000). However, because of the cation exchange between octahedral and tetrahedral sites, some spinels exhibit the extra peak of A_{1g} symmetry. Indeed it was shown using *ab initio* calculations based on the density functional theory that the cation exchange in $MgAl_2O_4$ spinel gives rise to the additional Raman mode at 727 cm^{-1} (Lazzeri and Thibaudeau 2006). For $CoFe_2O_4$ this additional mode is around 620-640 cm^{-1} and this presence in the Raman spectrum indicates that a part of divalent cations (Co^{2+}) occupies octahedral site. Thus, the $CoFe_2O_4$ crystals of YH-1 sample are partially disordered. The modes above 600 cm^{-1} correspond to the modes of tetrahedral group while those below 600 cm-1 represent the modes of octahedral group (Chandramohan et al. 2011; Nongjai et al. 2012; Kumar et al. 2014).

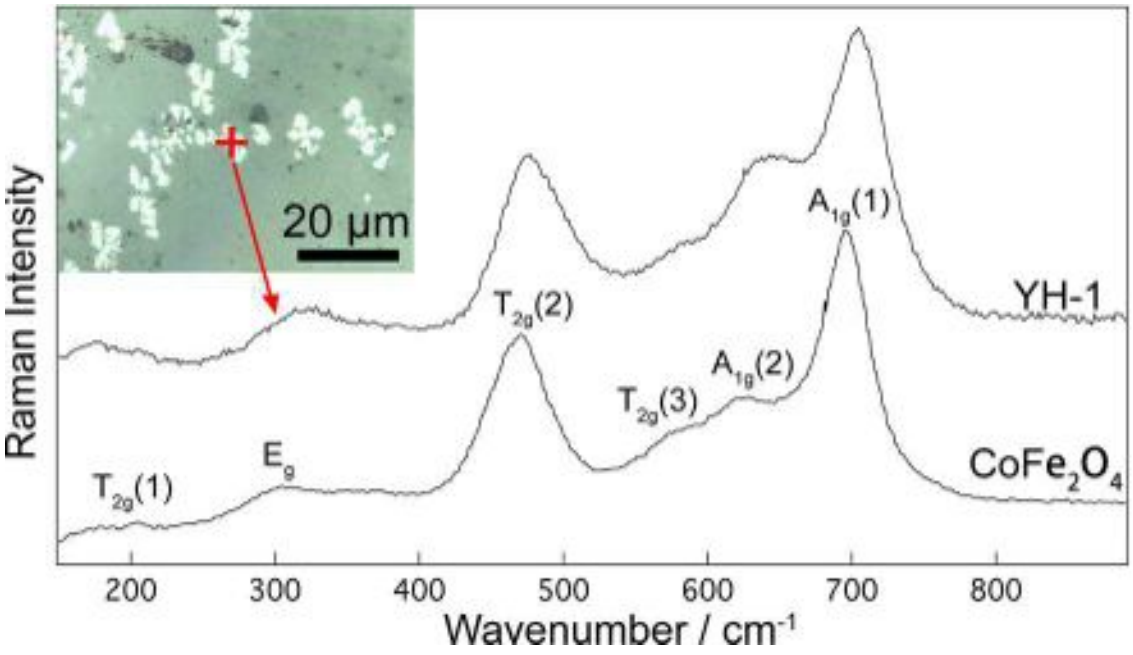

Figure 3.C.2 One of Raman spectra of the dendritic crystals observed in the sample YH-1 compared to the one of cobalt ferrite ($CoFe_2O_4$) crystal from reference (Wang and Ren 2006).

The spectra obtained for the other crystals for which we were able to measure

the Fe/Co ratio are shown in Figure 3.C.3. The sorting of spectra versus the value of ratio reveals an interesting evolution. All modes shift to low wavenumbers with the increase of ratio value while the relative intensity of $A_{1g}(2)$ extra mode change significantly. For the crystal with a ratio close to 1 (YJ-7), the two modes of A_{1g} symmetry have almost the same intensity while for the crystal with a ratio close to 3.9 (YH-7), the $A_{1g}(2)$ peak is hardly observed. In the paper focusing on the effect of Fe substitution in Co_3O_4 spinel structure, Bahlawane et al. showed the evolution of Co_3O_4 Raman spectrum versus the substitution rate (Bahlawane et al. 2009). The spectrum of the composition $Co_{1.42}Fe_{1.58}O_4$ (i.e. with Fe/Co=1.11) is very similar to the spectrum of YJ-7 sample (Figure 3.C.3) with two A_{1g} peaks of similar intensity. In their paper, compositions containing more Fe were not studied and we cannot use their results to interpret the other spectra. However, on the basis of SEM-EDS measurements we can consider that analyzed crystal of YH-8 sample corresponds also to an intermediate composition between Co_3O_4 and $CoFe_2O_4$ but with more Fe than YJ-7 sample ($Co_{1.2}Fe_{1.8}O_4$). The crystals with a ratio superior to 2 could be located in solid solution $CoFe_2O_4$-Fe_3O_4 and correspond to the compositions $Co_{0.9}Fe_{2.1}O_4$ (YJ-3), $Co_{0.85}Fe_{2.15}O4$ (YJ-5), $Co_{0.75}Fe_{2.25}O_4$ (YJ-1) and $Co_{0.6}Fe_{2.4}O_4$ (YH-7).

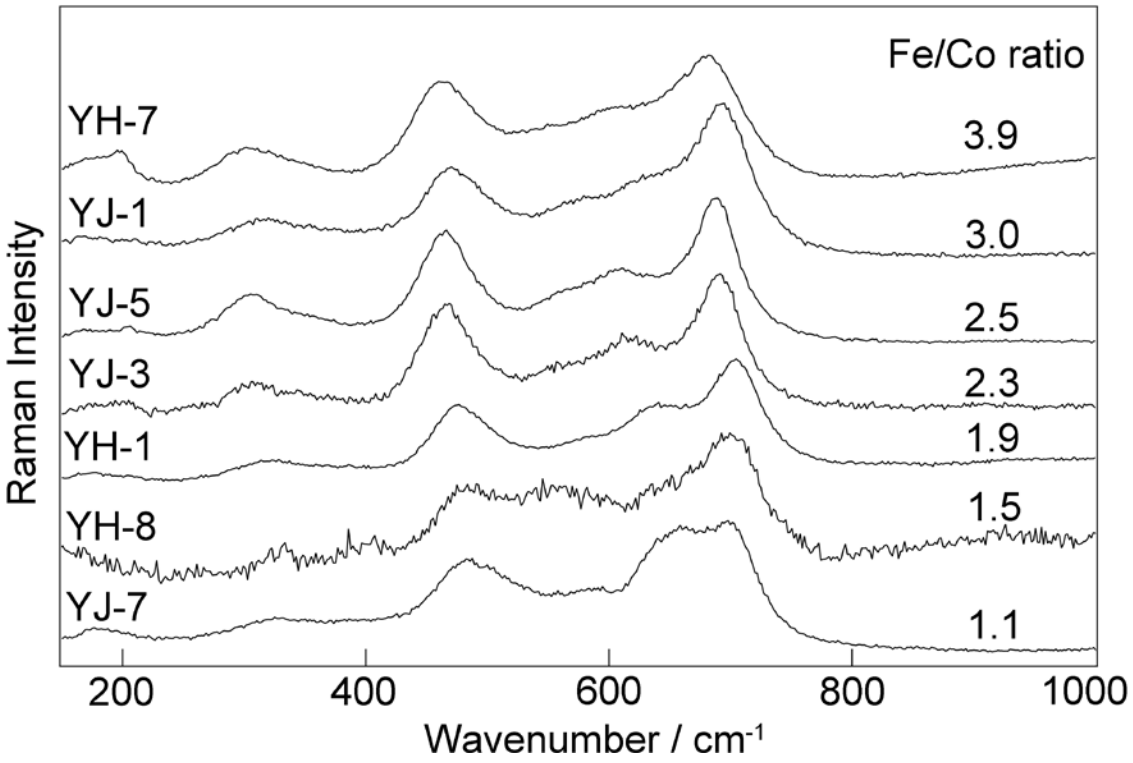

Figure 3.C.3 Comparison of Raman spectra of the spinel crystals from seven samples, for which the ratio Fe/Co were determined by SEM-EDS.

In Figure 3.C.4 and Figure 3.C.5, we drew the positions and FWHM of the main modes versus the iron rate (x) according to the formula $Co_{3-x}Fe_xO_4$. The evolution of the $T_{2g}(2)$ position is fairly linear with a negative slope corresponding to a rather shift of peak position to the low wavenumbers. The evolution of position of the two A_{1g} modes is not so linear. In fact the positions seem to shift slightly to the high wavenumbers for $x \leqslant 2$ and then to shift to the low wavenumbers. The inversion of behavior is more evident if one considers the relative position [$A_{1g}(1)$ - $T_{2g}(2)$] as shown in Figure 3.C.5. The FWHM are quite large in agreement with structural disorder (Figure 3.C.4). Only $A_{1g}(1)$ FWHM shows a significant evolution which could indicate an increase of disorder in octahedral site.

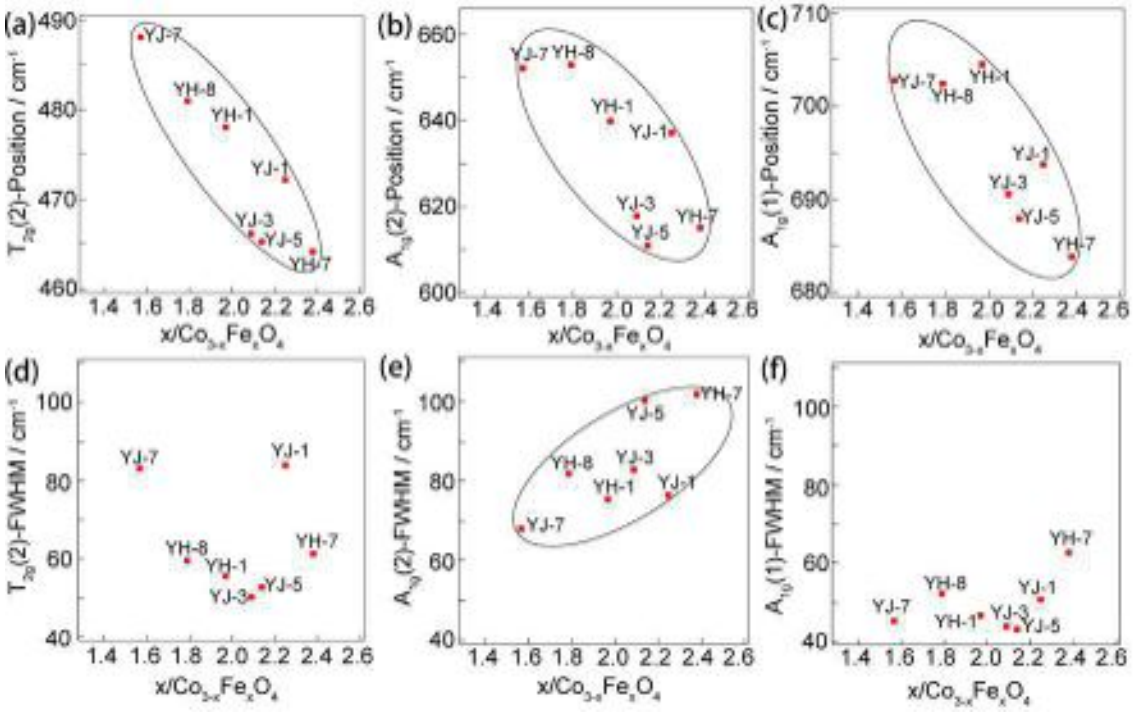

Figure 3.C.4 Graphical representations of $T_{2g}(2)$, $A_{1g}(2)$, and $A_{1g}(1)$ peak positions (a, b and c, respectively) and their full width at half maximum (FWHM) (d, e and f, respectively) versus the iron rate (x) according to the formula $Co_{3-x}Fe_xO_4$, respectively.

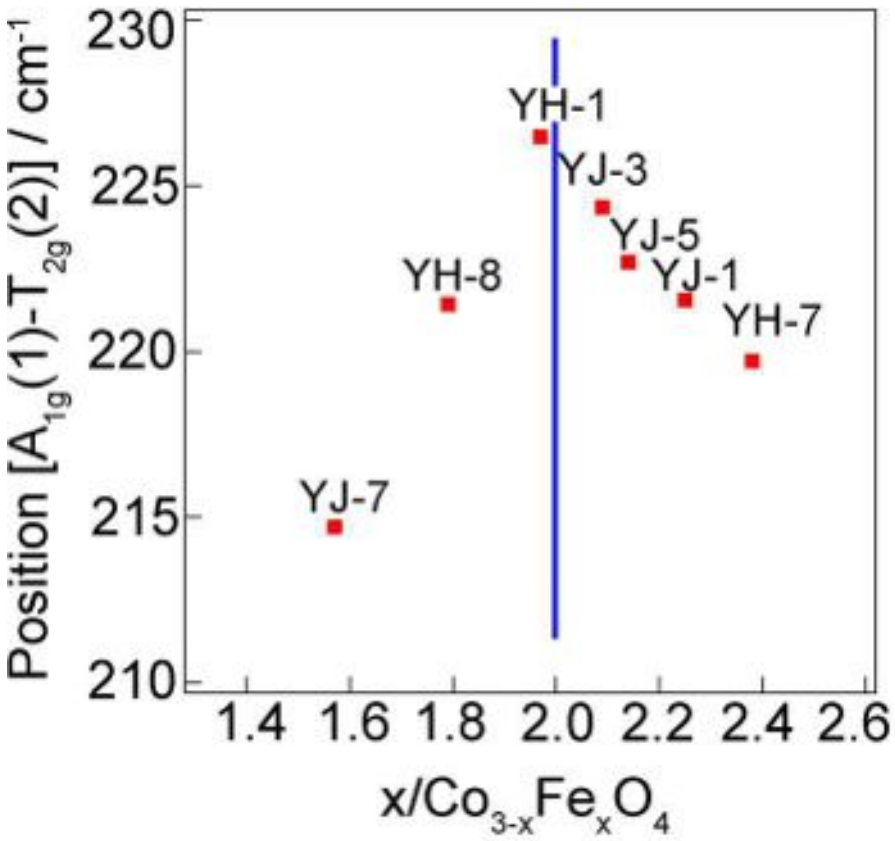

Figure 3.C.5 Plot of the difference of two main peaks $A_{1g}(1)$ and$T_{2g}(2)$ position versus the iron rate (x) according to the formula $Co_{3-x}Fe_xO_4$.

Raman spectra have been recorded from dendritic crystals too small to allow an accurate determination of Fe/Co ratio by SEM-EDS (Figure 3.C.6). These spectra are similar to the spectra previously shown and can be also attributed to $Co_{3-x}Fe_xO_4$ crystals. The histograms of $T_{2g}(2)$ and $A_{1g}(1)$ positions (Figure 3.C.7) reveal two types of populations. A main group, with $T_{2g}(2)$ and $A_{1g}(1)$ positions centered around 470 and 690 cm^{-1} respectively, formed by the crystals richer in iron, and a second group containing the crystals richer in cobalt. An analysis of the archeological data shows that there is no correlation between the archaeological groups and the composition of spinel crystals observed in the dark zones (Table 3.C.1). Spinels richer in iron were found as well in fragments of YJ group than in fragments of YH group and inversely spinels richer in cobalt were also found in a few fragments of the two groups (YJ-7, YH-1 and YH-8). For a few fragments, we have been able to analyze enough different crystals to show that the two populations could be present in the same sample, as shown in Figure 3.C.8, confirming the absence of correlation between the archaeological groups and the crystal compositions.

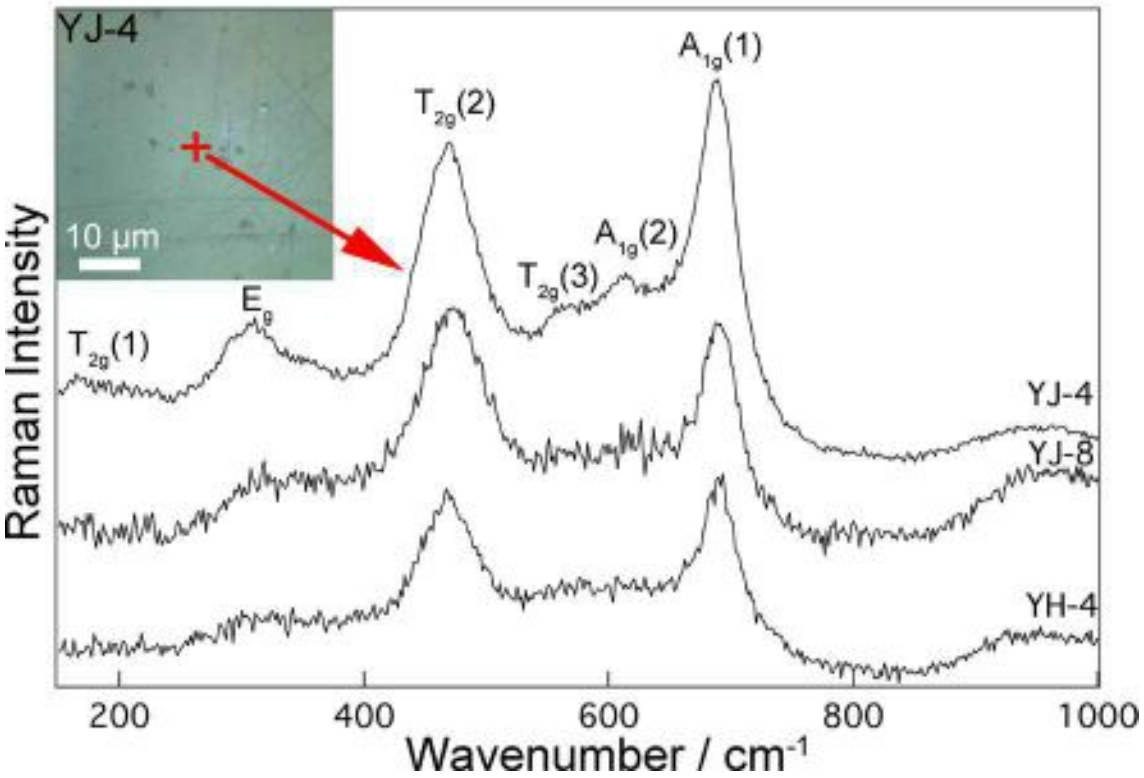

Figure 3.C.6 Raman spectra of cobalt ferrite crystals observed in sample YH-4, YJ-8 and YJ-4.

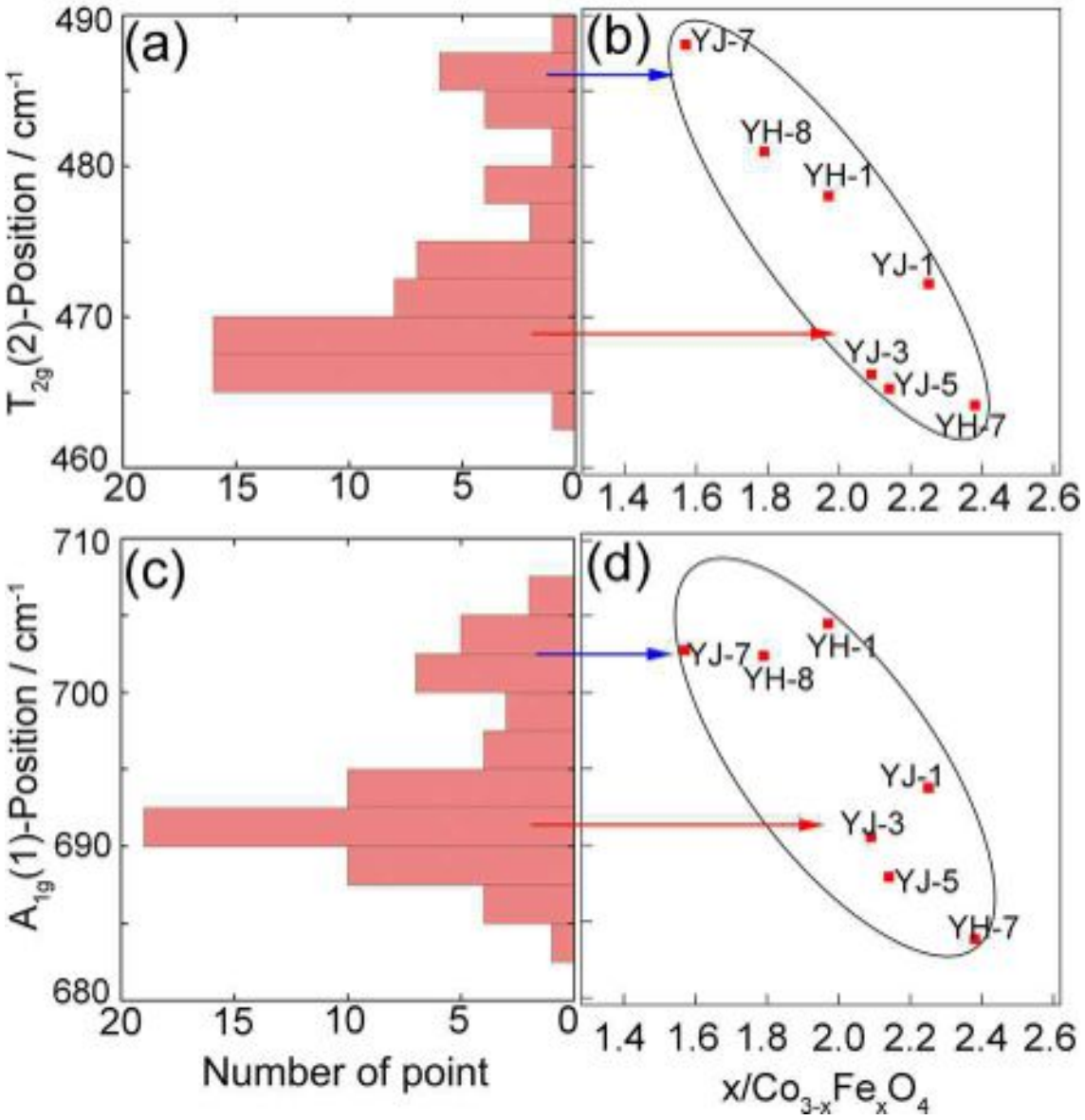

Figure 3.C.7 The histograms of $T_{2g}(2)$ and $A_{1g}(1)$ positions from all points analyzed by Raman spectra (a and c, respectively) compared to image of the $T_{2g}(2)$ and $A1_g(1)$ positions from seven samples versus the iron rate (x) according to the formula $Co_{3-x}Fe_xO_4$ (b and d, respectively).

	YJ-1	YJ-2	YJ-3	YJ-4	YJ-5	YJ-6	YJ-7	YJ-8	YH-1	YH-2	YH-3	YH-4	YH-5	YH-6	YH-7	YH-8	YG-1	YG-2	YG-3	YG-4	YG-5	YG-6
Spinel richer in Co							X		X							X						
Spinel richer in Fe	X		X	X	X			X	X			X			X	X						

Table 3.C.1 Two types of population of spinel crystals were found in ten samples (marked by cross): one type richer in Co and another type richer in Fe.

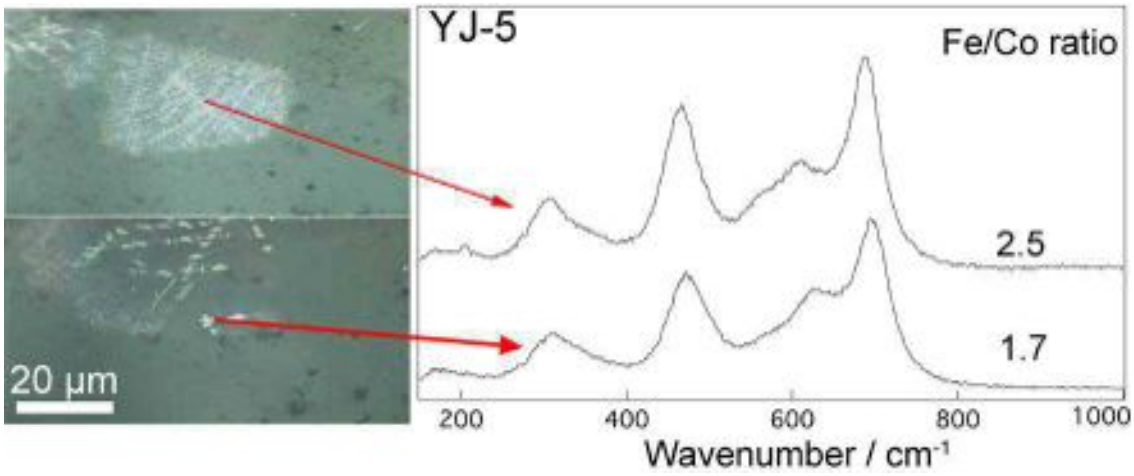

Figure 3.C.8 Raman spectra of cobalt ferrite crystals with different Fe/Co ratios observed in different zone of the sample YJ-5.

3.D Conclusion

Raman spectroscopy associated with SEM-EDS was successfully applied to study the blue decors of the Yuan Qinghua porcelain. We identified another type of spinel crystal containing Co in addition to Fe in the dark spots of blue decors, which was never found before in such porcelain. The investigations showed that these crystals had a spinel structure with a $Co_{3-x}Fe_xO_4$ composition ranging from x=1.4 to 2.4. The study of the composition distribution revealed two main crystal types: iron richer crystals (most numerous) with a composition centering around $Co_{0.8}Fe_{2.2}O_4$ and cobalt richer crystals centering around the $Co_{1.3}Fe_{1.7}O_4$ composition. On the basis of the studied corpus (22 samples) no correlation between spinel type and the archaeological group had be established. The results

also showed that the two types of spinel could be found in the same sample. The only observation that one can do concerns the dark zones: no dark zone was found among the 6 samples of the YG archaeological group while they were found in 3/4 and 1/2 samples of YJ and YH groups respectively. However the number and the size of analyzed samples are small and this conclusion could prove distortion.

The cobalt-based preparations of the Yuan period and, more precisely before the Ming Xuande era, are characterized by a higher iron concentration and a very few amount of manganese compared to the cobalt-based preparations made afterwards. These differences, could be explained why the black crystals of the Ming production have a composition close to $MnFe_2O_4$ and the ones of the Yuan productions are close to $CoFe_2O_4$. If it is proved, could be an interesting criterion to separate the productions before and after the Ming Xuande period but maybe also to help in finding counterfeit.

Inspired from these first results, I submitted a new proposal at ESRF combining SR-μ-XRF, FF-XANES and SR-μ-XRD. The proposal was accepted and the experiments were planned at the end of September 2016. Unfortunately, we had some problems in the sample preparation and the thin slices prepared for the experiments did not contain enough concentrated pigment zone. The data processing is in progress but it seems that we cannot expect as good results as for the Ming samples.

4 Reference

Bahlawane, N., Ngamou, P. H. T., Vannier, V., Kottke, T., Heberle, J., and Kohse-Höinghaus, K., 2009, Tailoring the properties and the reactivity of the spinel cobalt oxide, *Physical Chemistry Chemical Physics*, **11**(40), 9224–32.

Barilaro, D., Crupi, V., Majolino, D., Venuti, V., Barone, G., D'Acapito, F., Bardelli, F., and Giannici, F., 2007, Decorated pottery study: Analysis of pigments by x-ray absorbance spectroscopy measurements, *Journal of Applied Physics*, **101**(6), 064909.

Beijing Archaeological Insititute, 2007, *The Excavation Report of Ming Porcelain Pit in Maojiawan Archaeological Site*, Science Press.

Berry, A. J., O'Neill, H. S. C., Jayasuriya, K. D., Campbell, S. J., and Foran, G. J., 2003, XANES calibrations for the oxidation state of iron in a silicate glass, *American Mineralogist*, **88**(7), 967–77.

Bertrand, L., Bernard, S., Marone, F., Thoury, M., Reiche, I., Gourrier, A., Sciau, P., and Bergmann, U., 2016, Emerging approaches in synchrotron studies of materials from cultural and natural history collections, *Topics in Current Chemistry*, **374**(1), 1–39.

Calvin, S., 2013, *XAFS for Everyone*, CRC Press.

Chandramohan, P., Srinivasan, M. P., Velmurugan, S., and Narasimhan, S. V., 2011, Cation distribution and particle size effect on Raman spectrum of CoFe2O4, *Journal of Solid State Chemistry*, **184**(1), 89–96.

Charalambous, A. C., Sakalis, A. J., Kantiranis, N. A., Papadopoulou, L. C., Tsirliganis, N. C., and Stratis, J. A., 2010, Cypriot byzantine glazed pottery: A study of the Paphos Workshops, *Archaeometry*, **52**(4), 628–43.

Cheng, H. S., Zhang, Z. Q., Xia, H. N., Jiang, J. C., and Yang, F. J., 2002, Non-destructive analysis and appraisal of ancient Chinese porcelain by PIXE, *Nuclear Instruments and Methods in Physics Research Section B: Beam Interactions with Materials and Atoms*, **190**(1–4), 488–91.

Cheng, H. S., Zhang, Z. Q., Zhang, B., and Yang, F. J., 2004, The non-destructive identification of early Chinese porcelain by PIXE, *Nuclear Instruments and Methods in Physics Research Section B: Beam Interactions with Materials and Atoms*, Proceedings of the Sixteenth International Conference on Ion

Beam Analysis, **219–220**, 16–9.

Cheng, H. S., Zhang, B., Zhu, D., Yang, F. J., Sun, X. M., and Guo, M. S., 2005, Some new results of PIXE study on Chinese ancient porcelain, *Nuclear Instruments and Methods in Physics Research*, **240**(1–2), 527–31.

Cianchetta, I., Trentelman, K., Maish, J., Saunders, D., Foran, B., Walton, M., Sciau, P., Wang, T., Pouyet, E., Cotte, M., Meirer, F., Liu, Y., Pianetta, P., and Mehta, A., 2015, Evidence for an unorthodox firing sequence employed by the Berlin Painter: Deciphering ancient ceramic firing conditions through high-resolution material characterization and replication, *Journal of Analytical Atomic Spectrometry*, **30**(3), 666–76.

Colomban, P., 2003, Polymerization degree and Raman identification of ancient glasses used for jewelry, ceramic enamels and mosaics, *Journal of Non-Crystalline Solids*, Natural Glasses 4: Glasses in Geosciences, Environmental Sciences and Archeometry, **323**(1–3), 180–7.

Colomban, P., Milande, V., and Lucas, H., 2004a, On-site Raman analysis of Medici porcelain, *Journal of Raman Spectroscopy*, **35**(1), 68–72.

Colomban, P., Sagon, G., Huy, L. Q., Liem, N. Q., and Mazerolles, L., 2004b, Vietnamese (15th Century) Blue-And-White, Tam Thai and Lustre porcelains/stonewares: glaze composition and decoration techniques*, *Archaeometry*, **46**(1), 125–36.

Colomban, P., 2004, Raman spectrometry, a unique tool to analyze and classify ancient ceramics and glasses, *Applied Physics A*, **79**(2), 167–70.

Colomban, P., 2013, Rocks as blue, green and black pigments/dyes of glazed pottery and enamelled glass artefacts – A review, *European Journal of Mineralogy*, **25**(5), 863–79.

Cotte, M., Susini, J., Dik, J., and Janssens, K., 2010, Synchrotron-based X-ray absorption spectroscopy for art conservation: looking back and looking forward, *Accounts of Chemical Research*, **43**(6), 705–14.

Coutinho, M. L., Muralha, V. S. F., Mirao, J., and Veiga, J. P., 2014, Non-destructive characterization of oriental porcelain glazes and blue underglaze pigments using μ-EDXRF, μ-Raman and VP-SEM, *Applied Physics a-Materials Science & Processing*, **114**(3), 695–703.

Cowell, M., and Zhang, F., 2001, *In Catalogue of Late Yuan and Ming ceramics in*

the British Museum (ed. J. Harrison-Hall), British Museum Press, London.

Du, F., and Su, B., 2008, Further study of sources of the imported cobalt-blue pigment used on Jingdezhen porcelain from late 13 to early 15 centuries, *Science in China Series E: Technological Sciences*, **51**(3), 249–59.

Fayard, B., Pouyet, E., Berruyer, G., Bugnazet, D., Cornu, C., Cotte, M., Andrade, V. D., Chiaro, F. D., Hignette, O., Kieffer, J., Martin, T., Papillon, E., Salomé, M., and Sole, V. A., 2013, The new ID21 XANES full-field end-station at ESRF, *Journal of Physics: Conference Series*, **425**(19), 192001.

Fehrvri, G., 2000, *Ceramics of the Islamic World*, I.B.Tauris.

Figueiredo, M. O., Silva, T. P., and Veiga, J. P., 2012, A XANES study of cobalt speciation state in blue-and-white glazes from 16th to 17th century Chinese porcelains, *Journal of Electron Spectroscopy and Related Phenomena*, **185**(3–4), 97–102.

Frahm, E., 2014, Scanning electron microscopy (SEM): Applications in archaeology, In *Encyclopedia of Global Archaeology* (ed. C. Smith), 6487–95, Springer New York.

Gasparov, L. V., Tanner, D. B., Romero, D. B., Berger, H., Margaritondo, G., and Forró, L., 2000, Infrared and Raman studies of the Verwey transition in magnetite, *Physical Review B*, **62**(12), 7939–44.

Genin, M., 2007, *La Graufesenque, Millau, Aveyron. Volume II, Volume II,* Éditions de la Fédération Aquitania, Pessac.

Giuli, G., Paris, E., Pratesi, G., Koeberl, C., and Cipriani, C., 2003, Iron oxidation state in the Fe-rich layer and silica matrix of Libyan Desert Glass: A high-resolution XANES study, *Meteoritics & Planetary Science*, **38**(8), 1181–6.

Henderson, G., Neuville, D., and Downs, R., 2014, *Spectroscopic Methods in Mineralogy and Material Sciences*, Walter de Gruyter GmbH & Co KG.

Huang, Y., and Huang, B., 2006, The firing process of Yuan Dynasty Jingdezhen porcelain (First part), *Collection* (12), 54–5.

Huang, Y., and Huang, B., 2007a, The firing process of Yuan Dynasty Jingdezhen porcelain (Second part), *Collection* (01), 48–50.

Huang, Y., and Huang, B., 2007b, The firing process of Yuan Dynasty Jingdezhen porcelain (Third part), *Collection* (02), 39–41.

Hunault, M., Calas, G., Galoisy, L., Lelong, G., and Newville, M., 2014, Local ordering around tetrahedral Co^{2+} in silicate glasses, *Journal of the American Ceramic Society*, **97**(1), 60–2.

Impey, O. R., 1977, *Chinoiserie: the impact of Oriental styles on Western art and decoration*, Scribner.

Janssens, K., Vittiglio, G., Deraedt, I., Aerts, A., Vekemans, B., Vincze, L., Wei, F., De Ryck, I., Schalm, O., Adams, F., Rindby, A., Knöchel, A., Simionovici, A., and Snigirev, A., 2000, Use of microscopic XRF for non-destructive analysis in art and archaeometry, *X-Ray Spectrometry*, **29**(1), 73–91.

Kim, M. G., and Yo, C. H., 1999, X-ray Absorption spectroscopic study of chemically and electrochemically Li ion extracted $Li_yCo_{0.85}Al_{0.15}O_2$ Compounds, *The Journal of Physical Chemistry B*, **103**(31), 6457–65.

Kock, L. D., and De Waal, D., 2007, Raman studies of the underglaze blue pigment on ceramic artefacts of the Ming dynasty and of unknown origins, *Journal of Raman Spectroscopy*, **38**(11), 1480–7.

Kumar, A., Sharma, P., and Varshney, D., 2014, Structural, vibrational and dielectric study of Ni doped spinel Co ferrites: $Co_{1-x}Ni_xFe_2O_4$ (x=0.0, 0.5, 1.0), *Ceramics International*, **40**(8, Part B), 12855–60.

Lazzeri, M., and Thibaudeau, P., 2006, Raman spectrum of the normal and disordered $MgAl_2O_4$ spinel, *Physical Review B*, **74**(14), 140301.

Leon, Y., Lofrumento, C., Zoppi, A., Carles, R., Castellucci, E. M., and Sciau, P., 2010, Micro-Raman investigation of terra sigillata slips: a comparative study of central Italian and southern Gaul productions, *Journal of Raman Spectroscopy*, **41**(11), 1550–5.

Li, J. Z., 1998, *History of science and technology in China, Ceramics Volume*, Science Press, Beijing.

Li, X.-H., 2015, History and craft of Chinese export underglaze blue and white porcelain, *Ceramics-Technical*(40), 82–7.

Llusar, M., Forés, A., Badenes, J. A., Calbo, J., Tena, M. A., and Monrós, G., 2001, Colour analysis of some cobalt-based blue pigments, *Journal of the European Ceramic Society*, **21**(8), 1121–30.

Majumdar, S., Peralta-Videa, J. R., Castillo-Michel, H., Hong, J., Rico, C. M., and Gardea-Torresdey, J. L., 2012, Applications of synchrotron μ-XRF to study the distribution of biologically important elements in different environmental matrices: A review, *Analytica Chimica Acta*, **755**, 1–16.

Maurizio, C., El Habra, N., Rossetto, G., Merlini, M., Cattaruzza, E., Pandolfo, L., and Casarin, M., 2010, XAS and GIXRD study of Co sites in $CoAl_2O_4$ layers grown by MOCVD, *Chemistry of Materials*, **22**(5), 1933–42.

Meirer, F., Liu, Y., Pouyet, E., Fayard, B., Cotte, M., Sanchez, C., Andrews, J. C., Mehta, A., and Sciau, P., 2013, Full-field XANES analysis of Roman ceramics to estimate firing conditions—A novel probe to study hierarchical heterogeneous materials, *Journal of Analytical Atomic Spectrometry*, **28**(12), 1870–83.

Monari, G., and Manfredini, T., 1996, Coloring effects of synthetic inorganic cobalt pigments in fast-fired porcelainized tiles (ed. J. B. W. Jr), 167–72, John Wiley & Sons, Inc., Hoboken, NJ, USA.

Monico, L., Van der Snickt, G., Janssens, K., De Nolf, W., Miliani, C., Dik, J., Radepont, M., Hendriks, E., Geldof, M., and Cotte, M., 2011, Degradation process of lead chromate in paintings by Vincent van Gogh studied by means of synchrotron X-ray spectromicroscopy and related methods. 2. Original Paint Layer Samples, *Analytical Chemistry*, **83**(4), 1224–31.

Moore, N. H., 2009, *Delftware Dutch and English*, BiblioLife.

Nongjai, R., Khan, S., Asokan, K., Ahmed, H., and Khan, I., 2012, Magnetic and electrical properties of In doped cobalt ferrite nanoparticles, *Journal of Applied Physics*, **112**(8), 084321-8.

Pisano, R., 2015, *A Bridge Between Conceptual Frameworks: Sciences, Society and Technology Studies*, Springer.

Qiu, H., and Chen, M., 2009, The art of blue and white porcelain: origin and development, *Ceramic Studies Journal*(01), 21–4.

Qu, Y., Xu, J., Xi, X., Huang, C., and Yang, J., 2014, Microstructure characteristics of blue-and-white porcelain from the folk kiln of Ming and Qing Dynasties, *Ceramics International*, **40**, 8783–90.

Robinet, L., Spring, M., Pagès-Camagna, S., Vantelon, D., and Trcera, N., 2011, Investigation of the discoloration of smalt pigment in historic paintings by

micro-X-ray absorption spectroscopy at the Co K-Edge, *Analytical Chemistry*, **83**(13), 5145–52.

Tite, M. S., Freestone, I. C., and Bimson, M., 1984, A technological study of Chinese porcelain of the Yuan dynasty, *Archaeometry*, **26**(2), 139–54.

Wang, L., and Wang, C., 2011, Co speciation in blue decorations of blue-and-white porcelains from Jingdezhen kiln by using XAFS spectroscopy, *Journal of Analytical Atomic Spectrometry*, **26**(9), 1796–801.

Wang, W. H., and Ren, X., 2006, Flux growth of high-quality $CoFe_2O_4$ single crystals and their characterization, *Journal of Crystal Growth*, **289**(2), 605–8.

Watt, J. C. Y., 1979, Notes on the use of cobalt in later Chinese Ceramics, *Ars Orientalis*, **11**, 63–85.

Wen, R., Wang, C. S., Mao, Z. W., Huang, Y. Y., and Pollard, A. M., 2007, The chemical composition of blue pigment on Chinese blue-and-white porcelain of the Yuan and Ming dynaties (ad 1271–1644)*, *Archaeometry*, **49**(1), 101–15.

Wood, N., 1999, *Chinese Glazes: Their origins, chemistry, and recreation*, University of Pennsylvania Press.

Wood, N., Tite, M. S., Doherty, C., and Gilmore, B., 2007, A technological examination of ninth–tenth century ad abbasid blue-and-white ware from Iraq, and its comparison with eighth century ad Chinese blue-and-white Sancai ware*, *Archaeometry*, **49**(4), 665–84.

Wu, J., Leung, P. L., and Li, J. Z., 2007, A study of the composition of Chinese blue and white porcelain, *Studies in Conservation*, **52**(3), 188–98.

Yaocheng, C., Yanyi, G., and Hong, C., 1994, Sources of cobalt pigment used in Yuan blue and white porcelain wares, *Oriental art*, **40**(1), 14–9.

Yu, K. N., and Miao, J. M., 1996, Non-destructive analysis of Jingdezhen blue and white porcelains of the Ming dynasty using EDXRF, *X-Ray Spectrometry*, **25**(6), 281–5.

Zhu, J., Luo, W., Chen, D., Xu, W., Ming, C., Wang, C., and Wang, L., 2013, New insights into the role of Mn and Fe in coloring origin of blue decorations of blue-and-white porcelains by XANES spectroscopy, *Journal of Physics Conference Series*, **430**, 012066.

Zhu, T., Ding, X., Kusimba, C. M., and Feng, Z., 2015a, Using laser ablation inductively coupled plasma mass spectroscopy (LA-ICP-MS) to determine the provenance of the cobalt pigment of Qinghua porcelain from Jingdezhen in Yuan Dynasty of China (1271–1368AD), *Ceramics International*, **41**(8), 9878–84.

Zhu, T. Q., Zhang, Y. C., Xiong, H., Feng, Z. Y., Li, Q., and Cao, B. L., 2015b, Comparison of the different types of Qinghua porcelain from Jingdezhen in the Yuan dynasty of China (ad 1271–1368) by micro X-ray fluorescence spectroscopy (μ-XRF) and microscopy, *Archaeometry*. DOI: 10.1111/arcm.12215p

Zumbulyadis, N., 2006, *Meissen's blue and white Porcelain: Dining in royal splendor*, Schiffer Publishing, Limited.

Zuo, J., Du, G., Wu, R., and Wang, C., 2007, Study of Ming Yongle Qinghua porcelains using Raman spectroscopy, *The Journal of Light Scattering*, **19**(4), 395–9.

Chapter V General summary and perspectives

1 General summary

The multi-scale approach developed in this work is efficient to study the complex and heterogeneous structure of ancient ceramics. Through designing different methodological strategies, I successfully applied the approach for studying different ancient ceramics.

The first one concerned Roman marbled terra sigillata. The previous work had shown that the yellow compound of the slip was obtained from Ti-rich clay and its color originates from pseudobrookite crystals (Leon et al. 2010). However, pure pseudobrooktie is brown and not stable. Hence, my work was focused on the structural characteristics of the pseudobrookite crystals and to finally decipher the structure of the yellow compound. I firstly selected SR-μ-XRF and FF-XANES to systematically analyze the elemental composition and Ti-based phases, respectively. The results allowed locating the analytical zone rich in pseudobrookite crystals. Then, I used Raman spectroscopy to investigate the nature of the crystals. The results showed that the pseudobrookite crystals are substituted, i.e. transition elements (Fe and/or Ti) could be substituted by lighter atoms (Mg and/or Al) to tune the color of pure Fe_2TiO_5 (brown) to be a lighter color (yellow). Through increasing the disorder and thus enlarging the number of electronic configurations, the substitution increases the stability of pseudobrookite structure.

The second one concerned the firing protocol of Attic potteries. I tried to discover new possible firing protocol based on previous assumptions. Since the iron state is sensitive to firing process, I mainly selected FF-XANES associated with Raman spectroscopy to investigate the speciation and distribution of iron oxides in the slip. Before that, EPMA and SEM-EDS were firstly selected to analyze elemental composition in order to verify the category of the samples. Based on the data, we reconstructed the firing process, which was in agreement with the previous once-firing assumption but some of them i.e. the first oxidizing stage was at higher temperature or for others that the second stage (reduction) was more or less reducing.

The third one concerned the blue decors of Chinese Qinghua porcelains from two different periods: the mid-Ming dynasty (from the Ming Chenghua to Zhengde era, late 15th to early 16th century) and the Yuan dynasty (13th to early 14th century). For the former, my work was focused on obtaining an integrate aspect of the origin of the blue decors. I mainly selected FF-XANES and SR-μ-XANES to study the speciation (formal valence and coordination) of cobalt elements and the distributions of different species. Before that, I firstly used SR-μ-XRF to study the Co distribution and to locate the zone to be analyzed by FF-XANES and SR-μ-XANES. Finally, I used SR-μ-XRD to confirm the presence of the well-crystalized zone. The results showed that the blue color is attributed to Co^{2+}

in tetrahedral site and the formation of cobalt aluminate ($CoAl_2O_4$) plays a key role in hue variations. In addition, Mn plays a key role in darkening the blue decors and even enables some sample to be black in the absence of $CoAl_2O_4$ particles. For the Yuan productions, since the previous researches have been rare (Wen et al. 2007; Wu et al. 2007; Wang and Wang 2011), my work was focused on completing the fundamental information concerning the blue decors. I selected Raman spectroscopy combined with SEM-EDS to investigate the nature of the crystals present in blue decors. The results shown that the dendritic $CoFe_2O_4$ crystals are main constituent of the dark zone of the blue decors. It is the first time that these crystals were observed as the main constituent of the dark spots in blue decors. Inspiring on the primarily information, the further work is continued.

In summary, using a sampling strategy and combining a few numbers of different techniques, it is possible to rebuild partially the complex structure of an ancient ceramic and thus to obtain interesting information concerning manufacturing process and/or optical properties. The choice of analytical zone (or volume) is crucial and determines directly the nature of the obtained information. The choice of techniques determines the resolution (spatial and spectral) and the scale. The difficulty of the approach is directly linked to these choices, which must be done concerning the previous studies but also in function of the study aims. The method is highly dependent on the experimenter choices but it is an interesting alternative to a scan of a large volume (several mm^3 in the case of ceramics) of sample at high resolution allowing reconstructing entirely its structure and composition in details.

I showed that this approach is well suited for the study of ancient ceramics and could be used to better understand the nature of various colors and the manufacturing process of colored porcelains produced during the Tang dynasty (7^{th} - 10^{th} c. AD), for example. These porcelains present three colors (brown, yellow and green) as shown in Figure 2.1. Only a few researches have carried out investigations of the decors (Zhang and Guo 1985; Lin et al. 1999) and a thorough knowledge of the structure of decors would be very useful to better understand their color variation and their manufacturing processes. The first results revealed a complex in depth distribution of iron oxides (α-Fe_2O_3, ε-Fe_2O_3) from the surface to the body/glass interface with formation of dendritic at the surface (Figure 2.2).

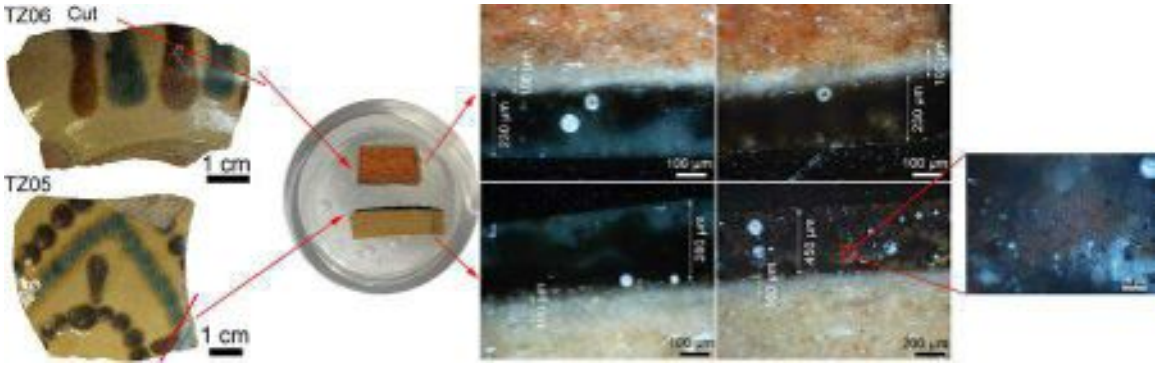

Figure 2.1 Colored porcelains of Tang dynasty (Sample TZ05 and TZ06).

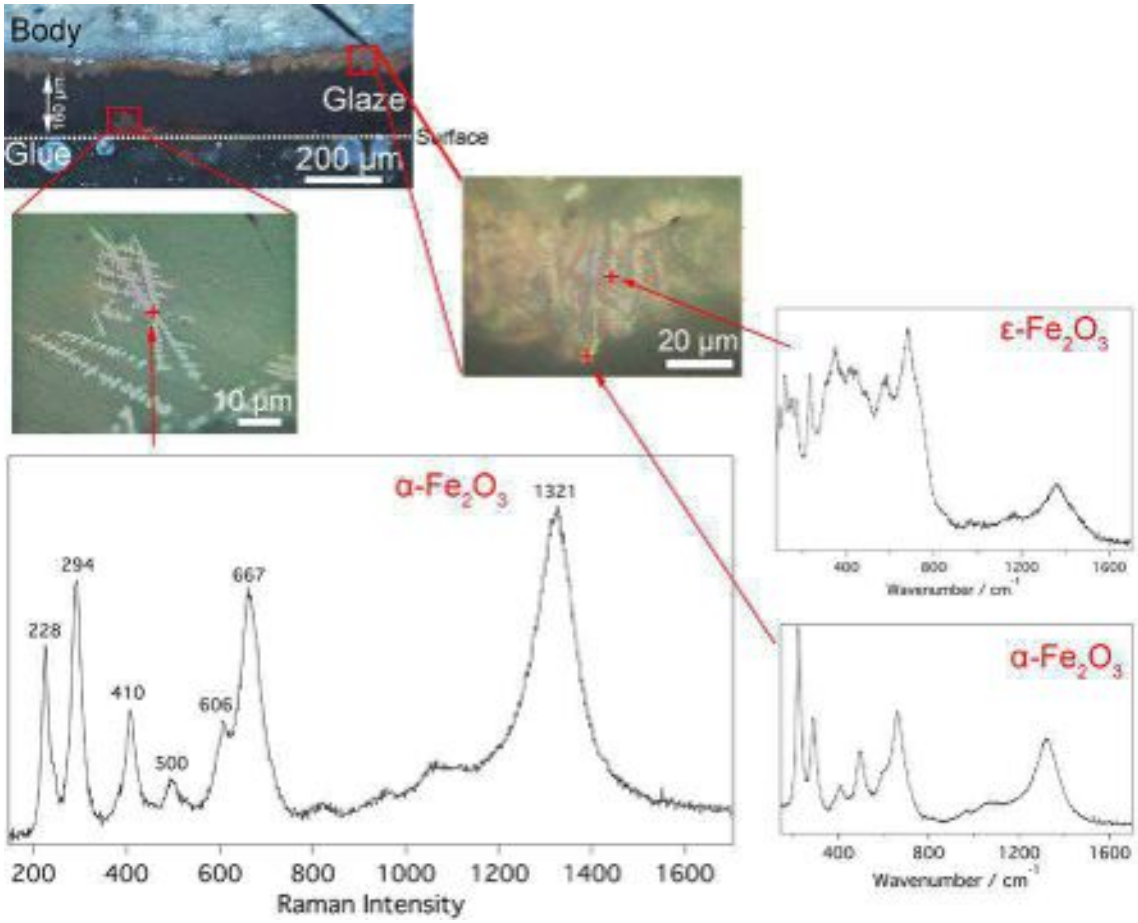

Figure 2.2 Results of Raman analyses performed on the red color zone of the glaze (Sample TZ02).

2 Perspectives

On the one hand, specific to the different cases investigated in this work, some issues need to be further studied. For the marbled terra sigillata, the yellow pigment is proved to be due to the presence of pseudobrookite particles. These particles are substituted by Al and/or Mg to improve their stability. The speciation of substitutions needs to be verified by further investigations, such as transmission electron microscopy. For the Attic pottery, the firing process of fragments with both single layer and double layer was investigated and proved to be consistent with the model of J.V. Noble 1960. However, the fragments with double layer can be also produced by complex firing and based on our samples we cannot conform or reject the complex firing. Therefore, the next work is to select the samples with both black slip and red slip on the surface to be analyzed by the same method strategy proposed in this work. For the Ming Chinese *Qinghua* porcelains, our work shown that the blue color of decorations is due to Co in tetragonal coordination, especially, $CoAl_2O_4$ particles and the particles are partially substituted. The speciation of substitutions needs to be verified by further investigations, such as transmission electron microscopy. Besides, the black color is proved to be due to Mn. The distribution of Mn was analyzed and the mineral structure of Mn needs to be further studied. In addition, our work was only focused on four typical Ming fragments and proposed a specific method strategy to analyze the structure of blue decors. The next work is to use the method strategy to investigate more fragments and conclude more general information concerning the blue decors. For the Yuan Chinese *Qinghua* porcelains, using the combination of Raman spectroscopy and SEM-EDS, we get information concerning the black spots and the blue decors need to be further analyzed by the multi-analytical synchrotron radiation based method strategy form a significant zone.

Besides, the approach proposed in this work is a practical method to reconstruct the structure of ancient ceramics by partially obtained data and thus to deduce the information concerning manufacturing process. But the difficulties of this approach are the choice of sampling strategy and the choice of analytical techniques. These choices must be done according to previous studies and in function of the aims, which requires experimenters not only know well the archaeological background of ancient ceramics but also know well the characteristics of available analytical techniques using in modern material science, including not only the “standard” techniques, such as EPMA, SEM-EDS, Raman spectroscopy, etc., but also the “latest” techniques, such as synchrotron based tomography with high resolution (nm). However, it is a big challenge both for traditional archaeologists and traditional modern material physicists. Therefore, to overcome this challenge, we need to make efforts to construct a bridge between the archaeometry and modern material science and to find common interests

between archaeologists and material scientists. On the one hand, archaeologists try to use modern science material science to solve the archaeological issues. Reciprocally, through analyze ancient cultural artifact, material scientists try to provide inspiring ideas to modern material science. For example, the combination of transmission electron microscopy, Raman spectroscopy and X-ray diffraction techniques was successfully used to identify the presence of iron oxides (ε-Fe_2O_3) in the lustrous black glaze of ancient Jian wares and through deciphering technologies behind the fabrication, one can thus potentially help researchers improve the ε-Fe_2O_3 synthesis (Dejoie et al. 2014).

3 Reference

Dejoie, C., Sciau, P., Li, W., Noé, L., Mehta, A., Chen, K., Luo, H., Kunz, M., Tamura, N., and Liu, Z., 2014, Learning from the past: Rare ε-Fe_2O_3 in the ancient black-glazed Jian (Tenmoku) wares, *Scientific Reports*, **4**.

Leon, Y., Sciau, P., Goudeau, P., Tamura, N., Webb, S., and Mehta, A., 2010, The nature of marbled terra sigillata slips: a combined μXRF and μXRD investigation, *Applied Physics A*, **99**(2), 419–25.

Lin, E. K., Yu, Y. C., Wang, C. W., Liu, T. Y., Wu, C. M., Chen, K. M., and Lin, S. S., 1999, PIXE analysis of ancient Chinese Changsha porcelain, *Nuclear Instruments & Methods in Physics Research Section B-Beam Interactions with Materials and Atoms*, **150**(1-4), 581–5.

Wang, L., and Wang, C., 2011, Co speciation in blue decorations of blue-and-white porcelains from Jingdezhen kiln by using XAFS spectroscopy, *Journal of Analytical Atomic Spectrometry*, **26**(9), 1796–801.

Wen, R., Wang, C. S., Mao, Z. W., Huang, Y. Y., and Pollard, A. M., 2007, The Chemical composition of blue pigment on Chinese blue and white porcelain of the Yuan and Ming dynaties (ad 1271–1644)*, *Archaeometry*, **49**(1), 101–15.

Wu, J., Leung, P. L., and Li, J. Z., 2007, A study of the composition of Chinese blue and white Porcelain, *Studies in Conservation*, **52**(3), 188–98.

Zhang, Z., and Guo, Y., 1985, A study on Changsha Tongguan coloured glaze and painted wares, *Journal of Jingdezhen Ceramic Institue*, **6**(1), 11–7.

Appendix

Appendix 1 Archaeological details of the fragments of Roman marbled terra sigillata.

Appendix 2 Photographs of the fragment of marbled terra sigillata.

Appendix 3 Quantitative elemental composition (wt%) obtained by electronic microprobe on the yellow slips of 17 sherds (excavated in Narbonne).

Appendix 4 Archaeological details of the Attic ceramics (excavated at Lattes, France).

Appendix 5 Photographs of the first type of the Greek ceramics (Attic sherds excavated at Lattes, France).

Appendix 6 Quantitative elemental composition (wt%) obtained by electronic microprobe on the slips of Attic sherds (excavated in Lattes, France).

Appendix 7 Archaeological details of the Yuan fragments.

Appendix 8 Photographs of the Yuan fragments.

Appendix 1 Archeaological details of the fragments of Roman marbled terra sigillata.

	Remarks1	Category	Excavated site	Period	Remarks2
PHS2012-CS06	N92835 (P13)	Marbled terra sigillata	La Nautique (port)	40-60 AD	O PASSEN
PHS2012-CS07	N91b Primus		La Nautique (port)	40-60 AD	Primus [OFIC.]
PHS2012-CS08	N92 P13 836		La Nautique (port)	40-60 AD	
PHS2012-CS09	P15		La Nautique (port)	40-60 AD	SECVNDI hybride R8/D27
PHS2012-CS10			La Nautique (port)	40-60 AD	
PHS2012-CS11			La Nautique (port)	40-60 AD	
PHS2012-CS12	Ci 27-7C-345		Clos de la Lombarde	30-100 AD	
PHS2012-CS13	Ci 95-III.9		Clos de la Lombarde	30-100 AD	
PHS2012-CS15	Ci 93. 32-83		Clos de la Lombarde	90-150 AD	
PHS2012-CS16	Ci 94-RA-36		Clos de la Lombarde	60-160 AD	
PHS2012-CS17	Ci 32-93-83		Clos de la Lombarde	15-60 AD	
PHS2012-CS18	Ci 23-7C-49		Clos de la Lombarde	30-100 AD	
PHS2012-CS19	Ci 95-III.29		Clos de la Lombarde	30-100 AD	
PHS2012-CS20	Ci 95-III.29		Clos de la Lombarde	70-120 AD	
PHS2012-CS21	Ci 94-RA-36		Clos de la Lombarde	70-120 AD	
PHS2012-CS22	Ci 98-10002		Clos de la Lombarde	70-120 AD	
PHS2012-CS23	US3095		CAT	70-80 AD	
PHS2012-CS24	US3093/3095		CAT	70-80 AD	
PHS2012-CS25	US3093/3095		CAT	70-80 AD	
PHS2012-CS26	US3093/3095		CAT	70-80 AD	
PHS2012-CS27	US3115		CAT	70-80 AD	
PHS2012-CS28	US3115		CAT	70-80 AD	
PHS2012-CS29	US3115		CAT	70-80 AD	

	Remarks	Excavated site	Category	Period
TSGM-B	G.77 S.92	La Graufesenque site, France	Marbled terra sigillata	40-60 AD
TSGM-C	G.77 S.92			40-60 AD
TSGM-D	G.25 T.23			40-60 AD
TSGM-E				40-60 AD
TSGM-F	1-G74-U66-2			40-60 AD
TSGM-H	3-G.73 HS			40-60 AD
TSGM-I	4-G.80 S.93			40-60 AD
TSGM-J	5-G.77 S.93			40-60 AD
TSGM-L	7-G.78 S.83			40-60 AD
TSGM-M	8-G.77 S.92			40-60 AD
TSGM-N	9-G50-5L HS			40-60 AD
TSGM-O	10-G.80 S.49			40-60 AD
TSGM-P	11-G.81 S.49			40-60 AD
TSGM-Q	12-G.74 V.81			40-60 AD
TSGM-R	13-G.76 T.33-C			40-60 AD
TSGM-S	14- G.73 S.94			40-60 AD
TSGM-T	15-G.77 S.92			40-60 AD
TSGM-V	17-G.71 HS			40-60 AD
TSGM-X	19-G.77 T.81			40-60 AD
TSGM-Y	20-G.77 T.81			40-60 AD

Appendix 2 Photographs of the fragment of marbled terra sigillata.

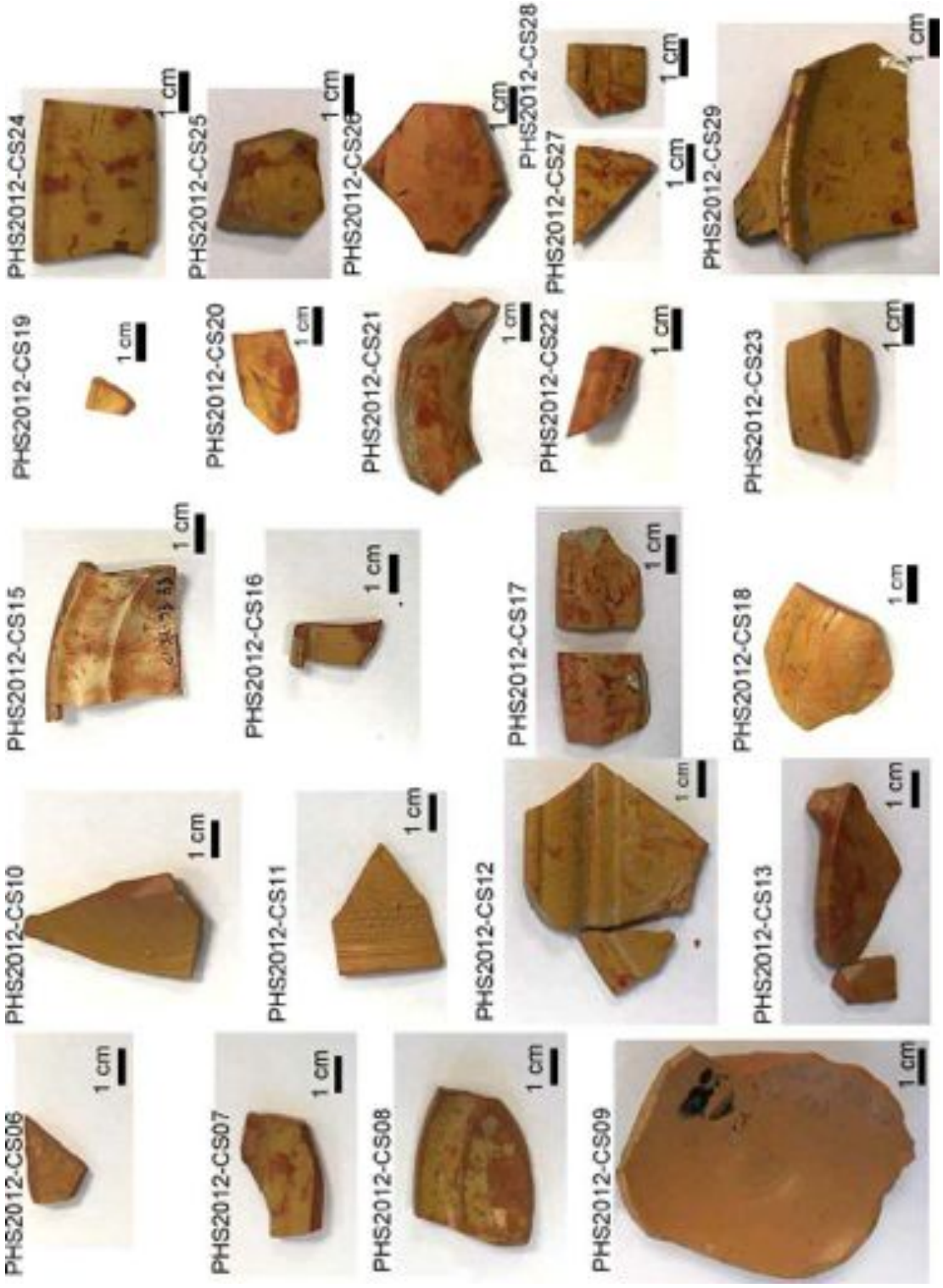

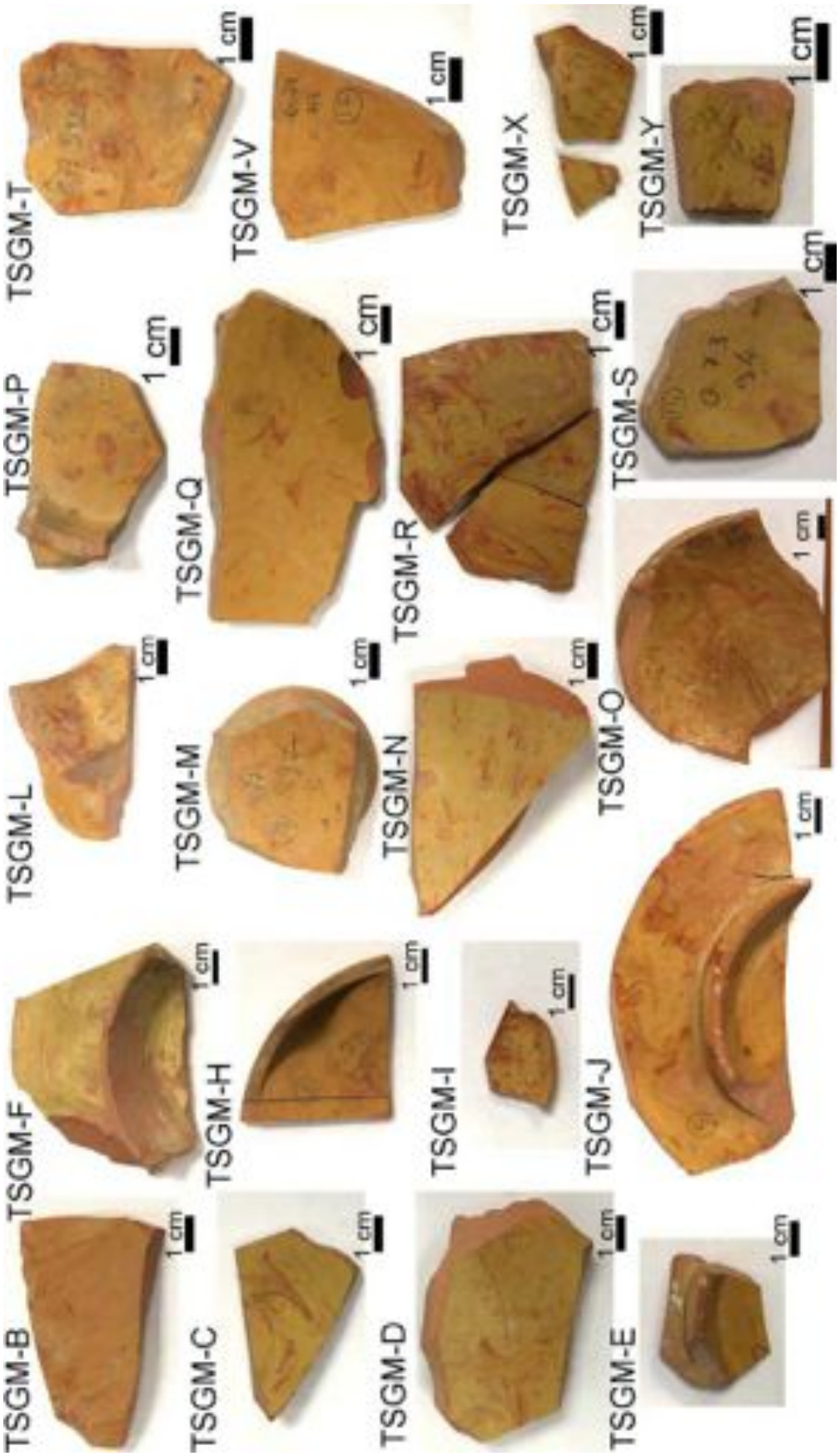
TSGM-B
TSGM-F
TSGM-L
TSGM-P
TSGM-T
TSGM-C
TSGM-H
TSGM-M
TSGM-Q
TSGM-V
TSGM-D
TSGM-I
TSGM-N
TSGM-R
TSGM-X
TSGM-E
TSGM-J
TSGM-O
TSGM-S
TSGM-Y
1 cm

Appendix 3 Quantitative elemental composition (wt%) obtained by electronic microprobe on the yellow slips of 17 sherds (excavated in Narbonne). The mean and standard deviation (in brackets) are given in bold.

Shards	Na_2O	MgO	Al_2O_3	SiO_2	P_2O_5	K_2O	CaO	TiO_2	MnO	Fe_2O_3	BaO	Sum
CS06	**0.04 (0.04)**	**3.22 (0.71)**	**23.21 (1.99)**	**56.74 (4.75)**	**0.09 (0.12)**	**8.59 (0.61)**	**1.53 (0.38)**	**2.26 (1.57)**	**0.03 (0.03)**	**4.26 (2.29)**	**0.45 (0.20)**	**97.03**
CS07	**0.04 (0.04)**	**3.51 (0.71)**	**23.01 (1.63)**	**57.19 (2.13)**	**0.08 (0.04)**	**7.89 (0.89)**	**2.05 (0.77)**	**2.43 (1.04)**	**0.03 (0.03)**	**3.74 (1.00)**	**0.06 (0.19)**	**97.66**
CS08	**0.11 (0.03)**	**2.31 (0.56)**	**29.06 (3.61)**	**52.67 (3.90)**	**0.02 (0.28)**	**8.99 (0.64)**	**1.67 (0.37)**	**2.48 (2.24)**	**0.04 (0.03)**	**2.61 (1.05)**	**0.07 (0.09)**	**99.55**
CS09	**0.13 (0.03)**	**2.36 (0.24)**	**29.62 (1.40)**	**52.19 (1.29)**	**0.02 (0.02)**	**9.30 (0.32)**	**1.85 (0.35)**	**1.94 (1.40)**	**0.04 (0.02)**	**2.50 (0.71)**	**0.08 (0.06)**	**99.50**
CS10	**0.09 (0.03)**	**2.54 (0.42)**	**27.85 (3.54)**	**52.87 (5.77)**	**0.03 (0.05)**	**9.26 (1.15)**	**1.44 (0.26)**	**2.38 (2.64)**	**0.04 (0.04)**	**3.45 (2.62)**	**0.11 (0.09)**	**99.02**
CS11	**0.10 (0.10)**	**2.71 (0.43)**	**28.13 (2.51)**	**53.23 (2.89)**	**0.04 (0.05)**	**8.96 (0.62)**	**1.90 (0.71)**	**1.87 (0.76)**	**0.05 (0.04)**	**2.97 (0.89)**	**0.17 (0.09)**	**98.72**
CS14	**0.08 (0.03)**	**2.95 (0.65)**	**24.92 (2.50)**	**54.42 (4.08)**	**0.05 (0.04)**	**9.51 (0.72)**	**1.42 (0.26)**	**2.52 (1.84)**	**0.03 (0.03)**	**4.05 (2.24)**	**0.10 (0.19)**	**98.89**
CS15	**0.31 (0.26)**	**0.50 (0.07)**	**35.74 (1.97)**	**51.75 (2.63)**	**0.07 (0.06)**	**6.39 (0.82)**	**0.77 (0.10)**	**1.01 (1.75)**	**0.03 (0.03)**	**3.42 (0.85)**	**0.20 (0.10)**	**96.69**
CS16	**0.09 (0.05)**	**3.18 (1.05)**	**20.91 (2.65)**	**55.71 (3.85)**	**0.11 (0.05)**	**7.37 (0.78)**	**2.79 (1.12)**	**3.79 (2.56)**	**0.03 (0.03)**	**5.98 (2.44)**	**0.08 (0.16)**	**98.47**
CS17	**0.06 (0.04)**	**2.51 (0.20)**	**29.60 (1.47)**	**53.55 (1.48)**	**0.04 (0.03)**	**8.13 (0.40)**	**1.24 (0.11)**	**2.17 (1.11)**	**0.02 (0.03)**	**2.63 (0.67)**	**0.22 (0.09)**	**100.94**
CS19	**0.06 (0.04)**	**2.71 (0.92)**	**24.40 (2.87)**	**54.51 (3.71)**	**0.11 (0.05)**	**8.01 (0.77)**	**2.02 (0.98)**	**3.44 (2.37)**	**0.04 (0.03)**	**4.68 (2.30)**	**0.16 (0.14)**	**97.61**
CS20	**0.08 (0.05)**	**2.44 (0.72)**	**27.89 (3.50)**	**51.81 (4.81)**	**0.05 (0.03)**	**7.79 (0.95)**	**1.83 (1.25)**	**3.78 (2.62)**	**0.03 (0.04)**	**4.24 (2.17)**	**1.47 (0.12)**	**99.91**
CS21	**0.04 (0.02)**	**2.86 (1.01)**	**23.21 (5.14)**	**58.47 (6.69)**	**0.06 (0.04)**	**7.81 (0.94)**	**1.29 (0.30)**	**2.08 (1.17)**	**0.01 (0.01)**	**4.15 (1.91)**	**0.20 (0.08)**	**96.72**
CS23	**0.07 (0.04)**	**2.78 (0.52)**	**22.40 (2.61)**	**57.50 (3.87)**	**0.12 (0.10)**	**7.71 (0.62)**	**1.72 (0.45)**	**3.15 (1.58)**	**0.03 (0.03)**	**4.48 (1.58)**	**0.32 (0.14)**	**98.94**
CS24	**0.07 (0.04)**	**2.75 (0.81)**	**21.04 (2.33)**	**55.96 (4.47)**	**0.09 (0.06)**	**8.55 (0.83)**	**2.85 (0.97)**	**3.82 (2.41)**	**0.03 (0.03)**	**4.80 (2.28)**	**0.14 (0.24)**	**98.45**
CS27	**0.03 (0.05)**	**2.52 (0.61)**	**24.95 (3.26)**	**57.26 (3.30)**	**0.08 (0.04)**	**6.99 (0.34)**	**1.27 (0.34)**	**3.11 (1.50)**	**0.02 (0.03)**	**3.72 (1.03)**	**0.25 (0.11)**	**98.85**
CS28	**0.05 (0.04)**	**2.31 (0.81)**	**23.00 (2.38)**	**57.07 (3.47)**	**0.09 (0.03)**	**6.92 (0.70)**	**2.00 (2.00)**	**2.93 (1.47)**	**0.04 (0.04)**	**3.85 (1.57)**	**0.21 (0.21)**	**98.54**

Appendix 4 Archaeological details of the Attic ceramics (excavated at Lattes, France).

		Remarks1	Category	Period	Remarks2
Series 1	PHS2015-CS30	US71030	Attic black slip	-375/-350	
	PHS2015-CS31	US71024	Attic black slip	-325/-300	
	PHS2015-CS32	US51118	Attic black slip	-425/-400	
	PHS2015-CS33	US51118	Attic black slip	-425/-400	Castulo cup
	PHS2015-CS34	US51121	Attic black slip	-425/-400	Misfired
	PHS2015-CS35	US53060	Attic black slip	-450/-425	
	PHS2015-CS36	US53038	Attic black slip	-450/-425	Castulo cup
	PHS2015-CS37	US53060	Attic black slip	-450/-425	
	PHS2015-CS38	US53564	Attic black slip	-450/-450	White slip
	PHS2015-CS39	US53564	Attic black slip	-450/-450	
	PHS2015-CS40	US53917	Attic black slip	-475/-450	Sherd of type C Delicate class
	PHS2015-CS41	US53787	Attic black slip	-475/-450	
	PHS2015-CS42	US53960	Attic black slip	-500/-475	Sherd of type C
	PHS2015-CS43	US53960	Attic black slip	-500/-475	
	PHS2015-CS44	US53336	Attic black slip	-450/-425	
	PHS2015-CS45	US53336	Attic Red Figure	-450/-425	Castulo cup
Series 2	PHS2016-CS46	US50336	Attic Red Figure	-425/-400	Published in Lattara 21*,n°270
	PHS2016-CS47	US50336, P3004, zone1	Attic black slip	-425/-400	
	PHS2016-CS48	US50336, P3004, zone1	Attic black slip	-425/-400	Black glaze (interior) and <red coral> slip
	PHS2016-CS49	US277751, zone27	Attic Red Figure	-475/-450	Published in Lattara 21*, n°405*
	PHS2016-CS50	US277719	Attic Red Figure	-475/-450	Published in Lattara 21*, n°33
	PHS2016-CS51	US53233, P3811, zone1	Attic black slip	-450/-425	Published in Lattara 21*, n°425
	PHS2016-CS52	US53141, P3697, zone1	Attic Red Figure	-500/-475	
	PHS2016-CS53	US53260, P3828, zone1	Attic Red Figure	-500/-475	Black slip with "red coral" slip
	PHS2016-CS55	US27782, P3620/21, zone27	Attic Red Figure	-475/-450	Published in Lattara 21*, n°438
	PHS2016-CS56	US27782, zone27	Attic black slip	-450/-425	Lip of cup with black gloss
	PHS2016-CS57	US27782, zone27	Attic black slip	-450/-425	Lip of cup with balck slip and <red coral> slip

* Chazalon, L., 2010. (La céramique attiques du Ve s. av. n. è. à Lattes. Lattara, 21: 529-650).

Appendix 5 Photographs of the first type of the Greek ceramics (Attic sherds excavated at Lattes, France)

Appendix 6 Quantitative elemental compostion (wt%) obtained by electronic microprobe on the slips of sherds (excavated in Lattes, France). The mean and standard deviation (in brackets) are given in bold. *The number of points was analyzed.

ID	Na_2O	MgO	Al_2O_3	SiO_2	K_2O	CaO	MnO	FeO	Cr_2O_3	BaO	TiO_2	P_2O_5	SUM
CS30 (20 pt)	**0.41 (0.04)**	**1.59 (0.10)**	**29.85 (0.50)**	**45.41 (0.89)**	**4.68 (0.31)**	**0.37 (0.17)**	**0.09 (0.04)**	**15.16 (1.34)**	**0.05 (0.01)**	**0.01 (0.01)**	**0.59 (0.39)**	**0.36 (0.05)**	**98.60**
CS32 (20 pt*)	**0.28 (0.03)**	**1.91 (0.06)**	**29.41 (0.32)**	**46.93 (0.50)**	**4.76 (0.16)**	**0.35 (0.07)**	**0.08 (0.05)**	**14.08 (0.69)**	**0.05 (0.01)**	**0.02 (0.02)**	**0.59 (0.14)**	**0.18 (0.02)**	**98.65**
CS33	**0.54 (0.09)**	**2.12 (0.09)**	**27.47 (0.36)**	**45.68 (0.71)**	**5.37 (0.84)**	**0.38 (0.11)**	**0.05 (0.03)**	**14.94 (1.05)**	**0.05 (0.03)**	**0.01 (0.01)**	**0.78 (0.14)**	**0.24 (0.05)**	**97.67**
CS34	**0.82**	**1.63**	**26.39**	**42.67**	**4.99**	**1.28**	**0.09**	**14.50**	**0.08**	**0.03**	**0.53**	**0.67**	**93.83**
CS35	**0.43 (0.05)**	**1.83 (0.13)**	**28.30 (1.44)**	**46.56 (2.31)**	**5.75 (0.26)**	**0.35 (0.08)**	**0.07 (0.03)**	**13.54 (1.85)**	**0.06 (0.03)**	**0.01 (0.01)**	**0.67 (0.21)**	**0.18 (0.04)**	**97.77**
CS36 (20 pt)	**0.40 (0.03)**	**1.78 (0.04)**	**28.63 (0.38)**	**45.22 (0.43)**	**5.80 (0.18)**	**0.73 (0.18)**	**0.06 (0.04)**	**14.37 (0.96)**	**0.06 (0.02)**	**0.01 (0.02)**	**0.63 (0.15)**	**0.17 (0.04)**	**97.86**
CS37	**0.42 (0.12)**	**2.19 (0.08)**	**27.26 (0.57)**	**46.49 (1.00)**	**5.48 (0.77)**	**0.21 (0.07)**	**0.07 (0.03)**	**14.65 (1.43)**	**0.07 (0.03)**	**0.01 (0.01)**	**0.77 (0.19)**	**0.19 (0.05)**	**97.86**
CS39 (20 pt)	**0.50 (0.10)**	**2.13 (0.12)**	**26.31 (0.77)**	**44.83 (0.81)**	**6.85 (0.75)**	**0.27 (0.06)**	**0.07 (0.03)**	**14.90 (1.34)**	**0.09 (0.02)**	**0.01 (0.02)**	**0.84 (0.20)**	**0.19 (0.04)**	**96.98**
CS40	**0.41 (0.08)**	**2.13 (0.07)**	**27.16 (0.76)**	**46.93 (0.98)**	**6.12 (0.57)**	**0.17 (0.04)**	**0.07 (0.04)**	**15.08 (1.28)**	**0.11 (0.4)**	**0.00 (0.01)**	**0.59 (0.13)**	**0.24 (0.04)**	**99.05**
CS41	**0.50 (0.12)**	**2.15 (0.15)**	**27.36 (0.65)**	**46.96 (1.00)**	**6.54 (0.67)**	**0.26 (0.18)**	**0.09 (0.16)**	**15.05 (1.48)**	**0.11 (0.03)**	**0.00 (0.01)**	**0.72 (0.18)**	**0.23 (0.03)**	**100.0**
CS42 (11 pt)	**0.54 (0.14)**	**2.10 (0.18)**	**27.82 (0.43)**	**44.58 (0.85)**	**5.80 (0.69)**	**0.36 (0.23)**	**0.11 (0.04)**	**15.48 (2.00)**	**0.06 (0.02)**	**0.01 (0.01)**	**0.46 (0.13)**	**0.12 (0.04)**	**97.45**
CS43	**0.56 (0.06)**	**1.65 (0.07)**	**29.59 (0.89)**	**45.47 (1.23)**	**4.73 (0.27)**	**0.41 (0.15)**	**0.06 (0.03)**	**13.87 (1.15)**	**0.06 (0.03)**	**0.01 (0.01)**	**0.47 (0.26)**	**0.15 (0.03)**	**97.14**
CS44	**0.81 (0.17)**	**2.24 (0.10)**	**27.35 (0.65)**	**44.44 (1.18)**	**5.92 (0.58)**	**0.63 (0.19)**	**0.10 (0.03)**	**14.48 (1.98)**	**0.04 (0.03)**	**0.01 (0.01)**	**0.61 (0.12)**	**0.23 (0.04)**	**96.88**
CS45	**0.12 (0.03)**	**2.03 (0.10)**	**28.58 (0.57)**	**46.62 (0.84)**	**2.65 (0.14)**	**0.62 (0.04)**	**0.09 (0.02)**	**16.34 (0.71)**	**0.06 (0.04)**	**0.01 (0.02)**	**0.96 (0.11)**	**0.26 (0.04)**	**98.39**
CS46	**0.49 (0.09)**	**2.11 (0.17)**	**27.87 (0.57)**	**45.67 (0.85)**	**5.06 (0.67)**	**0.56 (0.24)**	**0.07 (0.03)**	**15.61 (0.98)**	**0.05 (0.01)**	**0.02 (0.02)**	**0.92 (0.17)**	**0.32 (0.17)**	**98.79**
CS47	**0.60 (0.09)**	**1.70 (0.11)**	**28.92 (0.40)**	**45.87 (0.55)**	**6.88 (0.40)**	**0.57 (0.18)**	**0.06 (0.03)**	**14.12 (0.89)**	**0.05 (0.01)**	**0.01 (0.02)**	**0.62 (0.18)**	**0.22 (0.04)**	**98.79**
CS50	**0.78 (0.14)**	**1.73 (0.08)**	**27.95 (0.37)**	**44.19 (0.77)**	**5.03 (1.46)**	**0.73 (0.27)**	**0.05 (0.03)**	**15.57 (0.86)**	**0.05 (0.01)**	**0.01 (0.01)**	**0.89 (0.24)**	**0.55 (0.10)**	**97.57**
CS51	**0.38 (0.07)**	**1.79 (0.05)**	**29.42 (0.56)**	**46.77 (0.86)**	**4.09 (0.38)**	**0.47 (0.10)**	**0.10 (0.03)**	**14.79 (1.23)**	**0.06 (0.01)**	**0.01 (0.02)**	**0.62 (0.12)**	**0.21 (0.04)**	**98.73**
CS52	**0.24 (0.05)**	**1.74 (0.15)**	**29.91 (0.50)**	**46.44 (0.69)**	**3.76 (0.34)**	**0.36 (0.13)**	**0.07 (0.03)**	**14.89 (1.24)**	**0.06 (0.01)**	**0.01 (0.01)**	**0.63 (0.11)**	**0.19 (0.04)**	**98.33**
CS53	**0.44 (0.04)**	**2.09 (0.12)**	**28.80 (0.47)**	**45.69 (0.85)**	**6.15 (0.11)**	**0.23 (0.04)**	**0.04 (0.02)**	**13.80 (1.09)**	**0.07 (0.01)**	**0.00 (0.01)**	**0.35 (0.06)**	**0.16 (0.04)**	**98.33**
CS55	**0.54 (0.09)**	**1.96 (0.15)**	**27.64 (0.76)**	**46.53 (0.73)**	**5.73 (0.57)**	**0.19 (0.04)**	**0.06 (0.03)**	**14.65 (1.18)**	**0.10 (0.03)**	**0.00 (0.01)**	**0.87 (0.43)**	**0.19 (0.03)**	**98.50**
CS56	**1.29 (0.10)**	**1.98 (0.30)**	**26.90 (0.54)**	**43.96 (1.04)**	**7.45 (0.30)**	**0.92 (0.15)**	**0.06 (0.03)**	**12.91 (1.22)**	**0.05 (0.01)**	**0.02 (0.01)**	**0.56 (0.16)**	**0.29 (0.13)**	**96.63**
CS57	**0.17 (0.03)**	**1.75 (0.08)**	**30.18 (0.38)**	**46.15 (0.42)**	**5.15 (0.38)**	**0.73 (0.15)**	**0.06 (0.02)**	**13.88 (0.60)**	**0.06 (0.01)**	**0.01 (0.02)**	**0.48 (0.09)**	**0.24 (0.04)**	**99.27**

Appendix 7 Archaeological details of the Yuan fragments.

Sample number	Provenance	Dating of stratigraphy
YJ-1, YJ-2, YJ-3, YJ-4, YJ-5, YJ-6, YJ-7, YJ-8	Luomaqiao site in Jingdezhen, Jianxi, China	Yuan dynasty (13th to 14th century AD)
YH-1, YH-2, YH-3, YH-4, YH-5, YH-6, YH-7, YH-8	Shibaqiao site in Jingdezhen, Jianxi, China	Yuan dynasty (13th to 14th century AD)
YG-1, YG-2, YG-3, YG-4, YG-5, YG-6	Shibaqiao site in Jingdezhen, Jianxi, China	Yuan dynasty (13th to 14th century AD)

Appendix 8 Photographs of the Yuan fragments.

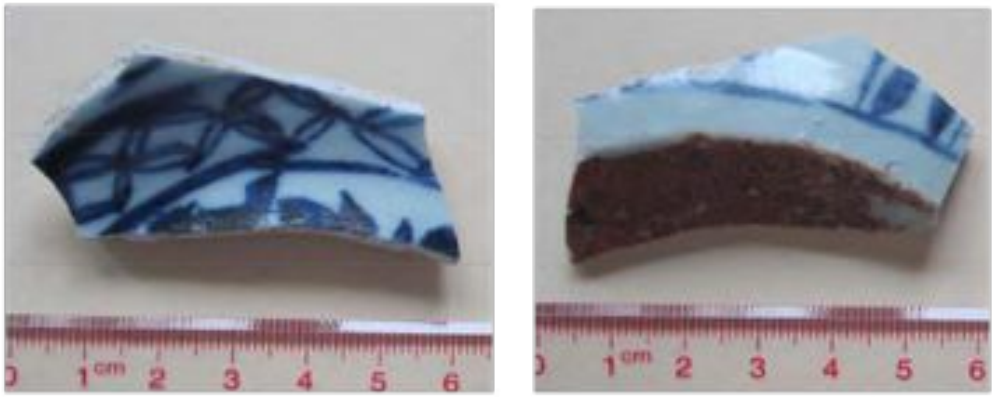

YJ-1

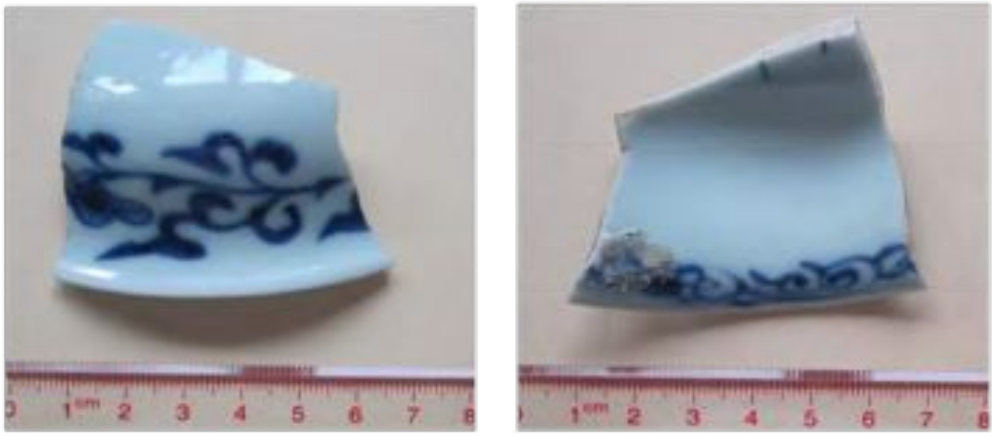

YJ-2

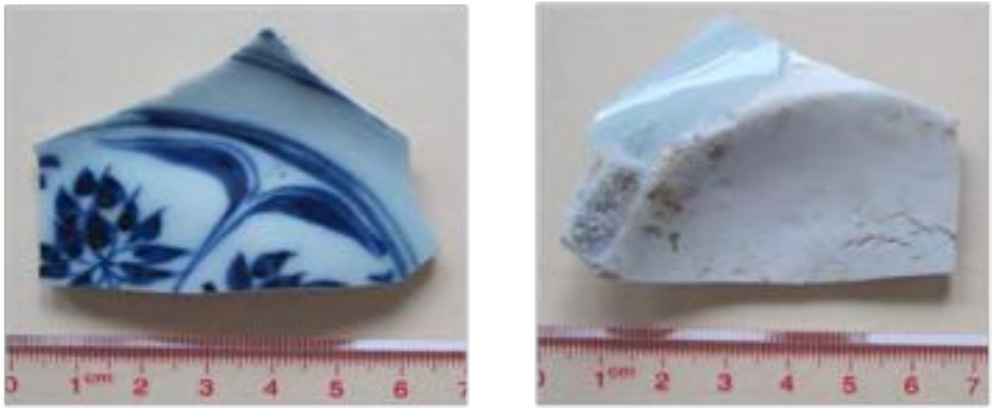

YJ-3

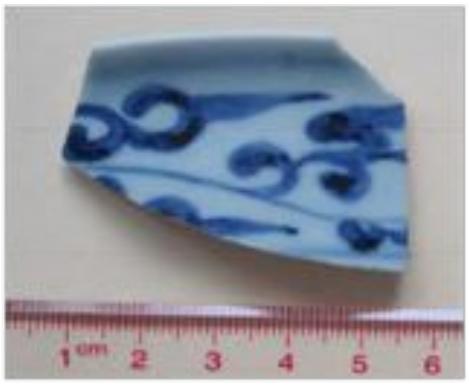

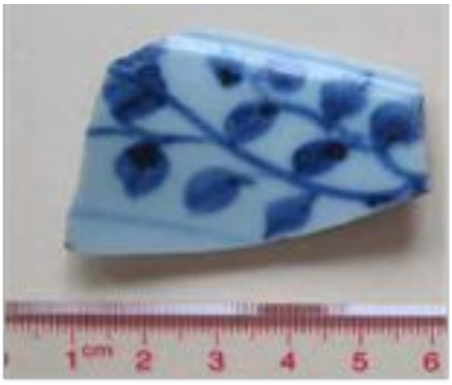

YJ-4

YJ-5

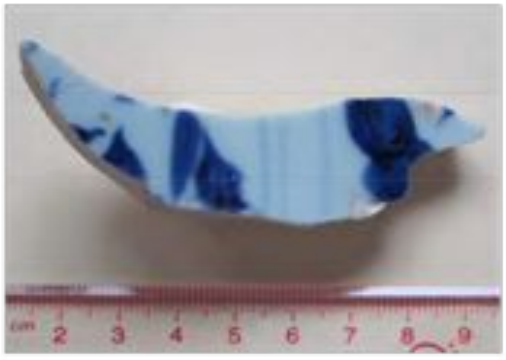

YJ-6

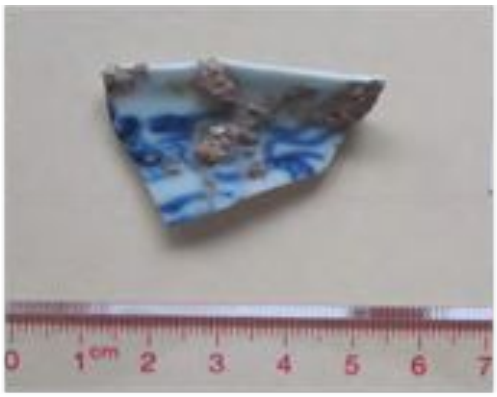

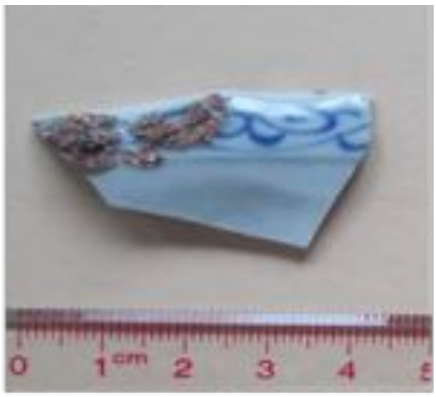

YJ-7

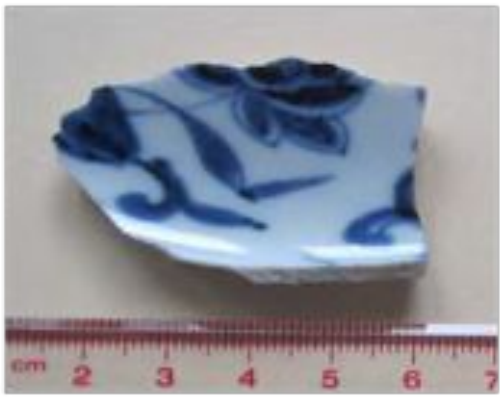

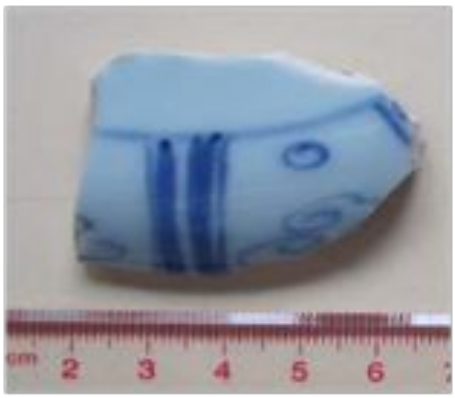

YJ-8

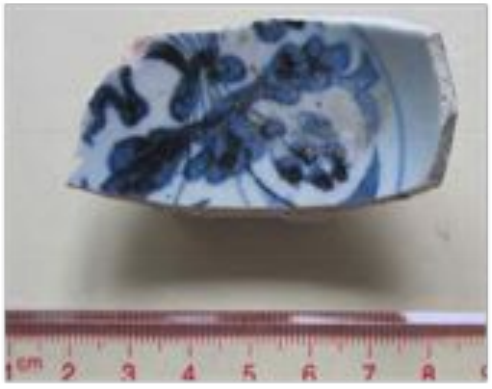

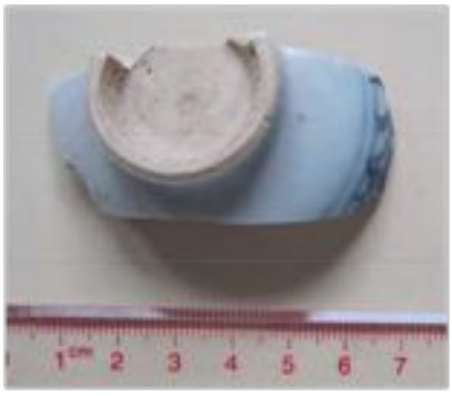

YH-1

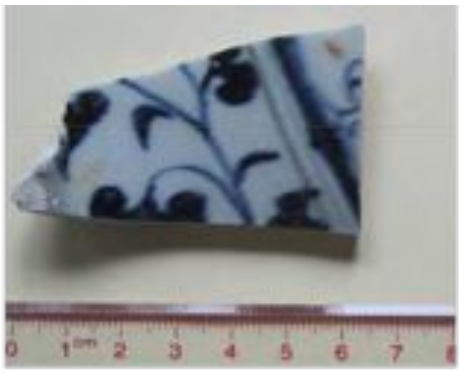

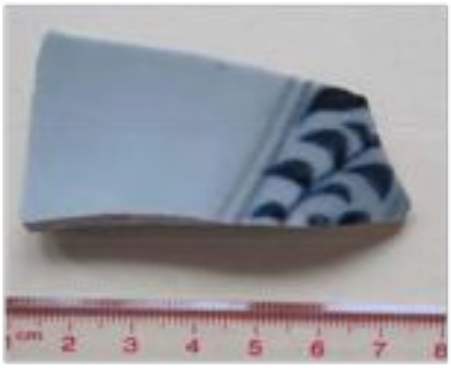

YH-2

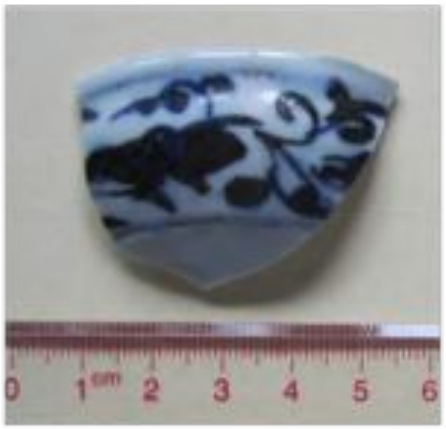

YH-3

YH-4

YH-8

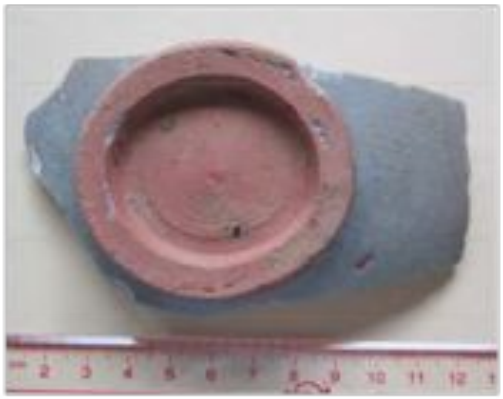

YG-1

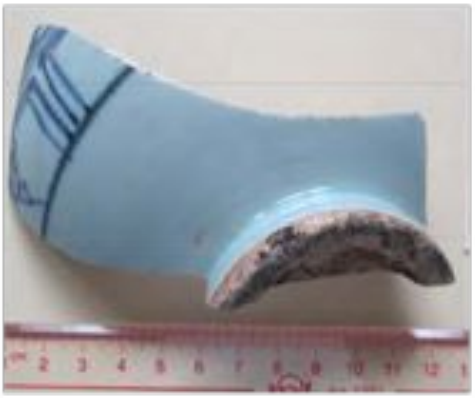

YG-2

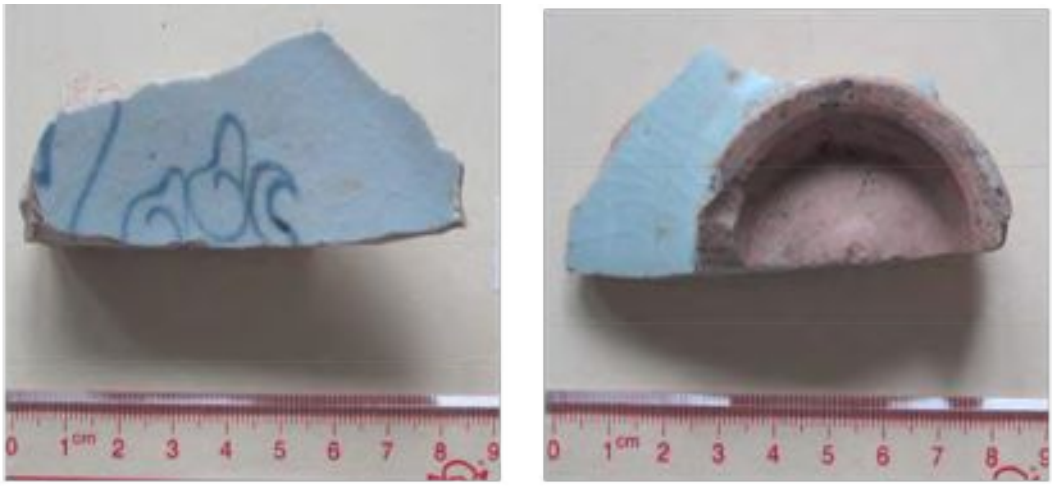

YG-6

French Abstract:

Une étude multi-échelle des anciennes céramiques en utilisant une série de techniques d'analyse

Résumé:

Les artefacts en céramique, fabriqués à partir d'argile puis durcis par la chaleur, ont été le premier matériau synthétique créé par les humains avec une ingéniosité unique (Lawrence et West 1982, Li 1998, Rice 2015). L'histoire de la céramique couvre environ vingt mille ans. Les céramiques les plus anciennes remontent à au moins 25 000 av. J.-C., découvertes à Dolni Vestonice et Pavlov en Moravie (République tchèque) (Vandiver et al., 1989, Bougard, 2011). C'étaient les fameuses céramiques gravettiennes sous forme de figurines humaines et animales. Mais la première apparition de vases de céramique était à la fin du paléolithique ou peu de temps après, ce qui a été interprété comme marquant le mouvement des sociétés humaines de «Upper Savagery» en «Lower Barbarism» (Morgan 1877). Jusqu'à la sédentarisation des êtres humains pendant la période néolithique, les poteries ont commencé à être fréquemment utilisées, comme les poteries peintes avec des décorations géométriques rouge et noir découverts dans les villages Yangshao de Chine, datés de 5000 avant JC à 3000 avant JC (Li 1998) . Après 4 000 av. J.-C., la technique générale de la production de céramique a été peu à peu connue des potiers et de nombreuses techniques de fabrication ont été développées, ce qui a intensifié les productions de poterie, telles que les innovations de roue et de moisissure de potier (Hofmann, Roux et Miroschedji 2009). Deux fameux cas sont des poteries grecques (fabriquées aux VIe et IVe siècles av. J.-C. à Athènes) (Noble 1960, Folsom, 1975) et Arretine romaine (datée du Ier siècle avant J.-C. au IVe siècle de notre ère) (Oswald et Pryce, 1920) Qui représentent l'accomplissement technique exceptionnel. Pendant le 14ème siècle avant JC, les productions de pierre ont été créées à cause du développement du four. Par exemple, des pierres de taille chinoises ont été produites pendant la période du Moyen-Shang (XVe-XIVe siècle av. J.-C.) dans le four pouvant atteindre 1200 ° C (Li 1998). Vers le même temps, des glaçures sont apparues et ont été utilisées pour couvrir les navires par un «glost naturel du four» et les ont protégés des cendres de bois pendant le tir (Rice 2015). Avec le développement des techniques de fabrication, l'héritage le plus durable des potiers, c'est-à-dire les porcelaines, est apparu pendant la dynastie des Tang (7ème au 10ème siècle) en Chine (Li 1998). Mais c'est pendant la dynastie Song et Yuan (Xe-XIVe siècle apr. J.-C.) que les productions de porcelaine ont atteint leur plus beau développement. Au cours de la dynastie Ming et Qing (XIVe-XVIIe siècle apr. J.-C.), les productions ont été massivement produites et produites au monde entier (Li 1998). Une des porcelaines chinoises célèbres est la porcelaine bleue et blanche, identifiée par son vernis transparent avec des décors bleu sous glaçure (Li 1998). L'exportation de porcelaines chinoises vers l'Europe a lourdement influencé l'industrie manufacturière des productions locales. Par exemple, à Delft, aux Pays-Bas, des céramiques bleues et blanches ont été

produites en grand nombre à partir du XVIIe siècle (Jorg, 1984; Moore, 2009).

Tout au long de l'histoire des artefacts en céramique, les productions ont été étudiées sous divers angles, notamment artistiques, esthétiques, classificatoires, minéralogiques et chimiques (Li 1998, Tite 2008, Rice 2015). En particulier, de nombreuses recherches archéologiques ont été consacrées à l'étude de la composition chimique et minérale des céramiques anciennes afin d'identifier leur date, leur origine, les matières premières et le processus de fabrication et enfin de découvrir l'histoire et la culture des êtres humains (Li 1998; Tite 2008, Rice 2015, Sciau et Goudeau 2015). Par exemple, la première étude de provenance de céramique à grande échelle, utilisant la spectroscopie d'émission optique, a été l'analyse chimique des céramiques peintes de Minoan et de Mycenaean (Catling et al., 1963) et les résultats indiquent que la période allant de 1400 av. En 1200 av. J.-C., les Mycéniens étaient la principale puissance mercantile de la Méditerranée orientale, exportant des poteries à Melos, Chios, Chypre, Rhodes, Syrie (Tell Atchana) et Egypte (Amarna).

En effet, les céramiques anciennes sont un matériau idéal pour l'archéométrie. La raison principale est que ces artefacts du patrimoine culturel ont une longue histoire et ont été récupérés dans presque toutes les régions du monde. Leur présence est rarement limitée par des situations géologiques ou environnementales ou des conditions de conservation. Bien qu'un vaisseau puisse casser, ses fragments peuvent survivre pendant des millénaires en raison de leur non périssabilité en fonction des propriétés physiques. Par conséquent, les recherches archéologiques modernes ont consacré une attention considérable à la céramique dans leurs rapports.

Les méthodes utilisées dans les recherches archéologiques modernes sont très bénéfiques de celles utilisées dans le domaine de la science des matériaux (Li 1998, Wood 1999, Tite 2008, Rice 2015, Sciau et Goudeau 2015, Gan et al.). Les méthodes d'étude de la microstructure, de la phase cristallographique et des défauts des matériaux modernes peuvent également être appliquées pour étudier les propriétés des céramiques anciennes. L'analyse des propriétés chimiques et minérales, en utilisant les techniques «initiales» telles que la fluorescence aux rayons X (Chen et al., 1994, Mantler et Schreiner 2000, Tang et al., 2001, Colomban et al., 2004, Prinsloo et al. Padilla et al, 2006, Wu et al, 2007, Wen et al., 2007, Majumdar et al., 2012, Zhu et al., 2015) et les techniques les plus récentes telles que la microscopie électronique à transmission (Maniatis et al. Sciau et al., 2006, Wu et al., 2007, Mirguet et al., 2009a; Mirguet et al. 2009b; Walton et al. 2013), ont fourni divers types d'informations archéologiques concernant l'histoire et la civilisation des êtres humains aux archéologues et les informations potentielles concernant l'amélioration de la synthèse des matériaux modernes aux chimistes et aux physiciens. Par exemple, la combinaison de la microscopie électronique à transmission, de la spectroscopie Raman et des techniques de diffraction des rayons X a été utilisée avec succès pour identifier la présence d'oxydes de fer (ε-Fe_2O_3) dans l'émaillage noir brillant des anciennes marchandises Jian et en déchiffrant les technologies derrière la fabrication, On peut donc potentiellement aider les chercheurs à améliorer la synthèse de ε-Fe_2O_3 (Dejoie et al., 2014).

Du point de vue de la science des matériaux, la structure de la poterie est une structure de couche assez complexe avec des hétérogénéités à

différentes échelles (nm à mm). Une céramique décorée est généralement constituée d'une pâte et d'un revêtement, qui englobe la décoration. Le revêtement peut avoir différente nature. Il est d'épaisseur très variable, de quelques dizaines de microns à plusieurs centaines de microns. La couche décorative peut être une partie du revêtement ou tout le revêtement. Elle est constituée d'une phase amorphe plus ou mois vitrifiée et de diverses particules cristallines, telles que des particules de colorant, des feldspath, etc., de taille allant du nanomètre à quelques microns.

La description de ce type de structure nécessite le balayage d'un grand volume (représentatif) (plusieurs mm^3) à haute résolution (nm). Ceci est réellement impossible et dans ce travail j'essaie de proposer une approche alternative basée sur une sélection de techniques d'échantillonnage et d'analyse. Des enquêtes rapides à faible résolution (souvent observation optique) sont utilisées pour définir les zones nécessitant des recherches à résolution plus élevée. À partir de l'ensemble des données, on essaie de reconstruire toute la structure. Il est également évident que le nombre d'échantillonnage et la technique impliquée doivent être faibles et pour cela, il est nécessaire d'inclure dans la sélection le type d'information requise.

Donc, dans le cadre de ma thèse, j'ai essayé de proposer une approche en sélectionnant diverses méthodes de préparation d'échantillons et une série de techniques analytiques pour étudier les propriétés des céramiques anciennes à différentes échelles.

L'approche est basée sur :

Premièrement, des investigations rapides (principalement l'observation optique) à faible résolution sont effectuées pour sélectionner et définir les zones nécessitant des analyses à résolution plus élevée.

Deuxièmement, les zones sélectionnées sont analysées à haute résolution avec des techniques appropriées en tenant compte des informations recherchées.

Troisièmement, on essaie de reconstruire la structure de l'objet à partir de ces données partielles et d'en déduire des informations concernant le processus de fabrication.

Je vais illustrer cette approche à travers trois exemples d'étude de céramique :

L'étude du processus de cuisson des poteries attiques (**chapitre III**).

L'étude de la composante jaune de revêtement de sigillata marbrée (**chapitre III**).

L'étude de la variation de couleur des décors bleus de porcelaines chinoises de la période Yuan et Ming (**chapitre IV**).

Le chapitre II décrit cette approche alternative à un balayage d'un grand volume (plusieurs mm^3 dans le cas de la céramique) de l'échantillon à haute résolution permettant de reconstituer entièrement sa structure et composition en détails. Les différents instruments utilisés dans cette approche sont présentés ainsi que leur potentiel application à l'analyse des céramiques

anciennes. Cette approche implique l'usage d'une série d'outils de laboratoires traditionnels et la mise en œuvre de techniques novatrices reposant sur le rayonnement synchrotron (Figure 1). La première catégorie de technique regroupe la microspectroscopie Raman, la microscopie à balayage électronique couplée à un spectroscope à rayons X à dispersion d'énergie (SEM-EDX, résolution nm), toutes deux mises en œuvre au CEMES-CNRS (Toulouse, France); la microsonde électronique (EPMA) mise en œuvre au Laboratoire Géoscience Environnement (GET) de Toulouse; et la spectroscopie de fluorescence X (XRF, résolution µm) mise en œuvre au laboratoire d'Archéométrie de l'Ecole de Sociologie et d'Anthropologie de l'Université Sun Yat-Sen à Canton (Chine). La deuxième catégorie de techniques comprend la spectroscopie de fluorescence X induite par le rayonnement synchrotron (SR-XRF, résolution entre 0.5 et 2 µm), la microscopie XANES (FF-XANES, résolution spatiale entre 0.3 et 1.4 µm sur une zone représentative entre 600 μm^2 et 2 mm^2) et la diffraction des rayons X induite par le rayonnement synchrotron (SR-XRD, résolution 1 µm). Ces techniques ont été mises en œuvre à l'ESRF (Grenoble, France) sur la ligne de faisceau ID21.

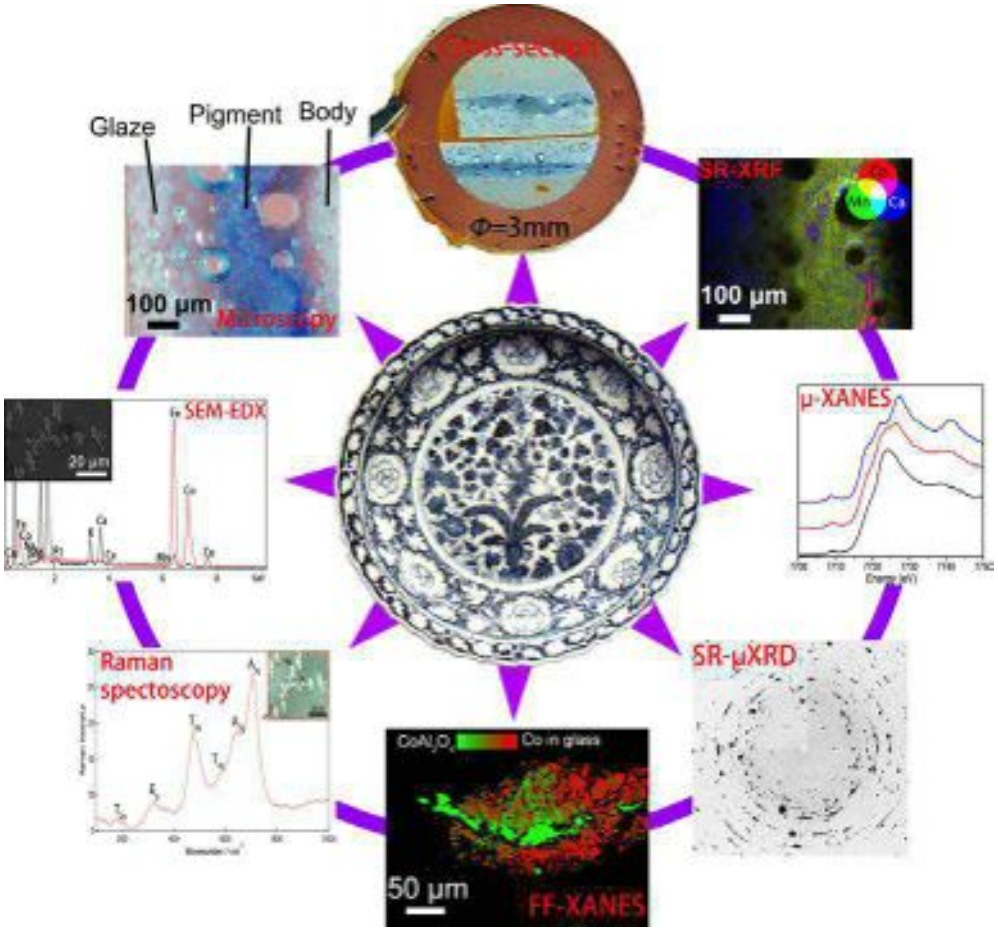

Figure 1 Exemple d'analyse d'une porcelaine chinoise par l'approche multi-scalaire: la céramique au centre est un plat en porcelaine Qinghua (1271-1368) mis au jour à Jingdezhen dans la province du Jianxi (Crédit: World Imaging, CC BY-SA 3.0). L'étude des décors de cette céramique ancienne a nécessité le développement d'une approche multi-scalaire consistant en l'usage d'une série d'outils analytiques.

La méthode de préparation des échantillons est également présentée en Figure 2, elle permet d'obtenir des prélèvements de céramique exploitables. Cette méthode de préparation s'inspire de la microscopie électronique en transmission. L'exemple présenté concerne la préparation de porcelaines chinoises Qinghua afin d'étudier les seuils d'absorption de Mn, Fe et Co dans les décors bleus (4). Plusieurs étapes de découpe (1-3) sont nécessaires afin d'obtenir deux fines lames présentant un décor bleu. Ces deux lames sont collées ensemble, glaçure contre glaçure, en utilisant de l'epoxy Gatan G-1, pour former un sandwich (5). Ce sandwich est ensuite découpé en plusieurs lamelles d'environ 500 mm et chacune d'elles est enrobée de résine et placée sur une lame de verre (6). Les tranches sont ensuite temporairement montées sur un support mobile en laiton (7). Après avoir poli la première face, le support mobile est chauffé afin de faire fondre la résine. L'échantillon est retourné et collé avec de la résine. Une grille de cuivre (utilisée comme référence pour l'épaisseur) est ajoutée sur le support et également collée avec de la résine. La tranche est polie afin d'avoir la même épaisseur que la grille de cuivre (40-60 µm). Pour finir, une rondelle de cuivre est collée à la fine lamelle pour conserver les échantillons, faciliter leur transport (9) et les installer sur les portes-échantillons des installations de ID21 (10).

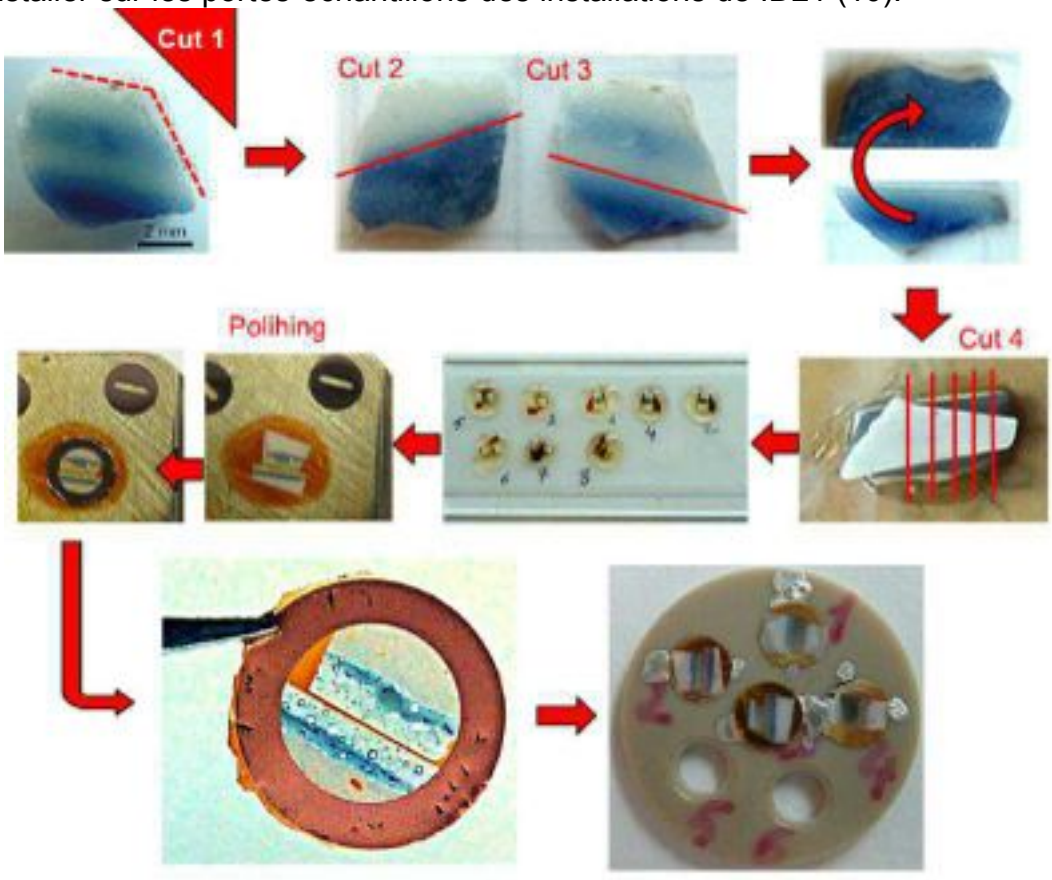

Figure 2 Principales étapes de la préparation des coupes transverses: depuis le fragment (1) jusqu'à la lamelle (9) placée sur le porte-échantillon spécifique de l'ID21 (10).

Le chapitre III présente l'étude du processus de cuisson des poteries attiques et L'étude de la composante jaune de revêtement de sigillata marbrée.

Les poteries attiques ont été produites à Athènes du VIe au IVe siècle av. J.-C. Les poteries attiques sont caractérisées par un revêtement noir brillant (Figure 3). La poterie de la figure noire a été le premier type développé à Athènes à partir de la fin du IIVe siècle av. J.-C. jusqu'à la fin du IVe siècle av. J.-C. (Figure 3a). La poterie de la figure rouge est apparue à la fin du VIe siècle av. J.-C. et avait été produite jusqu'au IVe siècle av. J.-C. (Figure 3b). La poterie «Coral Red Slip» est apparue pendant 540-530 av. J.-C. et n'a été produite que depuis moins d'un siècle par un petit groupe de potiers (Figure 3c). La poterie de La décoration noire avec impression a été produite du IVe au VIe siècle av. J.-C. (Figure 3d).

Figure 3 Attic poteries : (a) La poterie de la figure noire. (b) La poterie de la figure rouge. (c) La poterie «Coral Red Slip». (d) La poterie de La décoration noire avec impression.

La technique de cuisson de la façon de produire l'engobe noir a attiré de nombreux scientifiques depuis le milieu du 18ème siècle. En 1929, Binns et Fraser proposent un modèle selon lequel la engobe noire a été produite dans une seule cuisson: l'environnement du four a été soumis à un cycle à trois étapes d'oxydation-réduction-oxydation. En 1960, Noble décrit ce modèle en détail. Le procédé de cuisson proposé par Noble 1960 concernent trois phases : oxydation-réduction-oxydation :

-Dans la première phase, après que la poterie décorée est bien installée dans le four, la température du four est chauffée de la température ambiante pour atteindre environ 800 ° C. Dans cette phase, il permet aux oxydes de fer dans la pâte et l'engobe de former des minéraux de couleur rouge (Fe_2O_3), donnant un orange rougeâtre de toute la poterie.

-Dans la deuxième phase, la température commence à 800 °C et pourrait atteindre 945 ° C, puis retomber à 875 °C.Les minéraux de couleur rouge (Fe_2O_3) la pâte et la engobe sont transformés en minéraux noirs en magnétite (Fe_3O_4) ainsi qu'en hercynite ($FeAl_2O_4$) (Tang et al., 2001). L'engobe est vitrifié en raison de son argile fine tandis que la pâte fait de grains secondaires reste poreux.

-Dans la phase finale, la température se maintient à 875 °C. La pâte est tournée au rouge tandis que l'engobe vitrifié reste noir.

Même si le protocole de cuisson unique a été un modèle de consensus

pour expliquer la production de l'engobe noire (Walton 2013), sa reproduction selon ce protocole est encore difficile notamment pour obtenir le brillant élevé de l'engobe noir des attiques. En 2013, Walton a proposé l'hypothèse que la poterie serait faite par une double cuisson (Walton 2013). En 2015, Cianchetta a décrit la double cuisson en détail (Cianchetta 2015) :

-Une première cuisson est une cuisson oxydante. Après application d'une engobe homogène sur la surface, les poterie sont installées dans le four, puis chauffées sous atmosphère oxydante à haute température (850 °C). Après cette phase, une engobe vitrifiée rouge est formée (principalement, l'hématite). Les décors sur la poterie (zones destinées à être noires) sont ensuite peints avec une deuxième application d'engobe.

- La deuxième cuisson est la cuisson à trois étages (Noble 1960). La poterie décorée (zones destinées à être noires) est cuite par la cuisson à trois étages. Après la cuisson, l'engobe extérieur présente du noir (hercynite et magnétite) tandis que la pâte présente du rouge (hématite et maghémite). La première engobe ayant été vitrifiée et imperméable après la première cuisson, elle reste rouge (hématite).

Cependant, seules deux pièces célèbres ont été analysées dans le travail précédent. (Un peint par le peintre de Kleophrades a été analysé dans l' œuvre de Walton 2013 et un peint par le peintre de Berlin a été analysé dans l'œuvre de Cianchetta 2015). Donc, mon objectif est d'obtenir des informations sur le processus de cuisson de l'engobe noire des poteries attiques, pour cela, un grand corpus de fragments attiques (12 fragments) provenant des fouilles de Lattes a été sélectionné et analysé.

Des fragments sont excavés de Lattes et fourni par Eric Gailledrat (Figure 4). Tous ont l'engobe noir.

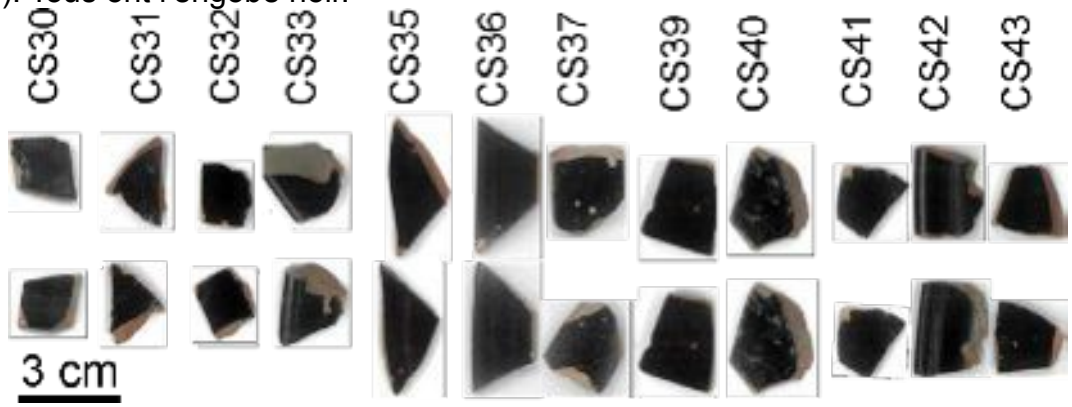

Figure 4 Des fragments sont excavés de Lattes et fourni par Eric Gailledrat.

L'information archéologique est donne par Table 1.

PHS2014-CS

	US	Catégorie	Remarques	Datation
CS30	71030	Attique vernis noir		-375/-350
/ 31	71024	Attique vernis noir		-325/-300
/ 32	51118	Attique vernis noir		-425/-400
/ 33	51118	Attique vernis noir	Castulo Cup	-425/-400
/ 34	51121	Attique vernis noir	Mauvaise cuisson ?	-425/-400
/ 35	53060	Attique vernis noir		-450/-425
/ 36	53038	Attique vernis noir	Castulo Cup	-450/-425
/ 37	53060	Attique vernis noir		-450/-425
/ 38	53564	Attique vernis noir	White slip	-450/-450
/ 39	53564	Attique vernis noir		-450/-450
/ 40	53917	Attique vernis noir	Coupe de type C, Delicate class	-475/-450
/ 41	53787	Attique vernis noir		-475/-450
/ 42	53960	Attique vernis noir	Coupe de type C	-500/-475
/ 43	53960	Attique vernis noir		-500/-475

Table 1 L'information archéologique de 12 fragments sélectionnés.

 La stratégie de la méthode conçue pour analyser les fragments. Tout d'abord, des échantillons de section transversale mince ont été préparés, ce qui est approprié pour être analysé à la fois par des techniques de laboratoire et de synchrotron. Deuxièmement, on a effectué un microscope optique et un microscope électronique à balayage (SEM) pour observer et sélectionner des échantillons nécessitant des investigations supplémentaires. Troisièmement, en raison du processus de cuisson est directement lié à l'état (valence, minéral) de fer, les échantillons sélectionnés a été analysé par FF-XANES pour identifier les espèces de Fe et de cartographier leurs distributions. Enfin, sur la base des données obtenues pour reconstruire la structure des poteries et en déduire le procédé de cuisson utilisé pour elles.

Tout d'abord, l'échantillonnage en coupe transversale a été sélectionné et les échantillons ont été observés au microscope optique. L'observation optique montre deux types d'échantillons: CS30, CS31, CS32, CS35, CS36, CS37, CS40, CS41, CS42, CS43) avec une seule couche d'engobe noire et les autres (CS33, CS39) avec double couches d'engobe. Par exemple, les échantillons en coupe transversale de CS32 et CS39 (Figure 5).

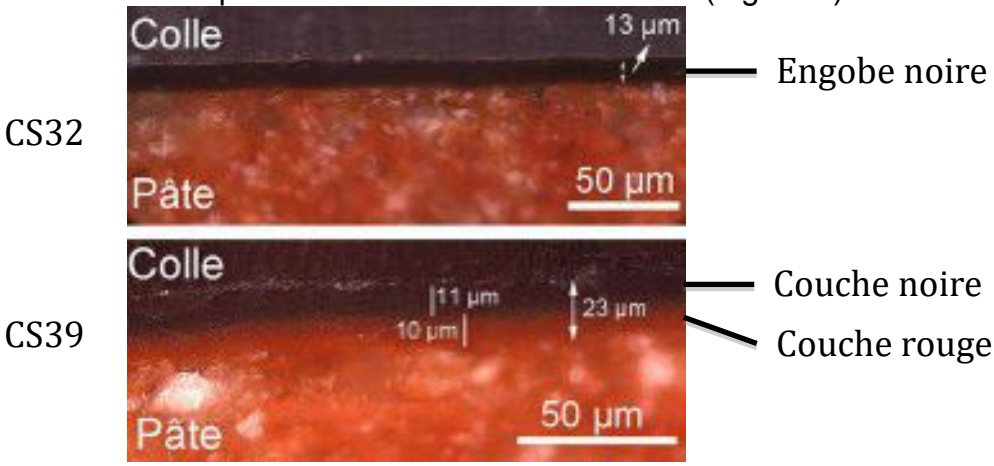

Figure 5 Deux types de vernis noir: échantillon CS32 et CS39.

Deuxièmement, des analyses de composition élémentaire classiques par la microsonde et la microscopie électronique à balayage (MEB)- analyse dispersive en énergie (EDS) ont été réalisées. Elles ont permis de comparer la composition avec l'étude précédente. Les résultats de la composition élémentaire sont cohérents avec les travaux précédents (Maniatis et al. 1993 et Mirti et al. 2006).

Troisièmement, FF-XANES a été choisi pour analyser les espèces de fer et leur distribution. Cette technique a permis d'analyser de grandes zones (~mm^2) avec une résolution sous-micrométrique (~0.7 m). Mais en présence de l'oxyde de fer hercynite et trivalent (α ou γ), la détection de la magnétite par XANES est très difficile. Par conséquent, la spectroscopie Raman a été choisie pour éliminer l'ambiguïté.

Pour des échantillons avec un seul engobe noir, les résultats montrent que le fer dans l'engobe est principalement valence bivalente avec formation d'hercynite ($FeAl_2O_4$) et de magnétite (Fe_3O_4). Dans la pâte, le fer est essentiellement de la valence trivalente avec formation de maghémite (γ-Fe_2O_3) et d'hématite (α-Fe_2O_3) (Figure 6). Les résultats sont cohérents avec le protocole de cuisson en trois étapes proposé par Noble en 1960.

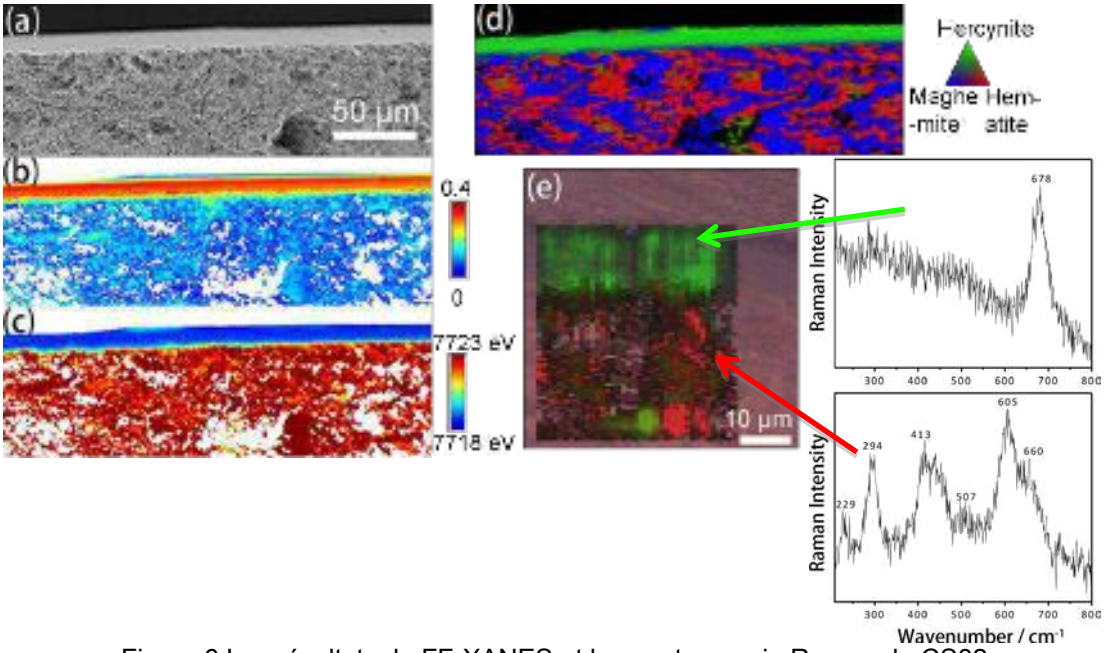

Figure 6 Les résultats de FF-XANES et la spectroscopie Raman de CS32.

Les résultats ont également révélé que le fer dans la surface d'engobe pourrait être plus (CS30 et CS31) ou moins (CS32, CS36, CS42 et CS43) réduit que dans le noyau d'engobe (Table 2). Ces deux situations sont compatibles avec le protocole de Noble de 1960. Ceci indique seulement que l'étape de réduction était sous une température plus élevée pour échantillons CS30 et CS31 et inversement que la troisième phase oxydante a commencé à une température plus élevée pour les échantillons CS32, CS36, CS42 et CS43.

	Body	Black slip	The surface
CS30	7122.5 (0.10)	7119.7 (0.33)	7119
CS31	7122.8 (0.07)	7119.4 (0.14)	7119.2
CS32	7122.5 (0.52)	7119.1 (0.13)	7119.4
CS36	7122.5 (0.39)	7119.2 (0.09)	7119.3
CS42	7122.5 (0.27)	7119.2 (0.10)	7119.4
CS43	7122.5 (0.27)	7119.6 (0.33)	7120.1

Table 2 Comparaison des valeurs moyennes de l'énergie des bords des pixels de la surface, le noyau l'engobe et la pâte. Pour CS31 et CS32, la surface est plus réduite que le noyau d'engobe. Pour les autres, la surface est moins réduite que le noyau d'engobe.

Pour des échantillons avec double couche d'engobe, les résultats (Figure 7) montrent que la présence d'hématite dans la couche d'engobe rouge est plus élevée que dans la pâte. Ils ont indiqué que la couche rouge ne peut être formée que dans la première étape d'oxydation et ne doit pas être formée dans la troisième étape d'oxydation. En fait, la température pendant la première étape pourrait être suffisamment élevée (> 825 ° C) pour vitrifier partiellement l'engobe. Les résultats (Figure 7) montrent également que le fer dans la couche noire extérieure est principalement divalente avec formation d'hercynite ($FeAl_2O_4$) et de magnétite (Fe_3O_4). Alors que dans la pâte, le fer est essentiellement trivalente avec la formation de maghémite (γ-Fe_2O_3) et l'hématite (α-Fe_2O_3). Ils ont aussi indiqué que, au cours de la deuxième étape de réduction, seule la couche extérieure d'engobe a dû être réduite et totalement vitrifiée. Pendant la phase finale, le fer de la pate a été oxydé pour être rouge. Les résultats sont cohérents avec le protocole de cuisson en trois étapes proposé par Noble en 1960 mais seulement avec une température plus élevée dans la première étape oxydante. Bien sûr, cette structuration de l'engobe est également conforme au protocole en deux cuissons proposés par l'équipe de Getty (Walton et al., 2013). Pour nos échantillons sans zone avec l'engobe rouge en surface, il n'est pas possible de choisir entre les deux hypothèses.

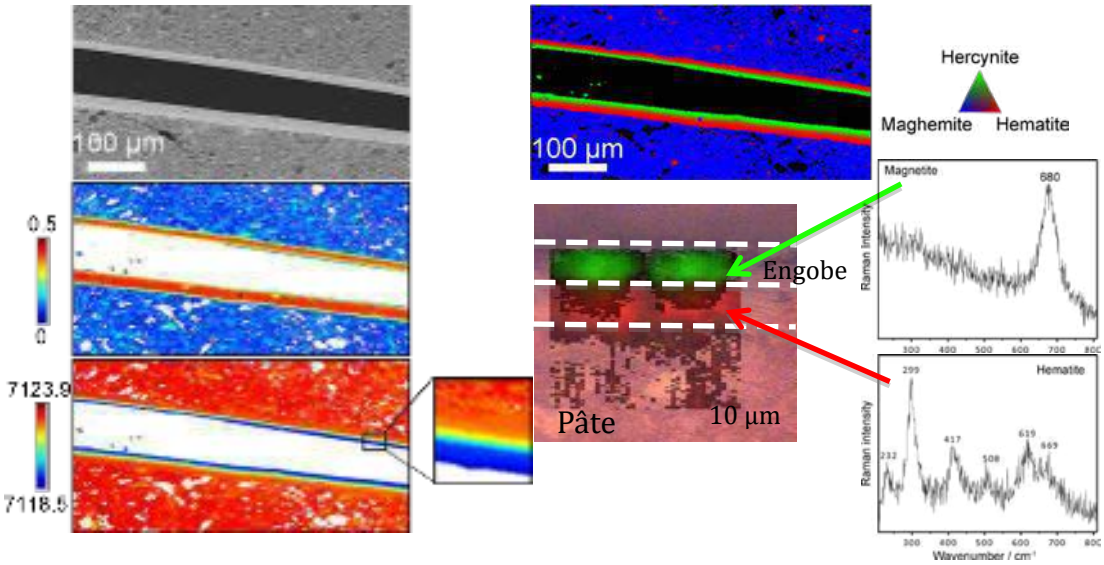

Figure 7 Les résultats de FF-XANES et la spectroscopie Raman de CS39.

 En résumé, le processus de cuisson des 12 fragments de céramique attique est en accord avec le processus de cuisson à trois étapes. Mais pour certains d'entre eux (CS33 et CS39), la première étape d'oxydation était à une température plus élevée ou pour d'autres (CS32, CS36, CS42 et CS43), la deuxième étape (réduction) était plus ou moins réduite. L'existence d'une double cuisson ne peut être ni confirmée ni rejetée par les échantillons étudiés. Il serait intéressant pour la poursuite des travaux de choisir les fragments à la fois avec du rouge et du noir et d'obtenir des informations concernant leur processus de fabrication par l'approche proposée dans ce travail.

Le vernis des sigillées marbrés se caractérise par une couleur jaune avec des veines rouges (Figure 8). Tout d'abord, l'échantillonnage en coupe transversale a été sélectionné et les échantillons ont été observés au microscope optique. L'observation optique montre que les deux vernis sont intimement liés, comme le montre l'image de droite de la Figure 6 où une couche de vernis rouge, d'une épaisseur de 14 µm, est bien mêlée à la couche de vernis jaune.

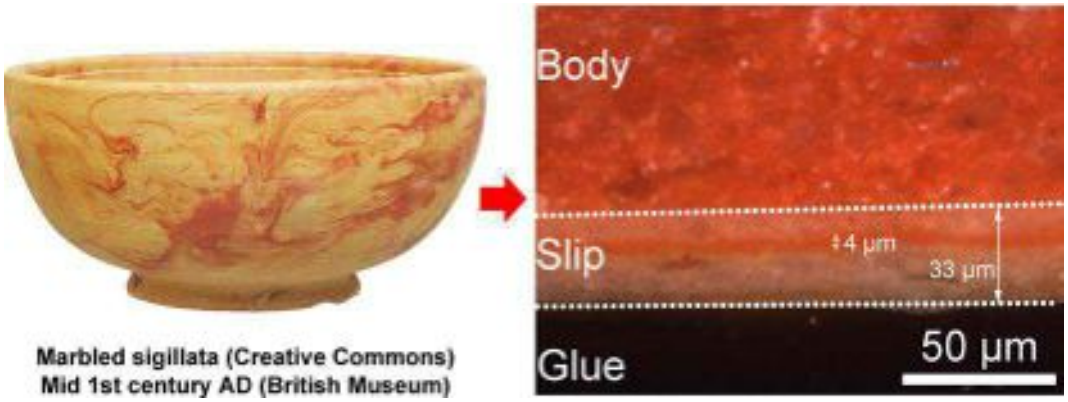

Figure 8 Une sigillée marbrée romaine typique (à gauche) et la coupe transverse de

l'échantillon contenant tous les composants pertinents (corps et vernis).

Puis, la spectroscopie Raman, les techniques à base de rayonnements synchrotron et la microsonde électronique ont été utilisées pour étudier le composé jaune des vernis (Figure 9). Les analyses par microsonde électronique réalisées sur un corpus significatif ont montré que le composé jaune a été obtenu à partir d'une préparation argileuse riche en titane. Les analyses XANES sur la raie K du titane confirment la présence massive de pseudobrookite (Fe_2TiO_5) en accord avec l'étude précédente. Les résultats Raman ont également permis d'identifier la présence de pseudobrookite après comparaison avec les spectres Raman de poudre de pseudobrookite synthétisée. L'étude d'un corpus significatif de sigillées marbrées (43 fragments) révèle que tous les échantillons montrent un spectre Raman, dans les zones jaunes, attribuable à la structure de la pseudobrookite. Cependant, ces spectres montrent des caractéristiques différentes des spectres de poudre de référence. Le décalage des pics et l'élargissement des raies pourraient être liés à la présence d'une pseudobrookite substituée en magnésium. Le magnésium joue un rôle clé dans la structure de la pseudobrookite: 1) il stabilise la structure en participant à une augmentation du désordre cationique et 2) il rend la couleur moins foncée et la fait virer au jaune ce qui explique la belle couleur jaune des sigillées marbrées. Ces résultats ont été publiés dans le Journal of Raman Spectroscopy.

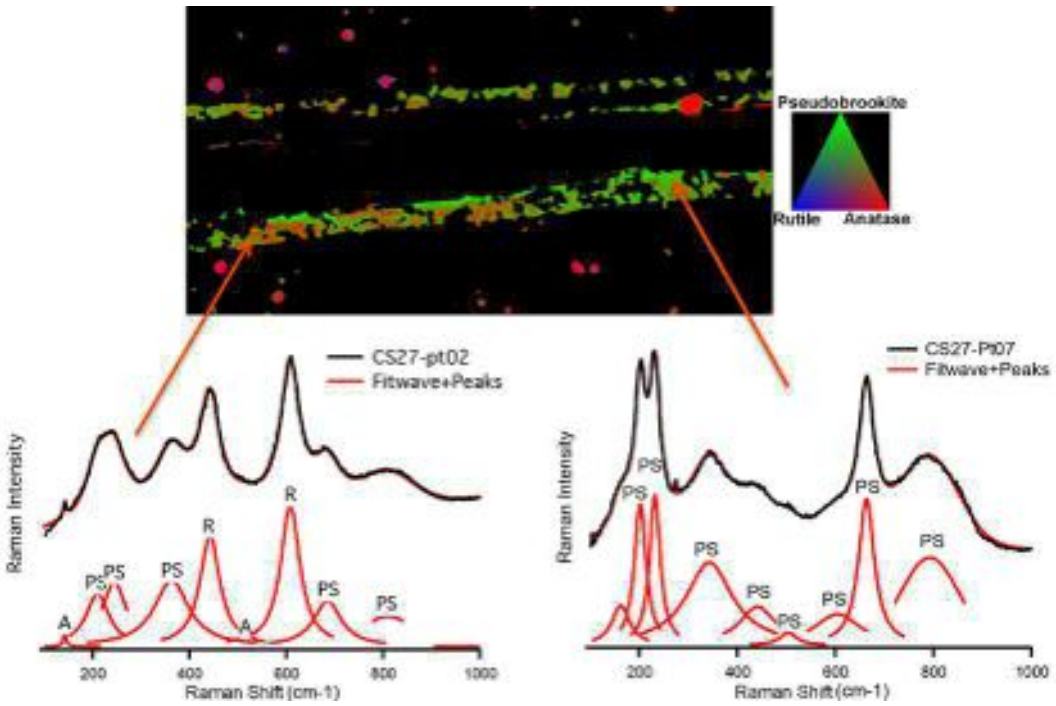

Figure 9 La cartographie des différente phase a été obtenue d'un affinement par moindre carré des références XANES pour la pseudobrookite (PS), le rutile (R) et l'anatase (A) pour chaque pixel XANES du vernis des sigillées marbrées (échantillon CS27). Le spectre Raman des particules de pseudobrookite correspondant à la cartographie des différentes phase est montré en dessou (les spectres originaux sont donnés en noir et fit-wave et les pics sont représentés en rouge).

Le chapitre IV présente l'étude de la variation de couleur des décors bleus de porcelaines chinoises de la période Yuan et Ming (**chapitre IV**).

La porcelaine chinoise Qinghua est caractérisée par un brillant blanc translucide avec un motif bleu peint en dessous (Figure 10). Elle apparue pendant la dynastie Tang (618-907). Mais la production est très rare pendent dynastie Song (960-1279). Pendant la dynastie Yuan, elle a atteint la maturité. (1206-1368) et pendant la dynastie Ming (1368-1644) et Qing (1638-1912), la production a été considérablement augmentée et exportée vers le monde entier.

Figure 10 Les production de porcelaine chinoise *Qinghua.*

En raison de la grande quantité de production Ming découverte, la plupart des études se sont concentrées sur la production de Ming pour expliquer la variation de couleur des décors bleus par deux aspects : composition chimique (Mn, Fe et Co) et composition cristallographique (couleur bleue: cristaux à base de cobalt (CoO, $CoAl_2O_4$) (Wang 2012) et bleu marine: oxydes de fer et de manganèse (Fe_3O_4, Mn_3O_4, $MnFe_2O_4$) (Wu 2007)). Cependant, la plupart des études précédentes n'ont été menées que sur plusieurs points plutôt que sur un aspect général, conduisant à une perte des informations clés. Donc, mon but est d'obtenir une information complète sur la variation de couleur des décors bleus, quatre Ming *Qinghua* fragments (Figure 11) typiques ont été sélectionné et analysés.

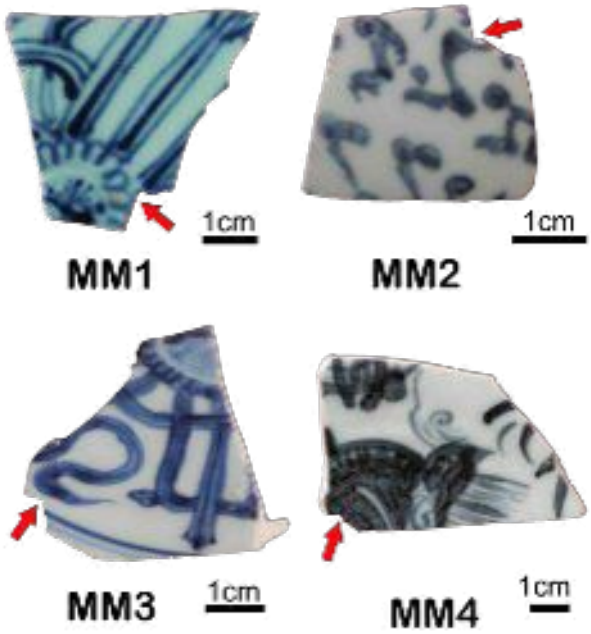

Figure 11 Quatre Ming fragments typiques sont sélectionnés. Ils ont excavées du site archéologique de Maojiawan de Beijing et fourni par l'Institut archéologique de Pékin. Ils sont les produits des ateliers folkloriques sont venus de Jingdezhen. Ils sont datées de l'ère Chenghua à l'ère Zhengde de la dynastie Ming (fin du XVe au début du XVIe siècle). Les zones d'échantillonnage sont indiquées par des flèches rouges.

Tout d'abord, une observation optique a été menée pour définir la zone nécessitant une investigation à haute résolution. Le pigment bleu a été appliqué sous la glaçure et dispersé dans la glaçure blanche après la cuisson. La variation de couleur des décors bleus est directement liée à la dispersion du pigment. Afin d'accéder à la zone dispersée de pigment, un échantillonnage en coupe transversale a été sélectionné. Une observation optique a été utilisée pour définir la zone dispersée de pigment. Par exemple, la section transversale de MM2-C3 est représentée par la Figure 12.

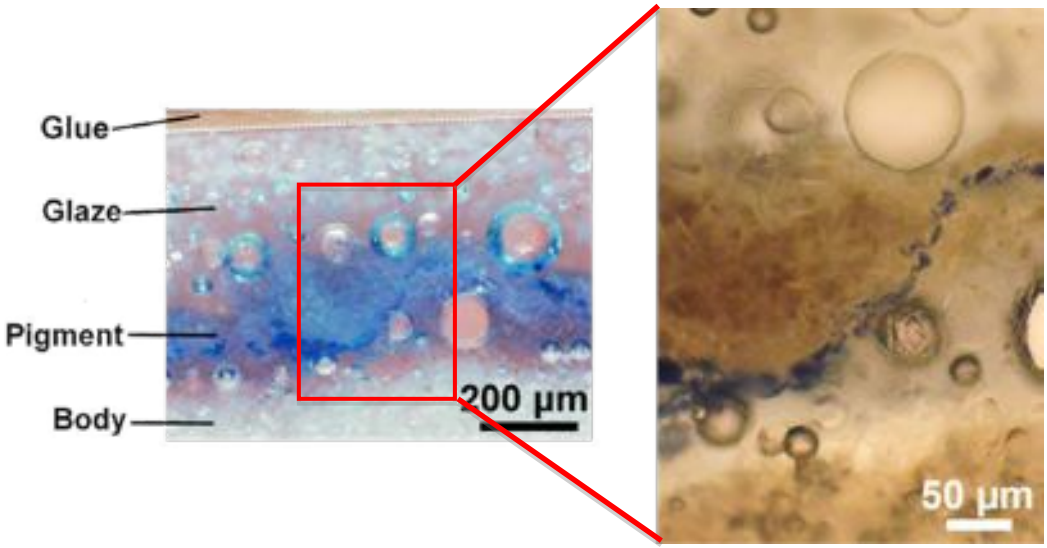

Figure 12 l'observation optique de la section transversale de MM2-C3.

 Puis, des techniques de synchrotron (SR-XRF, μ-XANES, μ-XRD) ont été choisies pour analyser la zone sélectionnée (Figure 13). Les résultats de SR-XRF illustrent des ions Fe à faible quantité sont répartis de façon homogène dans la glaçure entière sans différence significative dans les parties bleues et blanches. La valeur élevée de la quantité de Mn est plus élevée dans l'échantillon bleu foncé (MM2-C3) et l'échantillon noir (MM4-C2). Les ions Fe ne jouent pas un rôle significatif sur la couleur. Inversement, la quantité élevée de Mn dans les décors est la raison principale de l'obscurité de la couleur bleue. Les résultats de μ-XANES montrent que la Co spéciation est $CoAl_2O_4$ ou diffusée dans la glaçure. Pour les deux, Co est en coordination tétragonale. Les résultats de FF-XANES montrent la densité et la répartition des deux Co spéciations. Co en coordination tétragonale est la principale cause de la couleur bleue. La densité et la répartition des particules $CoAl_2O_4$ définissent la densité de la couleur bleue. μ-XRD a confirmé la présence de particules de $CoAl_2O_4$ et montre que les cristaux sont partiellement substitués par Fe ou Ni. Le TEM peux être utilisé pour identifier la substitution.

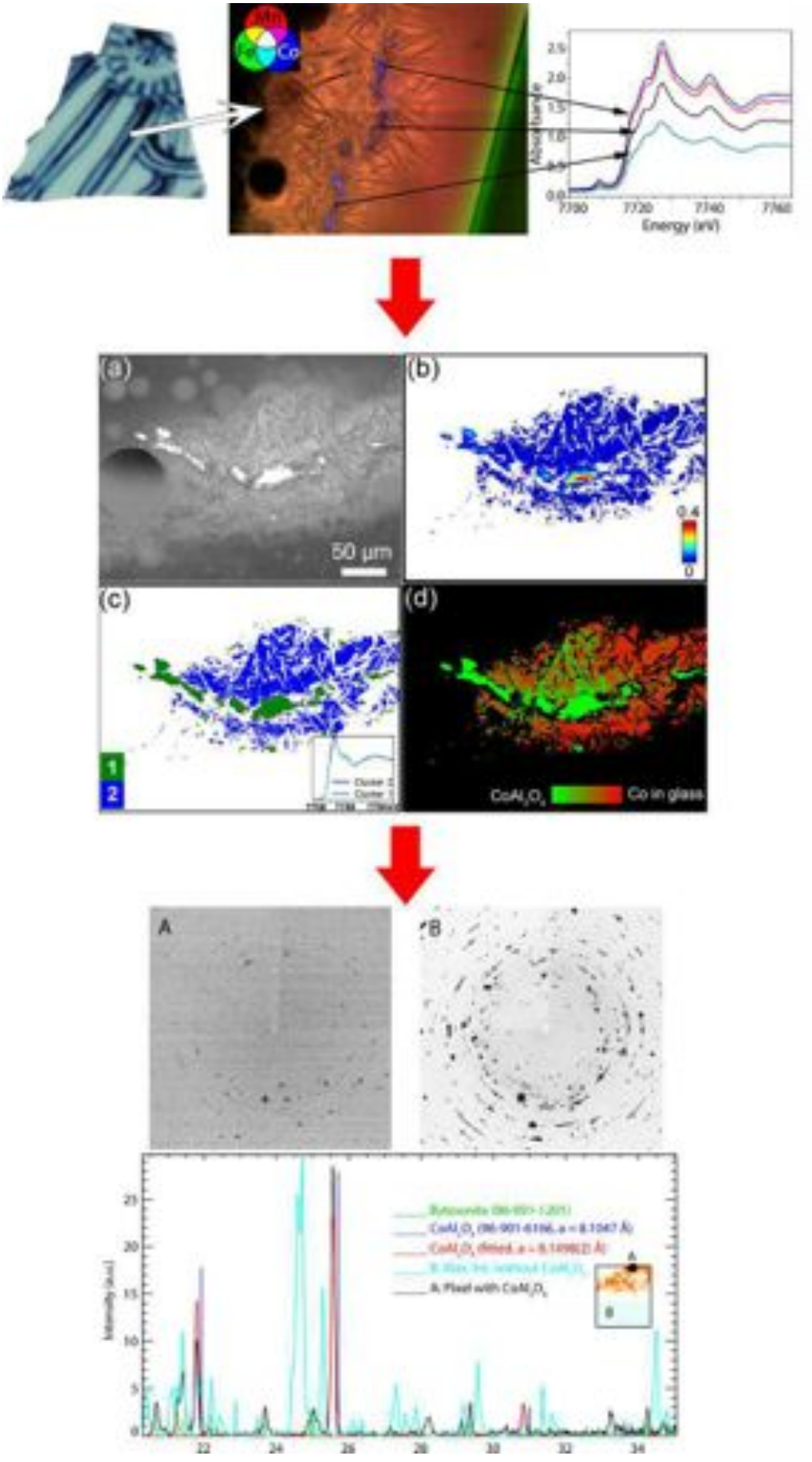
Al
Co
Absorbance
Energy (eV)
(a)
50 µm
(b)
0.4
0
(c)
1
2
(d)
$CoAl_2O_4$
Co in glass
A
B
Intensity (a.u.)

Figure 13 Analyse de l'origine de la couleur dans les décors bleus des porcelaines Qinghua de la dynastie Ming par une combinaison de μXRF, Full-field XANES au seuil-K du Co et μXRD à l'ESRF sur la ligne ID21. Les échantillons sont issus de fragments de porcelaine qui ont été préparés sous forme de fines coupes transverses. Les cartes μXRF montrent des concentrations particulières de Co et Ca dans la région pigmentaire et de Fe à la surface. Les résultats de Full-field XANES au seuil-K du Co (au milieu) révèlent la présence de deux espèces principales de Co dans le pigment et dans la glaçure (au milieu): (a) image en transmission enregistrée à 7670 eV, (b) cartographie de la hauteur du saut, (c) cartographie des cluster et des spectres XANES moyens obtenus par PCA (d) cartes de de spéciation obtenues par affinement par moindre carré (standards $CoAl_2O_4$ et Co dans la glaçure). La micro diffraction des rayons X permet de détemriner le paramètre de maille des pigments de Co (en bas).

Étant donné que la production de Yuan a été peu étudiée, j'ai choisi des techniques de laboratoire SEM-EDS et spectroscopie Raman pour extraire des informations concernant les décors bleus basés sur un corpus significatif (22 fragments). Tout d'abord, le SEM-EDS a été utilisé pour analyser la distribution élémentaire des décors bleus. L'image du signal des électrons rétrodiffusés m'a permis de positionner des éléments colorants (Mn, Fe et Co) et de chercher les cristaux apparentés, en raison du plus grand nombre atomique d'éléments colorants que d'autres (Si, Al, K, Ca, Na et Mg). Ensuite, la spectroscopie Raman a été utilisée pour analyser la nature de ces cristaux. La spectroscopie SEM-EDS et Raman a été effectuée sur l'échantillon de la vue en plan (Figure 14).

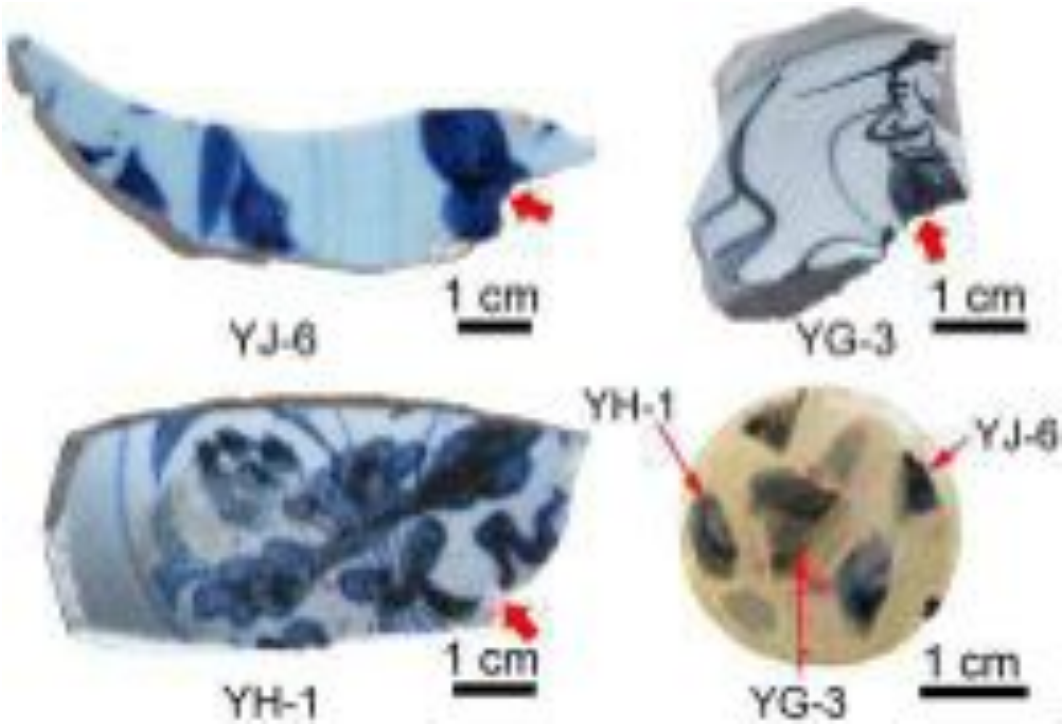

Figure 14 Des images optiques de trois fragments typiques (YJ-6, YG-3 et YH-1) et les échantillons préparés correspondants (la glaçure blanche de surface a été polie de quelques microns).

Puis, la spectroscopie Raman et la microscopie à balayage électronique couplée à un spectroscope à rayons X à dispersion d'énergie (SEM-EDX) ont

été utilisées pour analyser des porcelaines de l'époque Yuan. Les analyses SEM-EDX réalisées sur les taches noires présentes dans les décors bleus ont révélé la présence de cristaux dendritiques composés d'un oxyde mixte de cobalt et de fer (Figure 15). Le spectre Raman de ces cristaux est proche du spectre standard de la ferrite de cobalt ($CoFe_2O_4$). La comparaison des ratios Fe/Co obtenus par EDS et des spectres Raman correspondants a permis d'identifier deux types principaux de cristaux spinelles : un type riche en fer et un autre riche en cobalt. Les deux types de spinelles causent un obscurcissement des décors bleus. C'est la première fois que ces spinelles avec une composition proche de la ferrite de cobalt ont été observés comme principal constituant des taches noires dans les décors bleus des porcelaines *Qinghua*.

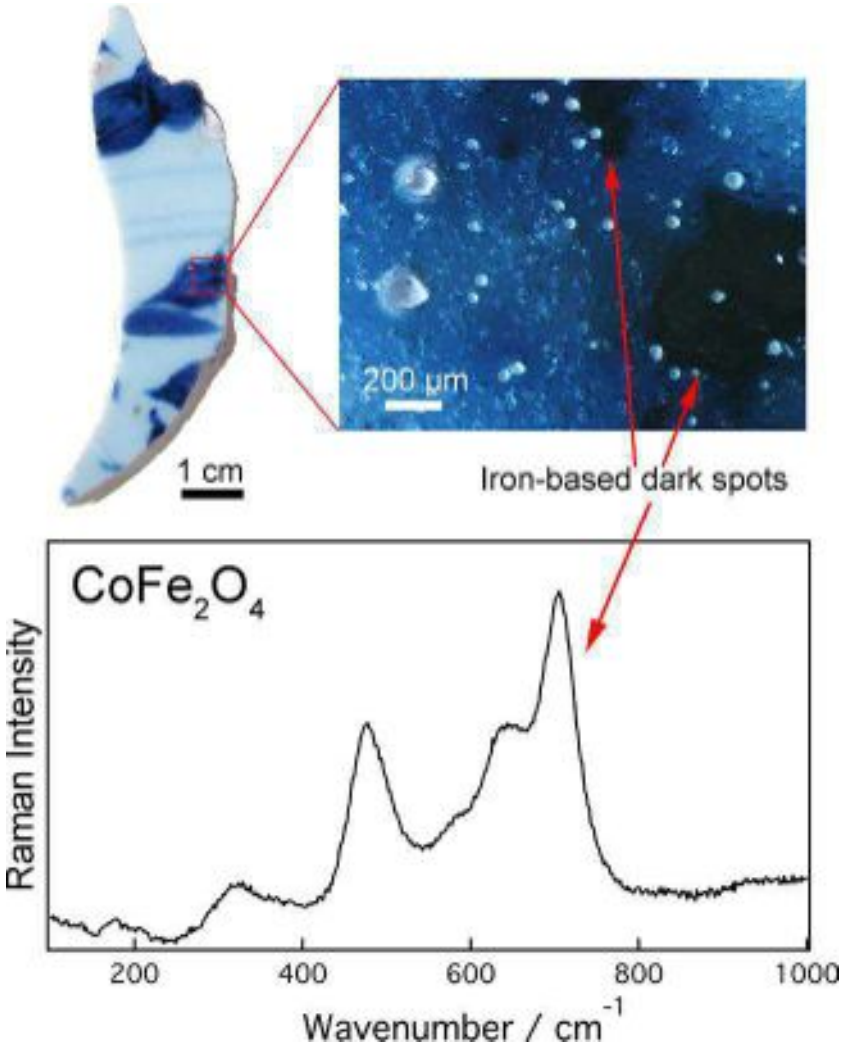

Figure 15 Un fragment de porcelaine *Qinghua* Yuan montrant des décors bleus avec des tâches noires. Les analyses Raman ont indiqué que les tâches noires sont dues à de la ferrite de cobalt ($CoFe_2O_4$).

En résumé, les techniques de laboratoire et le rayonnement synchrotron ont été sélectionnées pour étudier la variation de couleur des décors bleus. Cette combinaison de techniques peut également être utilisée efficacement pour analyser les décorations d'autres porcelaines colorées et déduire les informations concernant la variation de couleur des décors.

Le chapitre V présente les remarques conclusives et les perspectives de développement futur. En résumé, en utilisant une stratégie d'échantillonnage et en combinant des techniques différentes, il est possible de reconstruire partiellement la structure complexe d'une céramique ancienne et ainsi d'obtenir des informations intéressantes concernant le procédé de fabrication et / ou les propriétés optiques. Le choix de la zone analytique (ou volume) est crucial et détermine directement la nature de l'information obtenue. Le choix des techniques détermine la résolution (spatiale et spectrale) et l'échelle. La difficulté de l'approche est directement liée à ces choix, qui doivent être pris en compte dans les études antérieures mais aussi en fonction des objectifs de l'étude. La méthode dépend fortement des choix de l'expérimentateur mais elle est une alternative intéressante à un balayage d'un grand volume (plusieurs mm3 dans le cas de la céramique) d'échantillon à haute résolution permettant de reconstituer entièrement sa structure et composition en détails.

J'ai montré que cette approche est bien adaptée à l'étude des céramiques anciennes et pourrait être utilisée pour mieux comprendre la nature des différentes couleurs et le processus de fabrication des porcelaines colorées produites pendant la dynastie des Tang (7e - 10e s). Ces porcelaines présentent trois couleurs (brun, jaune et vert), comme le montre la Figure 16. Seules quelques recherches ont été menées sur l'étude des décors (Zhang et Guo, 1985, Lin et al., 1999) et une connaissance approfondie de la structure des décors serait très utile pour mieux comprendre leur variation de couleur et leurs processus de fabrication. Les premiers résultats ont révélé une distribution complexe d'oxydes de fer (α-Fe_2O_3 et ε-Fe_2O_3) en profondeur (de la surface à l'interface pâte/glaçure) avec formation de dendritiques en surface (Figure 17). □

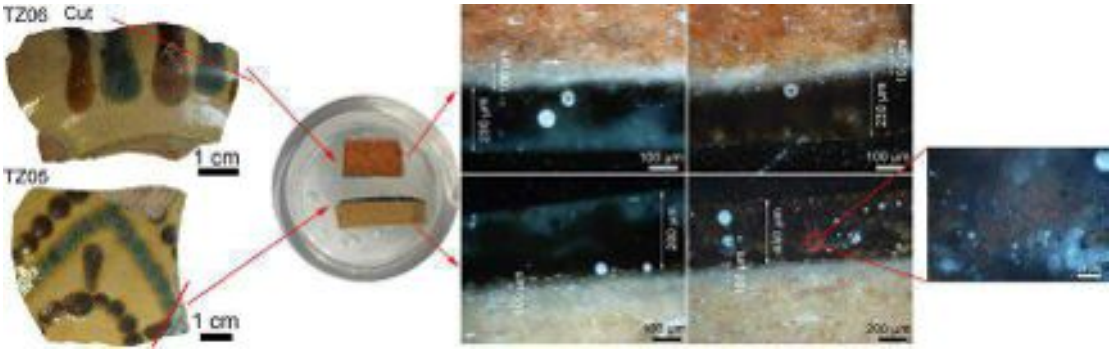

Figure 16 Porcelaines colorées de la dynastie des Tang (échantillon TZ05 et TZ06).

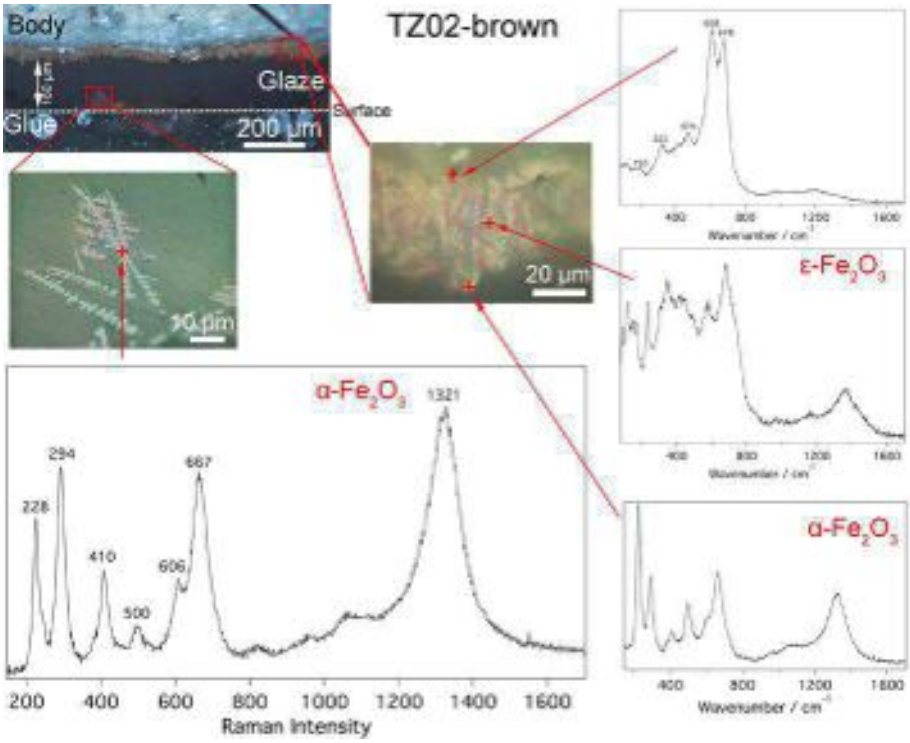

Figure 17 Résultats des analyses Raman effectuées sur la zone de couleur rouge de la glaçure (Echantillon TZ02).

Bibliographie

Boardman, J., 1985, Athenian Red Figure Vases: The Archaic Period: A Handbook Reprint edition ed., Thames & Hudson, London.

Boardman, J., 2006, The History of Greek Vases, Thames & Hudson, London.

Hobson, R., 1976, Chinese Pottery and Porcelain 1st edition ed., Dover Pubns, New York.

Johns, C., 1971, Arretine and Samian pottery 1st ed edition ed., British Museum, London.

Jorg, C. J. A., 1984, Interaction in ceramics: Oriental porcelain & Delftware, The Council, Hong Kong.

Lawrence, W. G., and West, R. R., 1982, Ceramic Science for the Potter 2 edition ed., Chilton Book Co., Radnor, Pa.

Leon, Y., Sciau, P., Goudeau, P., Tamura, N., Webb, S., and Mehta, A., 2010, The nature of marbled terra sigillata slips: a combined μXRF and μXRD investigation, Applied Physics A, 99(2), 419–25.

Li, J. Z., 1998, History of Science and Technology in China, Ceramics Volume, Science Press, Beijing.

Lin, E. K., Yu, Y. C., Wang, C. W., Liu, T. Y., Wu, C. M., Chen, K. M., and Lin, S. S., 1999, PIXE analysis of ancient Chinese Changsha porcelain, Nuclear Instruments & Methods in Physics Research Section B-Beam Interactions with Materials and Atoms, 150(1-4), 581–5.

Liu, Y., Andrews, J. C., Meirer, F., Mehta, A., Gil, S. C., Sciau, P., Mester, Z., and Pianetta, P., 2011, Applications of Hard X-ray Full-field Transmission X-ray Microscopy at SSRL, In AIP Conference Proceedings, Vol. 1365, 357–60, THE 10TH INTERNATIONAL CONFERENCE ON X-RAY MICROSCOPY, AIP Publishing.

Noble, J. V., 1960, The Technique of Attic Vase-Painting, American Journal of Archaeology, 64(4), 307–18.

Rice, P. M., 2015, Pottery Analysis, Second Edition: A Sourcebook, University of Chicago Press.

Sciau, P., and Goudeau, P., 2015, Ceramics in art and archaeology: a review of the materials science aspects, The European Physical Journal B, 88(5), 132.

Vandiver, P. B., Soffer, O., Klima, B., and Svoboda, J., 1989, The origins of ceramic technology at dolni vecaronstonice, czechoslovakia, Science (New York, N.Y.), 246(4933), 1002–8.

Wang, T., Sanchez, C., Groenen, J., and Sciau, P., 2016a, Raman spectroscopy analysis of terra sigillata: the yellow pigment of marbled sigillata, Journal of Raman Spectroscopy.

Wang, T., Zhu, T. Q., Feng, Z. Y., Fayard, B., Pouyet, E., Cotte, M., De Nolf, W., Salomé, M., and Sciau, P., 2016b, Synchrotron radiation-based multi-analytical approach for studying underglaze color: The microstructure of Chinese Qinghua blue decors (Ming dynasty), Analytica Chimica Acta, 928, 20–31.

Wang, L., and Wang, C., 2011, Co speciation in blue decorations of blue-and-white porcelains from Jingdezhen kiln by using XAFS spectroscopy, Journal of Analytical Atomic Spectrometry, 26(9), 1796–801.

Wen, R., Wang, C. S., Mao, Z. W., Huang, Y. Y., and Pollard, A. M., 2007, The Chemical composition of blue pigment on Chinese blue and white porcelain of the Yuan and Ming dynaties (ad 1271–1644)*, Archaeometry, 49(1), 101–15.

Wu, J., Leung, P. L., and Li, J. Z., 2007, A study of the composition of Chinese blue and white Porcelain, Studies in Conservation, 52(3), 188–98.

Zhang, Z., and Guo, Y., 1985, A study on Changsha Tongguan coloured glaze and painted wares, Journal of Jingdezhen Ceramic Institue, 6(1), 11–7.